AAAS

Science

26 JUNE 2025

WHEN AID ENDS

What U.S. assistance cuts mean for child health in Nepal

Recent PhD?

Science & SciLifeLab PRIZE
For Young Scientists

How about $30,000 US, having your essay published in *Science*, and being celebrated with a week of festivities in Stockholm, Sweden?

Apply now to the *Science* & SciLifeLab Prize for Young Scientists!

A global award aimed at young researchers

Every year, four early-career scientists from across the globe are awarded the *Science* & SciLifeLab Prize for Young Scientists for outstanding research they have conducted as part of their PhD.

The selected winners receive up to $30, 000 US in prize money for their accomplishments. In addition, all four winners are published in *Science* and invited by SciLifeLab to Sweden in December to participate in a unique week filled with events in honor of science. Here, they will be given the opportunity to meet with leading scientists in their field of research and create life-long connections to support their career.

Categories

The award is available in four categories:

- Cell and Molecular Biology
- Genomics, Proteomics and Systems Biology Approaches
- Ecology and Environment
- Molecular Medicine

More information

More information: scienceprize.scilifelab.se

Questions: scilifelabprize@aaas.org

Application deadline: July 15, 2025

Eligibility: applicants must have received their PhD between January 1, 2023 and December 31, 2024.

Enabled by the generous support of the Knut and Alice Wallenberg Foundation.

Knut and Alice Wallenberg Foundation

Science AAAS

SciLifeLab

CONTENTS

26 JUNE 2025
VOLUME 388
ISSUE 6754

1368 & 1389

EDITORIAL

NEWS

FEATURES

COMMENTARY

PERSPECTIVES

POLICY FORUM

ASU Science

PRIZE FOR TRANSFORMATIONAL IMPACT

Apply now to the Arizona State University and *Science* Prize for Transformational Impact!

Arizona State University and *Science* have partnered to create the **ASU–*Science* Prize for Transformational Impact**. This prize recognizes transformational research that uses innovative methods and approaches to identify problems and develop solutions with impacts on policy and decision-making.

The grand prize winner will receive a prize of **US$30,000** and their prize-winning essay will be published in *Science* online and print. A runner-up will receive **US$10,000** and have their essay published in *Science* online.

APPLY BY **AUGUST 15, 2025**

www. Science.org/ASU

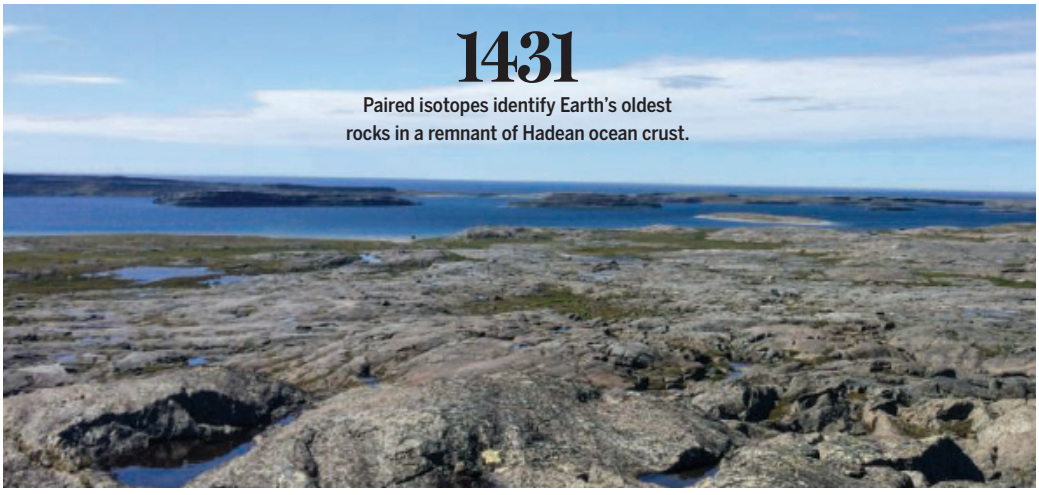

1431

Paired isotopes identify Earth's oldest rocks in a remnant of Hadean ocean crust.

PHOTO: JONATHAN O'NEIL

ON THE COVER

Radha Maurya, a 10-month-old living in the village of Nausahara, Nepal, is being treated for severe wasting. More cases of malnutrition like hers may go overlooked or untreated now that the U.S. has withdrawn funding for a program that helped screen children for wasting, ensure a steady supply of the nutrient-rich food paste used as treatment, and support staff at health posts in underserved Nepali communities. See page 1362. Photo: Uma Bista

Science **serves as a forum for discussion of important issues related to the advancement of science by publishing material on which a consensus has been reached as well as including the presentation of minority or conflicting points of view. Accordingly, all articles published in *Science*—including editorials, news, commentary, and book reviews—are signed and reflect the individual views of the authors and not official points of view adopted by AAAS or the institutions with which the authors are affiliated.** *Science* (ISSN 0036-8075) is published weekly on Thursday, except last week in December, by the American Association for the Advancement of Science, 1200 New York Avenue, NW, Washington, DC 20005. Periodicals mail postage (publication No. 484460) paid at Washington, DC, and additional mailing offices. The title *Science* is a registered trademark of the AAAS. Domestic individual membership, including subscription (12 months): $165 ($74 allocated to subscription). Domestic institutional subscription (51 issues): $2865; Foreign postage extra: Air assist delivery: $135. First class, airmail, student, and emeritus rates on request. Canadian rates with GST available upon request, GST #125488122. Publications Mail Agreement Number 1069624. **Printed in the U.S.A. Change of address:** Allow 4 weeks, giving old and new addresses and 8-digit account number. **Postmaster:** Send change of address to AAAS, P.O. Box 96178, Washington, DC 20090–6178. **Single-copy sales:** $15 each plus shipping and handling available from backissues.science.org; bulk rate on request. **Authorization to reproduce** material for internal or personal use under circumstances not falling within the fair use provisions of the Copyright Act can be obtained through the Copyright Clearance Center (CCC), www.copyright.com. The identification code for *Science* is 0036-8075. *Science* is indexed in the *Reader's Guide to Periodical Literature* and in several specialized indexes.

Science AAAS

EDITORIAL
science_editors@aaas.org

NEWS
science_news@aaas.org

INFORMATION FOR AUTHORS
science.org/authors/
science-information-authors

REPRINTS AND PERMISSIONS
science.org/help/
reprints-and-permissions

MULTIMEDIA CONTACTS
SciencePodcast@aaas.org
ScienceVideo@aaas.org

MEDIA CONTACTS
scipak@aaas.org

PRODUCT ADVERTISING & CUSTOM PUBLISHING
advertising.science.org
science_advertising@aaas.org

CLASSIFIED ADVERTISING
advertising.science.org/
science-careers
advertise@sciencecareers.org

JOB POSTING CUSTOMER SERVICE
employers.sciencecareers.org
support@sciencecareers.org

MEMBERSHIP AND INDIVIDUAL SUBSCRIPTIONS
science.org/subscriptions

MEMBER BENEFITS
aaas.org/membership/
benefits

INSTITUTIONAL SALES AND SITE LICENSES
science.org/librarian

Science AAAS

CHEN TIANQIAO & CHRISSY INSTITUTE

CO-HOST
ETH zürich

AI & MENTAL HEALTH

SEPTEMBER 8-9, 2025 | ZURICH

Mental health is a vast and growing worldwide problem. In addition to the suffering experienced by individuals and their affected family members it also has an enormous economic impact. Because it can affect people at a young age they will often need treatment for many years and during that period they will not be able to participate to their full potential in society.

REGISTER TODAY!

Ten times faster is not 10 times better

Alondra Nelson

As the Trump administration systematically defunds the American research ecosystem, while disingenuously promising a return to so-called "gold standard science," hope can be drawn from the new bipartisan initiative from Senators Martin Heinrich (Democrat, New Mexico) and Michael Rounds (Republican, South Dakota). Their American Science Acceleration Project (ASAP) seeks to make science in the United States "ten times faster by 2030" through five pillars: data, computing, artificial intelligence (AI), collaboration, and process improvement. But simply accelerating will exacerbate historical weaknesses in our innovation system and reproduce the damaging Silicon Valley ethos of "move fast and break things." Faster is not necessarily better when it comes to innovation and discovery. Supercharging a research ecosystem that already struggles with accessibility and public trust risks more than it achieves.

Supercharging a research ecosystem that already struggles with... public trust risks more than it achieves.

The initiative, now open for public comment (until 30 June), presents an opportunity to examine, restore, and improve publicly funded research as well as redefine what acceleration should mean in 21st-century science amid current political realities. Unfortunately, the proposal offers a narrowly technocratic interpretation of acceleration, mainly emphasizing an ever-greater role for AI, without critical analysis of where and how these tools are helpful or harmful. If the United States seeks faster breakthroughs, it must simultaneously consider ways to open the system to wider participation while ensuring that the public—as providers of research funding and data—benefits from research.

Consider ASAP's vision for democratizing access to "AI-ready" data that individuals provide with permission. When human genomic data became available, it indeed accelerated discoveries worldwide, expanding understanding of disease-causing mutations and human evolution. However, endeavors like the Human Genome Project have also shown that more care is necessary to respect refusal, protect privacy, and compensate data sharing.

ASAP's commitment to provide access to advanced computing does not go far enough. Current systems continue to favor established researchers at elite institutions. If "AI-ready" data—information that is provided with consent and is accessible for training machine learning models—require sophisticated preprocessing, then under-resourced institutions will be left out. A truly accelerated discovery ecosystem would prioritize distributing these capabilities as a first step.

ASAP also envisions scientists as "copilots" for AI, with computational approaches operating under human direction and oversight. This sounds reassuring, but implementation will be complex. Research often requires challenging fundamental assumptions in uncharted territory where no "correct" course exists.

When researchers use similar AI models trained on historical literature, they may be pushed toward incremental advances while missing paradigm-shifting discoveries. Take, for example, Barbara McClintock's work on DNA transposons, which was initially rejected because it challenged prevailing assumptions—assumptions that would be encoded into any AI system trained on existing science literature. Then there is the issue of who will have control over scientific results. Innovations, including the internet precursor Advanced Research Projects Agency Network, Global Positioning System technology, and many life-saving diagnostics, emerged from public investments that ultimately succeeded in offering benefits to a wide market over gains for a small group. When the originators of the Human Genome Project and AlphaFold (an AI system that predicts protein structures) chose open sharing over proprietary control, they enabled researchers and companies to build on this widely available information.

Accelerated science must also be regulated science. American pharmaceutical companies succeed not despite rigorous safety standards but because of them. Approval by the US Food and Drug Administration has been a benchmark precisely because it endeavors to balance innovation with accountability. Speed without legitimacy is self-defeating in a world where scientific credibility determines adoption.

ASAP's emphasis on cross-disciplinary teamwork addresses genuine limitations to the current system but needs to be broader. Challenges—from responsible AI development to climate adaptation—require expertise spanning multiple fields. Yet academic incentives still reward narrow specialization over collaborative breadth. The initiative's vision of attracting talent across the nation raises questions about whose talents count. Scientific collaboration has historically excluded knowledgeable community members who lack advanced degrees. Traditional fire management practices, community health insights, and enduring ecological knowledge might complement formal scientific research. Farmers working with climate scientists through systems that integrate remote-sensing data with traditional weather prediction methods might come up with better solutions—and a wider acceptance from the farmers themselves. There may be differences, but innovation accelerates through creative friction.

What should emerge from an effort like ASAP is an ecosystem that eliminates barriers to participation rather than one that accelerates inequities. The United States can either succumb to existing research patterns or fundamentally reshape them to address persistent hurdles. Only one of these paths leads to true innovation. □

Alondra Nelson is the Harold F. Linder Chair at the Institute for Advanced Study, Princeton, NJ, USA. anelson@ias.edu

10.1126/science.adz9545

NEWS

SEISMOLOGY

Japan wires up offshore trenches to warn of ruptures

Seafloor monitoring is revealing how "slow slip" earthquakes can lead to big ones **PAUL VOOSEN**

The 2011 Tōhoku earthquake triggered a deadly tsunami in the Fukushima region of Japan.

In August 2024, the Hyūga-Nada earthquake erupted off the southeast coast of Japan near the Nankai Trough, where a plate of ocean crust plunges into the mantle. The magnitude 7.1 earthquake injured 16 people and damaged a handful of buildings, and it stirred fears of something much worse. Subduction zones like the Nankai cause the world's largest earthquakes and tsunamis, and the Nankai had been quiet for more than 75 years, storing up strain like a spring. No one has forgotten the Tōhoku earthquake of 2011, when a convulsion near the Japan Trench, the country's other subduction zone, devastated the Fukushima region, killing nearly 20,000 people with a 40-meter-high wave.

Fortunately, Japan will soon be far better prepared than 15 years ago. In the next few months, it will finish work on an instrumented network of seafloor cables and wire it directly into a national early warning system. By detecting earthquakes closer to their source, the $120 million network, called N-net, will give power stations and bullet trains precious extra seconds to turn off and stop. Part of N-net came online just before the Hyūga-Nada quake and proved its mettle by quickly detecting the event and indicating that, even though the ocean plate slipped by 3 meters, the resulting tsunami measured only a few centimeters.

Combined with two other completed offshore networks, the system will cover the entirety of the two subduction zones and gather data from more than 200 instrumented nodes containing seismometers and pressure sensors. Japan has also deployed more than two dozen seafloor GPS stations. No other country menaced by subduction zones has anything like it, says Laura Wallace, a marine geodesist at the GEOMAR Helmholtz Centre for Ocean Research Kiel. "They're setting a standard that the rest of the world needs to catch up to."

The primary purpose of these networks is to provide warnings, says Shin Aoi, director-general of Japan's National Research Institute for Earth Science and Disaster Resilience. He estimates N-net will provide an additional 22 seconds of warning of a great earthquake near the Nankai Trough and 20 minutes more for a tsunami. But the networks, along with dense instrumentation on Japan itself, are also revealing fundamental insights into how subduction zones work, researchers report in two papers published in *Science* this week (pp. 1396 and 1401). "By observing up close, we can reveal phenomena in more detail," Aoi says.

Until early this century, it was thought that subducting plates either slip smoothly or become stuck, accumulating strain that eventually gets released in the jolt of an earthquake. But it's now known that these fault zones can also see periods of "slow slip," where the plates creep along nearly imperceptibly for months or years, generating odd, low-frequency seismic signals.

PHOTO: KIM KYUNG-HOON/REUTERS

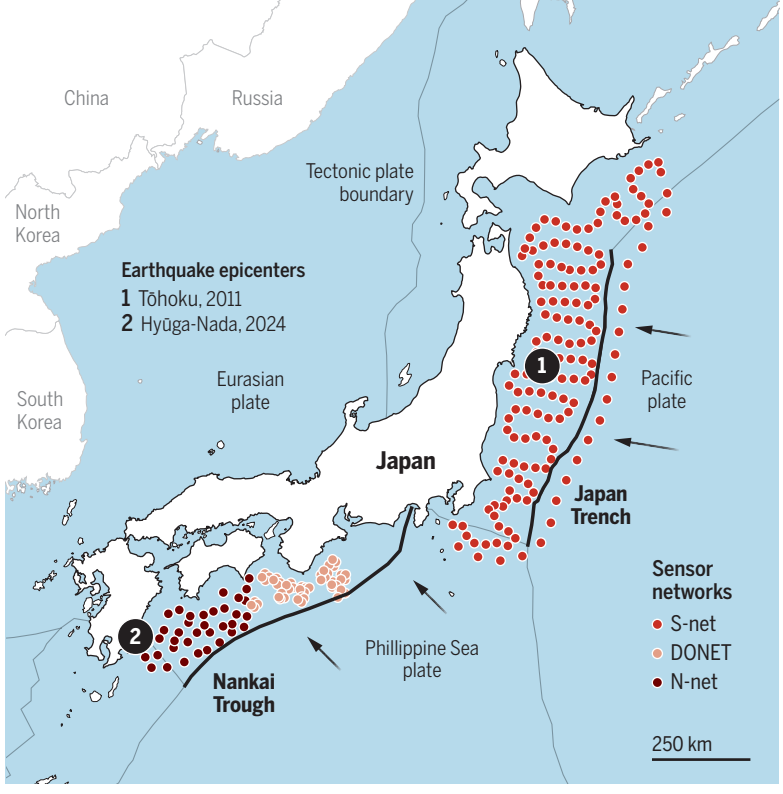

Seafloor sentinels Since the Tōhoku quake and tsunami struck in 2011, Japan has built three offshore monitoring networks comprising more than 200 instrument stations, connected to the mainland by optical fiber. The networks provide real-time warnings and insights into subduction zones, where one tectonic plate dives under another at a seafloor trench.

The 2011 Tōhoku quake highlighted how these slow-motion earthquakes are more than a curiosity. Two offshore sensors Japan had deployed at the time showed that one part of the locked fault had been slipping slowly for weeks before the main shock. The finding suggested the slow slip might have triggered the event by stressing other parts of the fault, raising hopes that monitoring slow slip events could help forecast major ruptures ahead of time. "Physically it's not a crazy thing to think the ground moves slowly before it moves quickly," says Emily Brodsky, an earthquake physicist at the University of California, Santa Cruz. "But practically nobody has ever seen it."

One *Science* study supports that idea. Based on the movement of GPS stations on land, researchers identified a series of escalating slow slip events deep in the Nankai subduction zone in the year leading up to the Hyūga-Nada quake—suggesting they had critically stressed the fault.

The other *Science* paper, in contrast, suggests slow slip, when it happens on the shallow part of the fault, can reduce the hazard of a giant earthquake. The data come from borehole observatories sunk into the rock below DONET, a second cable network deployed early last decade across the northern section of the Nankai Trough. By detecting tiny pressure changes in fluid trapped in the rock, the researchers documented two slow-slip events rippling past, in 2015 and 2020. They showed the slip traveled some 40 kilometers upward from the depths of the fault, almost all the way to the trench. "It's unzipping out to the trench, like an inchworm," says study co-author Demian Saffer, director of the University of Texas Institute for Geophysics. He says the repeated slip indicates the rocks in this shallow part of the fault could dissipate energy that might otherwise accumulate and drive dangerous, tsunami-causing ruptures.

Although the United States is far from reproducing Japan's offshore networks, it is taking steps toward a monitoring system for the Cascadia subduction zone, a trench in the Pacific Ocean where a future earthquake could threaten Seattle or Portland. Researchers last year finished deploying a set of seafloor GPS stations in the Cascadia and the Alaskan subduction zones. And the National Science Foundation is supporting the addition next year of four advanced instrument packages to a cable network it operates off the Oregon coast, with the hopes that they could also connect to earthquake and tsunami early warning networks. Later this year, U.S. researchers plan to propose an ambitious facility called SZ4D, which would monitor Chile's subduction zone, an offshore trench that in 1960 generated Earth's largest known earthquake at magnitude 9.5.

Executing those plans means finding cheaper ways to monitor rocks deep underwater and far offshore—so the systems don't require a tragedy to get them deployed. "The Japanese have the Cadillac," Wallace says. "We need to figure out how to get a pretty good Toyota Corolla for the rest of the world." □

CREDITS: (GRAPHIC) M. HERSHER/*SCIENCE*; (DATA) NATIONAL RESEARCH INSTITUTE FOR EARTH SCIENCE AND DISASTER RESILIENCE; U.S. GEOLOGICAL SURVEY

IN OTHER NEWS

FIRST WOMEN WINNERS FOR CLIMATE PRIZE Three climate scientists—two women and a man—won the 1 million Swiss franc ($1.1 million) Frontiers Planet Prize last week, marking the first time in the prize's 3-year history that women have been awarded. Arunima Malik, a University of Sydney sustainability researcher; Zahra Kalantari, an environmental and geosciences engineer at the KTH Royal Institute of Technology; and Zia Mehrabi, a climate and agriculture data scientist at the University of Colorado Boulder, were recognized for their work researching solutions to a rapidly warming planet. Over the prize's first 2 years seven men won, a trend that led to an open letter criticizing the committee's process. The prize can only go to a single recipient, for instance, which can encourage nominators to put forward only leaders of research teams—who are more often men. "I see this award as a recognition that we are also among the men ... to address the social challenges that we are facing," Kalantari told *Science*.
—Annika Inampudi

The National Academies is being reorganized, but its landmark Albert Einstein statue will stay.

RESEARCH POLICY

National Academies adopts new business model amid financial storm

Realignment of major program units aims to improve efficiency and make up for loss of federal contracts **JEFFREY MERVIS**

The National Academies of Sciences, Engineering, and Medicine (NASEM) last week announced the launch of a major downsizing to help cope with a significant loss of federal funding since President Donald Trump took office.

As many as one-fifth of the roughly 60 top-level advisory boards that generate ideas for the society's hallmark consensus reports could disappear as part of a restructuring of the National Research Council, NASEM's operating arm, says Marcia McNutt, president of the National Academy of Sciences and NRC chair, and former editor-in-chief of *Science*. Although the cancellation of federal contracts has forced her hand, McNutt thinks a leaner NRC should be able to provide policymakers with faster and more relevant scientific advice.

"To be honest, I wanted to streamline the NRC as soon as I arrived at the academy 9 years ago," McNutt says. "But everything was going along just fine. Finally, we have the trigger to do this."

The new structure will likely result in additional staff cuts. NASEM has already laid off 50 of its roughly 1000-person staff this year. McNutt foreshadowed possible further layoffs earlier this month but did not offer new details last week.

Reaction has been mixed among those involved in NRC activities. "I am glad to hear that the leadership is working to streamline the NRC's operations … and thinking creatively about additional avenues for engagement with the federal agencies," says Katharine Abraham, an economist at the University of Maryland and chair of NRC's Committee on National Statistics (CNSTAT), which has suffered significant staff layoffs after losing several contracts. But another board chair is worried. "None of us knows at this point how the configurations will impact our work," says Susan Rundell Singer, president of St. Olaf College and chair of the Board on Science Education.

NRC currently has seven major program units, most of which are organized around scientific disciplines such as health and medicine or engineering and the physical sciences. Each unit oversees as many as a dozen standing boards and committees—groups of volunteers that focus on specific topics, such as science education, population and public health, or food and nutrition. Those boards generate ideas for studies to be carried out by ad hoc panels of experts—assuming NRC staff can find a government agency, company, or foundation to foot the bill.

That structure has historically allowed NRC to tap into a deep pool of scientific talent and produce definitive studies on myriad topics. But it can also be unwieldy and inefficient, McNutt says. That's tolerable when budgets are flush. But it looms large when the U.S. government—which in 2023 provided about $200 million or 80% of NRC's budget—tightens its belt. That vulnerability became clear this year after the Trump administration killed 43 contracts, amounting to roughly 15% of its support.

The new structure collapses five of the discipline-specific units into two newly created "centers"—the Center on Health, People, and Places and the Center on Advancing Science and Technology. Each will oversee six program areas that, unlike the current boards, focus on topics rather than disciplines. That approach, McNutt says, is intended to appeal to potential sponsors who want to solve problems that require drawing on expertise in many disciplines.

The two remaining units have a stable funding source, McNutt says, and will be essentially unchanged: the Transportation Research Board, backed by the transportation sector, and the Gulf Research Program, spawned by a $500 million settlement from the 2010 *Deepwater Horizon* oil spill in the Gulf of Mexico.

McNutt is also creating three new offices, including one for strategy and engagement. It's designed to let "staff members that are really good at engaging with federal sponsors" secure funding, she explains, while other

PHOTO: FELIX ZAHN/PHOTOTHEK VIA GETTY IMAGES

staffers would manage the project. At present, staffers are expected to excel in both areas, she says.

McNutt says NASEM has yet to figure out how the existing boards and committees would fit into the new NRC structure. She estimates that "perhaps 20%" might disappear and the rest "will be working harder." That could mean having a standing board occasionally do the study itself rather than delegating it to a panel of experts that takes time and resources to assemble, McNutt says.

The new structure may also save money, McNutt says. "If we end up, as we hope, becoming a more efficient organization through this restructuring, then our overhead could actually go down, which would be fabulous."

Abrahams agrees. "The cost and lengthy timeline for commissioning a consensus study or workshop can be a real deterrent to those seeking help from the NRC," she says. "Lower overhead rates and a broader menu of options for engaging with federal agencies would be very positive developments."

At the same time, McNutt pledges to retain some of NRC's most prominent units, including CNSTAT, a 53-year-old panel with a congressional mandate to improve the quality of federal statistics, the Committee on Human Rights, and the Committee on International Security and Arms Control.

McNutt also pledged continued support for NRC's Roundtable on Black Men and Black Women in Science, Engineering, and Medicine and its Committee on Women in Science, Engineering and Medicine, despite the Trump administration's assault on diversity, equity, and inclusion programs. That committee already draws most of its support from private sources, McNutt notes. But private foundations can't be expected to step in and replace government contracts, she says, adding that right now it's more important that their support go toward narrowing shortfalls in government funding for basic research.

McNutt says many details of the restructuring need to be worked out before the plan is fully implemented in September. And she acknowledges that means more uncertainty for staff.

"We are already at a 15% contraction of our budget and our workload," she says. "Will we have to go higher? Thirty percent is our worst-case scenario. We hope that it won't be that bad. But we think that this new model could accommodate a cut of that amount." □

THEY SAID IT

It's not merely a hardware problem. It's the sovereignty of our digital future.

Lacina Koné, director general of Smart Africa, speaking to *The New York Times* about the continent's current low artificial intelligence capacity

BIOMEDICINE

Tumors may get energy boost from nerve cells' mitochondria

Study shows the organelles traveling through "bridges" into nearby cancer cells **MITCH LESLIE**

Cancer cells may acquire some of their destructive vigor from their healthy neighbors. A research team has found that neurons donate mitochondria, energy-producing organelles, to the malignant cells, a discovery that could explain why tumors often grow faster in the presence of nerves. By passing on their power stations, neurons may also increase cancer cells' ability to spread to other parts of the body, the group reports this week in *Nature*.

The study is "very important," says immunologist Jon Brestoff of the Washington University School of Medicine, who wasn't connected to the research. "It is the first to demonstrate that neurons transfer mitochondria to cancer cells." The findings also suggest blocking these transfers could be a new way to treat cancer.

Researchers used to think cells hoard their mitochondria, remnants of ancient symbiotic bacteria that provide metabolic fuel. But studies over the past 20 years or so have shown cells share the organelles promiscuously. Cancer cells can be recipients and donors. Earlier this year, for instance, Japanese researchers revealed that tumor cells and immune sentinels known as T cells sometimes swap mitochondria. The cancer cells use these exchanges to unload their faulty organelles on the T cells, impairing antitumor immunity.

A separate line of research has revealed that nerves promote growth of nearby tumors. One study, performed in 2017 by cancer neurobiologist Gustavo Ayala of the University of Texas Health Science Center at Houston and colleagues, found that prostate tumors shrank in lab animals when nerves to the gland were cut or silenced with Botox. Botox injections into the prostate gland in humans with tumors there also increased the death rate of the cancer cells. "We showed that cancer doesn't like to grow without nerves," Ayala says.

Cancer cells that have lost their nerve suffer from an impaired metabolism, the scientists also discovered. Cancer neurobiologist Simon Grelet of the University of South Alabama wondered whether they had been cut off from their source

of borrowed mitochondria. He, Ayala, and colleagues found that tiny bridges formed between breast cancer cells and neurons growing in dishes. When they labeled mitochondria in the neurons with a green protein, they saw the organelles traveling across the bridges into the cancer cells.

The researchers also genetically altered female mice so neurons in their abdominal fat carried green-tagged mitochondria. They then injected cancer cells into the fat. Three weeks later, some of the cancer cells showed telltale green spots.

Ayala, Grelet, and colleagues went on to show that such donated power generators can boost cancer cells engineered to lack working mitochondria of their own. These cells don't divide and their oxygen consumption, a sign of their metabolic activity, is low. But after 5 days in culture with nerve cells, their metabolism had rebounded and they reproduced vigorously, presumably because they acquired working mitochondria from their neighbors.

The green marker proteins the scientists originally used to observe the organelle transfers fade quickly, making it hard to study the long-term impact of the donated mitochondria. For a more lasting marker, the team genetically altered neurons and cancer cells so that when neurons' mitochondria hop to a cancer cell, the recipient permanently turns green.

The method helped reveal that recipient cells produced more adenosine triphosphate, the main energy source for cellular chemical reactions, among other metabolic benefits. Transfer of mitochondria "supercharges the cancer cells," Ayala says.

The researchers applied the technique, dubbed MitoTRACER, to investigate whether these revved up cancer cells would be more likely to metastasize, or move to new parts of the body. After raising mouse neurons and cancer cells together, they injected both kinds of cells into the abdominal fat of female mice. Abdominal tumors formed and soon spread to the lungs and brain.

The researchers analyzed cells from the original tumors and their metastases. Only about 5% of cancer cells in the original tumors had acquired mitochondria from neurons. However, 27% of cancer cells that reached the lungs and 46% of those in the brain sported mitochondria from nerve cells, indicating that transfer of the organelles can boost metastasis. To stymie cancer's spread, "target not just metastatic cells, but the supercharged cells," Grelet proposes.

The researchers also found evidence for mitochondrial transfer in cancer patients by analyzing tissue samples from prostate tumors. The closer cancer cells were to nerves, the more mitochondria they harbored.

"I love this paper" because MitoTRACER will be a boon "for people studying the role of mitochondrial transfer in disease," says cancer researcher Dionysios Watson of the University of Miami Miller School of Medicine. "I think the work is very compelling," adds immunologist Luca Gattinoni of the Leibniz Institute for Immunotherapy. The next task for researchers, he says, is "to find drugs that interfere efficiently with the [transfer] process." □

IN FOCUS

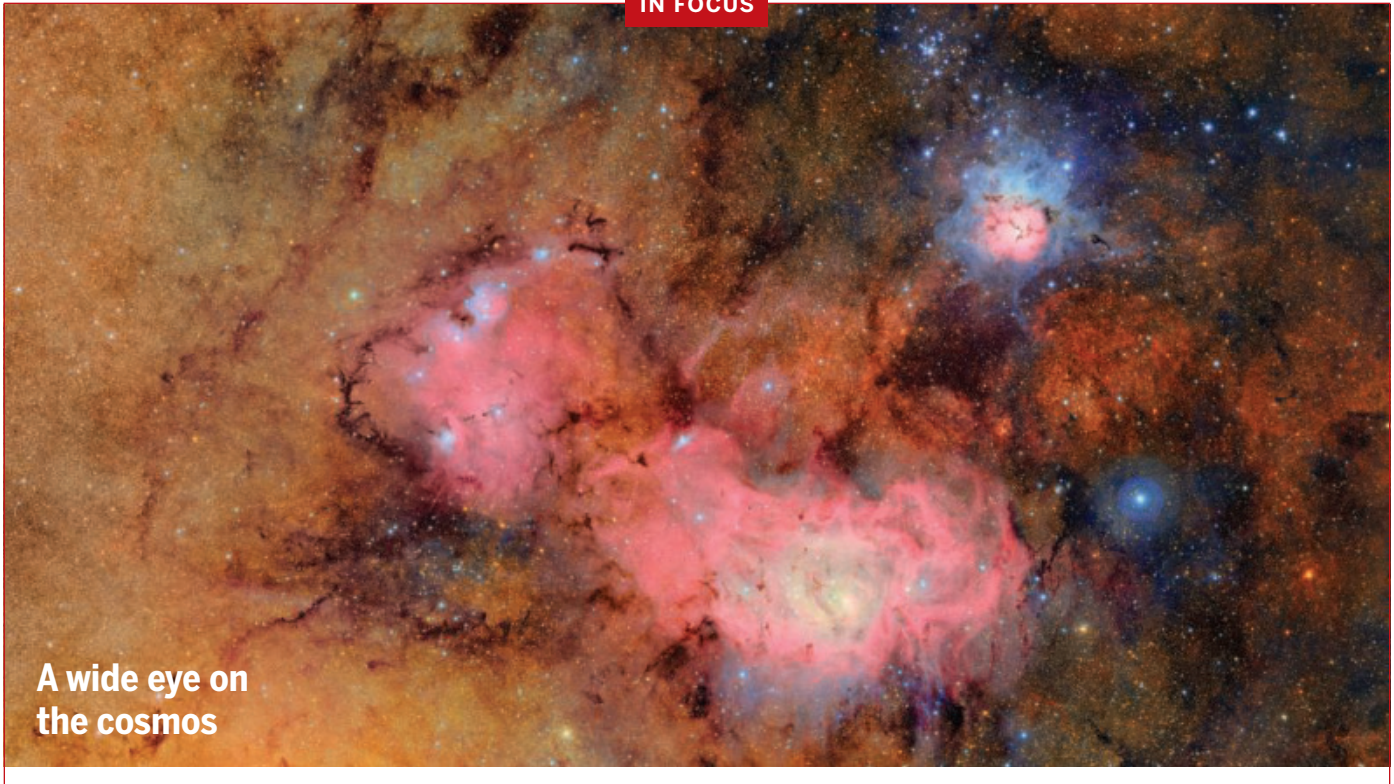

A wide eye on the cosmos

The Vera C. Rubin Observatory, a revolutionary new telescope that later this year will begin to survey the entire sky from its perch on Cerro Pachón in Chile, released its first images this week, including the one pictured above, showing the Trifid and Lagoon nebulae—clouds of gas from which stars are born.

PHOTO: NATIONAL SCIENCE FOUNDATION/DEPARTMENT OF ENERGY/VERA C. RUBIN OBSERVATORY

TRUMP ADMINISTRATION

Order to restore NIH grants heartens scientists

Federal judge decries NIH's rationale for killing blacklisted grants as capricious and arbitrary

SARA REARDON

A forceful ruling from a federal judge has kindled some hope among U.S. biomedical researchers whose grants on politically sensitive topics including racial health disparities, transgender health, and vaccine hesitancy have been canceled in recent months. "Have we no shame?" asked Judge William Young of the U.S. District Court for the District of Massachusetts on 16 June when he ordered the National Institutes of Health (NIH) and its parent agency, the Department of Health and Human Services (HHS), to immediately restore hundreds of canceled grants. Young said NIH's terminations were arbitrary and capricious, with no legally valid basis. The government's rationale, he said, was rooted in racial and gender bias. "I've sat on this bench now for 40 years and I've never seen government racial discrimination like this," he said.

This week, the judge issued his written ruling and the plaintiffs released a list of more than 900 terminated grants and "subawards," funding to institutions other than the main grant holder, that must now be restored. HHS and NIH have appealed the judge's decision, which is limited to NIH grants held by the plaintiffs and does not restore all of the grants terminated by the agency since President Donald Trump took office—nearly 2300, according to one estimate.

Researchers whose grants Young reinstated are cautiously optimistic. "I don't have a sense of what will come of it yet," says Nisha Acharya, an ophthalmologist at the University of California (UC) San Francisco. In March, NIH terminated her $3.3 million project studying the effects of shingles vaccination on ocular shingles infections. Acharya's project does not focus on vaccine hesitancy, a proscribed topic, but her grant appears to have been targeted because its summary included the word "hesitancy" in a different context.

Young's ruling addresses two separate lawsuits—one from a group of 16 attorneys general from Democratic-leaning states and one from individual researchers and members of specific unions including the American Public Health Association (APHA). It centers on NIH's claim that the canceled research is "unscientific" or supports discrimination that is "harm[ful to] the health of Americans"—wording cited in hundreds of NIH letters notifying scientists of the cancellations. The language largely mirrored Trump executive orders—some of which are blocked by temporary restraining orders—that attack diversity, equity, and inclusion (DEI) efforts; transgender health; and other charged topics.

> "I've never seen government racial discrimination like this."
>
> **William Young**
> U.S. District Court judge

"The court finds and rules that [NIH's] explanations are bereft of reasoning, virtually in their entirety," said Young, who was appointed by then-President Ronald Reagan in 1985. He called the directives to terminate grants on these topics "void and illegal." The plaintiffs had argued that after Trump political appointees asked NIH officials to review some of the grants, they spent only minutes before canceling the projects. Young also seemed unimpressed by the agency's failure to distinguish DEI from research into health disparities, such as studies on how certain drugs or diseases affect people from diverse backgrounds.

The judge's assertions that the government's reasoning was discriminatory "gave me some hope," said Jason Flatt, a social scientist at the University of Nevada, Las Vegas whose grants studying Alzheimer's disease in older LGBTQ+ people were terminated. "I think that for research to truly be beneficial for everyone it needs to include everyone." But Flatt says he's waiting to make decisions on future research until he gets more clarity about whether NIH will actually restore the funds. "This is a situation that has never happened before," he says.

It wasn't a complete win for the plaintiffs. They had argued that if NIH's underlying justifications are illegal, all grants terminated by the agency on those bases should be restored. But Young last week declined to expand the ruling or to allow the plaintiffs to submit an additional list of terminated research and training grants that they had planned to file on 23 June. "It's too late," he said.

Together, the plaintiffs' lists comprise more than 900 unique grant numbers, more than 100 of which are subawards. Among them are more than 150 training grants for students and junior scientists, many intended to increase workforce diversity. Young denied the APHA plaintiffs' request to withhold the names of union members supported by the grants, who APHA said "have a reasonable fear of retaliation, reputational damage, harassment, and threats."

In their appeal, filed on 23 June, NIH and HHS said Young did not have the authority to decide cases involving contracts. They also asked the judge to stay his ruling during the appeal because implementing it immediately "will result in millions of dollars irrevocably flowing out of the U.S. Treasury."

But the judge denied the stay, saying that his decision only requires the defendants to comply with Congress's wishes to spend the money "rather than sequestering funds (probably forever) during the course of the appeal." In a statement, HHS Director of Communications Andrew Nixon said, "HHS stands by its decision to end funding for research that prioritized ideological agendas over

scientific rigor and meaningful outcomes for the American people."

Future phases of the lawsuit being heard by Young will address a broader question: whether NIH must continue to fund research on politically charged topics—some of it mandated by Congress. Since Trump took office, NIH has "unpublished" nearly 100 notices of funding opportunity (NOFOs) calling for grant applications on topics including health disparities, workforce diversity, and research with sexual and gender minorities. The APHA plaintiffs' suit says both the agency's refusal to consider grant proposals already submitted under the withdrawn NOFOs and the extended delays to the scientific meetings that would normally review other proposals were unreasonable and illegal. NIH has asked the court to dismiss this part of the lawsuit, saying grant review meetings have restarted and the plaintiffs can't demonstrate that the delays harmed them personally.

NIH isn't the only research agency whose decision to cancel existing grants has been rejected by a federal court. This week, District Court Judge Rita Lin ordered the National Science Foundation, the Environmental Protection Agency, and the National Endowment for the Humanities to restore grants awarded to UC faculty that she concluded were terminated without adequate explanation or because they involved topics "blacklisted" by the Trump administration. Lin's ruling could be expanded to all federal agencies that have taken such actions against UC scientists, says UC Berkeley law professor Claudia Polsky, who brought the case as a class action suit.

Even if these rulings withstand appeal, the grant terminations may have lasting impact. Young's decision on NIH was "incredibly exciting to hear," says Alexis Koskan, a behavioral scientist at Arizona State University whose terminated project studying COVID-19 vaccine hesitancy among Hispanic parents would be restored. Yet Koskan isn't sure she will study the topic again, knowing that NIH wants to defund such research. "It's a very personal decision for scientists," she says. "I've been working for so long and it's incredibly important, but also what's a good use of my time and energy? I think that's the waters that researchers are navigating in general right now." □

SCIENTIFIC COMMUNITY

U.S. researchers speak up in local newspapers

Through two grassroots efforts, approximately 200 op-eds showcasing federally funded science have been published across the country

KATIE LANGIN

Cornell University doctoral student Isako Di Tomassi was taken aback by comments on local social media after thousands of federal workers, including her Ph.D. adviser—a U.S. Department of Agriculture scientist—were fired in February. Some people who posted on the neighborhood networking platform Nextdoor seemed pleased, with one writing that a lot of "stupid research has been stopped." She saw it differently. "We were actually in the middle of working on an apparent outbreak of a devastating crop disease," Di Tomassi says of her work with her adviser.

> **"I'm reaching out to you as a nerdy kid from Northport, Alabama."**
>
> **Kristina Visscher**
> University of Alabama at Birmingham

It suddenly hit her: "These are taxpayers here who have no idea what cool, awesome work is being done" in their backyard.

Since then, Di Tomassi has been part of a multipronged grassroots effort to encourage scientists around the country to submit op-eds to local news outlets showcasing federally funded research and why they should care that President Donald Trump's administration is slashing support for science. So far, approximately 200 op-eds have appeared in local news outlets in 43 states, discussing research on Alzheimer's disease, drought-tolerant trees, addiction treatments, and more. The latest wave came last week, following a campaign by graduate student groups around the country.

"There's a rhetoric that what we do is wasteful, and that we're not spending this money on things that actually help people," says Emma Scales, a Cornell Ph.D. student who worked with Di Tomassi to spearhead the graduate student effort. The op-eds, she says, counter that by saying, "Let me tell you, as a federally funded scientist, what it is that I do, why it's important, and why it helps our community."

Most have been published in the town or city where the writer grew up—a strategic recommendation by another campaign called Science Homecoming, launched in February to help scientists write persuasive opinion articles. "Scientists often live in big cities … because that's where the labs are," says Science Homecoming co-founder Jessica Cantlon, a psychology professor at Carnegie Mellon University. "But … they come from every town across the United States, all kinds of places. And so we thought, well, if scientists could write back to their hometowns … that might make it faster and easier for scientists to make connections with the public."

Nearly all the op-eds published so far have been penned by academic scientists who have worked on projects funded by the National Science Foundation (NSF) and the National Institutes of Health (NIH)—agencies whose budgets Trump has proposed lowering by 40% or more. Some spoke in personal terms about how fellowships and training opportunities that the government has now scaled back propelled them into a career in science. "The fight over federal science funding isn't solely about politics. It's about whether people like us—from rural towns, families of color and public schools—will ever get the chance to dream big," wrote early-career researchers Moana Bullock and Kylea Garces last week in *Bohemian*, a Northern California local newsweekly.

The agencies' funding for the 2026 fiscal year that starts on 1 October will ultimately be decided by Congress—and many letter writers have urged readers to write their elected representatives about the value of science. "Google your favorite technology: Whatever it is, it's likely that federally funded NIH and NSF research made it possible," Kristina Visscher, a professor of neurobiology at the University of Alabama at Birmingham, wrote this month on the website AL.com. Her letter, and many others, make it clear they're not writing on behalf of their employer: "I'm reaching out to you as a nerdy kid from Northport, Alabama," Visscher wrote.

Many letters emphasize that research funding doesn't just result in scientific

discoveries; it also generates economic activity for the community where the work is done. "In most research labs, the highest budget item is personnel," wrote Science Homecoming co-founder Steven Piantadosi, a psychology professor at the University of California, Berkeley, in a February op-ed in the *Montgomery County Sentinel*, a Maryland publication. Much of the roughly $3 billion in NIH and NSF funding received by the state's institutions each year, he continued, goes toward "paying someone's salary—someone who in turn uses their income to pay rent, buy groceries, support local businesses, and shop in stores."

Science Homecoming has put together a group of volunteer science communicators to help edit op-eds before they're submitted to local news outlets. The graduate student–led effort, Scientist Network for Advancing Policy, has also been hosting webinars for potential authors to learn from communication experts. Clay Risen, a former deputy op-ed editor for *The New York Times*, told attendees last month, "You have a short amount of attention, so you can't be throwing a lot at a reader." Find an angle that's relevant to your community, he recommended. "Maybe you research climate policy and your approach is pretty general, but what is the local story that brings that together?"

Zoë Emory, a Ph.D. student at the University of Notre Dame, used that strategy this month when writing about nuclear energy. "Here in central Pennsylvania, memories of the 1979 Three Mile Island accident still color public perception of nuclear energy," she wrote in the *Gettysburg Times*, referring to a partial meltdown at a nuclear facility that struck fear into the surrounding community. Emory, who grew up in a small town near Gettysburg, went on to describe her research on how to store nuclear waste safely and why it matters to the public. "This work contributes to a stable and sustainable energy sector, which affects your electricity access, your monthly bill, and the long-term health of our environment."

As Cantlon sees it, the letters aren't about changing readers' minds; the goal is to remind them of something they have come to take for granted. "It really is science that is the backbone of this country, and I think people understand that. So really, it's just a matter of triggering the memories of folks in these communities to think about something that is just quietly in the background, saving their life." □

IN FOCUS

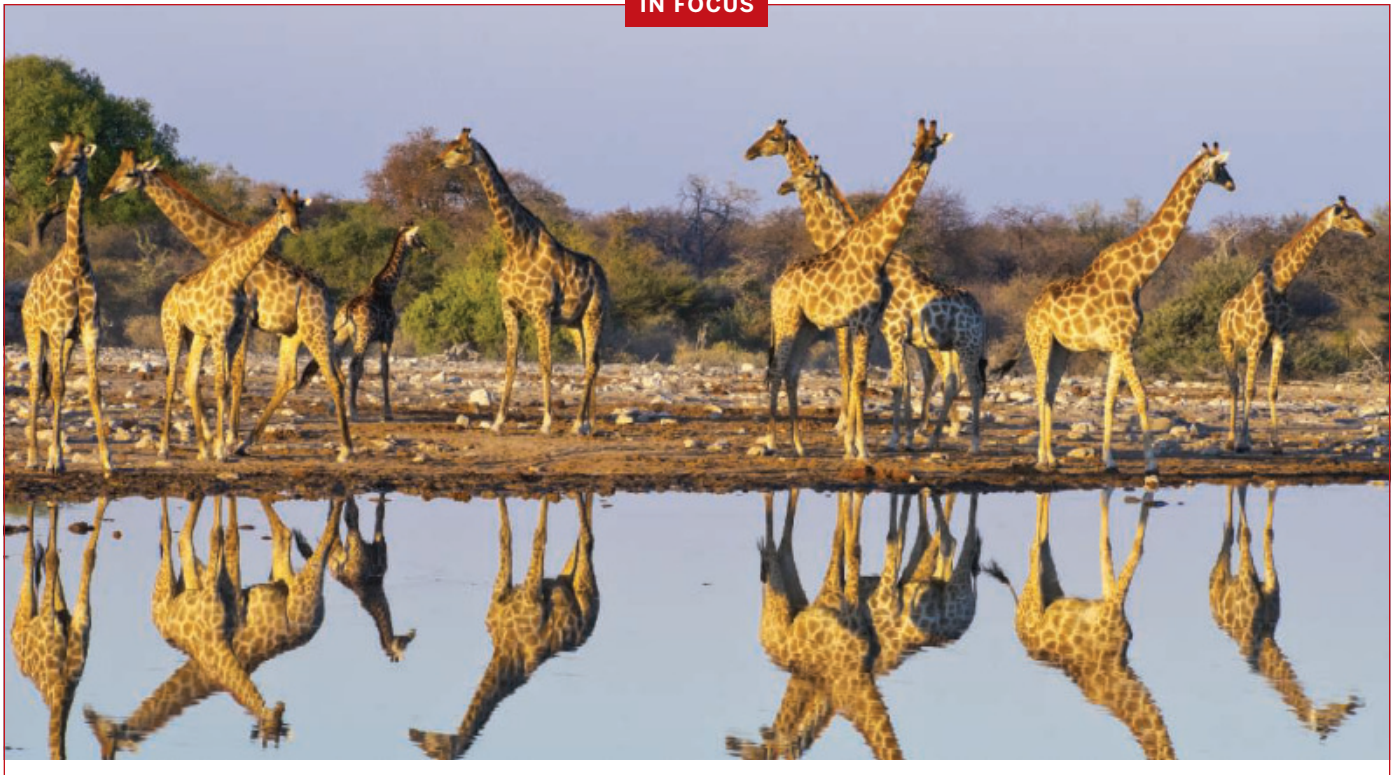

PHOTO: YVA MOMATIUK AND JOHN EASTCOTT/MINDEN

Giraffes on the rise

Efforts to save Africa's iconic giraffes are bearing fruit, according to data released last week by the Giraffe Conservation Foundation (GCF). Populations of three of the continent's four major types of giraffe—northern, reticulated, and southern—have grown in the past few years, and the Maasai giraffe population is stable, according the *State of Giraffe 2025* report. Over the past 50 years, giraffes have gone extinct in at least seven African countries, and researchers estimate overall numbers declined by 40% to less than 100,000 individuals. The new numbers are encouraging, says GCF Executive Director Stephanie Fennessy. But she cautions that ongoing habitat loss and other threats mean giraffes are still among the world's most threatened large mammals. —Maina Waruru

FEATURES

WITHOUT A LIFELINE

The United States reneged on its foreign aid commitments. Nepal's malnourished children and their families are paying the price

Anita Devi Jaiswal, mother of six, with her newborn baby boy in Kalaphanta, Nepal. Her youngest daughter died from malnutrition 2 weeks earlier.

CATHERINE OFFORD, in Lumbini province and Kathmandu, Nepal

Mina Jaiswal hadn't reached her second birthday when she died in April in Kalaphanta, a village set among a patchwork of rice and wheat fields in Nepal's western lowland plains. For the first year of her life, Mina seemed to grow normally, and played among the other children in this farming community along the border with India.

Then a few months ago, she became sick and started to lose weight, says her mother, Anita Devi Jaiswal. In March, a health worker wrapped a measuring tape around the toddler's upper arm and recorded just 10.5 centimeters. Mina was diagnosed with severe wasting, the most visible and deadly form of malnutrition.

She was prescribed ready-to-use therapeutic food (RUTF)—a nutrient-rich peanut-based paste that helps severely malnourished children recover weight. But the local health post's stocks of this potentially lifesaving treatment were empty. Her family was told to come back the following week. By early April they had received the RUTF sachets, but Mina had developed edema, a buildup of fluid associated with particularly severe wasting. "Her whole body was swollen," Anita says. "She gave up eating and drinking."

Health workers said Mina should go to a specialized treatment center, more than 1 hour's drive away. But her father says he had to work in the fields and take care of the rest of the family, including Anita, who was heavily pregnant with the family's sixth child. "I thought that I should take her once I had given birth," Anita says, holding her newborn baby in her lap. Mina died before they could make the trip.

Until U.S. President Donald Trump returned to office and ordered a freeze on foreign aid in January, Narainapur, the rural region that includes Kalaphanta, was one of 498 municipalities in Nepal targeted by a sweeping effort to save children like Mina. Led by the international nongovernmental organization (NGO) Helen Keller Intl, the work was funded by a $72 million award from the U.S. Agency for International Development (USAID) and was slated to run from 2024 to 2029. In March, as Mina's health was deteriorating, Helen Keller and local partners should have been working with the government to visit households and screen children for wasting, ensure a consistent supply of RUTF, and support overworked staff at health posts across the country. They'd also planned to tackle some of the myriad factors exacerbating poor nutrition in marginalized and underserved communities like Narainapur's, including a lack of family planning and nutritional education, as well as food insecurity.

But the project, known as USAID Integrated Nutrition, no longer exists. When it suspended foreign aid, Trump's administration issued a stop-work order forcing the program to halt operations. A late February letter from USAID, by then largely dismantled, said some of the project's malnutrition efforts could continue under a "limited waiver for life-saving humanitarian assistance." Days later, a new letter informed Helen Keller that the whole project had been terminated. Like the thousands of programs canceled via similar letters, USAID Integrated Nutrition, the administration determined, was "not in the [U.S.] national interest."

Global health experts are still working to estimate the full impact of the collapse in U.S. aid funding on worldwide efforts to fight malnutrition. Multiple reports have already linked USAID's dismantling to deaths among malnourished children in countries experiencing hunger crises including Nigeria and Somalia, even as RUTF piles up unused in USAID warehouses.

In Nepal, long considered a success story in reducing child malnutrition, the cuts are likely to jeopardize hard-won progress. USAID's withdrawal has already frozen hundreds of millions of dollars in government and NGO funding, ended programs in health and other sectors, and threatened thousands of aid jobs. Even critics of Nepal's reliance on foreign aid agree there will be significant repercussions from the United States's abrupt retreat, which comes as other international funders are also announcing aid cuts, says development anthropologist Jeevan Sharma, who co-directs the Centre for South Asian Studies at the University of Edinburgh and is studying some of the effects of USAID's withdrawal. "Nobody's celebrating it," he says. Even now, "There's a sense of shock."

The U.S. Department of State, which is reportedly absorbing what remains of USAID, did not answer questions from *Science* but said in an emailed statement it is "working to ensure that our foreign assistance and our policies are appropriately aligned." It added that it is "working with the Government of Nepal to continue to deepen our cooperation."

Types of malnutrition

Malnutrition in children includes multiple forms of undernutrition—wasting, stunting, vitamin and mineral deficiencies, and being underweight for one's age—as well as obesity and being overweight. Undernutrition is implicated in about half of deaths among children under age 5 worldwide.

WASTING
Low weight for height
Wasting usually reflects rapid weight loss due to illness or lack of nutritious food. Its most severe form increases a child's risk of death 10-fold.

STUNTING
Low height for age
Stunting typically reflects chronic undernutrition, which can harm physical and neurocognitive development, and has been linked to lower educational achievement and earning potential.

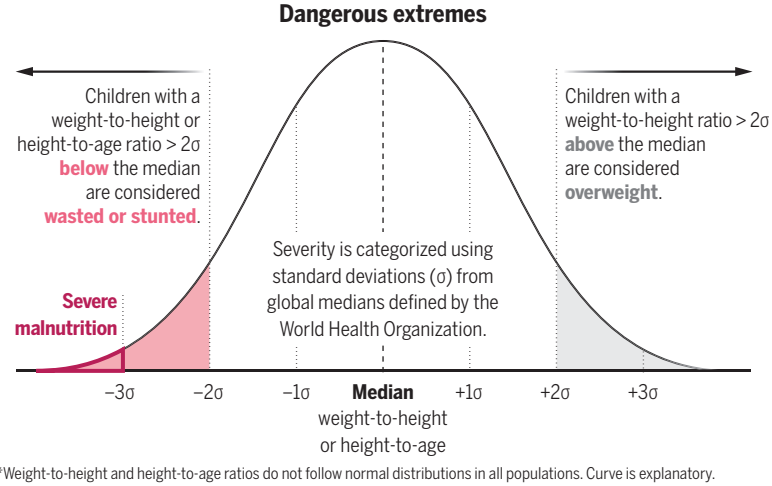

*Weight-to-height and height-to-age ratios do not follow normal distributions in all populations. Curve is explanatory.

This story is part of a series about the impacts of U.S. funding cuts on global health, supported by the Pulitzer Center.

CREDITS: (PHOTO, OPPOSITE PAGE) UMA BISTA; (GRAPHIC) M. HERSHER/*SCIENCE*; (DATA) WORLD HEALTH ORGANIZATION

As for USAID Integrated Nutrition, the program "had a direct impact on the lives of many children," says Chandrakala Sigdel, who spent 7 years as a nutrition facilitator in Narainapur and a nearby municipality. She worries the funding cuts mean "the number of malnourished children is likely to rise, and in the long run, this could push the entire nation back into the cycle of malnutrition. … That truly upsets me."

GLOBAL HEALTH EXPERTS have long argued that investing in child nutrition makes both humanitarian and economic sense. A lack of proper nutrition is implicated in roughly half of deaths in children under age 5. Although it's frequently associated with war and natural disasters, it is also driven by poverty, chronic food insecurity, and poor maternal health, among other factors. Children with the most severe form of wasting, a condition called severe acute malnutrition (SAM), are more than 10 times as likely to die as well-nourished children, usually from common illnesses. SAM affects more than 12 million children, more than half of whom are in southern Asia.

High in calories and nutrients, ready-to-use therapeutic food is standard treatment for severe malnutrition.

And about 150 million children worldwide are stunted—they're too short for their age—typically because of chronic poor nutrition.

Malnutrition undercuts a country's productivity, says Saskia Osendarp, executive director of the Micronutrient Forum, which studies and advocates for improvements in nutrition. She co-authored a commentary in *Nature* earlier this year warning that a complete cutoff of U.S. funds to treat wasting would not only take a direct toll—she and her colleagues estimated an additional 163,500 child deaths a year—but also have serious economic consequences. People who survive malnutrition can bear lasting scars, she explains, particularly if they were affected in the critical 1000-day developmental window from conception to 2 years old. For some, "Their immune systems will be impaired, they will do less well in school, they will grow up to be adults in jobs where they earn less."

Past U.S. administrations have viewed global nutrition funding as key to promoting resilient democracies and bolstering U.S. national security and prosperity. Since USAID's creation in 1961, Congress has approved billions of dollars for efforts to fight wasting, stunting, and nutrient deficiencies worldwide, including in Nepal. The relationship has not always been smooth: Some critics here have decried the government's dependence on foreign aid for health and other sectors and accused funders of undermining the country's sovereignty, fueling corruption, and propping up neocolonial narratives.

Still, when it comes to malnutrition rates, many credit aid from the U.S. and other international funders with helping turn the tide. Starting in the mid-1990s, Nepal went from having one of the highest levels of stunting in the world, at more than 60% of children under age 5 by some estimates, to less than half that by 2022. Wasting dropped in this time, too, from more than 11% to about 8%—though these figures mask substantial differences among provinces and communities (see map, left).

Nepal's government has helped drive this progress with increasing investments in health care, while surging remittances from Nepalis abroad have lifted many families out of poverty. International funders like USAID have contributed through both direct funding and support for government- and NGO-led nutrition programs, including a highly successful vitamin A supplementation initiative launched in 1993.

In 2011, USAID began a major nutrition-focused project called Suaahara, Nepali for "good nutrition." It ran for 5 years, and its follow-up, Suaahara II, spanned the next seven. Eventually reaching 389 municipalities in six of Nepal's seven provinces, the programs organized community activities and public health campaigns promoting good nutrition. They also supported local, provincial, and federal governments with staff training, procurement of com-

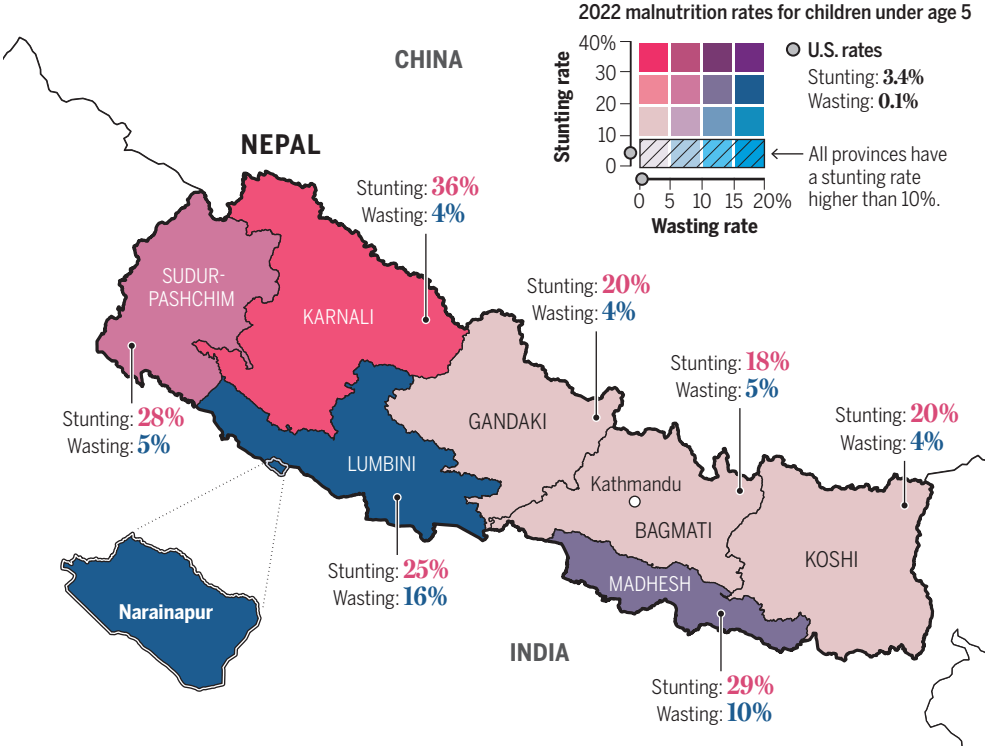

Uneven progress

Nepal has made progress against malnutrition in recent decades, but several provinces still have high rates of stunting, wasting, or both—and malnutrition remains far more common here than in the United States and other high-income countries. The capital city of Kathmandu and surrounding areas where people have better access to health care have far lower rates than do remoter and more disadvantaged areas like Narainapur.

CREDITS: (PHOTO) UMA BISTA; (GRAPHIC) M. HERSHER/*SCIENCE*; (DATA) 2022 NEPAL DEMOGRAPHIC AND HEALTH SURVEY; UNICEF; WORLD HEALTH ORGANIZATION; AND WORLD BANK JOINT CHILD MALNUTRITION ESTIMATES DATABASE

Villagers thresh lentils in Kalaphanta, Nepal, just a few kilometers from the Indian border. The community has high rates of childhood malnutrition.

PHOTO: UMA BISTA

modities such as RUTF, supplies of equipment, and overall health policy planning. While Nepal's government oversees health and other programs, USAID staff on the ground have been the ones "who often facilitate and make the system actually work," notes Sharma, who was a researcher at Tufts University, which collaborated on Suaahara I, as that program was first being implemented.

USAID Integrated Nutrition was supposed to be Suaahara's successor. Designed in collaboration with the Nepali government, it was going to scale up the program's efforts to all seven provinces, increase assistance for hard-to-reach communities, and gradually hand over all responsibility to local partners by the end of its 5-year run.

The perceived U.S. commitment was so strong that people in Nepal's government regularly spoke of "USAID" synonymously with nutritional programming, says Bhim Prasad Sakopta, chief of the health coordination division at Nepal's Ministry of Health and Population (MOHP). When other partners showed interest in investing in Nepal's health programs, he adds, "we would request they go to other sectors, not nutrition—because the U.S. is already doing something in nutrition."

BEFORE THE PROJECT disintegrated, Sigdel had been one of hundreds of contracted workers across Nepal tasked with implementing the country's integrated nutrition programming. As part of Suaahara II, she visited families' homes alongside female community health volunteers. She measured children's weight, height, and arm circumference; made referrals for those with wasting; and ensured treatment reached the kids who needed it. When requests for RUTF got delayed along the multistep chain from municipal health posts to regional logistics centers, she and her colleagues would use USAID's channels to break the jam.

Sigdel says many communities "are still unaware that malnutrition is a serious issue [that] can be treated through proper nutrition and timely visits to health care centers." She and other workers advised families on how to prevent malnutrition in the first place by preparing nutritious, varied meals including poultry and vegetables rather than unhealthy snack food, and regularly feeding children when they are sick, as conditions such as diarrhea can cause rapid weight loss.

Staff also advocated healthy spacing between births, because back-to-back pregnancies put strain on a mother's health and in turn increase the risk of low birth weight. They promoted breastfeeding, which can be challenging for many mothers without guidance. (The World Health Organization has called breastfeeding "one of the most effective ways to ensure child health and survival," in part because breastmilk protects babies against infections.) Other activities highlighted basic hygiene and sanitation, and how to properly introduce foods when babies reach about 6 months old. Some households in vulnerable areas also received equipment and agricultural training to try to boost production of nutritious crops.

The USAID projects' network of committed, community-based workers like Sigdel was one of the programs' greatest strengths, says Bibek Kumar Lal, who directs the family welfare division at MOHP and worked closely with USAID staff. "They had a very deep reach in the communities."

Data suggest the Suaahara programs drove significant improvements in a number of metrics, including maternal underweight, infant lengths, and child diet, which got better faster in target districts than in areas that weren't part of the program. There were also improvements in less tangible outcomes such as local governance and community health volunteers' knowledge. The gains emerged despite a serious earthquake in 2015, a complete overhaul of Nepal's political system the same year, and severe economic impacts from the COVID-19 pandemic, notes Edward Frongillo, who co-directs the Global Health Initiative

at the University of South Carolina and led one of the evaluations.

That's not to say Suahaara and its follow-ups didn't face criticism: Some people were concerned the multiple interventions and wide coverage might be spreading program resources too thin, Sharma notes. The impact of more focused interventions might have been easier to measure, too.

Despite such concerns, the projects had built up a lot of goodwill over the years, says Helen Keller's Pooja Pandey Rana, who directed both Suaahara II and USAID Integrated Nutrition. In expanding the work to new districts, the team built on the trust of communities and government staff accumulated through more than a decade of collaboration, she says. USAID Integrated Nutrition had already begun to ramp up activities in Narainapur and hundreds of other municipalities by the beginning of this year, and federal and regional governments had baked the project into their plans for the following fiscal year. "The ship was about to leave," Lal says, "when it sank."

As funding froze and then vanished, the team was forced to return equipment and terminate staff. Motorbikes once used to transport workers and commodities to vulnerable communities were left in a dry port on the outskirts of Kathmandu, alongside hundreds of other vehicles stranded from canceled USAID projects across the country. About 60 people from Helen Keller's Nepal office lost their jobs; and all of USAID Integrated Nutrition's contracted community staff were laid off—Sigdel among them.

AT THE KALAPHANTA HEALTH POST, a cluster of small buildings in a quiet goat-filled field where Mina came before she died, health workers are feeling the effects of the program's withdrawal. Ram Sundar Yadav oversees malnutrition cases here. He says the nine staff at the post were already stretched thin implementing more than 30 government health programs, including immunization, treatment for diseases such as tuberculosis, and vitamin supplementation, for some 1400 households. Now, they are demotivated and even more overworked. Among other support, his team had counted on USAID for referrals and follow up of malnutrition cases that might otherwise be overlooked.

Radha Maurya, a 10-month-old girl from the village of Nausahara, could easily have been one of those missed cases. After Radha's mother died just over 1 month after giving birth to her, the family bought formula just over the border in India to try to replace the breastmilk. But Radha struggled to put on weight and was so weak when she turned 8 months earlier this year that the family thought she wouldn't survive, says her grandmother Anokha Maurya. They took Radha to various traditional healers and tried different foods and drinks, but she continued to deteriorate. "Nobody here knew anything," Anokha says.

It wasn't until a neighbor told the family about a child with similar symptoms and recommended a visit to the health post that they brought Radha in for screening, where she was diagnosed with SAM. Although Radha, like Mina, had to wait for RUTF to arrive, the treatment helped. Several weeks later, she can lift her head for a few seconds at a time, and the corners of her mouth sometimes curve up when her relatives smile and speak to her as she lies in her grandmother's arms. Her father is still worried about her, and Anokha, who also helps with Radha's older siblings, says she fears for the family once she's gone. "I am raising them, for as long as God has given me life."

Health workers are also concerned about aid cuts' effects on nutrition for younger infants, who rely completely on milk. Kalpana Upadhyaya Subedi, a consultant physician at Paropakar Maternity and Women's Hospital, had been expecting support from USAID and other funders to expand a lactation counseling program and human milk bank to other hospitals across Nepal. That plan has now been shelved, alongside numerous others supporting maternal and newborn nutrition and health.

The disruption to nutrition efforts is likely to set back nationwide improvements in child health, several experts told *Science*. But it will take time to quantify the fallout—and not just because malnutrition takes time to develop. The aid withdrawal could also jeopardize government surveys used to monitor child health, Lal says.

Patchwork funding

In 2022, the United States was the largest single-nation direct funder of priority interventions to meet World Health Assembly (WHA) nutrition targets. Such interventions include treatment of wasting, stunting, and anemia, and promotion of breastfeeding. Excluded are other types of nutrition-relevant funding such as boosting agriculture or providing access to clean water.

$1.6 billion went to WHA priority nutrition interventions in 2022, the latest year for which analyzed data are available.*

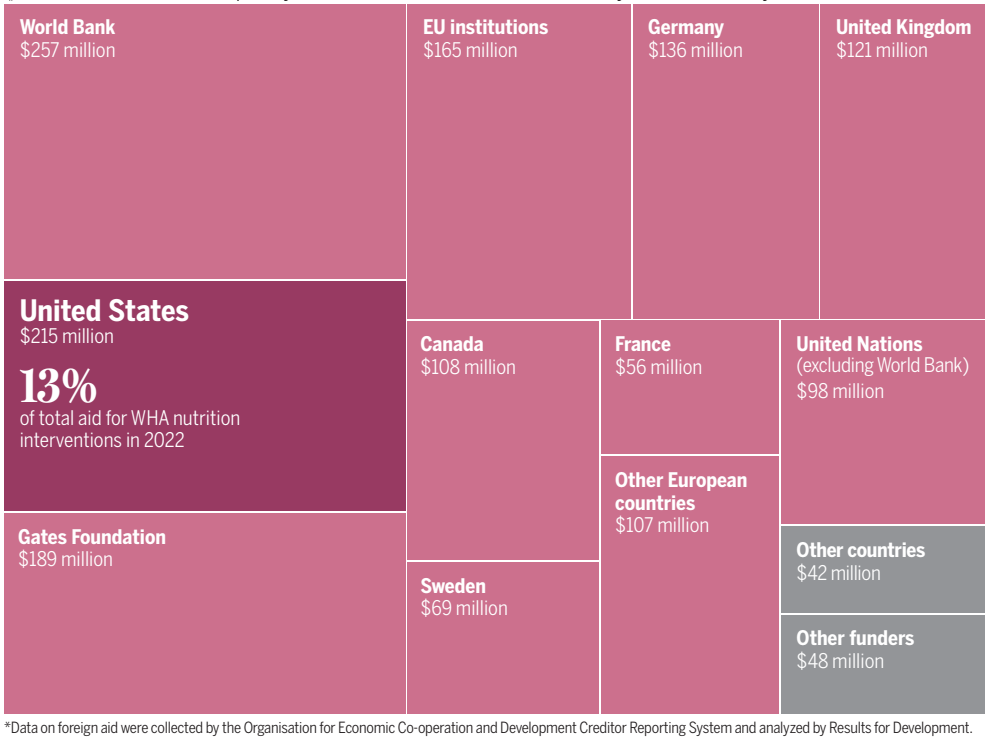

*Data on foreign aid were collected by the Organisation for Economic Co-operation and Development Creditor Reporting System and analyzed by Results for Development. The United Nations includes all official agencies, funds, programs, regional commissions, and other entities listed in U.N. System Documentation: https://research.un.org/en/docs/unsystem. Other funders include philanthropic organizations, independent development banks, and other sources not included elsewhere.

CREDITS: (GRAPHIC) M. HERSHER/*SCIENCE*; (DATA) RESULTS FOR DEVELOPMENT

"If those surveys are not conducted, we will not even know the impact," he says. "That is the most worrying part. We'll all be blind."

ON THE FIRST THURSDAY of May, as Nepal celebrates Labor Day, Rana sits in her team's stark former headquarters in Kathmandu. Less than 24 hours after the official closing of USAID Integrated Nutrition, she's organizing the clear-out of office equipment before remaining staff downsize to a smaller space in the building.

Asked in March about the project's termination, she told *Science* she had "never felt so hopeless." Now that some of the shock has passed, she and colleagues at Helen Keller have been identifying critical activities and strategizing how to keep them going with any funds they can find. It's challenging work: Her team is just one of many chasing a rapidly dwindling pot of aid money. "It's not just Nepal," Rana says. "Everywhere, this crisis is happening."

Others are also looking for solutions. Some health officials in Lumbini province, which includes Narainapur, say they have been working to stretch government funding designated for maternal and newborn health to include malnutrition services. Officials at MOHP are trying to interest development partners they previously directed away from nutrition to now "allocate at least a few resources" to the area, and have reached out to philanthropic organizations to explore possible collaborations, Sakopta says. Back in Narainapur, Sigdel, who has since found work supporting girls' education, says she still tries to share information about good nutrition with families she meets.

Many politicians and commentators have argued the crisis should force a rethink of how Nepal uses international money. "USAID's abrupt exit underscores the highly fragile, aid-dependent system," says Vibhav Pradhan, a researcher in public policy at the Institute for Integrated Development Studies in Kathmandu. The country needs to diversify its support, strengthen its governance, and build health systems that can withstand shocks like this in the future, he says. Sakopta adds that "the great lesson learned for us" is to allocate domestic rather than external resources for critical functions in health and other sectors. "Other resources, they are always uncertain. At any point … they may stop their funding."

Radha with her grandmother Anokha Maurya in Nausahara, Nepal. Radha's case of severe acute malnutrition was nearly missed by health workers.

PHOTO: UMA BISTA

The Nepali government will still be able to run other critical services such as essential vaccinations, Sakopta says, and may be able to cover some of the lost nutrition aid. The 2025–26 budget, issued at the end of the May, moderately upped funds for MOHP from about 4.6% to 4.9% of the total budget—though it's still unclear how much malnutrition work this will be able to support.

Long term, Nepal and other countries might be able to come up with better, more efficient ways to fund health and other services, notes John Hoddinott, an economist at Cornell University who studies nutrition. "People can be creative and innovative, and maybe that's what we'll see in this space."

But what frustrates many involved with terminated projects is how quickly they have been forced to adapt. With some warning, government officials and aid workers say, people could have planned and tried to mitigate the impact on human lives. Instead, as everyone scrambles to adjust, there will inevitably be families, facing situations like Mina's and Radha's, that "fall through the cracks," Rana says. "In the end, it's always the most vulnerable women and children that suffer." □

CHILDREN AT RISK

More from this series on how U.S. foreign aid cuts threaten child health around the world: https://scim.ag/USAID

COMMENTARY

PERSPECTIVES

MATERIALS SCIENCE

Now you see me, now you don't

Nanostructured reflecting plates in squid cells enable a rapid switch between colored and near-transparent states

Matthew D. Shawkey

The neck feathers of a pigeon can rapidly change color when viewed from different angles because of iridescence—an optical event caused by the nanoscale arrangement of materials in which the appearance of color depends on the angle of the incoming light ray (*1*–*3*). Can this structural coloration (color from a physical structure) also make an object appear transparent? Some squids are masters of disguise. They can change not only colors but also skin textures and patterns to mimic their surroundings with stunning accuracy in a few seconds (*4*). This includes shifting between colored, transparent, and mixed colored-transparent states. On page 1389 of this issue, Bogdanov *et al.* (*5*) report the process underlying a squid's dynamic transition between nearly transparent and colored states. Furthermore, the authors describe the development of multispectral composite materials inspired by nature's mechanism, which could be used in applications requiring camouflage or thermal management.

In contrast to pigments, which produce color by selectively absorbing certain wavelengths of light and reflecting others, structural coloration is based on light scattering by specific arrangements of materials at the nanometer scale (*3*). For example, a soap bubble has a higher refractive index than air (it bends light more than air), which causes light to scatter into its component wavelengths (colors) at the interface where a few-nanometers-thin layer of soap meets air. Interference between the scattered light waves can enhance or cancel certain wavelengths. This creates individual colors that vary with the thickness of a soap bubble at a given point and the angle of incident light, producing a rainbowlike iridescent structural color. Similarly, some animals, such as chameleons, can actively vary their structural colors based on external stimuli. A change in the distance between materials in the chameleon's skin, which are arranged in a crystalline structure, shifts colors across the visible light spectrum to match that of the surroundings such as leaves and rocks (*6*). However, becoming transparent is one trick chameleons have not yet mastered.

Iridophore cells in squid tissues allow squids to rapidly change their skin color by controlling light reflection.

Many cephalopods, including some squids and octopuses, can appear nearly transparent. They contain a specific protein called reflectin that enables dynamic changes of color and reflectance for disguise (*7*). However, how squids achieve the shift from colored to noncolored (transparent) states has been puzzling. Bogdanov *et al.* imaged live color-changing squid tissues to determine the mechanism behind this transition. The authors identified specific arrangements of reflecting plates in an iridophore, an iridescent cell in squid tissue. The periodic structure of plates caused sinusoidal variation of the refractive index within the iridophore (see the figure). Although other optical materials with refractive index gradients occur in living tissue, such as the moth eye (*8*), this previously unseen sine-wave distribution of refractive index allows squid tissues to become transparent.

Bogdanov *et al.* performed optical simulations to validate the proposed mechanism. A stack of reflecting plates was created, which changed color when stretched or compressed. The period of the sinusoidal refractive index gradient depended on the gap between the plates: A larger gap increased the period. Thus, the refractive index gradient could be modulated by the structural arrangement of the reflecting plates. Changing the period of sinusoidal refractive index waves enabled transition between colored (at a short period) and transparent (at a long period) states. Based on this mechanism, Bogdanov *et al.* designed and fabricated flexible composite films, each with a sinusoidal, triangle, or square refractive index gradient. These films all changed colors in response to mechanical (stretching) and chemical (addition of

PHOTO: SOLVIN ZANKL/MIDEN PICTURES

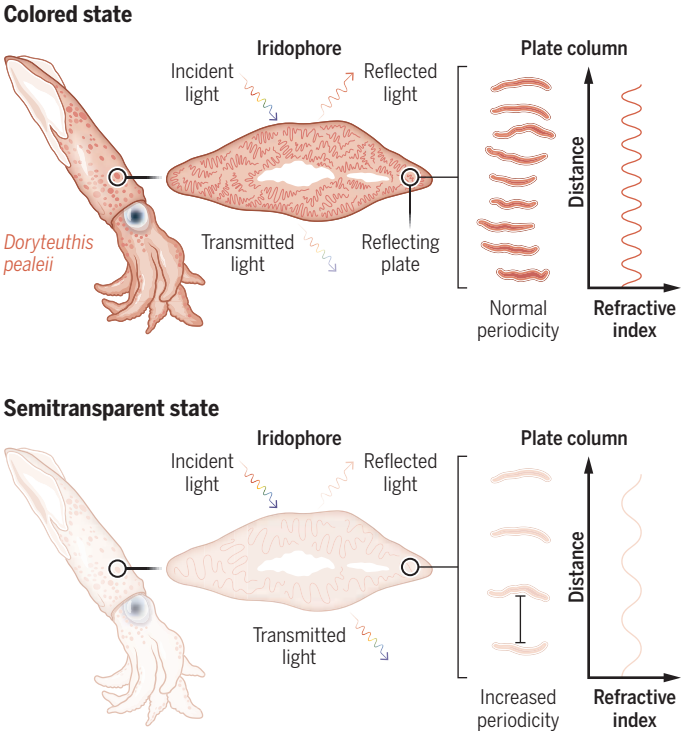

Master of disguise

Reflecting plates inside an iridophore cell of a squid are arranged in a distinct nanostructure. The specific arrangement varies the refractive index, which dictates how light interacts and determines the perception of color. Changes in the plates' arrangement by external stimuli cause a rapid switching between colored and transparent states.

chemicals) stimuli. However, the sinusoidal pattern best reproduced the dynamic transition between colored and transparent states, confirming it as the likely mechanism.

Although Bogdanov *et al.*'s composite materials displayed dynamic color change, these synthetic analogs still fall short of the remarkable abilities of squid skin, which are a product of millions of years of evolution. However, the designed materials are promising for engineering applications. The authors extended the iridescence phenomenon into near-infrared light waves that are not optically visible but can be detected as heat. This allowed the composite films to switch both optical and thermal properties, moving beyond what squids are known to do. What function could the next iterations of the bioinspired films of Bogdanov *et al.* achieve? The most obvious one is camouflage, but shifts between visible and near-infrared light waves could also bring dynamic coloration and thermal management to building materials and textiles. These examples show the practical aspects of the flashy color changes seen in nature. □

REFERENCES AND NOTES

1. I. C. Cuthill *et al.*, *Science* **357**, eaan0221 (2017).
2. S. M. Doucet, M. G. Meadows, *J. R. Soc. Interface* **6**, S115 (2009).
3. M. Srinivasarao, *Chem. Rev.* **99**, 1935 (1999).
4. L. M. Mäthger, E. J. Denton, N. J. Marshall, R. T. Hanlon, *J. R. Soc. Interface* **6**, S149 (2009).
5. G. Bogdanov *et al.*, *Science* **388**, 1389 (2025).
6. J. Teyssier, S. V. Saenko, D. van der Marel, M. C. Milinkovitch, *Nat. Commun.* **6**, 6368 (2015).
7. W. J. Crookes *et al.*, *Science* **303**, 235 (2004).
8. C. G. Bernhard, W. H. Miller, *Acta Physiol. Scand.* **56**, 385 (1962).

10.1126/science.ady8062

Evolution and Optics of Nanostructures Group, Department of Biology, Ghent University, Ghent, Belgium. Email: matthew.shawkey@ugent.be

GRAPHIC: A. FISHER/*SCIENCE*

SEISMOLOGY

Where slow and large earthquakes meet

Adjacent slow slip events affect megathrust earthquakes

Kazushige Obara

The Nankai Trough—a 900-km-long trench off the southeast coast of Japan—bears great risk for large earthquakes and tsunamis. In this location, the Philippine Sea Plate is sliding beneath the Eurasia Plate, building immense strain along the surface where the plates slip past each other (the fault plane). Large earthquakes are triggered when the accumulated stress on the locked (halted) fault plane approaches a critical strength over a wide area. A potential contributing factor to this scenario could be slow movement of rocks along the fault plane. Such slow earthquakes, lasting days to years, have taken place adjacent to a locked fault plane (*1*). On pages 1396 and 1401 of this issue, Edgington *et al.* (*2*) and Ozawa *et al.* (*3*), respectively, report a connection between slow earthquakes and large earthquakes in the Nankai Trough. The findings point to the importance of considering slow earthquakes when assessing seismic hazards.

Slow earthquakes are transitional phenomena. They occur in the region between locked and stably sliding fault planes in a subduction zone where an oceanic plate is sliding beneath a continental plate. These earthquakes have a slip velocity (the rate at which rocks move) between those of high-speed ruptures (~1 m/s) and slow stable sliding (~10^{-8} m/s). Among the different types of slow earthquakes, slow sliding on a fault with no emission of seismic waves is called a slow slip event. These events can last for days to weeks (short-term) or for months to years (long-term). Short-term slow slip events often spatiotemporally coincide with other slow earthquakes, such as an "episodic tremor and slip," which includes low-frequency tremors (1 to 10 Hz) and very-low-frequency earthquakes (0.01 to 0.1 Hz). Slow slip events have been observed preceding large earthquakes in the northern coast of Japan, Mexico, and Chile (*4*). These events migrated toward the nucleation zones of large earthquakes, which suggests that slow slip events can load stress in the locked fault planes that are associated with major earthquake rupture (*4*).

In the Nankai Trough, only interactions between different types of slow earthquakes have been observed, with no reports of interactions between slow and large earthquakes (*5*). In this region, different types of slow earthquakes occur in both shallow and deep sections of the locked fault plane and are distributed in different locations (see the figure). Deep under Earth's surface, long-term slow slip events and episodic tremors and slips occur within distinct zones at different depths. They divide into multiple segments at specific intervals. By contrast, near Earth's surface, these various phenomena randomly arise within the same depth range between the trench axis and the locked fault zone. This heterogeneity is thought to be due to variations in many factors, such as topography, lithology, frictional properties, and pore fluid pressure (*6*).

Evolution of slow earthquakes in the Nankai Trough

An oceanic plate is sliding beneath a continental plate in the Nankai Trough, accumulating immense strain that results in large earthquakes. Slow earthquakes, such as slow slips and episodic tremors, occur in both shallow and deep sections of the rupture area. These activities can migrate along the plate boundary fault plane, loading stress on adjacent areas. The spatiotemporal pattern of slow earthquake activities could be an indicator of potential large earthquakes.

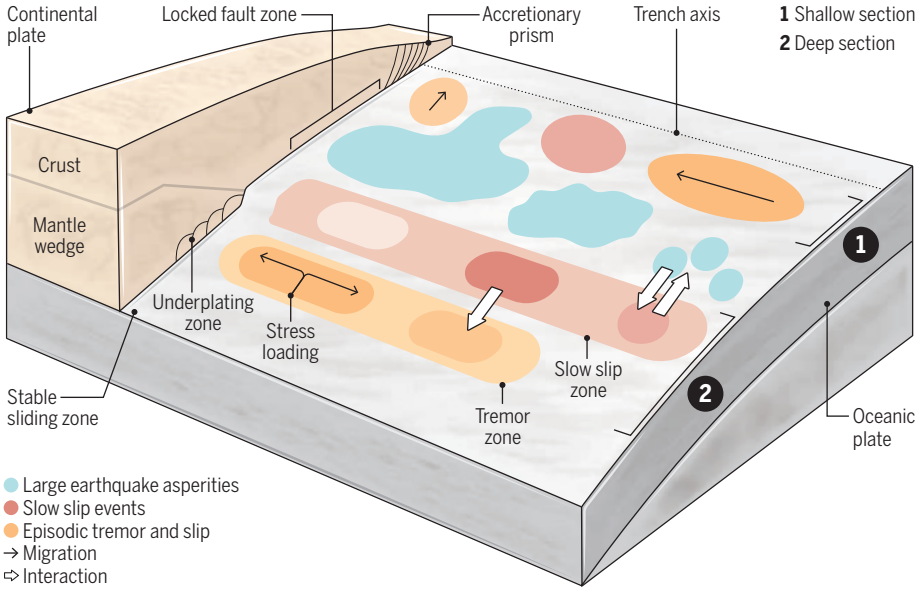

Using a Global Navigation Satellite System observation network, Ozawa *et al.* identified a long-term slow slip event that occurred in a deep section of the mainshock rupture area approximately 1 year before the 2024 large earthquake (magnitude of 7) in the Hyuga-Nada region, off the southern coast of Japan. Thirteen slow slip events have taken place in this location over the past three decades, and three slow slip events were followed by separate large earthquakes in 1996, 2019, and 2024. Given that the rupture area of the 2024 earthquake was unaffected by the earlier events, the authors proposed that the 2024 rupture occurred as a result of stress loading from repeating slow slip events before the earthquake. In this slow slip location, an afterslip (a slow transient shear after the mainshock) was detected, demonstrating two-way interactions between slow and large earthquakes.

In addition to stress transfer from slow earthquakes, these events may function as stress meters because of their high sensitivity to external stress perturbations in the surrounding region (*1*). A numerical simulation that incorporates a friction law indicated a shortening of the recurrence interval of slow slip events as a large earthquake approaches (*7*). As reported by Ozawa *et al.*, a slow slip event preceding the 2024 mainshock occurred 1 year after the previous slow slip event, whereas the average recurrence interval of slow slip events is about 2 years. However, given the large fluctuations in recurrence intervals observed in the simulation, additional longer-term monitoring is needed to better evaluate such trends.

Edgington *et al.* reconstructed detailed spatiotemporal evolution of two slow slip events in 2015 and 2020 by using pore fluid pressure data from three boreholes that were drilled into Earth's crust off the southeast coast of the Kii Peninsula in Central Japan. These holes are equipped with sensors to monitor activities such as pressure, tilt, strain, and deformation. The results showed that the slow slip started about 30 km landward and migrated toward the trench along the plate interface, possibly reaching the trench in both cases. This is contradictory to earlier conclusions that these slow slip events did not reach the trench because friction at the base of an accretionary prism (a series of sheared sediment wedges) was considered not favorable to generate an earthquake (*8*). Edgington *et al.* indicated that the boundary between the sliding plates, even near the trench, can accumulate and release stress, which raises the possibility of coseismic slip during a large earthquake—that is, high-speed fault rupture emitting strong seismic waves. This is consistent with the observation of frictional heating of the drilled samples obtained near the trench (*9*).

The spatiotemporal evolution of slow earthquake activity is an indicator of the state of the plate boundary. Episodic tremor and slip in the deep section of the locked fault plane often begins at the boundary of the stable sliding zone and the tremor zone. These events load a stress on the shallower side in the deep section, which promotes a larger tremor and slip event (*10*). Although slow slip events in the shallow section have shown similar migration behavior, other slow earthquakes such as tremors and very-low-frequency earthquakes in the same shallow section have shown different behaviors in 2015 and 2020. Additional active slow slip events also took place in this area and migrated along the trench axis during other episodes. These various slow earthquake behaviors in the shallow section could reflect heterogeneity and temporal changes in the structure of the plate boundary, which could be a result of the migration of pore water and other factors (*6*).

Ozawa *et al.* and Edgington *et al.* emphasize the importance of spatiotemporal evolution and locations of slow earthquakes to evaluating the occurrence of large earthquakes. However, the long-term slow slip events preceding the 2024 Hyuga-Nada mainshock were not associated with a clear migration of slip area. Long-term slow slip events take place over a larger area of the fault plane and have a greater slip length compared with short-term slow slip events. Consequently, even if migration did not occur, static stress loading on the adjacent region may have contributed to triggering the large earthquake. In the future, it should be possible to gather more detailed information on the slow earthquakes and establish a standard pattern of activity of such events. This should make it possible to evaluate the distinctiveness of individual slow earthquake activity, which might be related to the potential for large earthquakes. To this end, it is necessary to strengthen observation networks and monitoring technology. □

REFERENCES AND NOTES

1. K. Obara, A. Kato, *Science* **353**, 253 (2016).
2. J. R. Edgington, D. M. Saffer, C. A. Williams, *Science* **388**, 1396 (2025).
3. S. Ozawa, H. Munekane, H. Suito, H. Yarai, *Science* **388**, 1401 (2025).
4. A. Kato, Y. Ben-Zion, *Nat. Rev. Earth Environ.* **2**, 26 (2021).
5. H. Hirose *et al.*, *Science* **330**, 1502 (2010).
6. S. Takemura *et al.*, *Earth Planets Space* **75**, 164 (2023).
7. T. Matsuzawa, H. Hirose, B. Shibazaki, K. Obara, *J. Geophys. Res.* **115**, B12301 (2010).
8. E. Araki *et al.*, *Science* **356**, 1157 (2017).
9. A. Sakaguchi *et al.*, *Geology* **39**, 395 (2011).
10. A. G. Wech, K. C. Creager, *Nat. Geosci.* **4**, 624 (2011).

10.1126/science.ady7173

National Research Institute for Earth Science and Disaster Resilience, Tsukuba, Japan.
Email: obara@bosai.go.jp

GRAPHIC: A. MASTIN/*SCIENCE*

MICROBIOLOGY

A caged drug enables precision delivery

"GlycoCaging" uses gut bacteria to activate drugs for inflammatory bowel disease

Yuhao Xie and **Zhe-Sheng Chen**

Inflammatory bowel disease (IBD), particularly Crohn's disease and ulcerative colitis, is a chronic inflammatory disorder primarily affecting the lower gastrointestinal tract (small and large intestines) (*1*, *2*). Treating IBD remains a major global challenge owing to the difficulty in balancing therapeutic efficacy with systemic toxicity (*1*, *3*). Oral medications such as corticosteroids (for example, dexamethasone) are often absorbed prematurely in the upper gastrointestinal tract, limiting their delivery to the lower gut. Although dose escalation may improve efficacy, it often causes unacceptable systemic side effects (*1*, *4*). On page 1410 of this issue, Ma *et al.* (*5*) present a microbiota-driven drug delivery strategy called "GlycoCaging," which addresses this challenge by enabling precise drug release in the lower gastrointestinal tract. The approach shows the potential of integrating microbial biology with chemical engineering for advanced therapies.

The hallmark of IBD is chronic inflammation of the intestinal mucosa. Patients typically experience recurrent bouts of abdominal pain, bloody diarrhea, urgency, and weight loss, driven by an overactive immune response that damages the epithelial lining and disrupts barrier function (*1*, *4*). Anti-inflammatory corticosteroids such as dexamethasone ameliorate these symptoms by binding the intracellular glucocorticoid receptor in both colonic epithelial cells and infiltrating immune cells; the activated glucocorticoid receptor translocates to the nucleus, where it represses pro-inflammatory transcription factors and up-regulates anti-inflammatory genes, restoring mucosal integrity (*1*, *2*, *4*). However, systemic administration of dexamethasone and other steroids is associated with substantial off-target effects, including immunosuppression, osteoporosis, adrenal insufficiency, hyperglycemia, and Cushingoid features, which limit long-term use (*1*, *4*). Together, these safety concerns underscore the need for colon-selective delivery strategies that maximize local efficacy and minimize systemic exposure.

The GlycoCaging approach proposed by Ma *et al.* involves chemically conjugating drugs to xyloglucan heptasaccharide (XXXG)—a dietary fiber found in the cell walls of most whole plant foods—by means of a covalent glycosidic linkage (*6*, *7*). The XXXG cage protects the conjugated active drug from degradation by most digestive enzymes in the stomach and small intestine. On reaching the colon, specific xyloglucan-degrading enzymes—particularly those from the GH5_4 enzyme family produced by the *Bacteroides* genus of bacteria—recognize and hydrolyze the glycosidic linkage that connects the drug to the XXXG cage, releasing the active drug for therapeutic action (see the figure) (*6*, *8*). These xyloglucan-degrading enzymes are not produced by human cells or by bacteria present in the upper gastrointestinal tract, enabling the active drug to be released only in the lower gastrointestinal tract. In mouse models of IBD, oral treatment with GlycoCaged dexamethasone (XXXG-Dex) alleviated intestinal inflammation at doses 60 to 90% less than that required with conventional dexamethasone. Notably, drug concentrations detected in the lungs and blood of IBD mice treated with the XXXG-Dex were extremely low, indicating that this delivery approach substantially reduces systemic drug exposure and eliminates steroid-related toxic side effects such as lung inflammation.

Ma *et al.* found that active xyloglucan-degrading enzymes were widely present in fecal samples from both healthy individuals and individuals with IBD, indicating that the GlycoCaging approach could be applied to most patient populations. They also report that dietary xyloglucan supplementation increased the amount of bacterial enzyme present in the intestine of mice. This suggests that in the future, patients could modulate their intestinal bacterial enzyme activity through dietary adjustments to optimize the efficacy of the uncaging process. The authors demonstrated the broad biological applicability of the approach by generating XXXG conjugates with other anti-inflammatory drugs (such as 5-aminosalicylate, budesonide, and prednisolone) through distinct chemical synthesis methods.

The implications of the study by Ma *et al.* extend beyond improving existing IBD therapies. By enhancing the therapeutic index—a measure of the margin between the effective dose and the dose that causes toxicity—GlycoCaging also creates opportunities for drug repurposing (*9*). For example, highly potent anti-inflammatory agents that are approved for other conditions—but are too toxic when administered systemically—might now be repurposed for IBD by delivering them using GlycoCaging for colon-targeted release. Compared with developing

Delivering drugs straight to the colon

In the GlycoCaging approach, a therapeutic drug such as dexamethasone is linked to a xyloglucan heptasaccharide (XXXG) with a glycosidic linkage. The XXXG "cage" protects the drug from degradation and absorption as it travels through the upper gastrointestinal tract. Upon reaching the colon, xyloglucanase enzymes on the surface of colon-resident *Bacteroides* bacteria break the glycosidic linkage, thus releasing the active drug for absorption into the colonic epithelium.

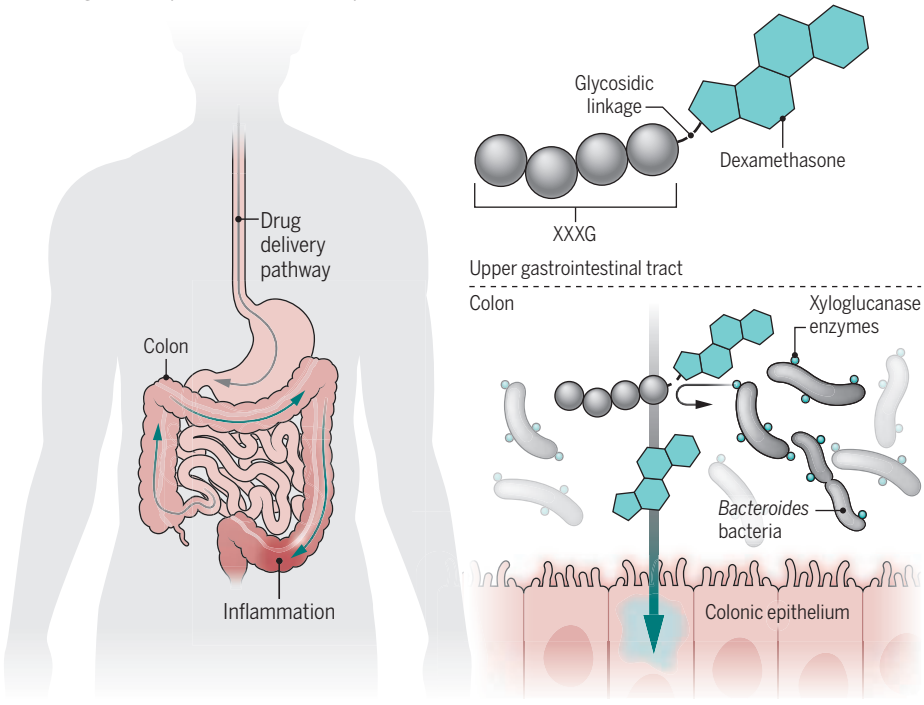

GRAPHIC: N. BURGESS/*SCIENCE*

drugs from scratch, such repurposing could substantially shorten drug development timelines and reduce costs (*9*). The approach also holds potential for use in other diseases such as the delivery of oral peptide- and protein-based drugs for colorectal cancer.

GlycoCaging also offers fresh perspectives for therapies that rely on microbial metabolism. In traditional microbiota-activated prodrugs, bacterial enzymes cleave a chemical linker to release the active drug, but because those linkers often mimic general bacterial substrates, they can be reduced by many different species and at varying rates. This yields unpredictable release profiles, with some patients experiencing premature activation (raising systemic exposure) and others delayed activation (reducing local efficacy). In the case of prodrugs for antibiotics, such indiscriminate activation may expose bacteria to sub-therapeutic drug concentrations, which over time can select for resistant strains and, in some cases, overstimulate bacterial growth as microbes attempt to metabolize the prodrug (*10*). By relying on the specific action of one group of colon-resident bacteria, GlycoCaging should not be subject to these limitations (*11*, *12*).

Translating GlycoCaging into clinical application presents critical challenges. Although xyloglucan-degrading enzymes are widely present in humans, variations in gut microbiota composition caused by diet, genetics, antibiotic use, or disease may substantially influence the activity and efficacy of caged drugs (*11*). Such variability could lead to divergent drug release rates among individuals. Although microbiome profiling and patient stratification techniques—methods that determine the exact makeup and abundance of xyloglucan-degrading bacteria in a patient's gut—could help account for this variability, cost-effective and rapid diagnostic methods for accurately characterizing an individual's gut microbiota are lacking. Additionally, dietary xyloglucan may compete with XXXG–drug conjugates for the same lytic enzymes and slow or alter drug release kinetics. Practical challenges in the scalable synthesis of precisely engineered XXXG-drug conjugates must also be resolved.

Future research could focus on evaluating GlycoCaging drugs in animal models that better replicate the diversity of human gut microbiomes and dietary patterns. These studies would help refine dosing strategies and assess long-term safety before clinical trials in individuals with IBD. It would also be helpful to explore a broader microbial enzyme repository to identify bacterial enzyme-dietary fiber pairs that are specific to different regions of the gut. This could enable GlycoCaging of drugs for specific release in other parts of the gastrointestinal tract. Moreover, combining GlycoCaging with probiotics (live beneficial bacteria) or prebiotics (nondigestible compounds that feed those bacteria) could ensure sustained drug release in the gastrointestinal tract. □

REFERENCES AND NOTES

1. T. L. Parigi *et al.*, *Lancet Gastroenterol. Hepatol.* **8**, 853 (2023).
2. G. G. Kaplan, *Nat. Rev. Gastroenterol. Hepatol.* **12**, 720 (2015).
3. A. Gilliland *et al.*, *Gastroenterology* **166**, 44 (2024).
4. A. Awad *et al.*, *Adv. Drug Deliv. Rev.* **181**, 114076 (2022).
5. W. J. Ma *et al.*, *Science* **388**, 1410 (2025).
6. H. V. Scheller, P. Ulvskov, *Annu. Rev. Plant Biol.* **61**, 263 (2010).
7. A. M. Rodd *et al.*, *Biotechnol. Biofuels Bioprod.* **17**, 116 (2024).
8. A. A. Verdegaal, A. L. Goodman, *Sci. Transl. Med.* **16**, eadg8357 (2024).
9. S. Pushpakom *et al.*, *Nat. Rev. Drug Discov.* **18**, 41 (2019).
10. X. Yang, H. C. Hang, *Science* **386**, eado8548 (2024).
11. K. Hou *et al.*, *Signal Transduct. Target. Ther.* **7**, 135 (2022).
12. D. J. Braccia *et al.*, *Drug Metab. Dispos.* **51**, 142 (2023).

ACKNOWLEDGMENTS

Y.H.X. expresses thanks for the teaching fellowship from the Department of Pharmaceutical Sciences, St. John's University. The authors acknowledge X. Ma (West China Hospital and Sichuan University) for constructive suggestions.

10.1126/science.ady9507

Department of Pharmaceutical Sciences, College of Pharmacy and Health Sciences, St. John's University, Queens, NY, USA. Email: chenz@stjohns.edu

PALEOGENOMICS

Genomic insights into social life in Neolithic Anatolia

Matriarchs and foragers emerge as important players in early farming villages

Benjamin S. Arbuckle

Ancient populations present in Anatolia, modern Türkiye, during the Neolithic period (~8000 to 6000 BCE) were defined by the emergence of early farming technologies and settlements constructed of mudbrick houses. Previous research has shown that these Anatolian farming communities expanded westward around 6500 BCE, colonizing much of the European continent (*1*). The assumption was that the Neolithic communities in Anatolia were male dominated and replaced more "primitive" forager populations as they moved west. On pages 1386 and 1385 of this issue, Yüncü *et al.* (*2*) and Koptekin *et al.* (*3*), respectively, describe paleogenomic evidence from ancient populations that challenges these assumptions and provides intimate new details of social life in the Neolithic period. Both studies reflect the advances of paleogenomics in addressing socially nuanced questions and dispute traditional narratives of human history.

The early farming communities present in Neolithic Anatolia maintained domestic cereal crops as well as livestock and often consisted of densely packed houses, carefully built of sundried mudbrick with human burials placed under house floors. The largest of these farming villages was Çatalhöyük in central Anatolia, which was made up of hundreds of houses and was occupied for more than a millennium (~7000 to 5800 BCE). The social organization of these complex communities has been the subject of speculation, as has the nature of their interactions with the local forager populations whom they encountered as they expanded westward.

Yüncü *et al.* analyzed genomes from 133 individuals buried in Çatalhöyük and produced a map of kin relations among the dead. The authors found patterns in the burials that reflected the persistent co-burial of maternal relatives and the presence of abundant grave goods specifically in burials identified through genetics as female. Siblings, aunts-nieces, and maternal cousins were frequently found co-buried under the floors of the same or adjacent buildings, indicating that houses were occupied by nuclear and extended families related through matrilines. Evidence suggestive of similar patterns has been observed at earlier communities in the region (~8000 BC) (*4, 5*), pointing to a widespread social architecture in which female lineages, and the clans that they presumably defined, were the indelible building blocks of Neolithic Anatolia.

Moreover, Çatalhöyük and other Neolithic communities in Anatolia are known for the abundance of figurines depicting female bodies, some seated in poses of power and authority (*6, 7*) (see the photo). Previous generations

Neolithic communities in Anatolia produced figurines depicting female bodies in poses of power and authority.

of scholars have tended to interpret the forms of these objects as representing fertility goddesses or pregnant women but more recently, they have begun to be viewed as senior women embodying considerable power. Yüncü *et al.* are conservative in their interpretation of matriarchy or female power at Çatalhöyük. However, if the sex patterns were reversed, there would likely be little hesitation in concluding that patriarchal power structures were at play. This is reflective of the difficulty that many scholars have in imagining a world characterized by substantial female power despite abundant archaeological, historic, and ethnographic evidence that matriarchal fields of power were and are widespread (*8*).

The dominance of maternal lineages at Çatalhöyük contrasts with the results of relatedness analyses from later Neolithic sites in Europe where male burials reflect a shift to patrilineality and likely patriarchal power structures, despite the descent of European Neolithic populations from Anatolian farming communities (*1*). One hypothetical scenario for this shift in kin relations is that migration away from ancestral Anatolian sites such as Çatalhöyük created opportunities for certain ambitious male lineages to renegotiate power relationships in newly settled communities, resulting in the emergence of the patrilineal systems of later Neolithic Europe (*9*). These windows into the social architecture of Neolithic communities indicate that the broader histories of social structures should be thought of not as inevitable and unchanging features of monolithic "peoples" but rather as the results of contested and dynamic historical processes.

Using 30 newly sequenced paleogenomes from individuals from both forager and early farmer sites in Anatolia, Koptekin *et al.* identify the genetic fingerprint of the local forager population of West Anatolia. These Early Holocene West Anatolians (EHWA) were contemporaries of those at Çatalhöyük and occupied the Aegean region before the westward expansion of central Anatolian farmers. The authors' analyses revealed complex social and demographic processes involved in the spread of farming technologies from Anatolia into Europe. Previous scholarship long imagined a wave of "advanced" farmers flowing westward across Europe replacing "simple" forager populations. The study of Koptekin *et al.* instead reveals a far more dynamic social history with local EHWA foragers acting with their own agency to create economies based on a combination of foraging and farming, sedentism and mobility, prior to the arrival of central Anatolian farmers (*10*). Rather than simply being replaced by incoming farmers, this local population went on to "admix" (i.e., socially and sexually interact) with these farmer communities, but in geographically and temporally diverse ways. This variation in admixture must represent a realm of prehistoric politics as individuals from these various interacting communities negotiated their positions on an intimate and personal scale. The descendants of the resulting "blended" farming population were hugely important, going on to establish the Neolithic of Europe with its economy and languages influencing the genomics, flavors, and sounds of much of western Eurasia for millennia to come (*1*, *9*).

Koptekin *et al.* also built identical-by-descent networks to look for shared genetic sequences indicating close familial ties between sites. This fine-grained analysis revealed unexpected connectivity between farmer sites separated by hundreds of kilometers, each exhibiting different cultural practices (i.e., architecture, economy, burials, etc.). This observation connects geographies that scholars long assumed were isolated, reimagining them instead as the locations of cultural boundaries, porous to movement but persistent in their maintenance of difference (*11*).

The studies by Yüncü *et al.* and Koptekin *et al.* provide a window into the rich social worlds of the Neolithic, which are starting to look less like the simplistic, progress-themed narratives inherited from previous generations of scholarship and more like the contingent, messy, and creative communities that are described in later historic and ethnographic records. By using increasingly powerful paleogenomic data to ask nuanced social questions, these authors are taking exciting steps toward turning prehistory into history. □

REFERENCES AND NOTES

1. I. Lazaridis *et al.*, *Science* **377**, eabm4247 (2022).
2. E. Yüncü *et al.*, *Science* **388**, eadr2915 (2025).
3. D. Koptekin *et al.*, *Science* **388**, eadr3326 (2025).
4. R. Yaka *et al.*, *Curr. Biol.* **31**, 2455 (2021).
5. N. E. Altınışık *et al.*, *Sci. Adv.* **8**, eabo3609 (2022).
6. C. Nakamura, L. Meskell, *J. Archaeol. Method Theory* **16**, 205 (2009).
7. Ç. Atakuman, H. C. Gemici, *Figurine-Making in the Neolithic Aegean*, S. Nanoglou, F. Mavridis, Eds. (Sidestone Press, 2024), pp. 113.
8. D. Graeber, D. Wengrow, *The Dawn of Everything* (Penguin, 2023).
9. M. Rivollat *et al.*, *Nature* **620**, 600 (2023).
10. B. Erdoğu, *Studia Praehistorica* **16**, 1 (2022).
11. D. W. Anthony, *J. Anthropol. Archaeol.* **70**, 101508 (2023).

10.1126/science.ady6939

Department of Anthropology, University of North Carolina at Chapel Hill, Chapel Hill, NC, USA. Email: bsarbu@email.unc.edu

Climate resilience investments in coastal communities such as Kuakata, Bangladesh, may not be effective without addressing increasing salinity intrusion.

PHOTO: MUNIR UZ ZAMAN/GETTY IMAGE

CLIMATE POLICY

Climate adaptation finance: From paper commitments to climate risk reduction

Science can help to target climate finance at better-quality adaptation

Jasper Verschuur[1,2,3], Nicola Ranger[3,4], Jim. W. Hall[3]

Climate adaptation finance is intended to fund activities to reduce the physical climate risks faced by countries. The quantity of adaptation finance has been a highly contentious political issue, and a critical negotiating point for developing countries in international climate negotiations. Yet we argue, as have others, that countries' resilience to the impacts of climate change will not be noticeably enhanced unless the international adaptation finance community shifts its focus from the quantity of finance to its quality and risk-reducing impacts. We provide five recommendations, underpinned by evidence from scientific research, to transform the quality of adaptation delivered with adaptation finance, to build credibility that it will cost-effectively reduce the future impacts of climate change. Doing so requires an urgent shift in efforts toward improving the enabling environment of governments, sectors, and communities to identify, appraise, prioritize, finance, implement, and monitor adaptation programs and projects.

At the United Nations climate conference (COP29) in Baku in November 2024, global leaders from developed nations agreed to a renewed pledge to increase climate finance for climate adaptation and mitigation to USD 300 billion per year, and up to USD 1.3 trillion in 2035. On paper, this more ambitious commitment would bring the adaptation finance distributed by the international community, at present amounting to around USD 30 billion annually, a small step closer to the estimated adaptation requirement of USD 215 to 387 billion annually by 2030 for emerging market and developing economies (EMDEs) (*1*). But despite its political importance, there is no reason to believe that the current adaptation finance system will have the desired impact of reducing climate risks to vulnerable people.

Part of the reason for focusing on inputs to climate finance rather than risk-reducing outputs is a lack of agreement among international policy-makers as to what successful adaptation looks like (*2*) and how it can be measured and monitored across countries (*3*). After years of limited progress toward the Global Goal on Adaptation (GGA), the joint commitment under the Paris Agreement to ensure adequate adaptation action, some encouraging developments have recently emerged. During COP28, a first set of targets and indicators toward the GGA was approved under the UAE Framework for Global Climate Resilience, and during COP29, Multilateral Development Banks (MDBs), who are at the forefront of distributing climate finance, released a common approach to measuring climate results. Several new climate risk tools and analytical products [e.g., the World Bank's Country Change and Development Reports (CCDRs)]

have been developed, and the International Monetary Fund (IMF) has piloted the inclusion of climate risk as relevant fiscal risk into their Financial Sector Assessment Program (FSAP).

Although these are welcome steps, there is still a chasm between top-down politically driven developments and the adaptation that is (not) materializing on the ground. Despite good intentions and skilled people dedicated to adaptation, the lack of impact is in part due to the culture in international policy and development finance that is quite disconnected from implementing adaptation. In particular, adaptation is not just about building new infrastructure, promoting climate-resilient agricultural practices, or retrofitting buildings, but also about improving the processes and capabilities of local and national institutions to lead adaptation efforts through the adaptation cycle (i.e., identify, appraise, prioritize, implement, and monitor). Although the latest climate and adaptation science is now at a stage that it can answer those questions that initially prevented the GGA from moving forward, the current underappreciation of improving the capabilities and processes of institutions is preventing it from delivering adaptation impact.

WHAT GOES IN, OR WHAT COMES OUT?

In their "Adaptation Gap Report," the United Nations Environmental Programme (UNEP) estimates the adaptation gap in EMDEs by comparing model-based assessments of adaptation needs (*1*) to the reported public international adaptation finance in the database maintained by the Development Assistance Committee (DAC) within the Organization for Economic Cooperation and Development (OECD) (*4*). However, modeled adaptation needs and reported adaptation finance are fundamentally different, making it unclear what the gap between them represents. Modeled adaptation needs cover the adaptation action necessary to reduce climate risk relative to a "no adaptation" counterfactual. This, in turn, is a function of the frequency and severity of present and future climatic hazards, the damage and losses that are incurred because of those hazards, and the lost economic opportunities because of real and perceived climate risks.

In contrast to this approach based on climate risk reduction, MDBs assign a simple "adaptation ratio" to each project that they finance. This ratio indicates the share of the project that is considered to be climate adaptation, based on the investment's adaptation intent. Data between 2016 and 2022 show that the MDBs have increased their adaptation finance by a factor of 4 in 6 years (see the first figure, top). This is driven by the fact that more projects have been classified as incorporating some form of adaptation, while the average adaptation spend per project (see the first figure, top) and share of financing across adaptation projects (see the first figure, bottom) have remained stable. In other words, MDBs have mainly added adaptation throughout their portfolio of development projects (i.e., adaptation mainstreaming), rather than focusing more finance on projects whose primary aim is climate adaptation. The mainstreaming of adaptation in development, in part motivated by the uptake of climate risk screening methodologies [e.g., the World Bank Resilience Rating System (RSS)], is to be welcomed. By applying the RSS framework, it was, for example, found that including climate adaptation in a transport connectivity project (worth USD 275 million) in Nepal would cost only 3% more, while ensuring the delivery of development benefits over the project lifetime (*5*).

The current reporting system adopted by MDBs (and others) could nonetheless incentivize box-ticking and mislabeling. There is no reason to believe that a dollar of adaptation finance spent in two different locations or on projects with a similar "adaptation ratio" will achieve equivalent risk-reducing benefit without examining the present and future climate risks and the efficiency of the proposed intervention. Yet quantification of expected climate risk reduction is either absent or not readily comparable. Therefore, current practice provides no way of knowing how adaptation investments "add up" to manage climate risk. The 2023 update to the MDBs' joint adaptation tracking methodology expanded the definition of adaptation finance further to include sectors like education, health, and social protection. Although undoubtedly important for effective adaptation, this broadening makes it even harder to compare the reported adaptation finance with countries' climate risk and adaptation needs.

In short, the current focus on measuring "what goes in" draws away attention from "what comes out" of the adaptation finance apparatus. Mainstreaming adaptation in development projects is key, in particular to ensure that new projects do not increase exposure to the impacts of climate change. Yet, dependence on the adaptation ratio for measuring adaptation finance risks insufficient and fragmented adaptation, especially given the systemic impacts that climate change may pose to communities, economies, and infrastructure (*6*) and the transformative adaptation that may be needed in response (*2*). For instance, climate resilience investments in low-lying deltas, like the Mekong and in the Bay of Bengal (*7*) (see the photo), may not be effective or sustainable without addressing the worsening salinity intrusion that coastal communities face over the coming decades as a result of sea-level rise and human activities.

THE CLIMATE INVESTMENT TRAP

Increasing finance through the existing adaptation finance apparatus, without noticeably reducing climate impacts, further increases the likelihood of countries becoming stuck in a "climate investment trap." Many EMDEs are making investments in sectors like real estate, infrastructure, and industry to spearhead growth, which increases a country's exposure to climate-related hazards. Investments to reduce

Mainstreaming adaptation funding

Multilateral development banks increased adaptation finance by a factor of 4 in 6 years (top), as more projects have been classified as incorporating some form of adaptation, while the average adaptation spend per project (top) and share of financing across types of adaptation projects (bottom) have remained stable. See supplementary materials for details on data.

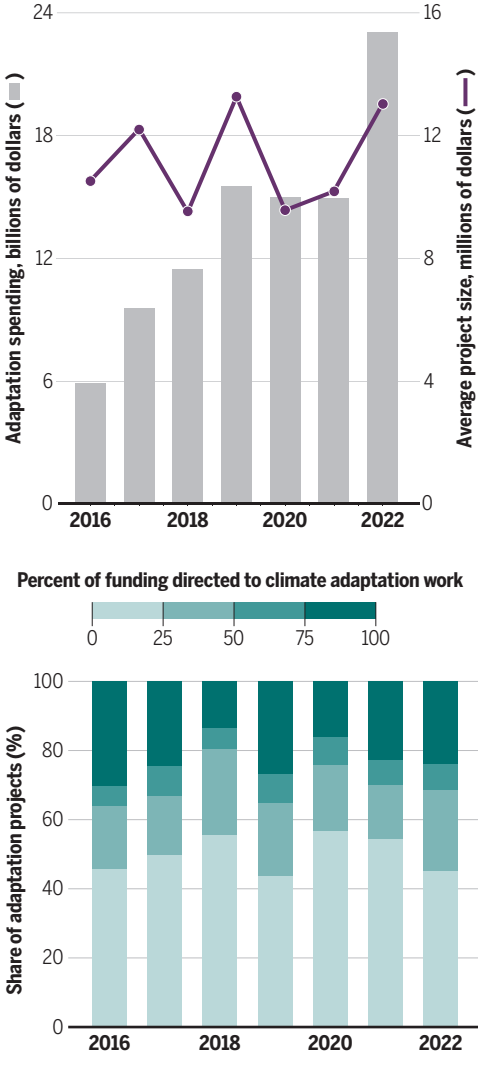

GRAPHIC: V. PENNEY/*SCIENCE*

climate risks often lag behind this growing exposure, resulting in elevated climate losses that are being exacerbated by climate change. Such losses affect government budgets (owing to reconstruction costs and lost taxation revenues) and elevate their debt-to-GDP (gross domestic product) ratio, a measure of debt distress.

Rising debt levels can, in turn, lower borrowing capacity and reduce investments in productive capital and adaptation, dragging the economy further. The rising debt crisis in many countries is only accelerating this vicious circle. For example, the Maldives, facing major adaptation challenges like those of other small island developing states, is required to spend around 8% of GDP on debt servicing in 2024–2025 (*8*), likely slowing down public investments in adaptation.

Most adaptation finance is through debt (see the second figure, top), with grants primarily benefiting low-income countries (see the second figure, bottom). Those countries relying on debt financing, though having a high debt-to-GDP ratio, already struggle to finance adaptation projects. Between 2016 and 2022, middle-income countries —which primarily rely on debt financing—with a ratio of above 50% received less than half the adaptation finance as a share of GDP relative to those with a ratio below 50% (see the second figure, bottom). Adaptation gains often emerge beyond loan repayment horizons, so even with the favorable conditions of MDB-backed loans, excessive debt for climate adaptation may be unaffordable.

The fiscal position of debt-ridden countries is unlikely to be alleviated soon. Although some initiatives have emerged to promote adaptation investment for high-debt countries, like debt-for-adaptation swaps, their scale has been too small to substantially improve debt sustainability or bridge the adaptation gap (*9*). In plain words, scaling up adaptation efforts simply cannot happen without improvements in fiscal sustainability, and vice versa.

FROM PAPER COMMITMENTS TO RISK REDUCTION

To accelerate adaptation, we highlight five focus areas to improve the capabilities, processes, and institutions throughout the adaptation cycle so that the latest developments in science can be turned into impact. These focus areas are intended to support countries in meeting their proposed commitments under the UAE Framework for Global Climate Resilience by 2030 to advance efforts throughout the adaptation cycle.

First, targeting effective adaptation actions depends upon comprehensive locally relevant climate risk information, both present-day and future risks under a range of climate and socioeconomic scenarios. This provides a platform upon which different sets of adaptation actions can be evaluated to establish their expected impact in terms of risk reduction. The need for science-based, yet place-specific, climate risk information is widely recognized (*10*). Despite the proliferation of datasets and tools, the provision of future climate data is often detached from adaptation planning (*11*), in part because of the disconnect between those providing climate information and those that have to embed this information into planning and project preparation. We call for strengthened capacity building efforts to enable EMDEs to perform such risk analysis themselves, supported by their own research institutions and building on local data but with globally reproducible tools. The "Global Infrastructure Resilient Index" of the Coalition for Climate Resilient Infrastructure is a good example of such a global tool, which can be a valuable starting point for nationally led risk assessments. These efforts should be supported by a set of guidelines, building on the World Bank's RSS, such that assessments can be standardized and, hence, can be compared. Such guidelines should be regularly updated, so that the evolution of climate risk can be tracked, and scientific advances in modeling climate risks can be incorporated.

Second, countries need to move toward more specific adaptation strategies based on the priority risks identified. At present, the quality of National Adaptation Plans (NAPs), which outline such strategies, is highly variable. Often, there is a mismatch between the aspirations set out in NAPs and the adaptation projects that are eventually financed. Overcoming this mismatch requires adaptation strategies that are specific in terms of their risk-reducing aspirations and the associated costs, and policy reforms needed to achieve them. A national perspective is essential to identify systemic adaptation actions, those that are interregional, cross-sectoral, or transformative in nature and require national coordination. The World Bank's CCDRs have taken a necessary first step in providing such a national, yet cross-sectoral, focus. However, such a national strategy needs to be integrated within sector-specific strategies for the most vulnerable sectors (e.g., water, agriculture, energy, transport, public services), and with local adaptation efforts. For instance, Bangladesh is planning to establish Locally Led Adaptation Hubs under its Mujib Climate Prosperity Plan 2022–2041 that can implement local adaptation projects and monitor progress in reducing the vulnerability of communities.

Third, NAPs should be supported by fiscal strategies with realistic financing plans and costs, which is rarely done in practice. Doing so is key for the implementation of NAPs, in particular the sequencing of investments, as well as balancing adaptation investments with financial instruments (e.g., insurance, catastrophe bonds). Taking this step requires integrating fiscal impact analysis within climate risk assessments, and vice versa. Such analysis should take a probabilistic view of present and future shocks, akin to traditional fiscal stress testing, and should capture multiple fiscal impact channels, such as impacts to government spending, consumption, tax revenues, and credit ratings. A recent study for Thailand (*12*) captured these impact channels and demonstrated how adaptation investments

A vicious circle: debt and adaptation

Most adaptation finance is through debt (top); grants primarily benefit low-income countries (bottom; middle-income grant funding is minimal and may be difficult to discern). Countries relying on debt, while having a high debt-to-GDP (gross domestic product) ratio, struggle to finance adaptation projects. Between 2016 and 2022, middle-income countries with a ratio above 50% received less than half the adaptation finance as a share of GDP relative to those with a ratio below 50% (bottom). See supplementary materials for details on data.

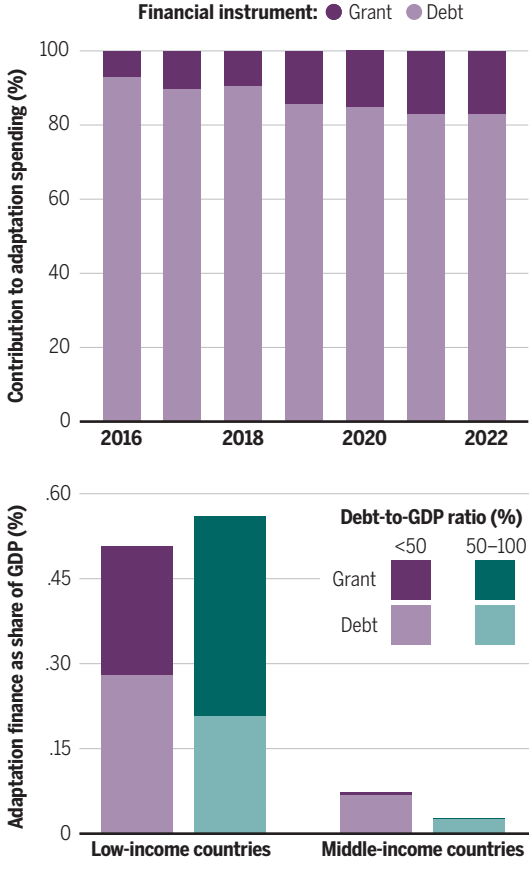

GRAPHIC: V. PENNEY/*SCIENCE*

...skilled human capacity...needs to be patiently built and retained within the governments and communities where it is most needed.

can reduce the risk of indebtedness. The IMF, through its Resilience and Sustainability Facility, and the Coalition of Finance Ministers for Climate Action have been instrumental in putting climate adaptation on the fiscal agenda but could take a more leading role in promoting efforts to develop fiscal strategies to fund NAPs.

Fourth, the implementation of adaptation strategies relies on robust project design that justifies the investment and its priority over those not undertaken. Yet, the capacity to identify and prioritize sustainable and cost-effective adaptation projects is severely limited in many countries. Too often, project preparation and prioritization are dependent on external consultants with inconsistent methodologies. Planners often lack the knowledge about what adaptation works, for whom, and under what circumstances (*13*). Project prioritization needs to rigorously compare the benefits of adaptation with the costs ex ante, i.e., within the framework of cost-benefit analysis (CBA). Though CBA has been widely criticized, it is a family of methods that can incorporate the risk-reducing benefits and the co-benefits of adaptation, i.e., the "triple dividend" (*14*). The latter is key, as in many cases the co-benefits of adaptation (e.g., carbon sequestration, income generation) can outweigh risk reduction benefits, especially if disasters do not materialize. The rigor of CBA, its flexibility to add new scientific insights, and its applicability across sectors can stimulate careful scrutiny of proposals and provides a framework within which questions of incommensurable value (i.e., cultural losses) and equity can be explored. Planning agencies, whether national or regional (i.e., for larger economies), are central to this, as they are well equipped to embed adaptation in a coherent fashion within long-term planning decisions. For instance, the Planning Institute of Jamaica has a mandate to mainstream adaptation into planning across the island's economy, as well as aligning and coordinating donor support for adaptation.

Fifth, structured monitoring of the benefits of adaptation ex post, in terms of avoided losses and co-benefits, is absent in almost all jurisdictions. Exceptions include those indicators included in the Sendai Framework for Disaster Risk Reduction, such as the availability of early warning systems. More rigorous metrics are needed to track the impacts of climate finance, evaluate value for money, promote learning, and establish ongoing adaptation needs. This, in turn, can refine ex ante assessments. Recent advances in high-frequency survey methods (e.g., phone surveys), remote-sensing data, and text-mining approaches can help build the evidence base for such a monitoring system. Establishing "impact observatories," which monitor a select number of high-risk places in a more continuous manner, can help improve our understanding of the complex interactions between adaptation and the daily lives of climate-vulnerable communities.

All five of the recommendations rely upon much strengthened capacity within governments, economic sectors, and communities. Building capacity for adaptation is a long-term program. It should be supported by global scientific endeavors to provide information on climate risks, the cost-effectiveness of adaptation options, and monitoring systems. Above all, it relies on skilled human capacity, which needs to be patiently built and retained within the governments and communities where it is most needed. Therefore, we urgently call for setting up a dedicated policy financing framework, ideally done jointly by the MDBs, to make the necessary first step in building this human capacity.

The fact that capacity building is a long-term program should not get in the way of early action. The economic investments that are taking place at the moment must be made resilient to climate change, simply because doing so upfront is a lot cheaper than retrofitting, or rebuilding, after a disaster. The climate finance that has already been committed needs to be turned into beneficial projects, without delay, using the tools that already exist, albeit imperfect. Above all, the rapid pace with which we observe increasing climate risks means that adaptation finance decisions still need to be made while we work to reorientate the adaptation finance system toward better outcomes. □

REFERENCES AND NOTES

1. UNEP, "Adaptation Gap Report 2024: Come hell and high water - As fires and floods hit the poor hardest, it is time for the world to step up adaptation actions" (United Nations Environment Programme, 2024); https://wedocs.unep.org/20.500.11822/46497.
2. E. L. F. Schipper, A. Mukherji, *Science* **386**, 624 (2024).
3. S. Fisher, *Clim. Dev.* **16**, 161 (2024).
4. OECD, Development Finance for Climate and Environment, *OECD DAC Extern. Dev. Financ.* (2024); https://web-archive.oecd.org/temp/2024-06-04/315401-climate-change.htm.
5. World Bank, "Resilience Rating System A methodology for building and tracking resilience to climate change" (2024); https://openknowledge.worldbank.org/handle/10986/35039#.
6. S. H. Eriksen *et al*., *Nat. Clim. Chang.* **14**, 1212 (2024).
7. S. Eslami *et al*., *Commun. Earth Environ.* **2**, 142 (2021).
8. World Bank, "Maldives Country Climate and Development Report" (2024).
9. D. Essers, D. Cassimon, M. Prowse, *Glob. Environ. Change* **71**, 102407 (2021).
10. World Bank, "Rising to the Challenge: Success Stories and Strategies for Achieving Climate Adaptation and Resilience" (2024).
11. A. Craig *et al*., *Clim. Policy* 10.1080/14693062.2025.2488988 (2025).
12. M. Bernhofen, M. Burke, A. Puranasamriddhi, N. Ranger, G. Shrimali, *SSRN Electron. J.* 10.2139/ssrn.4950708 (2024).
13. H. Runhaar, B. Wilk, Å. Persson, C. Uittenbroek, C. Wamsler, *Reg. Environ. Change* **18**, 1201 (2018).
14. T. Tanner *et al*., in *Realising the "Triple Dividend of Resilience". Climate Risk Management, Policy and Governance*, S. Surminski, T. Tanner, Eds. (Springer, 2016), pp. 1–29.

ACKNOWLEDGMENTS

J.V. acknowledges funding from the TU Delft Climate Safety and Security Centre. J.W.H received support from the Climate Compatible Growth Programme funded by the UK Foreign, Commonwealth and Development Office. All authors further acknowledge funding from the Oxford Martin School Systemic Resilience Initiative.

SUPPLEMENTARY MATERIALS

science.org/doi/10.1126/science.adx1950

Published online 19 June 2025; 10.1126/science.adx1950

[1]Department of Engineering Systems and Services, Faculty of Technology, Policy and Management, Delft University of Technology, Delft, Netherlands. [2]Climate Safety & Security Centre, TU Delft Campus The Hague, Delft University of Technology, Delft, Netherlands. [3]Environmental Change Institute, University of Oxford, Oxford, UK. [4]Global School of Sustainability, London School of Economics, London, UK. Email: j.verschuur@tudelft.nl

A volunteer harvests cabbage for a food bank in Irvine, CA, in 2021.

SCIENCE AND SOCIETY

Producing hunger

A scholar confronts how powerful groups use food as a means of control **Laura Stark**

Dana Simmons
University of California Press, 2025. 234 pp.

ON HUNGER | A professor at University of California, Riverside, Dana Simmons learned from student activists that a devastating number of the school's students—half of all undergraduates—live with uncertain access to food. In her new book, *On Hunger: Violence and Craving in America, from Starvation to Ozempic*, she travels the American history of hunger in a land of supposed plenty.

Ultimately, her story is one of political power. "Hunger is not a natural, biological, or genetic destiny," Simmons writes. "It is not just a matter of choices and habits." Instead, she explains in eight chapters that hunger is the effect of deliberate strategies in contexts of power imbalance. Hunger was—and remains—the effect of slow violence deployed by powerful institutions in four ways: to eliminate inconvenient others, to force labor or debt, to reward or punish, or to earn profits. In all instances, hunger is an individual experience that is imposed upon people collectively. "Hunger is produced," Simmons writes, "on purpose and to specific ends."

Produced by whom? Simmons documents how the US federal government eliminated Native tribes during the mid-1800s through a strategy of intentional starvation. The aim was to force Native peoples off their land and allow government access to valuable minerals, materials, and byways. "Work, sell or starve" was the command. In response, Native tribes fought—and indeed starved. Yet, in the white settler imagination, Native starvation was severed from its cause—namely, explicit government strategy—and instead falsely attributed to Native peoples' inability to "civilize" in a eugenicist timeline of social evolution.

These strategies seeped into the laboratories of experimental psychology at the turn of the 20th century, Simmons argues. In the name of science, cats and dogs were starved to the point of what researchers called "utter hunger" to set conditions for reward and punishment. Simmons explores the flaws in researchers' hunger-based designs, as well as their failures of compassion, documenting how the creation of hunger became an essential tool in the experimental social sciences.

Simmons's approach to the history of hunger is distinctive in that she insists on holding at the center of the story those with hungry bellies—human and animal—rather than the profiteers and powerholders. Continuing the story into the 1920s and 1930s, she follows labor activists who organized hunger marches to protest "starvation wages" and employers' extractive labor practices. In company towns and plantation zones, workers forged a political identity around hunger. "They accused employers and landlords of creating hunger conditions to suppress dissent and to extract more work for less pay," Simmons writes. Paradoxically, relief programs kept the inequitable economy in place. In the medical field, the new concept of individual "malnutrition" defanged the broader collectivist demands of workers.

In the aftermath of World War II, the concept of "the hungry" as a population was captured by Allied powers stuffed with fears of communism and collectivism. "The hungry had to be treated and reformed, bodily, mentally and politically," Simmons explains. "Their fate could not be left to their own judgment." Thus, international food aid programs in the postwar years came with the strong flavor of capitalist democracy. As the global economy grew, the processed-food industry profited from research around craving, addiction, "hedonic hunger," and the manufactured desire for self-control.

Toggling between sites of politics and science, Simmons shows that inmates were tortured by food as mass incarceration exploded in the 1970s. The American carceral growth extended from 1960s efforts to contain or push out Black and poor white workers from the formal labor force, particularly in the US South. The conflation of hunger with poverty, irresponsibility, and race did untold damage during this period. But it also catalyzed intrepid networks of "mutual aid" for an alternative, collectivist politics of hunger relief. Today, prison food practices have changed. Yet seeming luxuriant improvements (lots of cake) serve to satisfy cost targets and compliance standards, but not the people who must eat the food.

Amid cries for collectivism, the fangs of capitalism have animated hunger in the US to the present day. The compound that would later be marketed as the hunger-reducing drug Ozempic was first championed by its researchers as "cultural Marxist pharmacology," Simmons explains. Researchers working on human longing and wanting saw hunger as a food-based "product of late-capitalist overproduction" and drugs as a way "to defend oneself from capitalism with pharmaceuticals." By allowing people to resist food consumption, Ozempic empowers people to resist capitalism, the logic goes. Regardless of scientists' hopes and rhetoric, patented market-driven solutions have so far failed to address structural injustices at the starving heart of American food systems, laws, and culture.

Stories about the strategic production of hunger are at the top of the global news cycle today. At Riverside, students and colleagues have organized small-scale, community-led collective actions such as campus food pantries and pricing protests that are models and inspiration in the global struggle for food security. Thus, the history of hunger is not without its satisfactions, including stories of people joining together to give each other what they need: a community and relationships that feed bodies and souls. □

10.1126/science.ady0446

The reviewer is an associate professor at the Center for Medicine, Health, and Society, Vanderbilt University, Nashville, TN, USA. Email: laura.stark@vanderbilt.edu

SCIENCE LIVES

Facing life's wild unknowns

A field scientist candidly reflects on navigating personal and institutional challenges **Anna Farro Henderson**

Meltdown: The Making and Breaking of a Field Scientist
Sarah Boon
University of Alberta Press, 2025. 312 pp.

Sarah Boon forged her scientific identity working in the stunning and sometimes unforgiving forests and glaciers of British Columbia, the Canadian Rocky Mountains, and the Arctic, where she studied the relationship between snow, weather, and hydrologic processes. In *Meltdown: The Making and Breaking of a Field Scientist*, she documents her early training, her transition to conducting independent research, and the "glass obstacle course" she navigated to achieve academic tenure. But an early knee injury foreshadows future challenges. Readers follow along as Boon consistently puts her research first, not knowing that a clock on her scientific research career is ticking.

Growing up with an Earth scientist father whose lectures flattened the sublime beauty of the Rocky Mountains, Boon swore off science at a young age. She focused, instead, on literature, setting up a lending library as a child and typing up her own newspaper. Writing would prove a worthy lifelong companion.

Her eventual passion for science came later, after a number of field-based undergraduate classes at the University of Victoria. Through hiking and designing team projects, she learns "to tell the story of what forces had acted on [the landscape] and why it looked the way it did." It is here that long-term romances began with both the Hilda Glacier and her future husband. She would return to the glacier in Gore-Tex, fleece, and hiking boots for both her research and her wedding.

Boon's graduate research took her to the John Evans Glacier, which presented a Jenga-like challenge that the expedition team had to confront if the project was to succeed. Their days consisted of setting up temporary living quarters, supporting inexperienced and injured team members, navigating hazards, practicing mountaineering skills, planning food to sustain the team for weeks, waiting to fly in or out because of inclement weather, and cursing faulty equipment. The Arctic sun never set, and sometimes work went late into the night.

Living on a glacier as it "comes to life" in summer is an experience not captured by the static science of a textbook. Boon and her team had to rescue equipment, tents, and each other, as glacial melting causes icequakes, catastrophic drainage, artesian fountains, and raging rivers roiling with boulders. They learned that the process of discovering and developing new knowledge is messy, fraught, and uncertain.

Being in a male-dominated field complicated the underlying challenges Boon faced. She writes about working in all-male teams on expeditions and defending her qualifications and research to an all-male PhD committee. At the end of graduate school, she recalls feeling an urgency to "hurry to finish so I could get out and feel like myself again." But when she accepted a faculty position at the University of Lethbridge in Alberta, the department asked her to step aside and not apply for a grant that year to make way for a male colleague who would be applying. No matter how many publications and credentials she acquired, Boon often felt like an outsider falling behind.

Lacking contemporary female mentors, Boon finds kindred spirits in historic scientists and mountaineers such as Elizabeth Parker, Mary Schäffer, and Mary Vaux. These women serve as talismans and guardians, and their stories correct the false belief that women are a novelty in science. Boon does not find a real-time female mentor until she receives her faculty appointment, but their subsequent collaborations illustrate the role supportive relationships can play in research productivity.

For all the perils of the wilderness and institutional politics she navigates, in the end, Boon's health proves to be a barrier she cannot push through. Just as she achieves tenure and receives a major grant, she is incapacitated by a bipolar II disorder diagnosis. Boon writes that she now identifies as a "Spoonie"—a term used by people with disabilities and chronic illnesses to conceptualize the "limited number of spoons of energy [they have] each day." She finds that she can no longer contort herself to fit into the university system: "I had become my job and it had become me." The book ends as she comes to terms with building a new life and redefining success, embarking on a new career as a freelance writer and editor.

Boon's story is a reminder that although academic doors may slam shut, the world beyond remains expansive. Opportunities to explore the landscape, and ourselves, are vast and deeply necessary. □

The reviewer is at the Institute on the Environment, University of Minnesota, St. Paul, MN, USA. Email: ahenderson@gmail.com

10.1126/science.ady3159

PODCAST

Device and platform designs often fail to plan for user death.

https://scim.ag/DeathGlitch

SCIENCE OF DEATH

Facebook users die. So do iTunes customers. So do smart device users, YouTubers, and video game streamers. Yet few of today's technologies are built to accommodate this reality. This week on the *Science* podcast, Tamara Kneese, author of **Death Glitch**, explains how this fundamental design flaw has implications for everything from how we are remembered to how our assets are handled after death.

10.1126/science.adz3936

PHOTO: IMAGINECHINA LIMITED/ALAMY STOCK PHOTO

REVIEW SUMMARY

NATURAL HAZARDS

Cascading land surface hazards as a nexus in the Earth system

Brian J. Yanites*, Marin K. Clark, Joshua J. Roering, A. Joshua West, Dimitrios Zekkos, Jane W. Baldwin, Corina Cerovski-Darriau, Sean F. Gallen, Daniel E. Horton, Eric Kirby, Ben A. Leshchinsky, H. Benjamin Mason, Seulgi Moon, Katherine R. Barnhart, Adam Booth, Jonathan A. Czuba, Scott McCoy, Luke McGuire, Allison Pfeiffer, Jennifer Pierce

Full article and list of author affiliations: https://doi.org/10.1126/science.adp9559

BACKGROUND: Earth's surface is sculpted by numerous processes that move sediment, ranging from gradual and benign to abrupt and catastrophic. Although infrequent, high-magnitude sediment mobilization events can be hazardous to people and infrastructure, leaving topographic imprints on the landscape and remarkable narratives in the historical record. Hazardous events such as fires, storms, and earthquakes accelerate erosion and sediment transport, increasing landscape sensitivity to subsequent perturbations, thus forming a cascading hazard. Although the redistribution of sediment across Earth's landscape can result in higher risks to vulnerable populations, cascading processes are commonly unaccounted for in hazard assessments. Cascading hazards can occur almost immediately after triggering events, such as coseismic landslides, or over months, years, or even decades after an initial perturbation, such as debris flows after wildfires or flooding in channels alluviated by volcanic debris. Sediment cascades span Earth's surface, from mountaintops to river valleys, where erosion, deposition, and aggradation can lead to a myriad of hazardous processes, including decreased river conveyance capacity, which increases the likelihood of downstream flooding. An improved understanding of the magnitude, frequency, and persistence of cascading hazards is critical given the rapid changes in the frequency and severity of storms, fires, sea-level change, and cryospheric melting, as well as the expansion of high-population-density urban footprints in regions susceptible to solid Earth hazards. Understanding the full consequences and underlying physics of Earth's cascading land surface hazards can help minimize future human and economic losses.

ADVANCES: Recent research reveals crucial surface process interactions that link distinct components of Earth systems on human timescales (seconds to centuries) and give rise to cascading hazards. For example, solid Earth processes, such as earthquakes and volcanic eruptions, can generate widespread deformation and stress changes that affect rock strength and susceptibility to mass wasting. Likewise, the atmospheric triggering of hazards because of extreme precipitation, drought, and warming varies regionally and can be amplified or dampened depending on topography, geologic materials, and seismic activity, which are tied to the tectonic history of a region. New models capable of linking atmospheric forcings and solid Earth phenomena to land surface processes provide critical tools for quantifying how different Earth systems interact to initiate and sustain cascading hazards. Advances in high-resolution remote sensing tools provide accurate and extensive datasets to calibrate and validate models. Moreover, recent advances in critical zone science illuminate how the coupling of hydrologic, geologic, and biologic processes modifies near-surface material properties, altering their susceptibility to land surface hazards. These methodological and theoretical advances provide an opportunity to anticipate and forecast how the interaction of Earth systems affects land surface hazards in a changing world.

OUTLOOK: The science of land surface processes—encompassing the atmospheric, hydrospheric, biospheric, and solid Earth system sciences—is well positioned to advance our ability to forecast cascading hazards and enhance societal resilience through improved risk assessment and management. However, to achieve such advances, cross-disciplinary research teams are needed to address new research paradigms such as "How do different Earth systems interact to influence the magnitude, frequency, and longevity of impactful events?" Addressing these inherently complex and multidisciplinary questions requires a holistic approach to cascading hazard science that considers the impact of trigger magnitude, the influence of preconditioning along the cascade pathway from critical zone processes, and the interaction of processes along the cascade. Such advances can help interpret the emergence and persistence of cascading hazards and anticipate how they will be influenced by climate and land use changes. Linking Earth systems within a cascading hazard framework can inform theories, mechanistic models, and data analyses capable of quantifying the hazards of cascading processes on the ever-evolving Earth's surface, ultimately strengthening community resiliency and sustainability. □

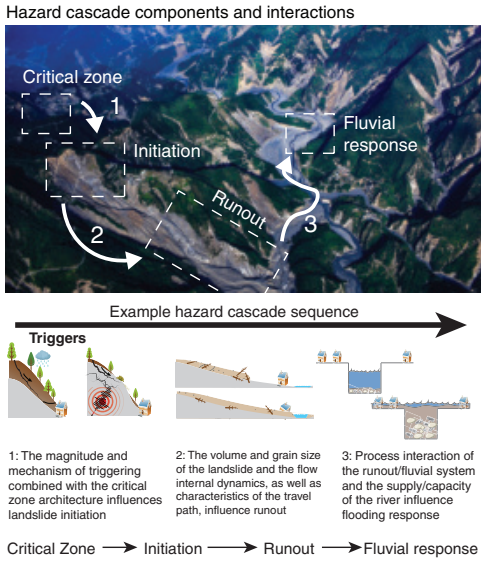

A photograph and a schematic illustration of how the interaction of Earth systems through surface process controls the emergence and persistence of cascading hazards. Processes at and near Earth's surface influence the strength and thickness of near-surface Earth materials, affecting how the mobilization of hillslope sediment will respond to triggers. The dynamics of the runout of this mobilized sediment can vary substantially owing to the interconnected upslope processes. As sediment works through fluvial systems, high sediment loads increase flood hazards and destabilize adjacent hillslopes, leading to further sediment mobilization. [Photo by Chi Po-lin and provided by the Chi Po-lin Foundation, copyright Above Taiwan Cinema]

*Corresponding author. Email: byanites@indiana.edu Cite this article as B. J. Yanites *et al.*, *Science* **388**, eadp9559 (2025). DOI: 10.1126/scsience.adp9559

RESEARCH

IN *SCIENCE* JOURNALS

Edited by **Michael Funk**

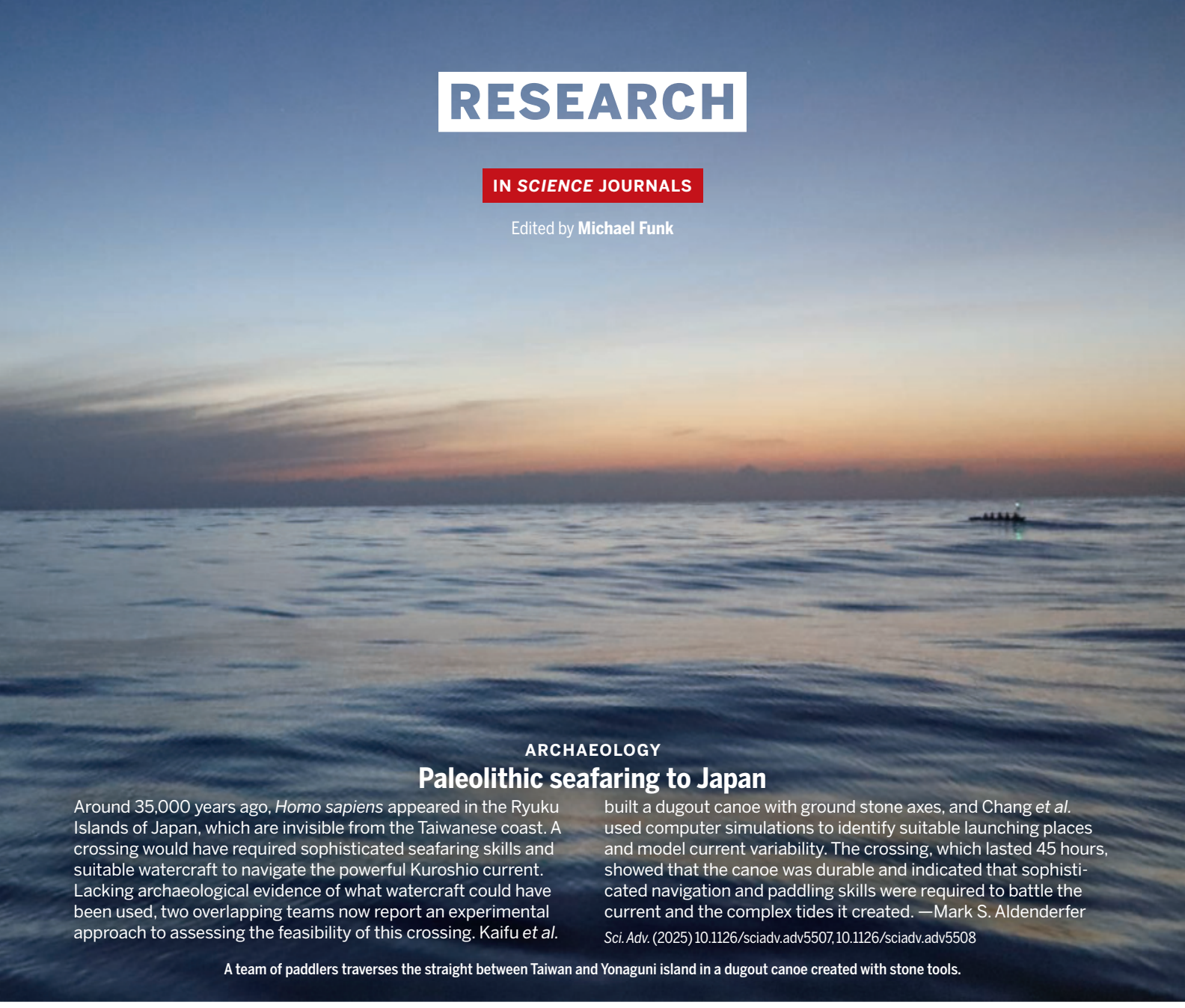

ARCHAEOLOGY

Paleolithic seafaring to Japan

Around 35,000 years ago, *Homo sapiens* appeared in the Ryuku Islands of Japan, which are invisible from the Taiwanese coast. A crossing would have required sophisticated seafaring skills and suitable watercraft to navigate the powerful Kuroshio current. Lacking archaeological evidence of what watercraft could have been used, two overlapping teams now report an experimental approach to assessing the feasibility of this crossing. Kaifu *et al.* built a dugout canoe with ground stone axes, and Chang *et al.* used computer simulations to identify suitable launching places and model current variability. The crossing, which lasted 45 hours, showed that the canoe was durable and indicated that sophisticated navigation and paddling skills were required to battle the current and the complex tides it created. —Mark S. Aldenderfer

Sci. Adv. (2025) 10.1126/sciadv.adv5507, 10.1126/sciadv.adv5508

A team of paddlers traverses the straight between Taiwan and Yonaguni island in a dugout canoe created with stone tools.

PHOTO: YOUSUKE KAIFU

PALEONTOLOGY

Revealing squid evolution

Cephalopods are one of the most successful marine invertebrates in modern oceans, and they have a 500-million-year-old history. However, we know very little about their evolution because soft-bodied animals rarely fossilize. Ikegami *et al*. developed an approach to reveal squid fossils, focusing on their beaks, the sole hard component of their bodies. They found that squids radiated rapidly after shedding their shells, reaching high levels of diversity by 100 million years ago. This finding shows both that squid body forms led to early success and that their radiation was not due to the end-Cretaceous extinction event. —Sacha Vignieri

Science p. 1406, 10.1126/science.adu6248

ADAPTATION

Fungal pathogen exerts pressure

Polygenic adaptation, in which selection acts on many variants at once, may serve an important role in adaptation, but it is harder to detect than selection acting on few loci of large effect. Metheringham *et al*. looked at genomic changes in the European ash, *Fraxinus excelsior*, the numbers of which have been decimated in recent decades by a fungal pathogen, *Hymenoscyphus fraxineus*. They found that a previously generated list of about 8000 potential variants showed significant differences in allele frequencies between juvenile and adult trees, and these differences were larger than randomly selected variants. This result suggests that polygenic adaptation may indeed be occurring in this population and that some of these variants may point to intervention targets. —Corinne Simonti

Science p. 1422, 10.1126/science.adp2990

ZEOLITES

Picking out extra-large pores

Microcrystal electron diffraction enabled rapid screening of combinatorial product mixtures for synthesis of two extra-large pore (ELP) nanosized aluminosilicate zeolites. Ma *et al*. screened 16 precursor gel compositions under two different hydrothermal processing

conditions. After synthesis optimization, they characterized these ELP zeolites as having 22-membered pores with free-sphere diameters of about 1.2 nanometers. These nanozeolites efficiently processed heavy petroleum fractions (commercial vacuum gas oil) into diesel and gasoline fuels. —Phil Szuromi

Science p. 1417, 10.1126/science.adv5073

PHYSICAL CHEMISTRY

Spontaneous urea formation

Urea, one of the simplest organic molecules containing carbon, nitrogen, and oxygen, is a key compound that connects chemistry and life. It is also one of the most important industrial chemicals, mainly used as fertilizer. Urea production usually relies on the direct reaction between ammonia and carbon dioxide under harsh conditions of high temperature and pressure. Using a combination of single-droplet experiments with quantum chemical modeling, Azizbaig Mohajer *et al*. detected spontaneous urea formation from these chemicals at the gas-liquid interface of aqueous aerosol droplets under ambient conditions (i.e. non-energetic conditions and without additional catalysts) enabled by chemical gradients across the surface of aqueous droplets. These findings have implications for various scientific disciplines. —Yury Suleymanov

Science p. 1426, 10.1126/science.adv2362

EARLY EARTH

What may be Earth's oldest rocks

Earth has a habit of renewing its crust through melting and recrystallization, thus erasing much of its early history. There are mineral fragments from the oldest eon, the Hadean, but there is little consensus on whether any intact, primordial crust still exists. Sole *et al*. revisited oceanic rocks from the Nuvvuagittuq Greenstone Belt in northeast Canada, comparing long- and short-lived samarium-neodymium isotope systems to determine when the rocks first crystallized. Their new tests point to an age of about 4.2 billion years, further evidence that a slice of Hadean crust may remain. —Angela Hessler

Science p. 1431, 10.1126/science.ads8461

ORGANIC CHEMISTRY

Subbing in sulfur

Site-selective modification of molecular frameworks can streamline drug discovery. Peripheral substituents have conventionally been easiest to manipulate, but there has been major recent progress in editing core atoms as well. Most of these methods have focused on carbon, nitrogen, and oxygen swaps. Zhang and Dong now report a protocol to introduce sulfur in place of the carbon and oxygen in cyclic ketones. A custom reagent promotes radical scission of both framework bonds to the ketone carbon, which is driven by aromatization of a triazole precursor. —Jake S. Yeston

Science p. 1436, 10.1126/science.adx2723

VACCINES

One shot for malaria

A major challenge for vaccine deployment is the need for booster immunizations. Using a microfluidic chip–based method, Guyon *et al.* created microcapsules containing the R21 malaria vaccine that break down over time in vivo, releasing the booster dose of vaccine at a time similar to when a boost would be administered. When given to mice along with the priming dose of R21 through a single injection, the microcapsules achieved nearly the same magnitude of antibody response as a standard prime-boost approach, offering high efficacy against malaria challenge. These microparticles, which also maintained immunogenicity with storage, represent an important advance for global immunization campaigns. —Courtney Malo

Sci. Transl. Med. (2025) 10.1126/scitranslmed.adw2256

IN OTHER JOURNALS

Edited by **Corinne Simonti** and **Jesse Smith**

NETWORK ECOLOGY

Pass the parasite

Networks of interactions between individuals in a population influence how pathogens and parasites are spread, but parasite infection can also change networks by affecting individuals' health, survival, reproduction, and behavior. Reynolds *et al.* examined daily network changes in female Trinidadian guppies *(Poecilia reticulata)* before and after infection by the ectoparasite *Gyrodactylus turnbulli* and compared these with uninfected populations. They found that although neither network nor subnetwork structure changed with infection, the number and strength of interactions did. Infected individuals increased their interactions with noninfected individuals, consistent with "off-loading" of parasites to decrease their individual burden. This demonstrates how individual behaviors can mediate the feedback between parasite and host population dynamics. —Bianca Lopez

Proc. R. Soc. B (2025) 10.1098/rspb.2025.0793

Parasite infection changes the behavior of Trinidadian guppies (*Poecilia reticulata*), increasing spread through individuals seeking symptom relief.

EXOPLANETS

Small stars with big planets

Planet formation models indicate that gas giants can be formed either in a protoplanetary disc when a rocky core accumulates gas from the disc (core accretion) or by fragmentation of the same collapsing gas cloud as the star forms (gravitational instability). Distinguishing between those origins has been difficult. Hotnisky *et al.* identified two large gas giant exoplanets orbiting small red dwarf stars. The planets are roughly eight and 10 times Jupiter's mass, which is more than 1% of the mass of the host stars. Such a high planet-to-star mass ratio indicates that the planets probably formed by gravitational instability. —Keith T. Smith

Astron. J. (2025) 10.3847/1538-3881/add2ef

CONSERVATION

Look to Indigenous lands

One need only look out the window of an airplane flying over tropical forests to see that our efforts to protect them are not working very well. If we want to retain these forests, we need to rethink how to protect them in the face of a capitalistic system that favors markets over nature. Alejo *et al.* looked at how lands under the care of Indigenous people fared relative to protected and "other" lands over the past 20 years in Panama. They found that although use-related disturbance occurred in Indigenous lands, there was less deforestation than in the other categories. Patterns of land use consistent with community values— for example, keeping agriculture at the forest edges—led to forest stability. —Sacha Vignieri

Ecol. Soc. (2025) 10.5751/ES-15540-300124

PHOTO: MIRKO ROSENAU/ISTOCK PHOTO

CELL BIOLOGY

Maintaining connections for pluripotency

Cytokinesis, the final stage of cell division, is usually a short-lived process. In mouse embryonic stem cells (mESCs), cytokinesis persists for several hours, which preserves their pluripotency. During cytokinesis, daughter cells remain connected through a microtubule-rich intercellular bridge. Stockmann *et al.* showed that KIF2A, a member of the kinesin-13 family of microtubule depolymerases, prolongs cytokinesis in mESCs. During cytokinesis, KIF2A is inhibited by Aurora kinases, which converts it from a microtubule depolymerase to a microtubule-stabilizing factor. KIF2A thereby safeguards mESC pluripotency by stabilizing the microtubules of the intercellular bridge. —Stella M. Hurtley

J. Cell Biol. (2025)
10.1083/jcb.202409157

ELECTROCHROMICS

Dual control of infrared and visible light

Thin films of pseudohexagonal niobium pentoxide (TT-Nb_2O_5) can independently modulate the absorption of visible and near-infrared light through lithium-ion intercalation for applications in smart window thermal management. Huang *et al.* found that lithium-ion insertion split and downward shifted unoccupied Nb 3d bands and upward shifted the Fermi level. These changes led to an increase in the near-infrared absorption at lower Li concentrations and an increase in both near-infrared and optical absorption at higher Li concentrations. These films displayed rapid switching kinetics, and there was no observed degradation of optical modulation after more than 10,000 switching cycles. —Phil Szuromi

Natl. Sci. Rev. (2025)
10.1093/nsr/nwaf154

HEALTH OUTCOMES

Healthy moves

Does exercising improve health outcomes for colon cancer patients? To definitively answer this question, Courneya *et al.* conducted a randomized trial across 55 centers with 889 patients in Canada and Australia. Over a 3-year period, after colon cancer patients completed chemotherapy, they were either assigned to a group that received health education content or a group that engaged in structured exercises. During 8-year follow-ups, disease-free survival was better among the structured exercise group (80.3%) compared with the health content group (73.9%). This suggests that exercising may be more beneficial than health education alone, although this group did suffer more musculoskeletal injuries. —Ekeoma Uzogara

N. Engl. J. Med. (2025)
10.1056/NEJMoa2502760

GLOBAL WARMING

Letting the sun shine in

The fraction of incident solar radiation absorbed by Earth has been increasing over the past 25 years, attributed mainly to a decrease in the amount of sunlight reflected by clouds. Clouds and cloud coverage can be affected on a large scale by changes in atmospheric general circulation or on a more local scale by variations in the physical and chemical state of the atmosphere. Tselioudis *et al.* analyzed satellite data from the CERES platform to show that storm cloud zones in the tropics and the midlatitudes have been shrinking in area over that period due to atmospheric circulation changes, thereby allowing more solar radiation to reach Earth's surface and heating the planet. —Jesse Smith

Geophys. Res. Lett. (2025)
10.1029/2025GL114882

RESEARCH ARTICLE SUMMARY

NEUROSCIENCE

Event structure sculpts neural population dynamics in the lateral entorhinal cortex

Benjamin R. Kanter*, Christine M. Lykken, Ignacio Polti, May-Britt Moser, Edvard I. Moser*

Full article and list of author affiliations: https://doi.org/10.1126/science.adr0927

INTRODUCTION: Our experience of the world unfolds as a stream of events that can later be reconstructed from memory in rich detail. The hippocampal formation, which is critical for such episodic memories, has been shown to exhibit slow changes in neural activity over time, most prominently in the lateral entorhinal cortex (LEC). It remains to be determined whether and how this drift in neural activity contributes to the temporal organization of episodic memories.

RATIONALE: Experiences are segmented into discrete events across a range of timescales from seconds to minutes or more. Event boundaries (i.e., transitions between successive events, such as changes in location, social setting, or behavior) affect memory for the duration and order of events, which suggests that event structure could play an important role in shaping the neural activity underlying such memories. To search for the neural mechanisms that determine how events are segmented and organized in time, we used high-density Neuropixels probes to record neural activity from an unprecedented number of neurons in the LEC and neighboring brain areas in freely behaving rats, across multiple behaviors and behavioral states, and in the presence of variations in event structure at multiple timescales.

RESULTS: Neural population activity in the LEC drifted continuously along a one-dimensional manifold during individual foraging sessions, such that activity traveled progressively farther away from the current state. Simultaneously recorded neural activity in the medial entorhinal cortex (MEC) and hippocampal area CA1 exhibited minimal drift. Recordings during natural sleep revealed that LEC population dynamics were nearly identical during rapid eye movement (REM) sleep and foraging, which suggests that drift does not require changes in external sensory information and instead is an inherent network phenomenon. During wakefulness, population dynamics abruptly shifted at event boundaries, leading to the segmentation of neural activity into discrete temporal units. During tasks with repeating temporal structure, the LEC simultaneously encoded event information across multiple timescales by traveling additionally in directions orthogonal to the drift. We uncovered potential mechanisms of both drifting and shifting dynamics in neural population activity. Drift could be explained by minute-scale variability in the firing rate of individual neurons broadly distributed throughout the LEC population. These slow variations were necessary and sufficient for drift at the population level. Shifts in population dynamics at event boundaries were driven by synchronous responses of neural ensembles in the LEC. Different ensembles responded at different event boundaries, such that individual events could be time-stamped in memory.

CONCLUSION: Drift of neural activity in the LEC is an inherent network phenomenon that continues at a constant rate during wakefulness and sleep but is briefly interrupted by abrupt shifts at moments of transition between events. These results identify a candidate mechanism for the segmentation of experience into discrete episodic memories, as reported in human study participants. Experience consists of a sequence of events across a wide range of timescales, organized hierarchically from seconds to minutes or more. We show that LEC activity simultaneously encodes event information across these different timescales without explicit reinforcement or extensive behavioral training. Together, our results identify a hierarchical neural coding scheme for organizing events in time. □

*Corresponding author. Email: benjamin.kanter@ntnu.no (B.R.K.); edvard.moser@ntnu.no (E.I.M.) Cite this article as B. R. Kanter *et al.*, *Science* **388**, eadr0927 (2025). DOI: 10.1126/science.adr0927

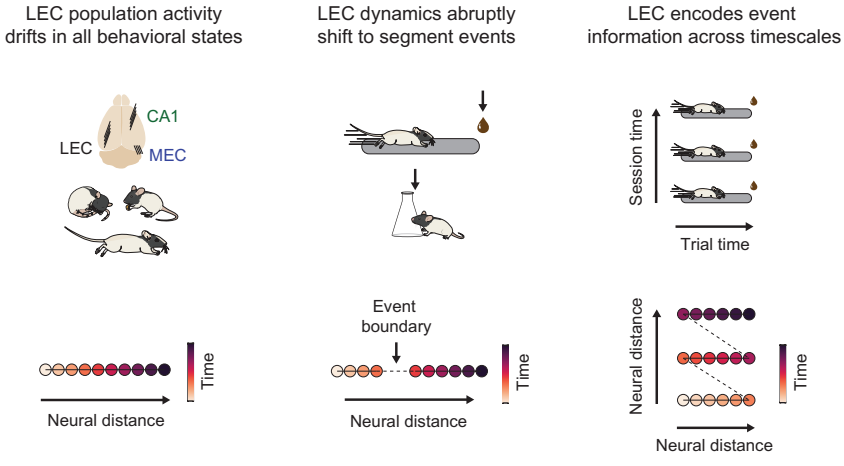

Neural population activity in the LEC organizes events in time. Activity inherently drifts over time regardless of behavioral state (left). In the awake state, activity abruptly shifts to segment events (middle). Activity travels in additional directions orthogonal to the drift to simultaneously encode event information across multiple timescales (right). The LEC uses a hierarchical coding scheme for organizing events in time. [Art adapted from SciDraw (scidraw.io), CC-BY 4.0]

RESEARCH ARTICLE SUMMARY

ANCIENT DNA

Out-of-Anatolia: Cultural and genetic interactions during the Neolithic expansion in the Aegean

Dilek Koptekin *et al.*

Full article and list of author affiliations: https://doi.org/10.1126/science.adr3326

INTRODUCTION: Neolithic farming cultures first developed in the Fertile Crescent around 10,000 years ago and later spread into Europe through the Aegean. How the Neolithic lifeways emerged in the Aegean, and particularly West Anatolia, has remained unknown, obscured by a lack of human ancient DNA from pre-Neolithic times.

RATIONALE: We studied population and cultural history of the Aegean using 30 new paleogenomes, including a 10,000-year-old individual from West Anatolia, combined with 408 published genomes. We also compiled a digitalized material culture that included 54 cultural traits from 16 sites from around 9000 years ago and joined this with 104 genomes from the same sites. This allowed us to reconstruct mobility and cultural change during the Neolithic transition in the Aegean.

RESULTS: We found at least 6000 years of genetic continuity in West Anatolia during the early Holocene, before the arrival of farming villages there. During this time, West Anatolians were in cultural exchange with their eastern neighbors from the Fertile Crescent, exploring sedentary lifeways. But these West Anatolians did not genetically mix with their neighbors in this early phase.

Things changed around 9000 years ago, when full-scale farming settlements began spreading across the Aegean. Our paleogenomic data show that this did not occur because of waves of migrant farmers from the east creating farming colonies in the Aegean and replacing local foragers. Rather, the transition unfolded as a fusion: Incoming groups of eastern origin joined together and genetically mixed with the descendants of the local foragers in the newly established villages. This was likely a complex process of coexistence and mutual innovation as well as eventual mixing. It further gave rise to the now-famous "Anatolian Farmer" genetic profile, which subsequently spread across the Aegean Sea and later throughout Europe. In this case, admixture with locals appears more limited and sporadic.

We further performed a comparative study of cultural and genetic data, asking whether cultural similarities among the 16 Neolithic settlements may be explained by their genetic similarities, which would be expected if culture was shaped by large-scale mobility and admixture history. We found that cultural similarities among villages could simply be explained by their geographic proximity, whereas their population genetic similarities did not have any explanatory power, implying that ideas mixed faster than people in this region.

CONCLUSION: The spread of Neolithic cultures in West Eurasia involved distinct mechanisms, from pure cultural adoption to mobility and admixture between incoming farmers and local foragers to rapid migration and spread. Further, cultural similarities among settlements were not shaped by large-scale mobility (as reflected in genetic data) but rather through background mobility. Our results thus challenge the widespread assumption that cultural entities frequently correspond to genetically homogeneous populations, supporting the archaeological adage, "pots don't equal people." Our study presents a fresh look at mechanisms of cultural change during one of humanity's most transformative periods. □

Corresponding author: Dilek Koptekin (dilek.koptekin@metu.edu.tr); Mehmet Somel (msomel@metu.edu.tr) Cite this article as D. Koptekin *et al.*, *Science* **388**, eadr3326 (2025). DOI: 10.1126/science. adr3326

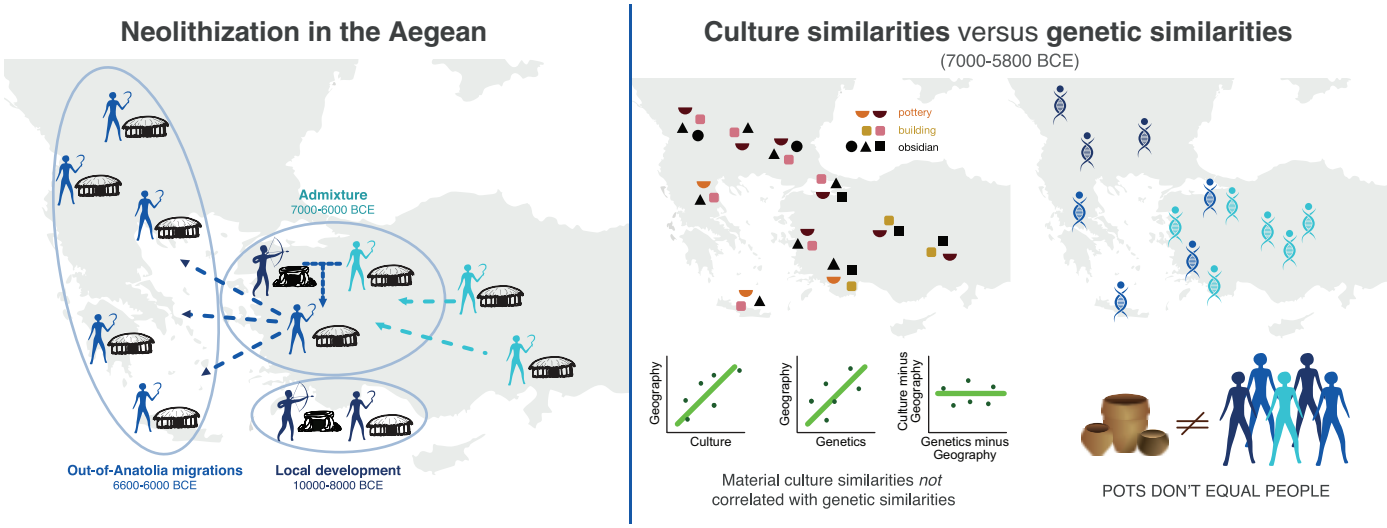

Diverse pathways to Neolithization and the uncoupling between cultural and genetic interactions in the Aegean. (Left) Neolithic practices in West Anatolia first started by cultural interactions, followed by mobility and admixture, and, lastly, migration into Europe. (Right) Comparative analysis of cultural and genetic similarity across 16 Neolithic settlements reveals no correlation between cultural and genetic similarities after controlling for geography.

RESEARCH ARTICLE SUMMARY

ANCIENT DNA

Female lineages and changing kinship patterns in Neolithic Çatalhöyük

Eren Yüncü†, Ayça Küçükakdağ Doğu†, Damla Kaptan†, Muhammed Sıddık Kılıç†, *et al.*

Full article and list of author affiliations: https://doi.org/10.1126/science.adr2915

INTRODUCTION: Çatalhöyük is a Neolithic settlement in Anatolia and a United Nations Educational, Scientific and Cultural Organization (UNESCO) World Heritage Site. Occupied for 1000 years (9000 to 8000 BCE), it is renowned for its size, apparent egalitarian social structure, and subfloor burials, where children and adults were buried within houses during their use. It is also known for its large corpus of female figurines, which were long debated as possible representatives of a "Mother Goddess" cult and signs of a matriarchal society.

RATIONALE: In this work, we studied social organization at Çatalhöyük, fusing rich archaeological data with a paleogenomic dataset of 131 individuals buried in 35 houses. We focused on identifying genetic ties between individuals buried together inside the same buildings.

RESULTS: Comparing genetic ties within and between buildings, we found that the maternal lineage had a key role in connecting Çatalhöyük household members, as represented by burials within each building. We estimated that 70 to 100% of the time, female offspring remained connected to buildings, whereas adult male offspring may have moved away. We also discovered preferential treatment of female infant and child burials, with five times more grave goods offered to females than to males.

Our data further show how social organization patterns changed over time in Çatalhöyük. In the early phases of the settlement, individuals buried together within houses frequently represented extended family members. Through time, the genetic composition of house burials became less homogeneous. In later periods, we found groups of neonates who were genetically unrelated but buried in the same house. Meanwhile, their mothers appear to have had similar diets. This implies that genetic relatedness became less central to social organization over time, which could be explained by fostering and adoption-like mechanisms becoming widespread, which is also observed today in various societies. Despite this shift, female-centered practices continued at Çatalhöyük through the occupation.

CONCLUSION: Our results reveal the malleable nature of social organization in Neolithic villages, with the composition of households possibly changing within a few dozen generations. We also found the first direct indication of female-centered practices in Neolithic Southwest Asia, a question of frequent debate. This female focus identified in Çatalhöyük is in sharp contrast to patterns observed in later European Neolithic sites, which have their origins in Anatolia. Many of these European societies show evidence of patrilocality—where males stay within their natal community upon attaining adulthood and females move out—and elaborate burial treatments that are frequently associated with males. The Çatalhöyük evidence now shows that such male-centered practices were not an inherent characteristic of early agricultural societies. □

Corresponding authors: Eren Yüncü (eren26285@gmail.com); Mehmet Somel (somel.mehmet@gmail.com) †These authors contributed equally to this work. **Cite this article as** E. Yüncü *et al.*, *Science* **388**, eadr2915 (2025). DOI: 10.1126/science.adr2915

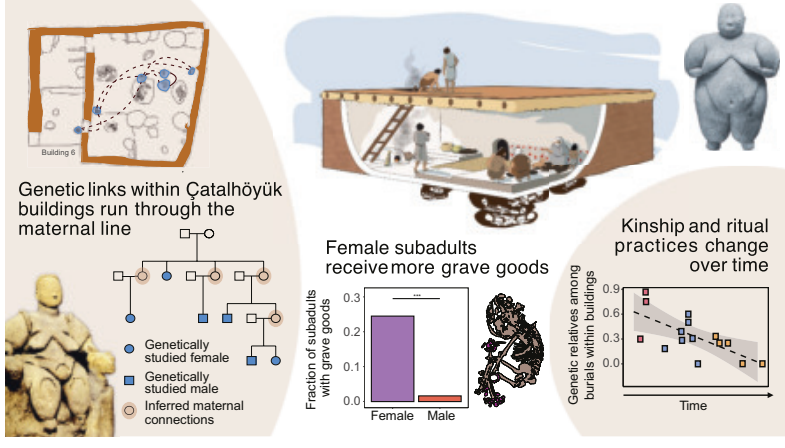

Female-centered practices and changing kinship patterns over time in Çatalhöyük. Shown are two Çatalhöyük figurines (credit: Mellaart International and the British Institute at Ankara). Centre: reconstruction of a typical Çatalhöyük building (credit: Kathryn Killackey). Left: Building 6 with six genetically studied burials (blue on building map) and their genetic connections (lines), and their inferred pedigree. Centre: Grave good frequencies and a stylized female infant burial with beads shown in purple. Lower right: The frequency of genetic relatives within 15 buildings, spanning about 500 years (bottom right).

CREDITS: (BOTTOM LEFT) MELLAART INTERNATIONAL; (TOP CENTER) K. KILLACKEY; (TOP RIGHT) THE BRITISH INSTITUTE AT ANKARA

RESEARCH ARTICLE SUMMARY

ORGAN REGENERATION

Reactivation of mammalian regeneration by turning on an evolutionarily disabled genetic switch

Weifeng Lin†, Xiaohui Jia†, Xiaofeng Shi†, Qiuya He†, Panyu Zhang†, Xianglei Zhang, Liping Zhang, Mingqi Wu, Tengfei Ren, Yufei Liu, Haohao Deng, Yanyao Li, Shiqi Liu, Shaoyong Huang, Jingmin Kang, Jun Luo*, Ziqing Deng*, Wei Wang*

Full article and list of author affiliations: https://doi.org/10.1126/science.adp0176

INTRODUCTION: Regeneration, an apparently beneficial trait, is well maintained in some animal lineages but has been lost in many others during evolution and speciation. A complete rescue of organ regeneration in mammals with limited regenerative capacity has not yet been achieved, primarily because of limited information on the linkage between the failure of regeneration and the genetic changes in the genome. Understanding what has occurred during animal evolution to drive the loss or gain of regeneration will shed new light on regenerative medicine.

RATIONALE: Identification of the causal mechanism underlying the failure of regeneration in mammals through comparative strategies is usually entangled by the large phylogenetic distance from highly regenerative species (mostly lower vertebrates). Exploration of principles in the evolution of regeneration demands an organ with easy accessibility and diverse regenerative capacities. One such mammalian organ is the ear pinna, which evolved to funnel sound from the surrounding environment for better distinguishing between ambient noise and predators or prey. The ear pinna possesses complex tissues such as skin and cartilage and exhibits remarkable diversity in the ability to regenerate full-thickness holes punched through this organ in placental mammals.

RESULTS: By performing a side-by-side comparison between regenerative species (rabbits, goats, and African spiny mice) and nonregenerative species (mice and rats), we found that the failure of regeneration in mice and rats was not due to the breakdown of tissue-loss triggered blastema formation and proliferation. Single-cell RNA sequencing and spatial transcriptomic analyses of rabbits and mice identified the response of wound-induced fibroblasts (WIFs) as a key difference between the regenerating and nonregenerating ear pinna. Gene overexpression studies discovered that *Aldehyde Dehydrogenase 1 Family Member A2* (*Aldh1a2*), encoding a rate-limiting enzyme for the synthesis of retinoic acid (RA) from retinaldehyde, was sufficient to rescue mouse ear pinna regeneration. The activation of *Aldh1a2* upon injury was correlated with the regenerative capacity of the tested species. Furthermore, we demonstrated that the deficiency of *Aldh1a2* expression, together with the augmented activity of the RA degradation pathway, contributed to insufficient RA production after injury and eventually the failure of regeneration. An exogenous supplement of RA—but not the synthetic precursor retinol—was sufficient to induce regeneration by directing WIFs to form new ear pinna tissues. The inactivation of multiple *Aldh1a2*-linked regulatory elements accounted for the injury-dependent deficiency of *Aldh1a2* in mice and rats. Importantly, activation of *Aldh1a2* driven by a single rabbit enhancer was sufficient to promote ear pinna regeneration in transgenic mice.

CONCLUSION: Our study identified a direct target involved in the evolution of regeneration and provided a potential framework for dissecting mechanisms underpinning the failure of regeneration in other organs or species. RA signaling is broadly involved in different contexts of regeneration including bone, limb, skin, nerve, and lung regeneration. The crosstalk between the RA pathway and the crucial regeneration regulator, AP-1 complex, further highlights the impact of RA deficiency on regeneration in some lineages. We propose that modulation of the RA pathway may be a hot spot for the evolution of regeneration in vertebrates. □

*Corresponding author. Email: wangwei@nibs.ac.cn (W.W.); dengziqing@genomics.cn (Z.Q.D.); luojun@nwafu.edu.cn (J.L.) †These authors contributed equally to this work. **Cite this article as W. Lin *et al.*, Science 388, eadp0176 (2025). DOI: 10.1126/science.adp0176**

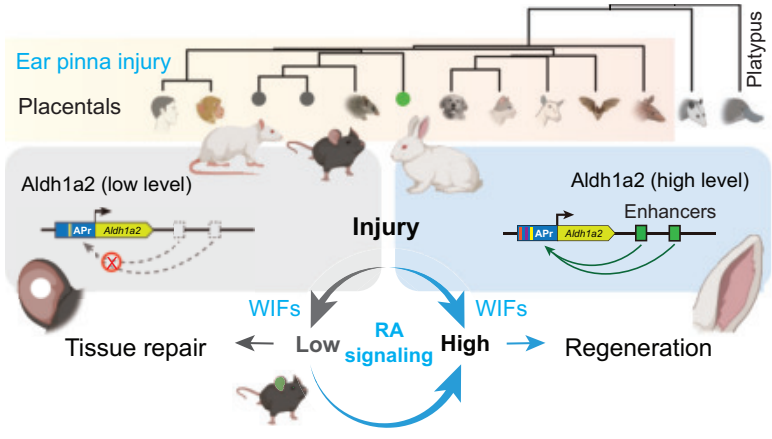

Evolution of regeneration in mammals. In regenerative rabbits, the *Aldh1a2*-linked enhancers interact with the promoter to activate robust expression of *Aldh1a2* upon ear pinna injury. The activities of such enhancers were lost in mice and rats during evolution, resulting in the deficiency of *Aldh1a2* expression and insufficient production of retinoic acid (RA) in these animals. The low RA signaling activities limited the morphogenic potential of WIFs and resulted in failure to regenerate, but switching on *Aldh1a2* or an exogenous supplement of RA was sufficient to reactivate regeneration.

RESEARCH ARTICLE SUMMARY

STRUCTURAL BIOLOGY

Structural basis of BAX pore formation

Ying Zhang†, Lu Tian†, Gaoxingyu Huang*†, Xiaofei Ge†, Fang Kong, Pengqi Wang, Yige Xu, Yigong Shi*

Full article and list of author affiliations: https://doi.org/10.1126/science.adv4314

INTRODUCTION: Apoptosis is essential for all metazoans. The BCL-2 family protein BAX regulates mitochondria permeability. In normal cells, BAX primarily exists as a monomer in the cytoplasm. The C-terminal helix α9 occupies a hydrophobic groove formed by helices α3-α5. During apoptosis, BAX is activated by the BH3-only proteins such as truncated BID (tBID) and translocates to the mitochondrial outer membrane (MOM). Upon membrane association, BAX undergoes further activation steps, including dissociation of the helix α1, separation of the latch (α6-α8) from the core region (α2-α5), and dimerization of the core region. The resulting activated BAX oligomers permeabilize the MOM, allowing the release of pro-apoptosis factors such as cytochrome *c* (Cyt *c*).

Unlike all other pore-forming proteins, activated BAX oligomers display vastly different sizes and irregular shapes, appearing as arcs, lines, and rings, each of which is capable of permeabilizing the MOM. To date, no atomic structure of the BAX oligomers has been reported. It is unclear how many molecules of BAX are needed to form a pore of a defined size. The molecular basis for the exceptional flexibility in size and shape of the BAX oligomers remains unknown.

RATIONALE: To understand the mechanism of BAX-mediated MOM permeabilization, we sought to determine the structure of the activated BAX oligomers. To facilitate structural investigation, we purified the recombinant human BAX protein and confirmed its membrane-permeabilizing activity using a liposome-based Cyt *c* release assay. To obtain the activated BAX oligomers, we overexpressed BAX in human embryonic kidney 293F cells. The activated BAX oligomers were detergent-extracted and purified for single-particle cryo–electron microscopy (cryo-EM) analysis.

RESULTS: Negative-staining EM showed that the BAX arcs, lines, and rings appear to have the same thickness, suggesting a shared repeating unit and a conserved organization. We defined this repeating unit, which contains a vertex at the center and two flanking arms. We processed the EM micrographs and obtained a reconstruction of the repeating unit at an average resolution of 3.2 Å, which allowed atomic modeling.

Each repeating unit comprises four BAX protomers, organized as a dimer of asymmetric dimers. The two protomers in an asymmetric dimer exhibit distinct conformations: type I and type II. Compared with the BAX monomer, α1 is disordered and α6 and α7 merge into a single helix in type I BAX protomer. The core of the BAX protomer, namely α2-α5, is nearly identical between type I and type II, but the conformation of α6-α9 is divergent. Type I and type II protomers associate with each other through their respective cores. Specifically, α2 (BH3 motif) of one protomer is recognized in a hydrophobic groove formed by α3-α5 of the other protomer, forming a classical "BH3-in-groove" binding mode.

Each BAX repeating unit has two pairs of α9 helices, one in each arm. Two neighboring units associate with each other through their respective α9 helices. This arrangement leaves a pair of α9 helices free on each end of the two-unit BAX oligomer. The sticky α9 helices on both ends are poised to recruit additional units, forming a line. End-to-end association within the same line results in a ring. Therefore, the interchangeable nature of the BAX arcs, lines, and rings is embedded in the sticky α9 helices at the ends of the repeating unit. To confirm the assembly principle, we generated the activated BAX rings and determined the cryo-EM structures of the BAX tetragon, pentagon, hexagon, and heptagon. The BAX repeating unit could be nicely fitted into the EM maps for these polygons, as was shown for the BAX pentagon.

To corroborate these structural findings, we generated missense mutations that target key residues at the inter-protomer interface of the BAX oligomer. These mutants exhibit compromised abilities to induce apoptosis in cells or to release Cyt *c* in the liposome assay.

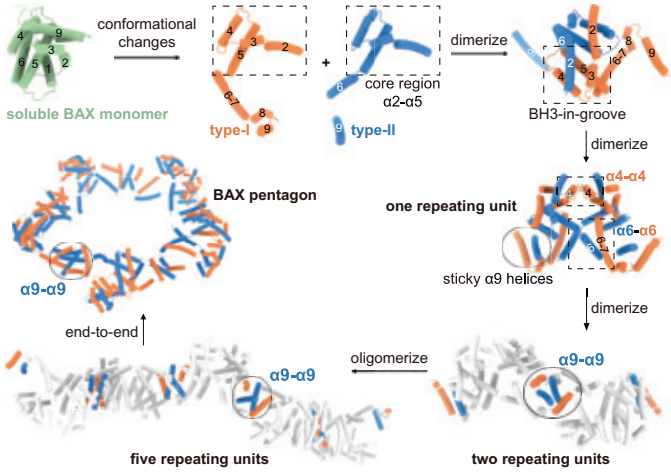

Cryo-EM structure of the activated BAX oligomers. Upon activation, BAX undergoes conformational changes. On the MOM, two BAX protomers (type I and type II) dimerize to form an asymmetric dimer through the "BH3-in-groove" mode. Two asymmetric dimers further dimerize to form the BAX repeating unit, leaving a pair of α9 helices exposed on either side. Neighboring repeating units connect to each other through their respective α9 helices, forming an arc or a line. End-to-end connection of a BAX line generates a ring.

CONCLUSION: Our results explain how the activated BAX oligomers permeabilize, or more accurately rupture, the MOM. Our structures also explain how the vastly different forms (arcs, lines, and rings) of BAX oligomers are assembled from the same repeating unit. □

*Corresponding author. Email: huanggaoxingyu@westlake.edu.cn (G.H.); syg@westlake.edu.cn (Y.S.) †These authors contributed equally to this work. Cite this article as Y. Zhang *et al.*, *Science* **388**, eadv4314 (2025). DOI: 10.1126/science.adv4314

OPTICAL MATERIALS

Gradient refractive indices enable squid structural color and inspire multispectral materials

Georgii Bogdanov[1]†, Aleksandra Anna Strzelecka[1]†, Nikhil Kaimal[1], Stephen L. Senft[2], Sanghoon Lee[1], Roger T. Hanlon[2], Alon A. Gorodetsky[1,3]*

The manipulation of light by means of materials with varying refractive index distributions is widespread among natural systems and modern technologies. However, understanding how animals leverage refractive index differences for dynamic color changes and then translating such insight into tunable optical devices remains challenging. We experimentally and computationally demonstrated that iridescent cells (iridophores) containing Bragg reflectors with sinusoidal-wave (rugate) refractive index profiles enable squid dorsal mantle tissues to reversibly transition between nearly transparent and vibrantly colored states. We then drew inspiration from these findings for the design and development of iridophore-inspired multispectral composite materials with tunable visible and infrared functionalities. Our study provides insight into squid dynamic structural coloration mechanisms and furnishes a technology for camouflage, heat management, display, and sensing applications.

Natural optical systems such as Morpho butterfly scales are covered with nanostructured Bragg gratings from alternating high–refractive index lamellae and low–refractive index air gaps, which produce their distinctive blue coloration (*1*, *2*). Loliginid squid eye lenses are filled with colloidal protein nanoparticle gels that feature concentration-dependent gradient refractive index distributions, which allow for correction of spherical aberration (*3*, *4*). Panther chameleons have skin cells that contain reconfigurable photonic lattices consisting of high–refractive index nanocrystals within a low–refractive index cytoplasm, which enable color changes and thermal regulation (*5*, *6*). Modern technologies such as lasers, fiber optics, photovoltaics, and sensors all leverage multilayered Bragg reflectors with sinusoidal-wave (rugate) refractive index profiles to achieve precise spectral control, mitigate scattering losses, enhance optical or thermal efficiency, and/or improve signal transmission (*7*–*12*). Microscopes, cameras, and other optical devices use miniaturized flat glass or plastic lenses with controlled-gradient refractive index distributions to more effectively focus light, minimize aberrations, and mitigate design constraints (*13*–*15*). Nanoporous or nanostructured radiative cooling platforms use engineered polymer films in which low–refractive index occlusions within a high–refractive index material lead to enhanced scattering of sunlight and improved thermal performance (*16*–*18*). Consequently, there are many reasons for wanting to understand how other natural systems take advantage of refractive index distributions for the dynamic manipulation of light across a wide range of the electromagnetic spectrum.

[1]Department of Chemical and Biomolecular Engineering, University of California, Irvine, Irvine, CA, USA. [2]Marine Biological Laboratory, Woods Hole, MA, USA. [3]Department of Materials Science and Engineering, University of California, Irvine, Irvine, CA, USA. ***Corresponding author. Email: alon.gorodetsky@uci.edu** †These authors contributed equally to this work.

One class of animals that has mastered the use of variable–refractive index structures for static and dynamic light manipulation are cephalopods, such as the squid *Doryteuthis pealeii*, depicted in Fig. 1A. This species achieves ultrafast camouflage and signaling by means of a stratified dorsal mantle skin architecture that contains neuromuscularly controlled pigmented organs called chromatophores and neurophysiologically controlled reflective cells called iridophores or iridocytes (Fig. 1A) (*19*, *20*). Whereas the overlaid pigmented chromatophores are organized into discoid units of larger organs surrounded by smaller ones on the mantle, the underlying iridophores are either distributed as individual cells (which typically have static angle-dependent colors) or grouped into large clusters called splotches (which have tunable transparencies and colorations) (*21*–*24*). The static and dynamic colorations of individual iridophores were ascribed to Bragg reflector–like structures made from discrete alternating layers of a high–refractive index protein called reflectin and low–refractive index extracellular space (*25*–*32*). However, the cells' morphologies and refractive index distributions were not directly characterized in three dimensions (table S1). Moreover, such studies did not address the central question of how splotch iridophores are able to transition from transparent to colorful across the entire visible range while also maintaining spectral (color) purity (table S1).

An emerging body of work has focused on developing materials with simultaneously dynamic visible and infrared functionalities for applications, including camouflage, heat management, displays, sensors, and wearables. Such tunable multispectral systems have proven challenging to develop, with the few reported electrochromic, thermochromic, liquid crystalline, nanoporous, or wrinkled materials classes exhibiting substantial performance trade-offs (table S2) (*33*–*37*). For example, electrochromics demonstrate excellent visible and infrared reflectance intensity modulation with good visible-wavelength shifts but have proven difficult to reversibly and stably actuate by multiple methods (*33*). Thermochromics achieve good visible reflectance and infrared transmittance intensity modulation with exceptional visible-wavelength shifts but suffer from slow response times, high operating temperatures, and small areas (*34*). Liquid crystals show good visible reflectance intensity modulation with moderate visible-wavelength shifts across many actuation cycles but have minimal infrared tunability, unclear angular dependences, and moderate areas (*35*). Nanoporous films achieve excellent visible and infrared transmittance intensity modulation over large active areas but cannot change color, rapidly respond to actuation, or survive repeated actuation (*36*). Wrinkled surfaces similarly exhibit excellent visible and infrared transmittance intensity modulation on rapid subsecond timescales but again cannot change color and offer only limited device-design flexibility (*37*). To date, no single class of dynamically reconfigurable visible-to-infrared materials has excelled across all of the desirable figures of merit, therefore opening opportunities for using bioinspired approaches to engineer alternatives with superior capabilities. In this work, we elucidated the fundamental optical mechanisms by which squid dorsal mantle splotches achieve their refractive index distribution–driven dynamic transparency- and color-changing functionalities and then translated our findings to the development of squid skin–inspired tunable light– and heat-managing materials with advanced performance.

Optical characterization of squid splotches

We began by studying the dynamic iridescent colorations and tunable transparencies of the chromatophore-overlaid squid dorsal mantle splotches (Fig. 1, A and B). We visualized live splotch-containing tissues with digital camera imaging, stereomicroscopy, and visible spectroscopy (see methods). The arrayed splotches beneath the pigmented punctate or expanded chromatophores featured vibrant, viewing angle–dependent blue, green, yellow, orange, and red structural colorations spanning the visible spectrum (Fig. 1C). The individual splotches readily transitioned from transparent to red to orange to green with an accompanying spectral shift of up to 200 nm when exposed to a neurophysiological

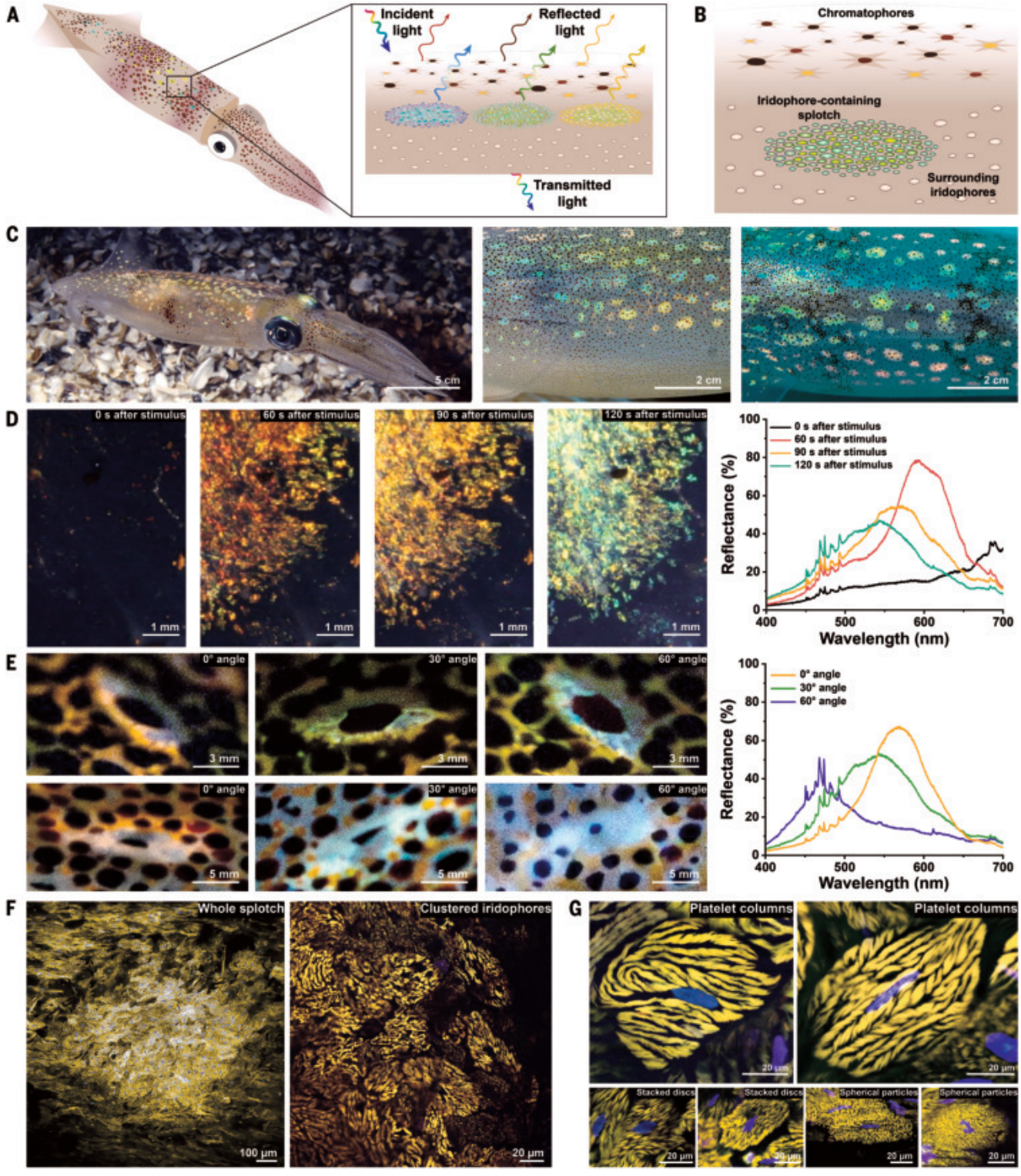

Fig. 1. The visible appearances and tissue-level architectures of squid dorsal mantle splotches. (**A**) A schematic of the squid *D. pealeii* and its dorsal mantle, which contains colorful chromatophore-overlaid splotches. (**B**) A schematic of the architecture of squid skin, which contains pigmented chromatophores, iridophore-packed splotches, and individual iridophores. (**C**) Digital camera images of the entire body (left), lateral side (middle), and dorsal mantle (right) of a squid, which show the splotches' blue, green, yellow, orange, and red iridescent (angle-dependent) colors. (**D**) Digital camera images (left) and representative reflectance spectra (right) obtained for individual splotches transitioning from transparent to red to orange to green at 0, 60, 90, and 120 s, respectively, when subjected to a chemical neurophysiological stimulus. (**E**) Digital camera images of individual splotches beneath expanded or contracted chromatophores (left) and representative reflectance spectra (right) obtained at ~0°, ~30°, and ~60° viewing angles. (**F**) A confocal microscopy image of a whole squid splotch (left) and the clustered iridophores within its interior (right). (**G**) Confocal microscopy images of the most common squid splotch iridophores filled with winding platelet columns (top) and two less common squid splotch iridophores filled with distributed stacked discs or packed spherical particles (bottom). Note that the splotch and iridophores in (F) and (G) are labeled with a nonspecific contrast-enhancing stain (yellow) and a nuclear marker (blue).

stimulus (acetylcholine) (Fig. 1D and movie S1) (*22*, *24*, *29*). The individual splotches also displayed iridescent (angle-dependent) colorations across a spectral range of 150 nm regardless of whether they were covered by contracted or expanded chromatophores (Fig. 1E) (*38*, *39*). The splotches' iridescent behavior and broadened tissue-level spectra generally resembled those reported for the skin of *D. pealeii* and other squid species (*22*, *24*, *30*). These experiments systematically benchmarked the squid splotches' natural dynamic color- and transparency-changing functionalities.

We investigated the tissue- and cellular-level architectures of the dorsal mantle iridophores (Fig. 1, A and B). We visualized chemically fixed splotch-containing tissues with confocal microscopy, immunofluorescence microscopy, and microspectrophotometry (see methods). The three iridophore types found inside the splotches featured unexpected morphologies, that is, most were filled with winding platelet columns, some contained distributed stacked discs, and some contained packed spherical particles (corresponding to an estimated ~96, ~2, and ~2% of the splotch cell population, respectively) (Fig. 1, F and G). By contrast, the two iridophore types found outside the splotches featured the previously reported morphologies, that is, they were filled with either parallel wrinkled plates or herringbone-patterned straight plates (corresponding to ~50% each of the surrounding cell population) (fig. S1) (*25*–*27*, *29*–*32*). Regardless of their morphologies, these five iridophore types possessed internal hierarchical structures consisting of the high–refractive index protein reflectin, in general agreement with prior findings (fig. S2) (*27*, *28*, *30*, *31*, *40*, *41*). The most common splotch iridophores filled with winding platelet columns individually maintained their iridescent colors but revealed narrowed cellular-level spectra (fig. S3). These experiments showed that the splotches' three internal iridophore types were morphologically distinct from the two surrounding iridophore types.

We next interrogated the cellular-level optical properties of the various dorsal mantle iridophore types (Fig. 2, A and B). We visualized the iridophores' global morphologies and refractive index distributions with holotomography (see methods) (*42*, *43*). The dominant iridophore type constituting ~96% of the splotches' cells featured a winding three-dimensional architecture, with ~10 to ~40 platelet columns per cell, ~5 to ~45 platelets within each column, and ~100- to ~700-nm periodicities for the platelets (Fig. 2, C and D, fig. S4, and movies S2 to S5). This iridophore type also possessed gradient three-dimensional refractive index distributions and sinusoidal-wave refractive index profiles along the platelet columns, with a range of ~1.35 to ~1.42 and a mean of ~1.39 for the platelet refractive indices (Fig. 2, C and D, figs. S5 to S7, and movies S2 to S5). By comparison, the two less common iridophore types inside the splotches and the two known iridophore types outside the splotches featured their expected architectures (see the previous paragraph) and possessed distinctive gradient three-dimensional refractive index distributions (figs. S8 and S9 and movies S6 to S9). The highest refractive index magnitudes for our five iridophore types corresponded to their reflectin protein–packed internal ultrastructures, with the observed refractive index profiles presumably arising from reflectin isoform concentration gradients (*27*). These experiments and analyses together elucidated the most common splotch iridophores' three-dimensional morphologies and showed that these cells unexpectedly featured sinusoidal-wave, as opposed to discrete, refractive index profiles (table S1).

We computationally modeled the optical properties of the most common dorsal mantle splotch iridophore type, which is filled with winding platelet columns (Fig. 2, A and B). We conceptualized such iridophores as individual columnar Bragg reflectors with different possible refractive index distributions and variable geometric parameters and simulated their reflectance spectra and visible appearances (fig. S10) (see methods). The Bragg reflectors with experimentally determined sinusoidal-wave refractive index profiles, varying periodicities, and different maximum refractive indices featured obvious first-order peaks, but suppressed higher-order peaks, with periodicity-dictated wavelengths and refractive index–dictated intensities (Fig. 2E and fig. S11). These simulated reflectors were predicted to possess visible colorations and the ability to become completely transparent for periodicities of ≤300 nm and maximum refractive indices of ≤1.5 (Fig. 2F and fig. S11). By comparison, analogous Bragg reflectors with hypothetical triangle- or square-wave refractive index profiles featured both first- and higher-order peaks and were predicted to possess either nonunique (redundant) colorations or a more limited capability for complete transparency (fig. S12). The computational model could reproduce the narrow reflectances and pure colorations observed for individual iridophores (Fig. 2G and fig. S3) and suggested that the broad reflectances obtained for the whole splotches originated from geometrically variable and/or orientationally disordered iridophore populations (fig. S13). A version of this model with modified input parameters could capture the primarily specular reflectance spectra trends and iridescent visible colorations obtained for nanocolumnar metal oxide Bragg reflectors with sinusoidal-, triangle-, or square-wave refractive index profiles (Fig. 2H and figs. S14 to S17). The combined calculations indicated that squid splotches could transition between transparent and spectrally pure colorful states specifically because of their constituent iridophores' sinusoidal-wave refractive index profiles (table S1).

Development of squid-inspired multispectral materials

We proceeded to design and evaluate visible appearance–changing composite materials inspired by the dorsal mantle splotches and their most common iridophores (Fig. 3, A and B). We fabricated elastomeric composite materials from nanocolumnar metal oxide Bragg reflectors with sinusoidal-wave refractive index profiles (fig. S18) and characterized them with digital camera imaging, visible spectroscopy, scanning electron microscopy, and microspectrophotometry (see methods) (*44*, *45*). The composites featured vibrant Bragg reflector–dictated blue, green, or yellow colors with narrowband reflectance and transmittance peaks at ~470, ~520, and ~580 nm (from both specular and diffuse contributions), with their transparency increasing when applied mechanical strain modified the surface microstructure (Fig. 3C and figs. S19 to S21). The composite materials also readily transitioned from blue to green, green to orange, or yellow to red—with spectral shifts of up to 90 nm and some transparency changes—when chemical stimuli modified their internal refractive indices (Fig. 3D and fig. S22). These composites' changes in transparency and color could even be enhanced and better controlled through simultaneous mechanical and chemical actuation (fig. S23). A computational model that was modified to account for the polymer matrices captured the actuation-dependent visible transmittances, reflectances, and appearances that we experimentally observed for the composite materials (figs. S24 to S26). These computationally validated experiments demonstrated that our artificial composite materials reproduced key aspects of the natural transparency- and color-changing functionalities of individual squid dorsal mantle splotches.

We prepared and assessed arrayed visible appearance-changing composite materials inspired by the arrangement of the squid splotches on the dorsal mantle (Fig. 3, A and B). We fabricated straightforward and sophisticated arrays from multiple different colored composite materials (fig. S18) and characterized them with digital camera imaging and visible spectroscopy (see methods). The straightforward arrays' blue, green, or yellow colors became less vibrant upon stretching in air but were red-shifted when submerged under water (Fig. 3E and movies S10 and S11). These arrays also became more transparent at increased viewing angles, and their spectra were blue-shifted at increased incidence angles, with weaker angular dependences when compared with natural iridescent systems (fig. S27 and movies S10 and S11) (*38*, *39*). The more sophisticated arrays not only featured comparable visible appearances and similar overall behavior above different backgrounds in air and water but were also reminiscent of disruptive camouflage when positioned at different angles above a checkerboard pattern (Fig. 3F, fig. S28, and movies S12 and S13) (*46*). These experiments demonstrated that our arrayed composite materials reproduced some of the collective visible

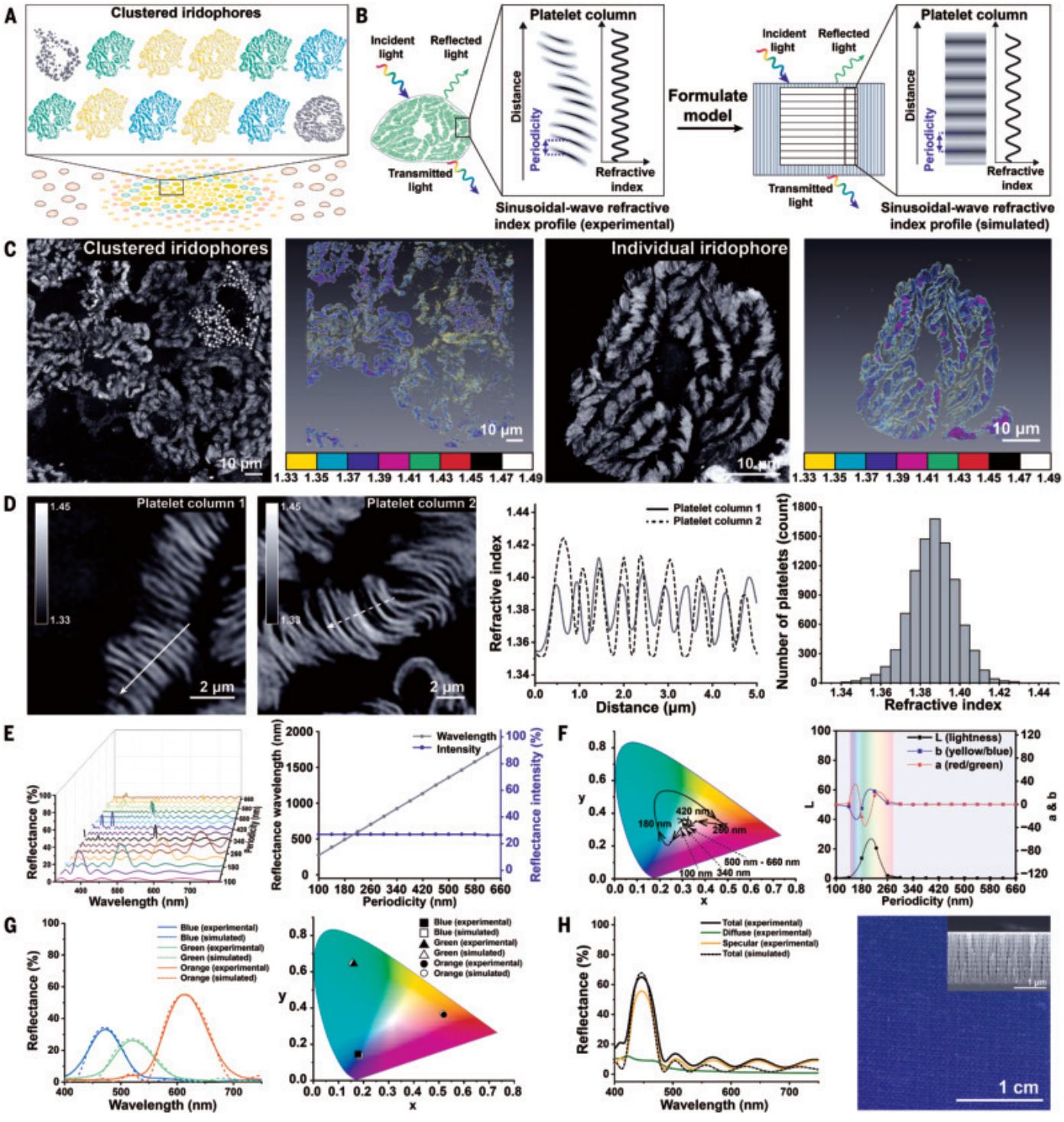

Fig. 2. The three-dimensional refractive index mapping and computational optical modeling of squid dorsal mantle splotch iridophores. (**A**) A schematic of a dorsal mantle splotch and its internal iridophores (inset). (**B**) A schematic of formulating an optical model for the most common dorsal mantle splotch iridophores. (**C**) Holotomography phase images and corresponding three-dimensional refractive index maps for clustered (left) and individual (right) winding platelet column–filled dorsal mantle splotch iridophores. The colored legends indicate the refractive index ranges. (**D**) Typical holotomography phase images (left and middle left), representative refractive index profiles (middle right), and mean platelet refractive indices (right) for the winding platelet columns. The white arrows indicate the locations of the profiles. (**E**) Representative simulated reflectance spectra (left) and corresponding peak wavelengths and intensities (right) for a model columnar Bragg reflector with variable periodicities and sinusoidal-wave refractive index profiles. (**F**) Representative CIE chromaticity diagram (left) and color space parameter plot (right) calculated from the spectra obtained for a model columnar Bragg reflector with variable periodicities and sinusoidal-wave refractive index profiles. The rainbow and gray regions indicate coloration and transparency, respectively. (**G**) Experimental and simulated reflectance spectra (left) and corresponding calculated CIE chromaticity diagram (right) for blue, green, and orange winding platelet column–filled iridophores. (**H**) Experimental and simulated reflectance spectra (left) and corresponding digital camera and cross-sectional scanning electron microscopy images (right) for nanocolumnar metal oxide Bragg reflectors with sinusoidal-wave refractive index profiles.

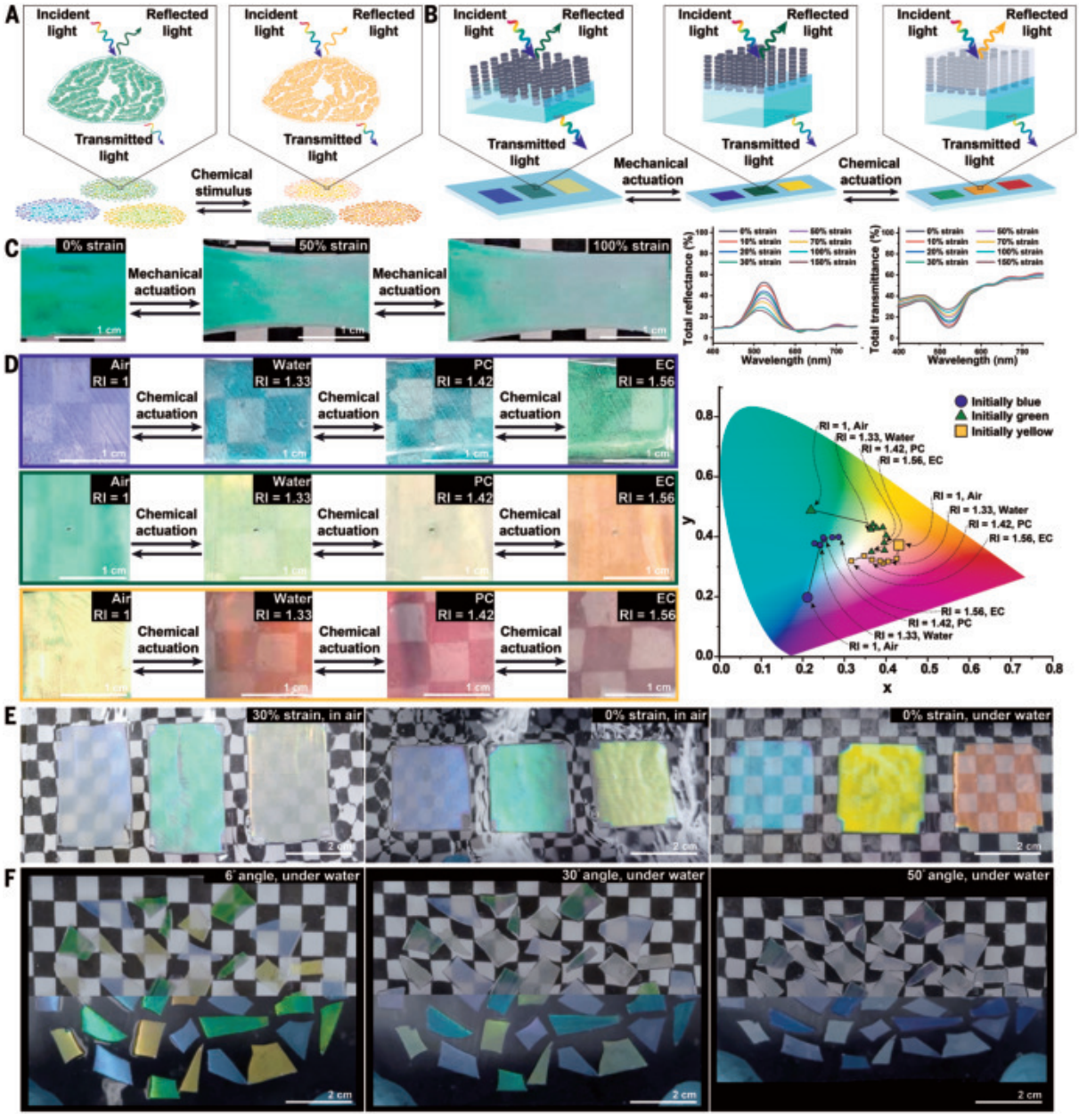

Fig. 3. The design and validation of individual and arrayed visible appearance–changing composite materials inspired by squid splotches. (**A**) A schematic of squid dorsal mantle splotches containing winding platelet column–filled iridophores (inset), which change their reflection of incident light and overall appearances when subjected to a chemical (neurophysiological) stimulus. (**B**) A schematic of visible appearance–changing composite materials incorporating nanocolumnar metal oxide Bragg reflectors (inset), which change their reflection of incident visible light and overall visible appearances upon reversible mechanical and/or chemical actuation. (**C**) Digital camera images of initially green visible appearance–changing composite materials (left) and corresponding visible reflectance and transmittance spectra (right) before actuation and after mechanical actuation by different strains of ≤150%. (**D**) Digital camera images of initially blue, green, or yellow visible appearance–changing composite materials (left) and corresponding CIE chromaticity diagrams (right) before actuation and after chemical actuation by various solvents with refractive indices of ≤1.56. EC, ethyl cinnamate; PC, propylene carbonate; RI, refractive index. (**E**) Digital camera images of straightforward arrayed blue, green, and yellow visible appearance–changing composite materials during mechanical actuation in air (left), without any actuation in air (middle), and during chemical actuation when submerged under water (right) above a checkerboard background. (**F**) Digital camera images of sophisticated arrayed blue, green, and yellow visible appearance–changing composite materials at different viewing angles when submerged under water above checkerboard (top) and black (bottom) backgrounds.

camouflage capabilities of multiple squid dorsal mantle splotches, even in demanding underwater environments.

We in turn developed multispectral appearance-changing composite materials by augmenting our iridophore-inspired color-changing layer with a chromatophore-inspired thermoregulatory layer (Fig. 4, A and B). We fabricated elastomeric composite materials from both nanocolumnar metal oxide Bragg reflectors and nanostructured metal films (fig. S29) and characterized them with digital and thermal camera imaging, visible and infrared spectroscopy, and microspectrophotometry (see methods) (*47*, *48*). The composites featured different colorful Bragg reflector–determined visible appearances with corresponding narrowband reflectances and transmittances (from diffuse contributions), becoming more transparent when stretched and changing color when subjected to chemical stimuli (Fig. 4, C and D, and figs. S30 to S33). The composite materials also possessed metal film–determined apparent temperatures and thermal appearances with initial high reflectances, low transmittances, and low

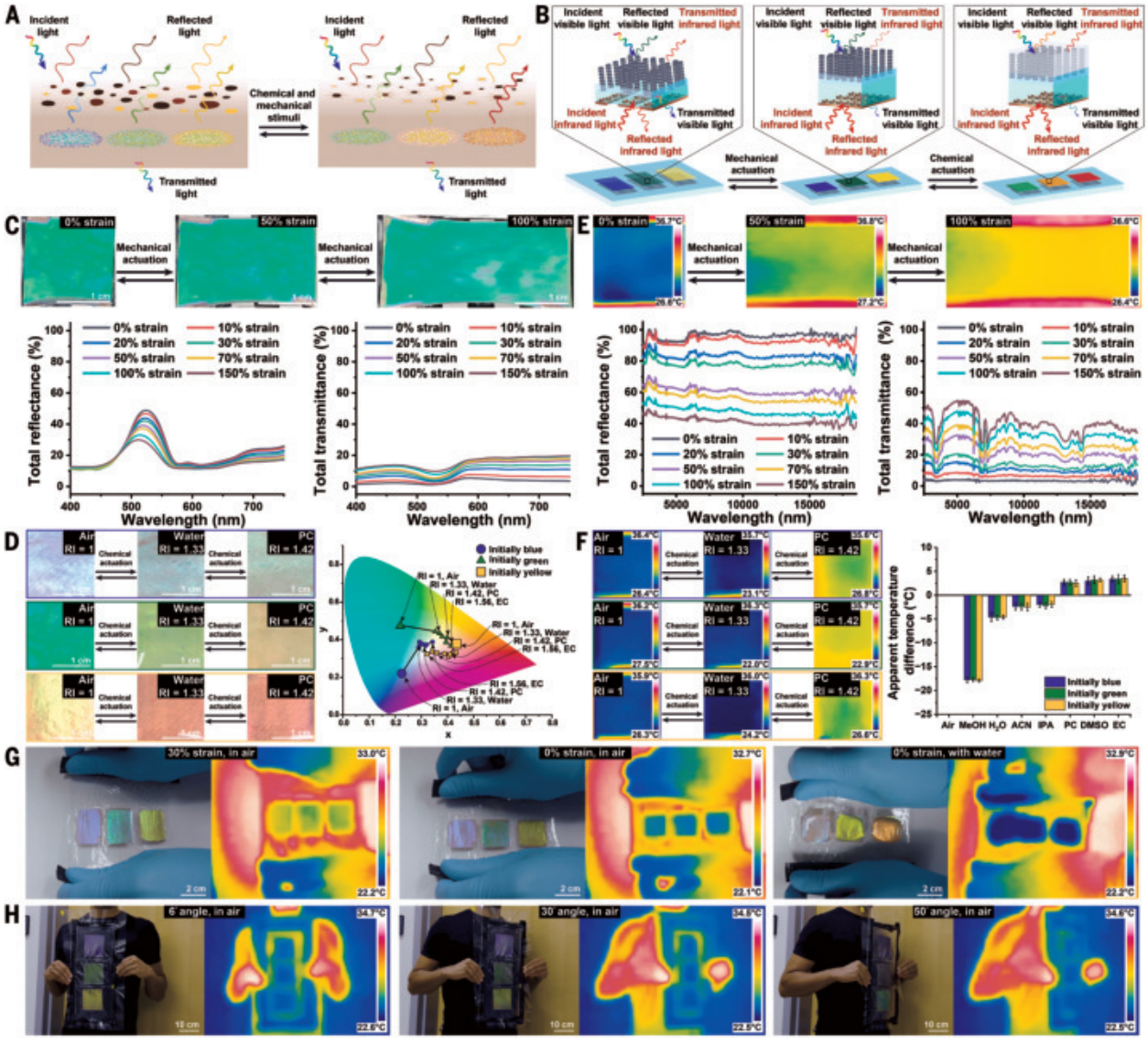

Fig. 4. The design and validation of individual and arrayed multispectral appearance-changing composite materials inspired by squid splotches and chromatophores. (**A**) A schematic of squid dorsal mantle splotches and overlaid chromatophores, which change their transmission and reflection of incident light and their overall appearances when subjected to chemical (neurophysiological) and mechanical (neuromuscular) stimuli, respectively. (**B**) A schematic of multispectral appearance-changing composite materials incorporating nanocolumnar metal oxide Bragg reflectors and nanostructured metal films (inset), which change their transmission and reflection of incident visible-to-infrared light and their overall multispectral appearances upon reversible mechanical and/or chemical actuation. (**C**) Digital camera images of initially green multispectral appearance-changing composite materials (top) and corresponding visible reflectance and transmittance spectra (bottom) before actuation and after mechanical actuation by different strains of ≤150%. (**D**) Digital camera images of initially blue, green, or yellow multispectral appearance-changing composite materials (left) and corresponding CIE chromaticity diagrams (right) before actuation and after chemical actuation by various solvents with refractive indices of ≤1.56. (**E**) Thermal camera images of initially green multispectral appearance-changing composite materials (top) and the corresponding infrared reflectance and transmittance spectra (bottom) before actuation and after mechanical actuation by different strains. (**F**) Thermal camera images of initially blue, green, or yellow multispectral appearance-changing composite materials (left) and corresponding apparent temperature difference plots (right) before actuation and after chemical actuation by various solvents. Error bars represent the standard deviations of the mean. ACN, acetonitrile; DMSO, dimethyl sulfoxide; EC, ethyl cinnamate; IPA, isopropanol; MeOH, methanol; PC, propylene carbonate. (**G**) Simultaneously collected digital and thermal camera images of small-area arrayed multispectral appearance-changing composite materials during mechanical actuation in air (left), without any actuation in air (middle), and during chemical actuation with water (right) above a heated surface. (**H**) Simultaneously collected digital and thermal camera images of large-area arrayed multispectral appearance-changing composite materials at different viewing angles in front of a human torso.

absorptances (from both specular and diffuse contributions), all of which subsequently changed when applied strain rearranged the metal film microstructure (Fig. 4E, figs. S34 to S36, and table S3). The composite materials moreover exhibited apparent temperature differences ranging from −18° to +4°C when subjected to various chemical stimuli, which presumably altered heat transfer occurring through radiative and other processes (Fig. 4F and fig. S37). The composites were readily deformable with Young's moduli of 1 MPa, sustained elongations of 790% before failure, exhibited rapid response times of 300 ms when mechanically actuated, and withstood 25,000 actuation cycles with minimal or no performance degradation (figs. S38 and S39 and movie S14). A computational model that was further modified to account for the metal films captured the actuation-dependent visible and/or infrared transmittances, reflectances, and appearances that we experimentally observed

for the composite materials (figs. S40 to S43). These experiments extended the visible appearance–changing capabilities of our composite materials into the infrared spectral range, with most of the resulting figures of merit exceeding those reported for emerging dynamic multispectral camouflage technologies (table S2) (*33*–*37*).

We prepared and assessed arrayed multispectral appearance-changing composite materials inspired by the arrangement of the squid dorsal mantle splotches underneath overlaid chromatophores (Fig. 4, A and B). We fabricated small- and large-area arrays from different multispectral composite materials (fig. S29) and characterized them with tandem digital and thermal camera imaging and visible and infrared spectroscopy (see methods). The small-area arrays' colorations became slightly more transparent and their apparent temperatures increased when stretched above a heated surface (Fig. 4G and movie S15), but their colorations became red-shifted and their apparent temperatures decreased when covered with water above a heated surface (Fig. 4G and movie S16). At increased viewing and incidence angles, these arrays' visible appearances and spectra became moderately blue-shifted, but their thermal appearances and infrared spectra remained nearly unchanged, revealing advantageous weak multispectral angle-dependent characteristics (fig. S44 and movie S17). The large-area arrays not only featured similar visible and thermal appearances to those of the small-area arrays but were also large enough to function as personal multispectral camouflage systems when positioned at different angles in front of a human torso (Fig. 4H and movie S18). These experiments further underscored the advantageous visible-to-infrared appearance-changing functionalities of our composite materials within the context of emerging dynamic multispectral camouflage technologies (table S2) (*33*–*37*).

Conclusions

We used a combined experimental and computational approach to resolve the question of how squid splotch iridophores can dynamically transition between nearly transparent and vibrantly colored states. Our observations reveal that the iridophores' tunable optical properties arise from their constituent winding platelet columns with sinusoidal-wave (rugate) refractive index profiles. The developed methodology thus advances scientific understanding of structural coloration in cephalopod iridophores and could provide insight into other animals' light-manipulating cells, where gradient refractive index distributions may play important roles. Furthermore, we engineered composite materials that recreate the dynamic transparency- and color-changing functionalities of squid dorsal mantle splotches and then expanded these capabilities from the visible into the infrared region of the electromagnetic spectrum. Our findings show that such multispectral composite materials feature a desirable combination of metrics when compared with other state-of-the-art systems. The technology we have described here therefore appears promising for camouflage, heat management, display, and sensing applications.

REFERENCES AND NOTES

1. P. Vukusic, J. R. Sambles, *Nature* **424**, 852–855 (2003).
2. M. D. Shawkey, N. I. Morehouse, P. Vukusic, *J. R. Soc. Interface* **6**, S221–S231 (2009).
3. J. Cai, J. P. Townsend, T. C. Dodson, P. A. Heiney, A. M. Sweeney, *Science* **357**, 564–569 (2017).
4. B. K. Pierscionek, J. W. Regini, *Prog. Retin. Eye Res.* **31**, 332–349 (2012).
5. D. Stuart-Fox, A. Moussalli, *Philos. Trans. R. Soc. London Ser. B* **364**, 463–470 (2009).
6. J. Teyssier, S. V. Saenko, D. van der Marel, M. C. Milinkovitch, *Nat. Commun.* **6**, 6368 (2015).
7. B. G. Bovard, *Appl. Opt.* **32**, 5427–5442 (1993).
8. O. Stenzel, *Optical Coatings: Material Aspects in Theory and Practice* (Springer, 2014).
9. A. Othonos, *Rev. Sci. Instrum.* **68**, 4309–4341 (1997).
10. E. Lorenzo *et al.*, *Appl. Opt.* **44**, 5415–5421 (2005).
11. M. Peters *et al.*, *Energies* **3**, 171–193 (2010).
12. F. Cunin *et al.*, *Nat. Mater.* **1**, 39–41 (2002).
13. R. Dylla-Spears *et al.*, *Sci. Adv.* **6**, eabc7429 (2020).
14. D. Gibson *et al.*, in *Proceedings Volume 10998, Advanced Optics for Imaging Applications: UV through LWIR IV* (SPIE, 2019).
15. A. M. Boyd, *Opt. Eng.* **57**, 085103 (2018).
16. C. Lin *et al.*, *Adv. Mater.* **37,** 2409738 (2025).
17. P. C. Hsu *et al.*, *Science* **353**, 1019–1023 (2016).
18. J. Mandal *et al.*, *Science* **362**, 315–319 (2018).
19. R. T. Hanlon, J. B. Messenger, *Cephalopod Behaviour* (Cambridge Univ. Press, ed. 2, 2018).
20. R. A. Cloney, S. L. Brocco, *Am. Zool.* **23**, 581–592 (1983).
21. G. R. R. Bell *et al.*, *Invertebr. Biol.* **132**, 120–132 (2013).
22. L. M. Mäthger, R. T. Hanlon, *Cell Tissue Res.* **329**, 179–186 (2007).
23. R. T. Hanlon, *Malacologia* **23**, 89–119 (1982).
24. T. J. Wardill, P. T. Gonzalez-Bellido, R. J. Crook, R. T. Hanlon, *Proc. Biol. Sci.* **279**, 4243–4252 (2012).
25. S. Mirow, *Z. Zellforsch. Mikrosk. Anat.* **125**, 176–190 (1972).
26. D. G. DeMartini, D. V. Krogstad, D. E. Morse, *Proc. Natl. Acad. Sci. U.S.A.* **110**, 2552–2556 (2013).
27. D. G. DeMartini, M. Izumi, A. T. Weaver, E. Pandolfi, D. E. Morse, *J. Biol. Chem.* **290**, 15238–15249 (2015).
28. W. J. Crookes *et al.*, *Science* **303**, 235–238 (2004).
29. K. M. Cooper, R. T. Hanlon, B. U. Budelmann, *Cell Tissue Res.* **259**, 15–24 (1990).
30. A. R. Tao *et al.*, *Biomaterials* **31**, 793–801 (2010).
31. D. G. DeMartini *et al.*, *J. Exp. Biol.* **216**, 3733–3741 (2013).
32. A. Ghoshal, D. G. Demartini, E. Eck, D. E. Morse, *J. R. Soc. Interface* **10**, 20130386 (2013).
33. M. Li, D. Liu, H. Cheng, L. Peng, M. Zu, *Sci. Adv.* **6**, eaba3494 (2020).
34. X. Li *et al.*, *Opt. Mater. Express* **12**, 1251–1262 (2022).
35. X. Zhang *et al.*, *Angew. Chem. Int. Ed.* **61**, e202211030 (2022).
36. J. Mandal *et al.*, *Joule* **3**, 3088–3099 (2019).
37. C. Xu, M. Colorado Escobar, A. A. Gorodetsky, *Adv. Mater.* **32**, 1905717 (2020).
38. H. Gruson *et al.*, *Interface Focus* **9**, 20180049 (2019).
39. D. Stuart-Fox, L. Ospina-Rozo, L. Ng, A. M. Franklin, *Trends Ecol. Evol.* **36**, 187–195 (2021).
40. J. L. Weiss *et al.*, *Biochim. Biophys. Acta* **1668**, 164–174 (2005).
41. M. Izumi *et al.*, *J. R. Soc. Interface* **7**, 549–560 (2010).
42. Y. Park, C. Depeursinge, G. Popescu, *Nat. Photonics* **12**, 578–589 (2018).
43. V. Balasubramani *et al.*, *Appl. Opt.* **60**, B65–B80 (2021).
44. M. M. Hawkeye, thesis, University of Alberta (2011).
45. A. C. van Popta, M. M. Hawkeye, J. C. Sit, M. J. Brett, *Opt. Lett.* **29**, 2545–2547 (2004).
46. R. T. Hanlon *et al.*, *Philos. Trans. R. Soc. London Ser. B* **364**, 429–437 (2009).
47. M. A. Badshah, E. M. Leung, P. Liu, A. A. Strzelecka, A. A. Gorodetsky, *Nat. Sustain.* **5**, 434–443 (2022).
48. S. Lee, E. M. Leung, M. A. Badshah, A. A. Strzelecka, A. A. Gorodetsky, *APL Bioeng.* **8**, 046101 (2024).

ACKNOWLEDGMENTS

We acknowledge the Marine Resources Center personnel at the Marine Biological Laboratory for the collection of live squid over multiple years, even in difficult weather. We acknowledge the laboratories of M. McFall-Ngai and E. G. Ruby for donating the reflectin-specific antibodies. We acknowledge M. W. Chan for her assistance with the visible and infrared spectra collection. We thank the Laser Spectroscopy Labs at the University of California, Irvine (UC Irvine) and the UC Irvine Materials Research Institute (IMRI) for access to experimental facilities. We thank the Optical Biology Core Facility of the Developmental Biology Center at UC Irvine, a shared resource supported by Cancer Center support grant CA-62203 and Center for Complex Biological Systems support grant GM-076516 at UC Irvine, for the use of microscopy instrumentation. We thank the National Institutes of Health (grant R37AI50661 to M. McFall-Ngai and grant R01OD11024 to E. G. Ruby) for enabling the production of the reflectin-specific antibodies. **Funding:** This work was supported by the Defense Advanced Research Projects Agency (cooperative agreement D16AP00034 to A.A.G.), the Air Force Office of Scientific Research (grants FA9550-20-1-0412 and FA2386-14-1-3026 to A.A.G. and grant FA9550-22-1-0467 to R.T.H.), and UES, Inc. (subcontract S-168-11X-001 to A.A.G. under prime contract FA8650-19-D-6109/FA8650-19-F-6110). R.T.H. thanks the Sholley Foundation and the Ben Veniste Family Foundation for gifts that provided partial support. **Author contributions:** A.A.G., G.B., R.T.H., and S.L.S. conceived the squid skin experiments, and A.A.G. and A.A.S. conceived the composite material experiments. S.L.S. and R.T.H. maintained live squid for the experiments. N.K. and S.L.S. extracted iridophore layers from the squid skin. G.B., S.L.S., and R.T.H. performed the digital camera imaging. G.B., S.L.S., and N.K. performed the confocal imaging. G.B. and N.K. performed the holotomography imaging. G.B. and A.A.S. performed the holotomography data analysis. G.B. and A.A.S. performed the computational modeling. A.A.S. and S.L. fabricated the materials, performed the scanning electron microscopy imaging, collected the visible and infrared spectra, and completed the tensile and stability testing. A.A.S., S.L., and G.B. performed the visible and thermal camera imaging of the materials with assistance from N.K. G.B., A.A.S., N.K., S.L., and A.A.G. wrote the manuscript with assistance from S.L.S. and R.T.H. **Competing interests:** G.B., A.A.S., N.K., S.L., and A.A.G. will be listed as inventors on an invention disclosure to UC Irvine, which describes the design and working principles of the reported multispectral composite materials. A.A.G. is a founder of SquidTek, Inc., which has previously optioned patents from UC Irvine for related composite materials. **Data and materials availability:** All data needed to evaluate the conclusions in the paper are present in the paper and/or the supplementary materials.

SUPPLEMENTARY MATERIALS

science.org/doi/10.1126/science.adn1570
Materials and Methods; Figs. S1 to S44; Tables S1 to S5; References (*49*–*87*);
MDAR Reproducibility Checklist; Movies S1 to S18

Submitted 26 November 2023; resubmitted 21 January 2025; accepted 2 May 2025

10.1126/science.adn1570

EARTHQUAKE CYCLE

Migrating shallow slow slip on the Nankai Trough megathrust captured by borehole observatories

Joshua R. Edgington[1], Demian M. Saffer[1]*, Charles A. Williams[2]

Patterns of strain accumulation and release offshore in subduction zones are directly linked to the potential for shallow coseismic slip and tsunamigenesis, but these patterns remain elusive. In this work, we analyze formation pore pressure records from three offshore borehole observatories at the Nankai subduction zone, Honshu, Japan, to capture detailed slip-time histories of two slow slip events (SSEs) along the outermost reaches of the plate boundary. Slip initiates ~30 kilometers landward of the trench; migrates seaward at 1 to 2 kilometers per day to within a few kilometers of, and possibly breaching, the trench; and coincides with the onset and migration of tremor and/or very-low-frequency earthquakes. The SSE source region lies in a zone of high pore fluid pressure and low stress, which provides clear observational evidence linking these factors to shallow slow earthquakes.

Subduction zones generate Earth's largest and most hazardous earthquakes and tsunamis. The patterns of strain accumulation and release along the offshore reaches of subduction megathrusts are particularly important toward understanding hazards associated with shallow coseismic slip and tsunamigenesis (*1*); yet, detailed constraints on fault slip behavior and locking in these regions remain elusive. In this work, we report on detailed observations of offshore fault slip events captured by borehole observatories in the Nankai Trough, offshore southern Honshu, Japan.

The plate interface along the Nankai Trough is among the best studied and monitored subduction zones globally. It hosts a spectrum of slip behavior, including great (M8+ class) earthquakes and both deep (~30 to 50 km) (*2*, *3*) and shallow (near-trench; <15 km) low-frequency earthquakes and very-low-frequency earthquakes (LFEs and VLFEs) (*4*, *5*), tremor (*2*, *6*–*10*), and slow slip events (SSEs) (*11*). SSEs represent fault slip at rates too slow to radiate seismic energy but can accommodate several to tens of centimeters of slip over a duration of days to weeks (*11*, *12*). The relationship between SSEs and large earthquakes remains poorly understood but has emerged as a topic of considerable interest: Recent observations suggest that in some cases, SSEs can be triggered by static or dynamic stress changes from nearby earthquakes (*13*), whereas in other cases, SSEs may precede large earthquakes (*3*, *14*, *15*). Similarly, the causative relationships between SSEs and tremor also remain ambiguous but hold important clues to unravel the underlying physical processes that govern SSEs in subduction zones as well as a wide range of other geologic environments, such as transform faults (*16*–*20*).

A key challenge in rigorously testing hypotheses for the mechanisms that underpin SSE occurrence—and more broadly those that seek to explain the spectrum of fault slip behavior observed globally (*6*, *18*)—has been a lack of detailed constraints on their location and spatiotemporal evolution. Establishing these constaints would allow direct linkage to estimated in situ conditions, inferred fault rheology, and observational geophysical data that define rock properties and fault geometry (*21*). Shallow subduction zone SSEs offer an ideal opportunity to probe these questions because they are amenable to high-resolution seismic imaging and sampling of the source region by drilling to characterize in situ conditions, lithology, and fault properties (*21*, *22*). However, their offshore location, long duration, and typically small total slip makes these events difficult to detect and locate using land-based Global Positioning System (GPS) arrays. Over the past decade, seafloor and borehole-based offshore geodetic monitoring have provided key insights into SSE occurrence (*11*, *23*, *24*). In particular, the high fidelity, high sensitivity, and temporal resolution of borehole data allow for detailed investigations of the magnitude, distribution, and evolution of shallow SSE slip.

Currently, an array of sensors monitors the Nankai Trough continuously and in real time as part of the DONET (Dense Ocean-floor Network System for Earthquakes and Tsunamis) cabled network (*25*). These sensors include ocean-bottom absolute pressure gauges (APGs), seismometers, and three subseafloor borehole observatories that monitor pore pressure both at the seafloor and within the formation below, installed in Integrated Ocean Drilling Program (IODP) drillholes (*26*–*28*) (Fig. 1). Previous work has identified recurring SSEs in this region using formation pore pressure as a proxy for volumetric strain and has reported approximate source locations on the basis of simplified elastic models (*5*, *11*). Although these studies provide clear evidence for SSE occurrence, outstanding questions remain about the location, evolution, and amount of slip in these events. In this work, we analyze pore pressure transients from two previously identified SSEs: one in October 2015 and another in March to May of 2020 (*5*, *11*) (Fig. 2). We present detailed slip-time histories for both, using borehole pore pressure records in tandem with a two-dimensional (2D) elastic finite element model that accounts for realistic first-order spatial variations in elastic properties. For both SSEs, we show that slip migrates, potentially all the way to the trench, and is coincident in time and space with previously identified tremor and VLFE activity interpreted to occur on the plate interface (*11*). The location of the SSE source fault, in both events, corresponds to a zone of previously identified high pore pressure, low stress, and low seismic velocity, which provides strong evidence supporting the connection between these factors and slow earthquake phenomena.

Analysis of formation pressure and modeling of slip events

At the Nankai Trough, continuous formation pore pressure records were collected at three instrumented boreholes along a transect offshore of the Kii Peninsula: IODP Hole C0002G (34 km landward of the trench; installed in 2010), Hole C0010A (25 km landward; installed in 2010), and Hole C0006G (2 km landward; installed in 2018) (Fig. 1). Once oceanographic tides were removed, we filtered the data to remove higher-frequency (minutes to hours) noise (materials and methods). Transient SSE strain signals ("transients") manifest as substantial deviations from otherwise near-constant background pressure (*11*) (Fig. 2). In the 2015 and 2020 SSEs, these transients occur sequentially in time and space, first at Hole C0002G, then at C0010A, and last (for the 2020 event) at C0006G. A reversal in sign, indicating a shift from compression to dilatation, is observed at Hole C0010A during both events. This, alongside the sequential onset of the strain transients, qualitatively suggests that slip migrates trenchward over time.

To link these strain transients in the accretionary prism quantitatively to slip on the décollement below, we generate Greens functions using the elastic finite element code PyLith (*29*–*31*) (supplementary materials and fig. S1). This model accounts for observed accretionary wedge and décollement geometry and for spatially varying elastic moduli, constrained by a combination of logging-while-drilling data at several boreholes (*27*, *32*, *33*), seismic surveys (*34*), and vertical

[1]University of Texas Institute for Geophysics, Austin, TX, USA. [2]GNS Science | Te Pū Ao, Lower Hutt, New Zealand. *Corresponding author. Email: demian@ig.utexas.edu

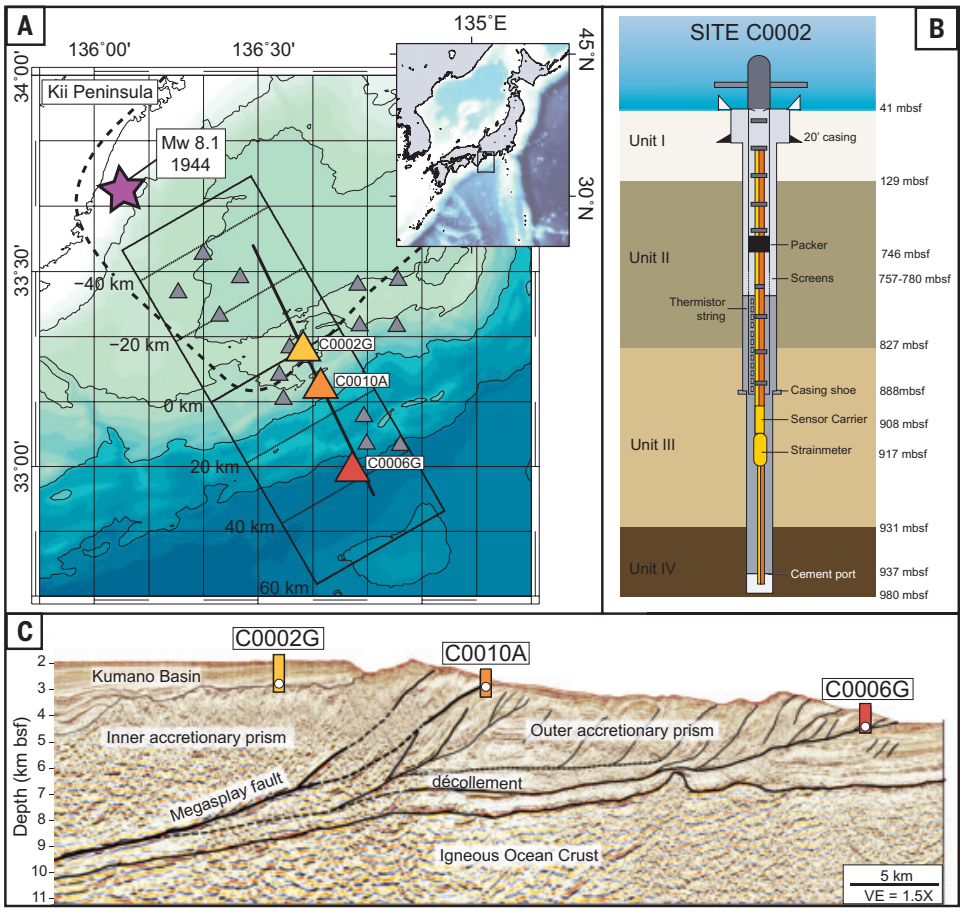

Fig. 1. Nankai subduction zone and borehole observatory locations. (**A**) Map of study area (location shown in inset), including epicenter and zone of coseismic slip in the 1944 Tonankai earthquake (pink star and black dashed outline, respectively), borehole observatories (colored triangles), and DONET seafloor sensors (gray triangles). (**B**) Schematic of Hole C0002G [instrumentation after (*24*)]. Holes C0010A and C0006G have similar configurations. (**C**) Seismic section [location shown in (A); after (*57*)], with boreholes and approximate pore pressure screen depths shown by white dots [C0002G: 937 to 980 m below seafloor (mbsf); C0010A: 389.2 to 407.6 mbsf; C0006G: 446 to 495 mbsf].

seismic profiling that provides constraints on both compressional and shear wave velocities (*35*). The resulting elastic structure is also highly consistent with recent regional-scale seismic velocity (compressional wave speeds only) models of the subduction zone (*36*). Previous studies in the Hikurangi subduction zone (*37*, *38*) have shown that SSE inversion results are strongly influenced by elastic moduli variations, particularly for shallow events. Because the boreholes occur along a single transect, we simulated fault slip in 2D. For each borehole site, we generated a library of Greens functions that define the expected volumetric strains in response to unit slip on the fault as a function of both slip patch width (for 5-, 10-, 20-, and 40-km-wide slipping patches) and centroid position (every 1 km) along the décollement from the trench to 54 km landward (fig. S1, table S1, and materials and methods). Beyond 44 km from the trench, the expected strain at all three sites is consistently compressive in sign (positive) or approaches zero (fig. S2). Thus, the range of slip patch locations that we considered fully captures the range of plausible solutions because an extended parameter space would yield model responses outside the observed extensional signal at Site C0002 (Fig. 2 and Fig. 3). These simulated volumetric strains were converted to expected pore pressure changes on the basis of poro-elastic theory, using conversion factors [units of kilopascals per microstrain (μS)] defined from experimentally determined sediment properties [5.7 kPa μS^{-1} at Site C0002 and 4.7 kPa μS^{-1} at C0010 and C0006 (*11*, *21*, *39*)].

The low noise and high temporal resolution of pore pressure records allows for identification of pressure shifts as little as 0.02 to 0.04 kPa (with the exception of higher noise at Hole C0010A during the 2020 event, which limits the detection of pressure shifts to >~0.2 kPa) (Fig. 2). This in turn allows separation of each SSE into a series of 2-day subevents, in which pressure changes are clearly distinguishable above the noise level of the data. Because the sparsity of observations is not amenable to a formal inversion ($n = 2$ in 2015; $n = 3$ in 2020), we instead conducted an optimization exercise using a forward grid search. We considered a wide range of potential slip patch positions and identified the best-fitting slipping patch location and amount of slip for each 2-day interval by minimizing the misfit between the observed pressure change (weighted inversely by noise for each of the three borehole time series) and our library of simulated pressure changes (materials and methods). This optimization returned a best-fitting slip-time history for each SSE.

To further explore the robustness of the optimizations, and as a comparison to assess the extent of detail that can be resolved by the data, we also considered a set of simplified end-member scenarios, including: (i) a fixed migration model (prescribed linear migration of a slip patch, with slip magnitude as a free parameter), (ii) a fixed slip model (prescribed slip magnitude, with patch position as the free parameter), and (iii) fixed position (i.e., nonmigrating event with prescribed position, and slip magnitude as the free parameter). The optimized (lowest possible error) models for each of these scenarios are shown in figs. S3, S4, and S5, respectively.

Slip migration of shallow SSEs

Our results show that the location of the centroid of slip during both SSEs migrates toward, and potentially all the way to, the trench (Fig. 3). This result is robust regardless of the choice of slip patch width because all optimizations returned similarly good fits to the data. For both SSEs, the centroid of slip begins about 30 km landward of the trench and migrates to within ≤5 km of the trench. Calculated along-dip migration rates are 1.2 km day^{-1} and 2.1 km day^{-1} for the 2015 SSE and 2020 SSE, respectively. Daily slip (i.e., fault slip rates) was similar for the two events, averaging 0.37 cm day^{-1} (0.75 cm for each 2-day window) and decreasing to ~0.2 cm day^{-1} toward the end of the event and as slip approached the trench. The pattern of cumulative slip for both SSEs is also similar, with most of the slip occurring 10 to 30 km from the trench and decreasing with proximity to the trench (Fig. 4). Peak total slip in the 2015 SSE reaches 4.7 cm at 20 km from the trench and 2 cm at 27 km from the trench for the 2020 SSE. For all model scenarios that we explored, best-fitting slip distributions generated <<5 mm of total vertical displacement at the seafloor (and at most locations <~0.1 to 0.2 mm), such that the events would not be resolvable in seafloor APG records, which generally require

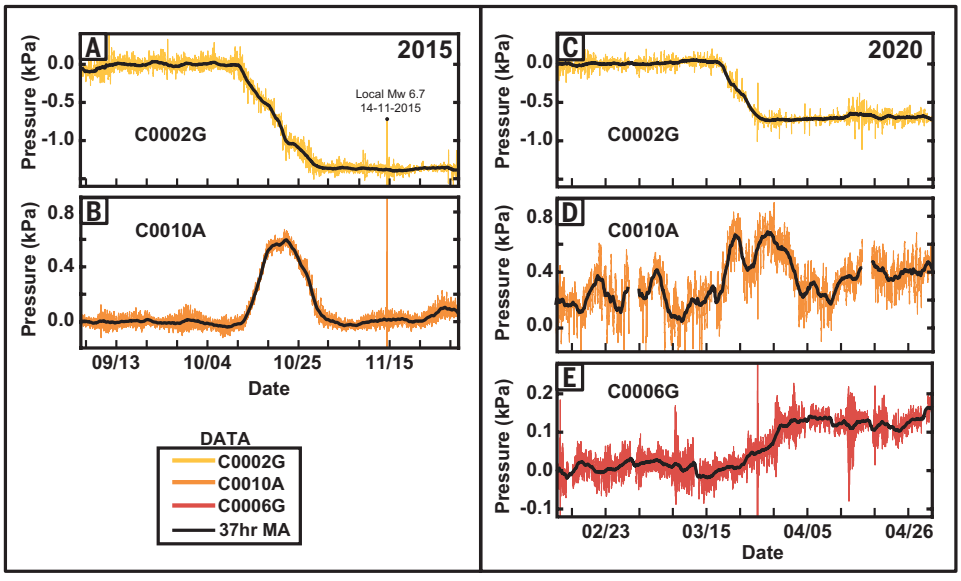

Fig. 2. Pressure records showing strain response from SSEs. (**A** and **B**) Pressure records after removal of ocean tidal loading signal and detrending for instrument drift [after (*11*)] for the 2015 SSE at Holes C0002G (A) and C0010A (B). The response to a local magnitude (Mw) 6.7 earthquake is labeled. (**C** to **E**) Pressure records for the 2020 SSE at Holes C0002G (C), C0010A (D), and C0006G (E). Data are color coded for each borehole site as in Fig. 1, and black lines show data smoothed with a 37-hour moving average (37hr MA). Tick marks represent 1 week, with dates as noted. Pressure transients for the 2015 SSE are larger than those for the 2020 SSE, which suggests a larger event overall.

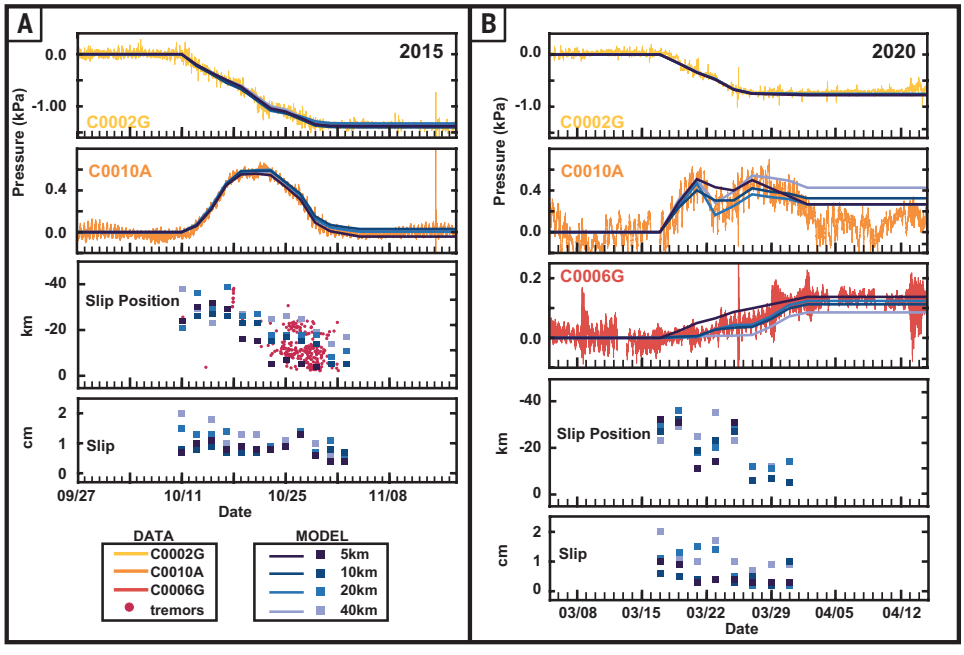

Fig. 3. Spatiotemporal evolution of SSE Slip. (**A** and **B**) Best-fitting optimizations for the 2015 (A) and 2020 (B) SSEs. The top two panels in (A) and the top three panels in (B) show the resulting best-fitting model pore pressure time series for four different assumed slip patch widths (see legend; blue lines) overlain on the same pressure records as in Fig. 2 but focused on the time windows of the SSEs (data shown by yellow, orange, and red curves). The lower two panels in (A) and (B) show the best-fitting slip position and amount of slip for each 2-day window (see legend; blue squares). The locations of coincident tremors during the 2015 SSE are plotted as red dots. Tick marks represent 1-day intervals, with dates as noted.

displacements of >~1 cm to be detectable in the presence of oceanographic noise (*23*) (fig. S6).

The migration of the centroid of slip during the 2015 SSE also tracks in time and space with a coincident tremor swarm interpreted to occur on the plate interface (*11*, *40*, *41*) (Fig. 3). The tremors migrated at about 1 km day^{-1}, and the onset of the swarm was synchronous and approximately colocated with the leading edge of the slip patch as it migrated trenchward. Although the 2020 SSE was not accompanied by active tremor, five identified VLFEs coincide with its timing and migration (*5*). The migration rates of both SSEs are comparable to the updip (trenchward) migration of accompanying VLFE and tremor (*10*), although they are somewhat slower than alongstrike (margin-parallel) migration rates of slow earthquakes during large swarms observed in the region in 2004, 2009, and 2020 (*10*, *42*).

The robustness of the slip models is supported by the simple end-member scenarios with fixed linear migration and with fixed slip. The former yielded a best-fitting slip evolution with near-constant daily slip that is comparable to the average daily slip in the optimized model shown in Fig. 3. Similarly, the latter returned a best-fitting slip evolution with clear trenchward migration, similar to the optimized model. Notably, these simple model variants produced slight but quantifiably poorer fits to the data when compared with our full optimizations (Fig. 3, figs. S3 and S4, and table S2). Conversely, when slip position was fixed (i.e., no migration permitted), optimizations returned substantially poorer fits to the data, reflected both in the comparison of the predicted and observed pressure time series (fig. S5) and in the larger misfits for these cases (table S2).

An upper bound (<1 cm) on SSE slip near the trench is especially well defined by the pressure record at Hole C0006G. Owing to its location within a few kilometers of the trench and only a few hundred meters vertically above the fault, the C0006G observatory is highly sensitive to strain along the shallowest reaches of the megathrust (<5 km from the trench; <2-km depth below seafloor). Slip greater than ~1 cm within ~8 km of the trench would lead to pressure signals >>1 kPa (fig. S1), well in excess of the observed pressure excursions. This high sensitivity suggests more generally that the trenchward-most monitoring site provides an important and powerful constraint on slip along the uppermost kilometers of the megathrust. Similarly,

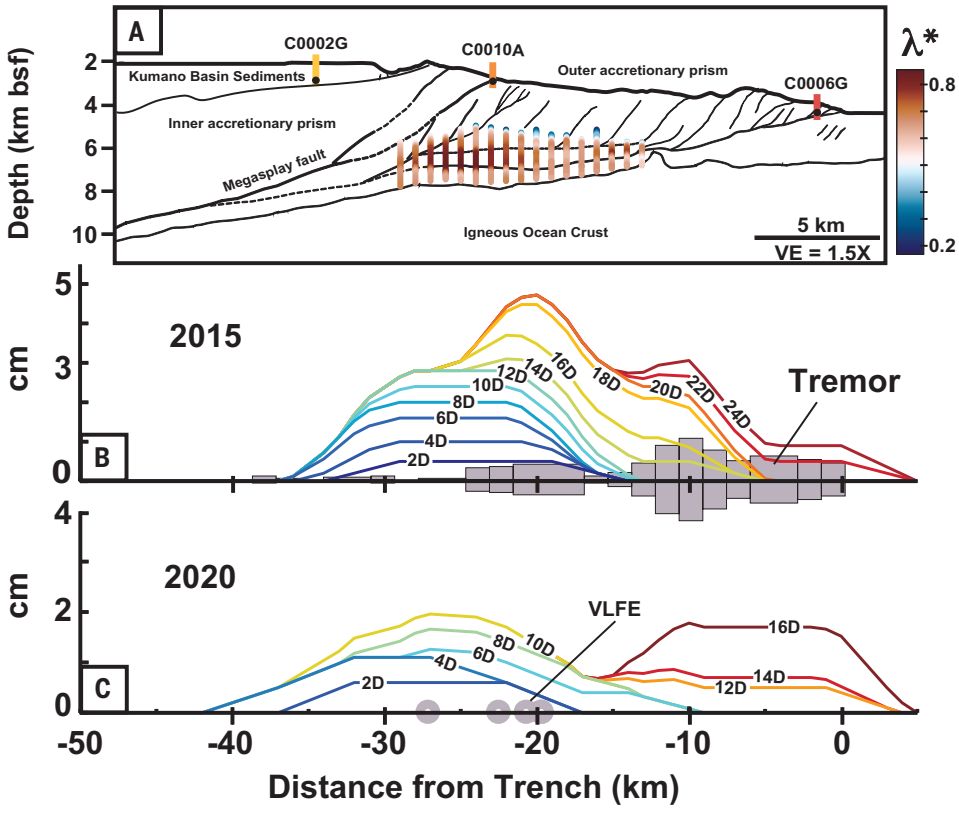

Fig. 4. Cumulative SSE slip distribution. (**A**) Line drawing of seismic interpretation from Fig. 1C [after (*57*)], showing region of elevated pore pressure quantified from compressional wave speeds, with pore pressure ratio (λ*: λ* ranges from 0 to 1—0 at hydrostatic pressure to 1 at lithostatic pressure) plotted as colored bars over the seismic interpretation [from (*50*)]. (**B** and **C**) Evolving slip distribution for the 2015 and 2020 SSEs, respectively. Lines are color coded by time from onset of each SSE (also labeled in days). The locations of the 2015 tremor swarm are marked with bars (B) scaled by tremor count, and locations of coincident VLFEs during the 2020 SSE are marked as gray circles (C).

we can rule out major slip on the megasplay fault that branches from the plate interface ~40 km from the trench (Fig. 1) because pressure at C0010A is highly sensitive to slip on this fault: Greens functions generated for slip on the megasplay show that slip >5 mm leads to pore pressure shifts that are positive in sign only and well in excess of 1 kPa, both inconsistent with the observations.

Finally, the reported pattern and rate of migration are not sensitive to slip patch width (Fig. 3). Smaller patch widths (5 km) yielded nominally overall higher errors, whereas patch widths of 10 to 40 km returned the lowest errors for both SSEs; but in all cases, they fall well within the noise level (2 s) in the data for every subevent (with the exception of a single 2-day window on 25 October for the 10-km patch; table S2). A slip patch dimension of 10 to 40 km is comparable to that obtained from inversions of sparse seafloor geodetic data at other margins (*12*, *37*, *38*, *43*) and consistent with previous simplified models for these events (*5*) and with the approximate dimensions of tremor and VLFE swarm previously identified during the 2015 event (*11*) and the shallow SSE in 2016 (*11*, *40*). Given the limited number of borehole stations, we cannot rule out more complex or heterogeneous slip distributions or patch geometries; our models provide constraints only on the position of the centroid of slip in each subevent and only in two dimensions. However, we argue that this set of constraints—albeit simplified—captures the primary features and distribution of SSE slip. The interpretation of a largely coherent migrating slip patch is also consistent with time-dependent inversions of analogous shallow SSEs offshore of the North Island of New Zealand (*43*). Similarly, whereas a 3D analysis is not justified by the available data, our optimizations yielded a lower bound on the magnitude of slip; if slip is out of plane by more than ~10 to 20 km, the slip would require larger displacements to generate the observed strain transients. However, tremor and LFEs and/or VLFEs that accompany these two SSEs (and others), as well as previously reported LFE and/or VLFE swarms in this region (*4*, *9*, *44*), were centered on and restricted to within ~10 km of the model and drilling transect and migrated primarily up-dip (*11*, *45*) (rather than along-strike), which suggests that the recurring SSEs are focused along the corridor offshore of the Kii Peninsula coincident with the drilling transect.

Implications for SSE processes, megathrust slip, and coupling

Our analysis shows that slip during the two shallow SSEs systematically migrated trenchward over the ~2- to 3-week duration of each event. This is evident from inspection of the pressure record at C0010A and the transition from increasing pressure, to neutral, to decreasing pressure, which indicates that the borehole was sequentially located within the compressional and then extensional lobes of the event (Fig. 2 and Fig. 3). Migration of slip is required to explain this pattern, and in detail we find that it is needed to explain the detailed timing and magnitude of pressure (and hence strain) signals during both events at the three boreholes (Fig. 3 and figs. S2 and S3). Our optimizations for both SSEs also show that slip reaches to within a few kilometers, and possibly all the way to, the trench. Finally, the simplified fixed slip and fixed migration models both provide reasonable fits to the data (and each, to first-order, returns the other as a best-fitting result), whereas even the best-fitting models with a fixed position patch provide a quantitatively and qualitatively poor fit to the data, strongly supporting the interpretation of migrating slip.

This interpretation is further corroborated by the coincident tremor swarm along the décollement during the 2015 SSE (*40*, *41*) and the coincident VLFEs during the 2020 SSE (*5*). Tremor initiated simultaneously with the arrival of SSE slip; we postulate that it may have nucleated at the leading edge of the slip patch, where stresses were highest, and then continued toward the trench as slow slip propagated (*40*, *46*). Although the two SSEs exhibit similar slip patterns, there is no tremor swarm observed in association with the 2020 event. This may be because of the overall larger slip in the 2015 event or because of the larger gradient in displacement in the area where tremor initiated (10 to 20 km from the trench), which would have, in principle, led to higher stressing rates at the rupture front as slip migrated (Fig. 4).

The restriction of tremor to only a portion of the megathrust at Nankai suggests that its origin may be related to distinct fault properties, including fault roughness (*47*, *48*), geometry (*41*, *46*), and/or variations in elastic moduli that may reflect fluid content (*49*). One key implication of this pattern, which has also been suggested by previous work on the basis of the far larger (three orders of magnitude) moment

of the SSE compared with that of tremor (*11*), is that slow slip drives the tremor rather than the reverse. This inference is also supported by (i) the observation of strain (and interpreted SSE slip) without observed tremor during the first ~12 days of the 2015 event; (ii) the fact that tremor appears restricted to only a portion of the interface; and (iii) the lack of observed tremor during the 2020 SSE, as well as other SSEs reported in previous work (*11*). This contrasts with the interpretation of synchronous tremor and slip for deep SSEs in Cascadia and Geurrero, Mexico (*16*), suggesting that the relationship between fault slip and tremor may vary with setting, in situ conditions, or fault properties.

The initiation and peak slip in both SSEs occurs ~10 to 30 km from the trench (Fig. 4). This lies in a zone of documented low *P*-wave velocity and quantified excess pore fluid pressure along and surrounding the plate interface (*50*) (Fig. 4). Although previously based on the approximate locations of SSE slip patches here and elsewhere (*11*, *21*), the detailed constraints on slip distribution that we report provide a so-called "smoking gun" in the form of a clear correlation between slow slip, elevated pore pressure, and low total and differential stresses (*51*). This supports a view, largely rooted in theoretical and numerical arguments, that elevated fluid pressure promotes both slow earthquake phenomena (including SSEs) and reduced seismic coupling across a wide range of tectonic and geologic settings globally (*52*).

Finally, the overall location and distribution of slip in these two events, taken together with the observation of recurring SSEs (*5*, *11*), reveals that the shallowest and most trenchward portion of the plate boundary—updip of the interseismically locked zone that fails in M8-class earthquakes (*53*, *54*)—is capable of accumulation and periodic release of strain energy. The occurrence of SSEs along the outermost reaches of the plate interface is also consistent with partial (~50%) locking of the megathrust in this region, documented by offshore geodetic campaigns (GNSS-A) over decadal timescales (*54*). A key implication is that the slip and locking behavior of the outermost portion of the subduction thrust is governed by its local frictional and rheological properties (*55*) and that its apparent partial coupling, as recorded by GNSS-A over decadal timescales, is not simply the result of a stress shadow from the locked zone below (*56*). This carries important implications for geodetic models, the mechanics of strain accumulation offshore, and the resulting outlook for hazard associated with shallow coseismic slip.

REFERENCES AND NOTES

1. T. Lay, *Tectonophysics* **733**, 4–36 (2018).
2. K. Obara, H. Hirose, F. Yamamizu, K. Kasahara, *Geophys. Res. Lett.* **31**, L23602 (2004).
3. K. Obara, A. Kato, *Science* **353**, 253–257 (2016).
4. Y. Ito, K. Obara, *Geophys. Res. Lett.* **33**, L09302 (2006).
5. K. Ariyoshi *et al.*, *Front. Earth Sci.* **8**, 600793 (2021).
6. S. Ide, D. R. Shelly, G. C. Beroza, *Geophys. Res. Lett.* **34**, L03308 (2007).
7. K. Obana, S. Kodaira, *Earth Planet. Sci. Lett.* **287**, 168–174 (2009).
8. S. Yabe, S. Baba, T. Tonegawa, M. Nakano, S. Takemura, *Tectonophysics* **800**, 228714 (2021).
9. H. Sugioka *et al.*, *Nat. Geosci.* **5**, 414–418 (2012).
10. S. Takemura, K. Obara, K. Shiomi, S. Baba, *J. Geophys. Res. Solid Earth* **127**, e2021JB023073 (2022).
11. E. Araki *et al.*, *Science* **356**, 1157–1160 (2017).
12. L. M. Wallace *et al.*, *Science* **352**, 701–704 (2016).
13. L. M. Wallace *et al.*, *Nat. Geosci.* **10**, 765–770 (2017).
14. Y. Ito, R. Hino, S. Suzuki, Y. Kaneda, *Geophys. Res. Lett.* **42**, 1725–1731 (2015).
15. L. Muotote, Y. Itoh, O. Lengliné, Z. Duputel, A. Socquet, *J. Geophys. Res. Solid Earth* **128**, e2023JB026603 (2023).
16. W. B. Frank, E. E. Brodsky, *Sci. Adv.* **5**, eaaw9386 (2019).
17. Z. Peng, J. E. Vidale, A. G. Wech, R. M. Nadeau, K. C. Creager, *J. Geophys. Res. Solid Earth* **114**, B00A06 (2009).
18. Z. Peng, J. Gomberg, *Nat. Geosci.* **3**, 599–607 (2010).
19. A. M. Thomas, R. Bürgmann, D. R. Shelly, N. M. Beeler, M. L. Rudolph, *J. Geophys. Res. Solid Earth* **117**, B05301 (2012).
20. P. Martínez-Garzón *et al.*, *Earth Planet. Sci. Lett.* **510**, 209–218 (2019).
21. D. M. Saffer, L. M. Wallace, *Nat. Geosci.* **8**, 594–600 (2015).
22. P. M. Barnes *et al.*, *Sci. Adv.* **6**, eaay3314 (2020).
23. L. M. Wallace *et al.*, *J. Geophys. Res. Solid Earth* **121**, 8338–8351 (2016).
24. E. E. Davis, H. Villinger, T. Sun, *Earth Planet. Sci. Lett.* **410**, 117–127 (2015).
25. Y. Kaneda *et al.*, in *Seafloor Observatories: A New Vision of the Earth from the Abyss*, P. Favali, L. Beranzoli, A. De Santis, Eds. (Springer, 2015), pp. 643–662.
26. A. Kopf, E. Araki, S. Toczko, Expedition 332 Scientists, "NanTroSEIZE Stage 2: Riserless Observatory," in *Proceedings of the IODP*, vol. 332 (Integrated Ocean Drilling Program Management International, Inc., 2011); https://doi.org/10.2204/iodp.proc.332.2011.
27. D. Saffer, A. Kopf, S. Toczko, Expedition 365 Scientists, "Expedition 365 summary," *Proceedings of the International Ocean Discovery Program*, vol. 365 (International Ocean Discovery Program, 2017); https://doi.org/10.14379/iodp.proc.365.101.2017.
28. K. Becker, M. Kinoshita, S. Toczko, Expedition 380 Scientists, "Expedition 380 summary," *Proceedings of the International Ocean Discovery Program*, vol. 380 (International Ocean Discovery Program, 2018); https://doi.org/10.14379/iodp.proc.380.101.2018.
29. B. Aagaard, M. Knepley, C. Williams, PyLith, version 2.2.1 (Computational Infrastructure for Geodynamics, 2017); https://geodynamics.org/resources/pylith/.
30. B. Aagaard, M. G. Knepley, C. A. Williams, PyLith User Manual, version 2.2.0 (Computational Infrastructure for Geodynamics, 2017).
31. B. Aagaard, M. G. Knepley, C. A. Williams, *J. Geophys. Res. Solid Earth* **118**, 3059–3079 (2013).
32. J. Ashi, S. Lallemant, H. Masago, Expedition 315 Scientists, "Expedition 315 summary," in *Proceedings of the IODP*, vol. 314/315/316 (Integrated Ocean Drilling Program Management International, Inc., 2009); https://doi.org/10.2204/iodp.proc.314315316.121.2009.
33. E. J. Screaton, G. Kimura, D. Curewitz, Expedition 316 Scientists, "Expedition 316 summary," in *Proceedings of the IODP*, vol. 314/315/316 (Integrated Ocean Drilling Program Management International, Inc., 2009); https://doi.org/10.2204/iodp.proc.314315316.131.2009.
34. A. Nakanishi *et al.*, in *Geology and Tectonics of Subduction Zones: A Tribute to Gaku Kimura*, T. Byrne *et al.*, Eds. (Geological Society of America, 2018), pp. 69–86.
35. T. Tsuji *et al.*, *Geophysics* **76**, WA71–WA82 (2011).
36. A. F. Arnulf *et al.*, *Nat. Geosci.* **15**, 143–148 (2022).
37. C. A. Williams, L. M. Wallace, *Geophys. Res. Lett.* **45**, 7462–7470 (2018).
38. C. A. Williams, L. M. Wallace, *Geophys. Res. Lett.* **42**, 1113–1121 (2015).
39. K. Wang, in *Hydrogeology of the Oceanic Lithosphere*, E. E. Davis, H. Elderfield, Eds. (Cambridge Univ. Press, 2004), pp. 376–413.
40. M. Nakano, T. Hori, E. Araki, S. Kodaira, S. Ide, *Nat. Commun.* **9**, 984 (2018).
41. Y. Hashimoto *et al.*, *Sci. Rep.* **12**, 2677 (2022).
42. K. Tamaribuchi, M. Ogiso, A. Noda, *J. Geophys. Res. Solid Earth* **127**, e2022JB024403 (2022).
43. N. M. Bartlow, L. M. Wallace, J. Beavan, S. Bannister, P. Segall, *J. Geophys. Res. Solid Earth* **119**, 734–753 (2014).
44. Y. Ito, K. Obara, K. Shiomi, S. Sekine, H. Hirose, *Science* **315**, 503–506 (2007).
45. S. Annoura, T. Hashimoto, N. Kamaya, A. Katsumata, *Geophys. Res. Lett.* **44**, 3564–3571 (2017).
46. K. Shiraishi, Y. Yamada, M. Nakano, M. Kinoshita, G. Kimura, *Earth Planets Space* **72**, 72 (2020).
47. T. Nishimura, Y. Yokota, K. Tadokoro, T. Ochi, *Geosphere* **14**, 535–551 (2018).
48. S. Baba, S. Takemura, K. Obara, A. Noda, *Geophys. Res. Lett.* **47**, e2020GL088089 (2020).
49. T. Tonegawa *et al.*, *Nat. Commun.* **8**, 2048 (2017).
50. H. Kitajima, D. Saffer, *Geophys. Res. Lett.* **39**, L23301 (2012).
51. H. J. Tobin, D. M. Saffer, D. A. Castillo, T. Hirose, *Geology* **50**, 1229–1233 (2022).
52. Y. Liu, J. R. Rice, *J. Geophys. Res. Solid Earth* **112**, B09404 (2007).
53. M. Kikuchi, M. Nakamura, K. Yoshikawa, *Earth Planets Space* **55**, 159–172 (2003).
54. Y. Yokota, T. Ishikawa, S. Watanabe, T. Tashiro, A. Asada, *Nature* **534**, 374–377 (2016).
55. S. Shreedharan, D. Saffer, L. M. Wallace, C. Williams, *Science* **379**, 712–717 (2023).
56. R. Almeida *et al.*, *Geophys. Res. Lett.* **45**, 4754–4763 (2018).
57. M. Strasser *et al.*, *Nat. Geosci.* **2**, 648–652 (2009).
58. J. Edgington, Data and code repository for: Migrating shallow slow slip on the Nankai trough megathrust, captured by borehole observatories, dataset, Zenodo (2024). https://doi.org/10.5281/zenodo.13737403

ACKNOWLEDGMENTS

We thank L. Wallace and P. Flemings for insightful discussions. This work used data collected from borehole observatories that were made possible through efforts of the IODP and through the DONET cabled observatory installed and supported by the Japan Agency for Marine-Earth Science and Technology (JAMSTEC). **Funding:** Observatory installation and data acquisition were funded by National Science Foundation awards 0623633 and 1334436 to D.M.S. D.M.S. acknowledges funding from a US Science Support Program postexpedition award and the Scott Petty Jr. Director's Chair endowment. Contributions from C.A.W. were funded by the Ministry of Business, Innovation and Employment (MBIE) through the Understanding Zealandia Programme (Strategic Science Investment Fund, contract C05X1702). J.R.E. was funded by a University of Texas Jackson School graduate fellowship. **Author contributions:** Conceptualization: J.R.E., D.M.S., C.A.W.; Funding acquisition: D.M.S.; Investigation: J.R.E., D.M.S.; Methodology: J.R.E., D.M.S., C.A.W.; Project administration: D.M.S.; Supervision: J.R.E., D.M.S., C.A.W.; Visualization: J.R.E., D.M.S.; Writing – original draft: J.R.E., D.M.S., C.A.W.; Writing – review & editing: J.R.E., D.M.S., C.A.W. **Competing interests:** The authors declare that they have no competing interests. **Data and materials availability:** Data and code repository are available at Zenodo (*58*).

SUPPLEMENTARY MATERIALS

science.org/doi/10.1126/science.ads9715
Materials and Methods; Figs. S1 to S6; Tables S1 and S2; References (*59*–*66*)

Submitted 9 September 2024; accepted 3 April 2025

10.1126/science.ads9715

EARTHQUAKE CYCLE

Interplate slip before, during, and after the 2024 M_w 7 Hyuga-nada earthquake, southwest Japan

Shinzaburo Ozawa*, Hiroshi Munekane, Hisashi Suito, Hiroshi Yarai

Using Global Navigation Satellite System data, we investigated the interplate slip before, during, and after the 2024 Hyuga-nada earthquake in Japan. Before the earthquake, a moment magnitude (M_w) 6.0 slow-slip event (SSE) was observed from late 2023 in a downdip extension of the mainshock. The coseismic slip was adjacent to the 1996 Hyuga-nada earthquake source. The afterslip resolved near the hypocenter area and in the downdip extension of the mainshock, reaching M_w 6.7 on 16 September 2024. Leading up to the earthquake, the recurrence interval for SSEs in the preslip area shortened from an average of 2 years, estimated from observations over the past 30 years, to 1 year, consistent with simulations in which the weakening of the Nankai megathrust was attributed to the cause.

An earthquake cycle consists of an interseismic backslip period of strain accumulation and a mainshock that releases the accumulated energy (*1*). This cycle is likely preceded by backslip weakening and preslips (*2*) and frequently followed by afterslips, in the case of interplate earthquakes (*3*). Detailed investigation of earthquake cycles is crucial for forecasting earthquake risk. In this study, we focused on interplate slippage associated with the Hyuga-nada earthquakes in Kyushu, southwest Japan, on the basis of data from the dense Global Navigation Satellite System (GNSS) network.

In the Hyuga-nada area, the Philippine Sea Plate subducts beneath the Amur Plate at a rate of 4 to 6 cm/year in a northwesterly direction (Fig. 1) (*4*), generating strong interplate earthquakes (M_w 6.8 to 7.0) every 20 to 30 years (*5*). The most recent earthquakes occurred on 19 October (M_w 6.8) and 3 December 1996 (M_w 6.7) (*6*), and ~30 years later on 8 August 2024 (M_w 7). The GNSS network in Kyushu detected the signal preceding the earthquake along with coseismic and postseismic crustal deformation. Using the acquired crustal deformation data, we estimated the preseismic, coseismic, and postseismic interplate slips for the 2024 Hyuga-nada earthquake.

We analyzed the preslips and afterslips after correcting for the viscoelastic deformations after the 2011 Tohoku and 2016 Kumamoto earthquakes (*7*) (see materials and methods). The linear trend of the position time series for each region (*7*) was subtracted from the entire time series (fig. S1). In the preslip analysis, we incorporated four Mogi sources to account for volcanic deformation related to the Aso, Kirishima, Aira, and Sakurajima volcanoes of Kyushu (Fig. 1B) [e.g., (*8, 9*)]. Coseismic offsets were removed by subtracting the offsets between coordinates averaged over the 7 days before and 2 days after the earthquake.

A network inversion filter (NIF) (*7, 10*) was applied to the displacement time series at 130 GNSS sites selected relative to site 0388 (Fig. 1) for 1 July 2023 to 6 August 2024, to analyze the preceding stage of the earthquake. We also applied the NIF to data collected between 1 January 2018 and 6 August 2024 (fig. S2) to analyze slow-slip event (SSE) recurrence in the 6 years after the 2016 Kumamoto earthquakes (*11*). For postseismic deformations, we used data collected during 10 July to 16 September 2024. We set slip to zero before the earthquake for the postseismic analysis. Checkerboard tests indicate good resolution in the Hyuga-nada area (figs. S3 and S4), with resolution matrices showing little effect from the null subspace (figs. S5 and S6) (*12*). For the coseismic slip, we estimated the slip distribution by applying least-squares inversion to the coseismic offsets with a Laplacian smoothing constraint. In all analyses, slip direction was fixed to be opposite the motion of the Philippine Sea plate (*4*).

Figure 2, A to C, shows the detrended position time series every 3 days at the selected sites for 1 January 2022 to 6 August 2024. Southward displacements of up to 5 mm were observed at sites 1088, 0483, and P211 in 2024, suggesting an SSE beginning in November 2023. The deviation from the trend beginning in January 2023 is attributed to a prior SSE. Stacking displacements of sites 1088, 0483, P211, and 0716 show a clear transient between late 2023 to early 2024 (fig. S7). Figure 2, D to F, show daily position time series after correcting for the coseismic offsets for July to September 2024. Southeastward postseismic deformation indicated an afterslip. Figure 3 shows the raw and modeled spatial distributions of crustal deformation before, during, and after the earthquake. Transient preseismic crustal deformation during 1 July 2023 to 6 August 2024 showed southward displacements at sites 0483 and P211 and southeastward displacement at site 1088, indicating an SSE before the earthquake (Fig. 3A). The signals at sites 1088, 0483, and P211 before the earthquake were beyond the 3σ error threshold, whereas no other regions showed spatially correlated displacements beyond 3σ suggestive of any transient events before the earthquake (fig. S8). Transient and error estimates in Fig. 3 were conducted by applying the ordinary Kalman filter to the single position time series with a state-space model of trend and autoregressive components (*13*) (see materials and methods). Some sites (i.e., 1087, 0488) showed irregular deviations attributed to other environmental factors (see materials and methods and figs. S9 to S11). Coseismic deformation showed an eastward displacement of up to 15 cm at site 1088 (Fig. 3B). Postseismic deformation showed southeastward displacements (<2 cm) during 6 August to 16 September 2024 (Fig. 3C).

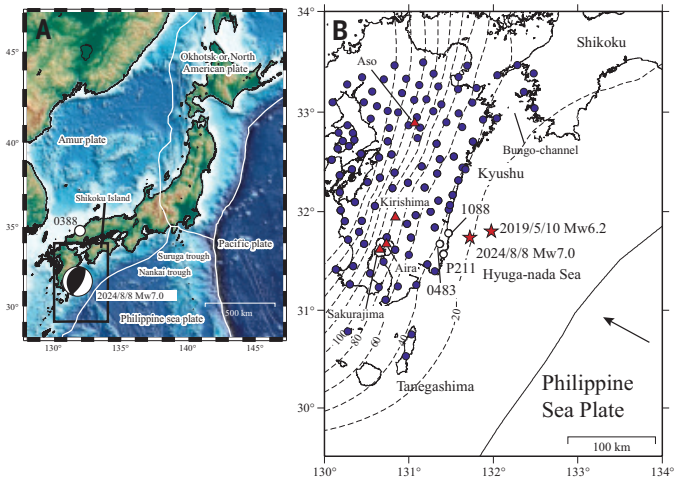

Fig. 1. Tectonic setting of Japan and the Hyuga-nada area. (**A**) Tectonic setting showing four plates converging around Japan. Centroid Moment Tensor solution shows the mechanism of the 2024 M_w 7 Hyuga-nada earthquake. (**B**) Enlargement of rectangular area in (A). Broken contours show iso-depth contours of plate interface between the subducting Philippine Sea and overriding Amur plates (contour interval: 20 km). Blue circles show the locations of GNSS sites used in the network inversion filter; white circles show the locations of GNSS sites that correspond to the position time series shown in Fig. 2. Stars mark the epicenters of the 10 May 2019, M_w 6.2 and 8 August 2024, M_w 7 Hyuga-nada earthquakes. Triangles mark the location of active volcanoes in Kyushu.

Geospatial Information Authority of Japan, Tsukuba, Ibaraki, Japan. *Corresponding author. Email: ozawa-s96sa@mlit.go.jp

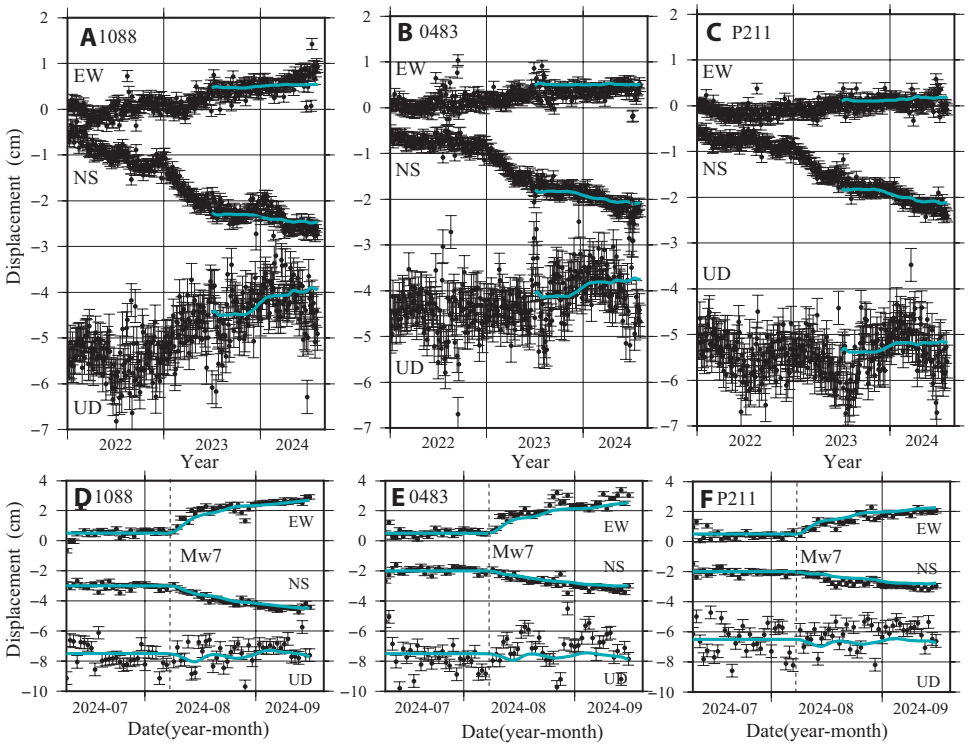

Fig. 2. Detrended position time series. Each series was averaged over 3 days for the preseismic stage (**A** to **C**) and every day during the 2024 Hyuga-nada earthquake (**D** to **F**) for GNSS sites 1088, 0483, and P211, relative to site 0388. Site locations are shown in Fig. 1B. Displacement includes east–west (EW), north–south (NS), and up–down (UD) components, with eastward, northward, and upward representing positive values, respectively. Blue lines are the transients computed from the optimal model beginning 1 July 2023; data for the 18 months prior are included for multi-annual context. Dashed vertical lines in (D) to (F) denote the 2024 Hyuga-nada earthquake. For simplicity, the effects of the estimated Mogi sources were extracted from the data in (A) to (C). Error bars indicate 1σ.

Pre-, co-, and postseismic slippage

The NIF identified the preceding SSE in the downdip extension of the mainshock area (Fig. 4A). The time evolution of the seismic moment suggested that the SSE continued until the earthquake, reaching 12×10^{17} N·m (equivalent to M_w 6.0) on 6 August 2024, with a rigidity of 30 GPa. The step-like behavior of the seismic moment ~2 months before the mainshock was near the limit of detectability (Fig. 4E); however, the estimated preslip signal was well beyond the 3σ error threshold (fig. S12). The negative slope of the moment evolution in Fig. 4E appeared because we applied a non-negativity constraint in the transition equation and not in the observation equation, which adjusts the solution without non-negativity constraints after the prediction step. Two apparent accelerations in May and August 2024 may be nonslip data fluctuations, considering their proximity to the 3σ limit, the postacceleration decrease in moment, and that these accelerations are not resolved in the 6-year preslip analysis. Overall, the moment gradually increased within ±3σ from November 2023 to August 2024, leading to the M_w 7 earthquake. The estimated coseismic slip area (Fig. 4B) was located adjacent to the source area of the 1996 Hyuga-nada earthquakes (*6*) and presented a maximum slip of >3 m and seismic moment of 380×10^{17} N·m, equivalent to M_w 7.0. The average stress drop was 32 MPa, which is within the typical range for earthquakes of M_w >7 (*14*). The peak afterslip was located 20 km south of the hypocenter, in the updip extension of the hypocentral area and downdip extension of the hypocenter (Fig. 4C). The estimated moment reached 140×10^{17} N·m, equivalent to M_w 6.7, on 16 September 2024, and decelerated slightly (Fig. 4F). Notably, a separate SSE started near Tanegashima 150 km southwest of the epicenter after the Hyuga-nada earthquake (Fig. 4D).

The steplike changes in the cumulative moment shortly before the mainshock (Fig. 4E) suggests the possible occurrence of a short-term SSE of several days to a month (*15*) occurring after a multimonth SSE. Even though a time-varying error was assigned to the position time series on the basis of the scattering of coordinates in the 10-day time window, we observed a high moment rate before the earthquake (fig. S13) that continued until the earthquake. Several studies reported that SSEs can precede and trigger large earthquakes (*16*–*19*). In this study, spatiotemporal proximity indicated that the preceding SSE triggered the mainshock through two possible mechanisms. The first mechanism was a static stress perturbation induced by the SSE in the earthquake source area. The Coulomb failure stress change (ΔCFS) increased by ~10 kPa owing to the SSE in the mainshock area, which was slightly less than the typical 20 to 60 kPa required for triggering earthquakes (*20*) (fig. S14A). The second mechanism was an enhanced weakening of the earthquake nucleation area, owing to the limited extent of the SSE in the locked region (*21*, *22*).

To assess the sensitivity of the preslip solution to the data correction method, we applied the NIF to the data without viscoelastic correction and confirmed occurrence of the preslip (fig. S15). The time evolution of the moment in fig. S15 suggests transient behavior, which cannot be explained by viscoelasticity. We confirmed this preslip signal using another dataset corrected for viscoelastic deformation (fig. S16) (*23*). These findings suggest that the preslip signal is insensitive to the applied viscoelastic correction, although the different viscoelastic deformation correction increased its magnitude slightly. The signal in 2024 was also inconsistent with annually repeated cycles (Fig. 2, A to C). We applied the NIF to the data with annual and semi-annual components corrected for July 2021 to October 2022, when there were no transients reported. The resulting preslip signal is shown in fig. S17. Considering the similar result with and without annual correction, and the lack of annual variation in the observations (except for some vertical components in Fig. 2, A to C) and estimated moment, seasonal changes had little effect on our results. Figure S18 shows volume changes of the Mogi sources at four volcanoes, indicating that volcanic deformation had little effect on crustal deformation in the short-term preslip analysis. We confirmed the reliability of the preslip signal by applying a Markov chain Monte Carlo (MCMC) method (see materials and methods) (*24*) to the crustal deformation in Fig. 3A (fig. S19), which showed preslip over the 3σ range using fully Bayesian estimates.

The spatiotemporal evolution of the preslip suggested little propagation during the analyzed period (fig. S20). Our model mostly reproduced the data in Fig. 2 within the error range. The mismatch between Fig. 3, A and D, was within the data scattering, whereas goodness-of-fit slightly improved by allowing variable rake (fig. S21). Even with variable rake, the resulting preslip was in almost the same location as that in the fixed rake analysis (fig. S21). Although we can improve goodness-of-fit by varying the spatial hyperparameter, the adjustment does not change the conclusion of preslip occurrence. In addition, this level of deviation can be caused by analytical assumptions such as homogeneous

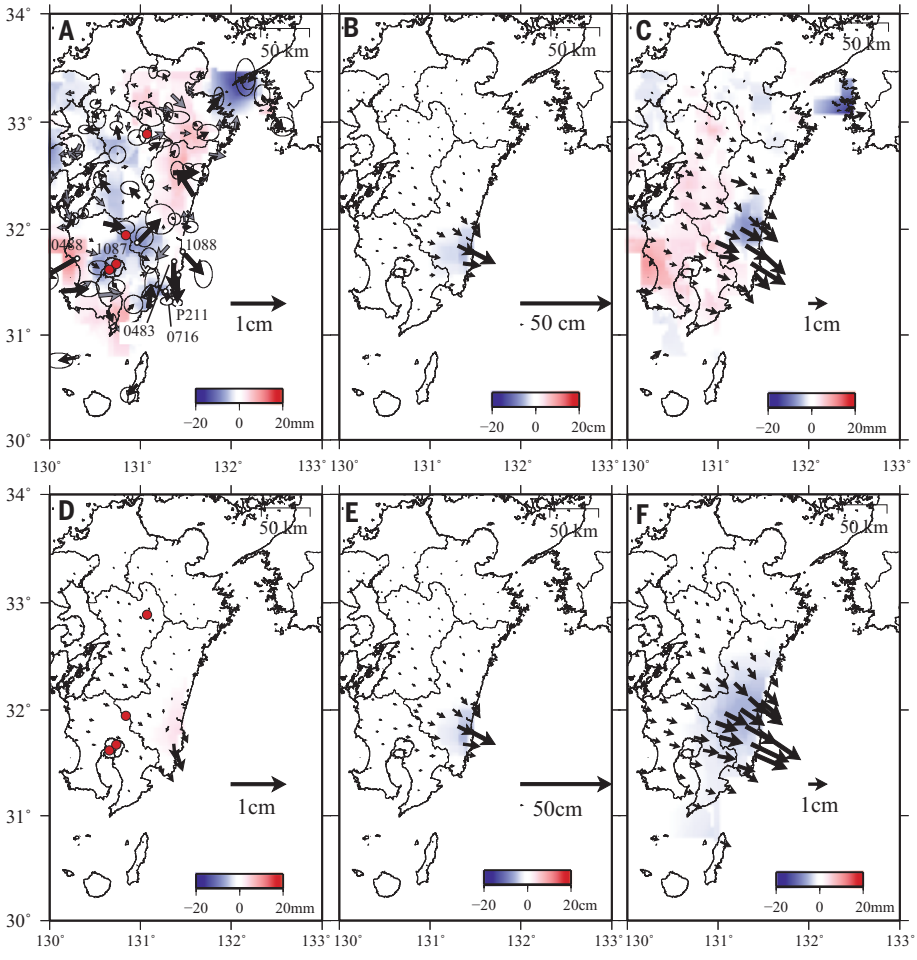

Fig. 3. Pre-, co-, and postseismic crustal deformation. (**A**) Observed deformation for 10 July 2023 to 6 August 2024. Black arrows indicate horizontal displacement exceeding 3σ, and gray arrows indicate displacement below 3σ. The red-blue spectrum shows vertical displacements, which were interpolated using the GMT (*36*) "nearneighbor" command with a search radius of 2 min. Error ellipsoid shows a 3σ error. (**B**) Coseismic deformation on 8 August 2024. (**C**) 6 August 2024–16 September 2024. (**D** to **F**) Computed crustal deformation from the optimal models corresponding to (A) to (C). Red circles show the locations of the Mogi sources used in the analysis. For simplicity, the effects of the estimated Mogi sources were extracted from (A) and (D).

elastic half-space, plate geometry, regularization issues, misalignment of slip direction, and subtle misfit of trend estimates.

In the southern Hyuga-nada area, SSEs have recurred approximately every 2 years since 1996 (*25*, *26*) (fig. S22A), including four Bungo SSEs [e.g., (*7*)] (some slip occurred in 2018 to 2019; Fig. 5A). In the past 6 years, SSEs occurred near the southern Hyuga-nada area during August 2018 to September 2019, June 2020 to March 2021, and December 2022 to June 2023 (Fig. 5, A to E) (*7*), indicating that the recurrence interval decreased from ~2 years to 1 year over a 1σ range before the 2024 Hyuga-nada earthquake (fig. S22A). The volume changes of the Mogi sources for the 6-year analysis are shown in fig. S23 with observation and calculation from the optimal model shown in fig. S24. Volcanic deformation had little effect on our results without Mogi source analysis (figs. S25 and S26). For the 6-year analysis, we also applied the NIF with varying viscoelasticity (*23*). The results in figs. S27 and S28 show that different viscoelastic corrections have little impact; however, the overall moment is affected. As for the annual changes, we applied NIF to the data with annual and semi-annual corrections estimated for the period between July 2021 and October 2022. The results in figs. S29 and S30 show the small effect of annual corrections; however, moment rate or slip rate increased relative to those without annual corrections. Therefore, the difference in viscoelastic correction and annual correction does not change our main results for the 6 years pre-earthquake analysis.

Although Bungo SSEs with magnitudes of M_w 7 may exert complex effects on Hyuga-nada SSEs (*27*), the 30-year observation data showed limited variation in recurrence time (fig. S22A), suggesting the limited influence of Bungo SSEs. Considering the long-term independence of Hyuga-nada SSE recurrence time from outside events such as Bungo SSEs and the 2016 Kumamoto earthquake, we consider the shortening of the recurrence time right before the 2024 earthquake to have been out of the fluctuation range of Hyuga-nada SSEs under the frequent influence of outside events. The observed shortening in recurrence time right before the earthquake was consistent with several simulations (*28*, *29*). However, the simulated recurrence shortening occurred over a series of intervals, whereas in this study, it occurred over the final one or possibly two intervals just before the earthquake. No clear decrease in predicted slip rate has been observed except in the last four cases (fig. S22B). Slip rates before the 10 May 2019 and 8 August 2024, earthquakes were low compared with those of the 2020–2021 and 2022–2023 events. Takagi *et al.* (*26*) assumed uniform slippage on a rectangular fault for the events before 2018, which may bias a comparison with this study after 2018. The shortening of the recurrence interval is attributed to the increased slip velocity between the locked and SSE regions nearing the earthquake occurrence, whereas the peak slip rate decrease may be due to a decrease in SSE size owing to the erosion of this area by earthquake nucleation (*29*). Before the M_w 6.2 earthquake on 10 May 2019, an SSE occurred in the down-dip extension of the mainshock (Fig. 5A) (*7*). Furthermore, the #1 event in a previous study (*26*) preceded and continued through the 1996 Hyuga-nada earthquakes. If this report is true, the present study is the third case in which an SSE preceded the mainshock in Hyuga-nada, suggesting that SSEs may frequently precede the mainshock in this area.

Using a 6-year model with optimized hyperparameters (fig. S31), we show that goodness-of-fit to the data (fig. S32) improves with computed values explaining observation within the 3σ range by optimizing hyperparameters. However, the optimization of hyperparameters keeps the characteristic features in Fig. 5, A to D, in that SSE appears in the same Hyuga-nada area with the same timing as shown in fig. S31. Therefore, our conclusion changes only slightly with optimization of hyperparameters to improve goodness-of-fit to data. With regard to the reasonability of the model (Fig. 4A), it is less affected by subtle misfit, which accumulates in long-period data, than the 6-year preslip model (Fig. 5, A to D). The results of the short-term preslip analysis in Fig. 4A are more reasonable than those of the spatially very rough model in fig. S31; however, the conclusion does not change. Therefore, adopting a spatial hyperparameter that produces a consistent result with Fig. 4A for the 6-year pre-earthquake analysis adopted in this study is appropriate.

Coseismic slips during the 2024 earthquake occurred in a distinct source area from the 1996 Hyuga-nada earthquakes (*6*), showing three adjacent asperities in this narrow area with recurrent slips. Spatial variation in the rake had little effect on the results (fig. S33). An afterslip

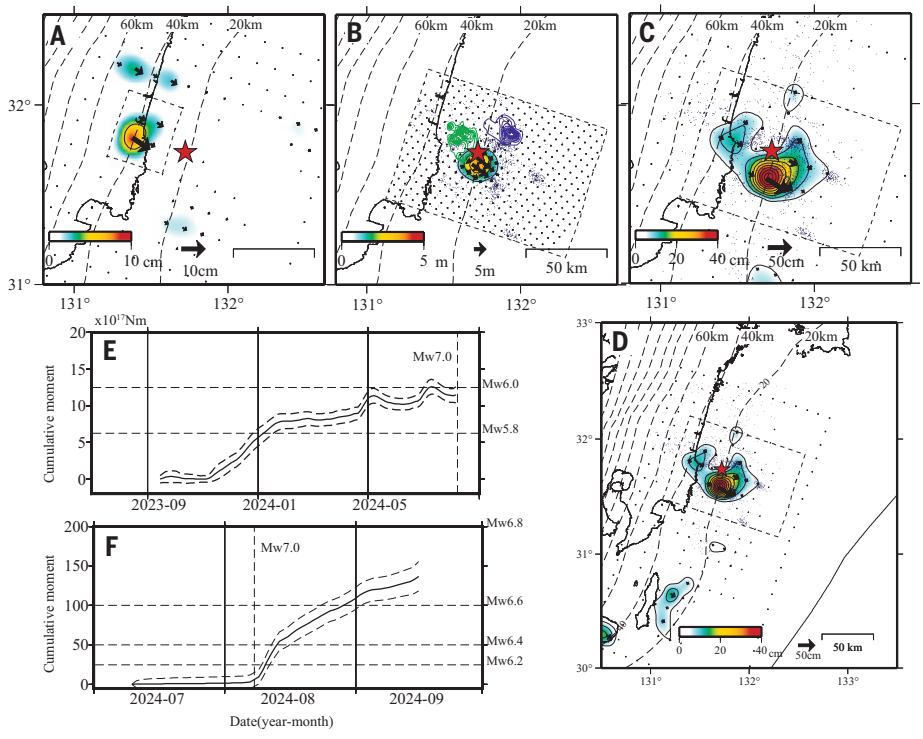

Fig. 4. Estimated interplate slip at plate interface. (**A**) Preseismic SSE (contour interval: 5 cm) 10 July 2023 to 6 August 2024. (**B**) Coseismic slip (contour interval: 1 m) 8 August 2024. Blue and green contours show the source areas of the 19 October 1996, M_w 6.8 and 3 December 1996, M_w 6.7 earthquakes, respectively. (**C** and **D**) Afterslip (contour interval: 5 cm) 6 August 2024 to 16 September 2024, zoomed out in (D) to show a separate southern SSE near Tanegashima, with blue dots indicating the epicenters of aftershocks. Colors show the magnitude of the aseismic or coseismic slip, with black arrows showing slips >3σ and gray arrows <3σ. The contour indicates the magnitude of slip. Broken contours indicate an iso-depth of the plate interface between the subducting Philippine Sea Plate and overriding Amur Plate (contour interval: 20 km). (**E**) Cumulative moment of preseismic SSE over the rectangular area in (A), with a broken contour indicating a 3σ range. (**F**) Cumulative moment of postseismic slip over the rectangular area in (C) and (D), with a broken contour indicating a 3σ range. Vertical broken lines indicate the dates of M_w 7 earthquakes.

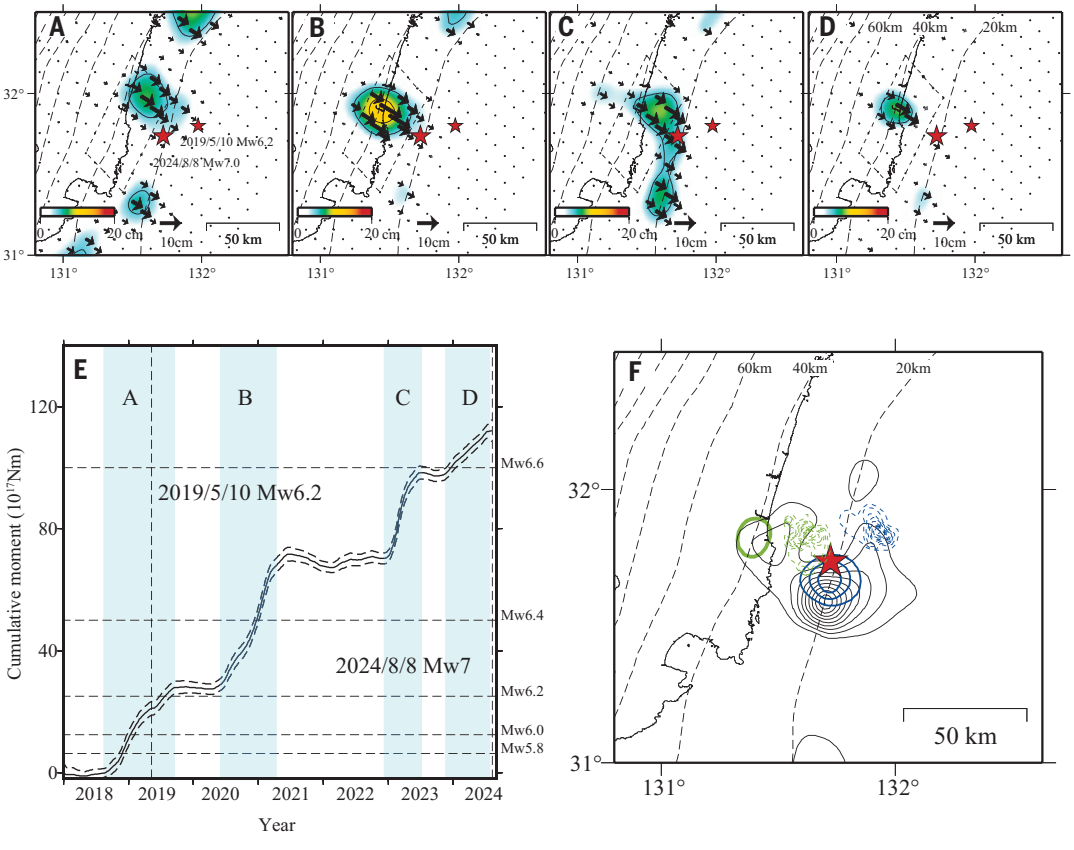

Fig. 5. Recent SSEs in the Hyuga-nada region. (**A**) Slip distribution in August 2018 to September 2019. Iso-depth contour interval of the plate interface is 20 km. (**B**) June 2020 to March 2021. (**C**) December 2022 to June 2024. (**D**) November 2023 to August 2024. The stars mark the epicenters of the 10 May 2019, and 8 August 2024, earthquakes. Colors show the magnitude of the aseismic slip, with black arrows showing slips >3σ and gray arrows <3σ. The contour shows the magnitude of the aseismic slip. (**E**) Cumulative moment of the rectangular area in (A) to (D). Shaded area indicates SSE period for (A) to (D). Broken lines show a 3σ range. Vertical broken lines indicate the 10 May 2019 and 8 August 2024 earthquakes. (**F**) Comparison of preceding (green, contour interval: 5 cm), coseismic (blue, contour interval: 1 m), and postseismic (black, contour interval: 5 cm) slip areas. Light green and blue broken contours show the source area of the 1996 Hyuga-nada earthquakes (*6*). Broken contours indicate iso-depth of the Philippine Sea Plate with a contour interval of 20 km. Star shows the epicenter of the 2024 earthquake.

of M_w 6.7 was estimated to occur around the hypocentral area as of 16 September 2024, at a slip rate of 1 to 2 cm/day and an order of magnitude exceeding the <1 mm/day of long-term SSEs in the Hyuga-nada area (*26*) and slightly higher than that of short-term SSEs. Viscoelastic deformation of the mainshock indicated a maximum displacement of 0.5 mm inland over 30 days after the mainshock (fig. S34), which is considered negligible.

The slip in the downdip area of the mainshock occurred several days after the start of the afterslip in the hypocentral area (fig. S35A). The temporal evolution estimated from the slip history of the downdip area showed SSE-like behavior (fig. S35A). Therefore, we believe that the SSE was induced by the mainshock and afterslip in its downdip extension, where the SSE recurred. Furthermore, the mainshock potentially triggered the Tanegashima SSE (fig. S35D) (*7*) through a dynamic rather than a static stress change (*30*), considering the negligible stress change from the mainshock in the current region (fig. S14B). Spatiotemporal evolution suggested little propagation of the afterslip over time (fig. S36). The excitation of SSEs after the mainshock contradicts the quiescence model (*31*). The moment energy of the afterslip was ~40% that of the mainshock. The temporal evolution suggested the continuation of the afterslip to 16 September 2024. The total moment of the 1996 Hyuga-nada earthquake afterslip for 1 month was ~20% that of the mainshock, whereas the total moment until 2004 was ~400% that of the mainshock in 1996 (*25*). The release of up to 40% of the mainshock energy over 1 month was roughly comparable to the 1996 case. Previous studies have shown that the interquartile range of the afterslip-to-coseismic-slip moment ratio varied globally from 9 to 32% (*3*). Therefore, the afterslip in the Hyuga-nada earthquake seems to have released large amounts of energy relative to other cases worldwide.

Implications for seismic hazard assessment

The 2024 Hyuga-nada earthquake provides a typical example of pre-, co-, and postseismic slip cycles, which is rarely documented in other regions of the world because of the low availability of data compared with southwest Japan. The observed pre-, co-, and postseismic interplate slips have important implications for seismic hazard assessments. The three cases in which SSEs preceded the mainshock may reflect a tendency for SSEs to precede mid-to-large interplate earthquakes. Notably, this study confirms the shortening of the recurrence interval of SSEs and possible slip rate decrease in the months (November 2023 to August 2024) before the mainshock, as predicted by several simulation studies [e.g., (*28*, *29*)]. Assuming a high slip rate between May and August 2024, shortly before the mainshock, the shortening of the recurrence time was further accelerated immediately before the earthquake, consistent with the simulation studies based on friction law. Owing to the importance of SSEs in triggering mainshocks (*32*), their monitoring and description can inform the development of improved forecast models of interplate earthquakes in similar contexts. The separation between the 2024 coseismic slip and 1996 source areas suggests three asperities in the Hyuga-nada area that recur alternately (Fig. 5F). This is a crucial factor in earthquake prediction models, which assume that the same asperities are shared between characteristic earthquakes within the same areas. The occurrence of the slip around the hypocentral to downdip extension areas reflects the complicated roles of afterslips and SSEs in the seismic cycle.

The mainshock and its afterslip increased the stress state in neighboring areas, particularly in the 1996 source area (fig. S14). Current evidence suggests the occurrence of a super cycle (*33*) that includes the 1662 Hyuga-nada earthquake (M_w 7.9) (*34*) with a recurrence time of 400 years (*35*). Considering the stress change in the 1996 source area and the time lapse from the 1662 earthquake, the characterization of the 2024 Hyuga-nada earthquake afterslips and SSEs will be indispensable for seismic risk assessment in this region. Because the Hyuga-nada earthquake ruptured the westernmost part of the Nankai Trough, its deformation may contribute to the forthcoming mega-thrust earthquake in this area, highlighting the urgent need for continued monitoring in the Nankai Trough area.

REFERENCES AND NOTES

1. J. C. Savage, *J. Geophys. Res.* **88**, 4984–4996 (1983).
2. J. H. Dieterich, *J. Geophys. Res.* **83**, 3940–3948 (1978).
3. R. M. Churchill, M. J. Werner, J. Biggs, Å. Fagereng, *J. Geophys. Res. Solid Earth* **127**, JB023897 (2022).
4. C. Kreemer, G. Blewitt, E. C. Klein, *Geochem. Geophys. Geosyst.* **15**, 3849–3889 (2014).
5. K. Shiono, T. Mikumo, Y. Ishikawa, *J. Phys. Earth* **28**, 17–43 (1980).
6. Y. Yagi, M. Kikuchi, S. Yoshida, T. Sagiya, *Geophys. Res. Lett.* **26**, 3161–3164 (1999).
7. S. Ozawa, H. Muneakane, H. Suito, *Earth Planets Space* **76**, 23 (2024).
8. A. Nobile *et al.*, *Bull. Volcanol.* **79**, 32 (2017).
9. S. Nakao *et al.*, *Earth Planets Space* **65**, 505–515 (2013).
10. J. J. McGuire, P. Segall, *Geophys. J. Int.* **155**, 778–788 (2003).
11. T. Kobayashi, H. Yarai, S. Kawamoto, Y. Morishita, S. Fujiwara, Y. Hiyama, in *International Symposium on Advancing Geodesy in a Changing World: Proceedings of the IAG Scientific Assembly, Kobe, Japan, July 30–August 4, 2017* (Springer International Publishing, 2019), pp. 193–200.
12. J. J. Lévêque, L. Rivera, G. Wittlinger, *Geophys. J. Int.* **115**, 313–318 (1993).
13. G. Kitagawa, W. Gersch, *Smoothness Priors Analysis of Time Series* (Springer Science & Business Media, 2012).
14. S. Shimmoto, *J. Geophys. Res. Solid Earth* **127**, e2022JB025157 (2022).
15. T. Nishimura, *Prog. Earth Planet. Sci.* **1**, 22 (2014).
16. M. Radiguet *et al.*, *Nat. Geosci.* **9**, 829–833 (2016).
17. S. Ruiz *et al.*, *Geophys. Res. Lett.* **44**, 10290–10297 (2017).
18. S. E. Graham *et al.*, *Geophys. J. Int.* **197**, 1593–1607 (2014).
19. F. Boudin *et al.*, *Geophys. J. Int.* **228**, 2092–2121 (2022).
20. G. C. King, R. S. Stein, J. Lin, *Bull. Seismol. Soc. Am.* **84**, 935–953 (1994).
21. P. Segall, A. M. Rubin, A. M. Bradley, J. R. Rice, *J. Geophys. Res. Solid Earth* **115**, B12305 (2010).
22. P. Segall, A. M. Bradley, *J. Appl. Mech.* **79**, 031013 (2012).
23. F. F. Pollitz, T. Kobayashi, H. Yarai, B. Shibazaki, T. Matsumoto, *Geophys. Res. Lett.* **44**, 8795–8803 (2017).
24. J. I. Fukuda, K. M. Johnson, *Bull. Seismol. Soc. Am.* **98**, 1128–1146 (2008).
25. H. Yarai, S. Ozawa, *J. Geophys. Res. Solid Earth* **118**, 2512–2527 (2013).
26. R. Takagi, N. Uchida, K. Obara, *J. Geophys. Res.* **124**, 3853–3880 (2019).
27. H. Hirose, T. Matsushima, T. Tabei, T. Nishimura, *Earth Planets Space* **75**, 77 (2023).
28. T. Matsuzawa, H. Hirose, B. Shibazaki, K. Obara, *J. Geophys. Res. Solid Earth* **115**, B12301 (2010).
29. Y. Luo, Z. Liu, *Geochem. Geophys. Geosyst.* **20**, 852–871 (2019).
30. L. M. Wallace *et al.*, *Nat. Geosci.* **10**, 765–770 (2017).
31. P. Segall, A. M. Bradley, *Geophys. Res. Lett.* **39**, L18308 (2012).
32. P. Danré, L. De Barros, F. Cappa, J. P. Ampuero, *J. Geophys. Res. Solid Earth* **127**, e2022JB025571 (2022).
33. T. Kobayashi, H. Munekane, M. Kuwahara, H. Furui, *Geophys. J. Int.* **236**, 1068–1088 (2024).
34. K. Ioki, Y. Yamashita, Y. Kase, *Pure Appl. Geophys.* **180**, 1897–1907 (2023).
35. Y. Yamashita, T. Hori, Characteristics of seismicity around the August 8, 2024 Hyuga-nada earthquake (M7.1) and possible future scenarios (in Japanese). In *Annual Meeting of Japan Seismological Society, Niigata, Japan* (2024).
36. P. Wessel, W. H. F. Smith, *Eos* **79**, 579–579 (1998).
37. S. Ozawa, Network Inversion Filter with Mogi source and without random walk of station, Zenodo (2025); https://doi.org/10.5281/zenodo.14927544.

ACKNOWLEDGMENTS

Hypocentral data for low-frequency earthquakes were obtained from the Japan Meteorological Agency. The code for Green's function was obtained from Y. Aoki of the Earthquake Research Institute of Japan. **Funding:** Geospatial Information Authority of Japan. **Author contributions:** Conceptualization: S.O., H.M.. Methodology: S.O. Investigation: S.O., H.M., H.S., H.Y. Visualization: S.O. Funding acquisition: H.Y. Project administration: H.Y. Supervision: H.Y. Writing – original draft: S.O., H.M. Writing – review & editing: S.O., H.M. **Competing interests:** The authors declare that they have no competing interests. **Data and materials availability:** We used GEONET F5 solutions, available on the Geospatial Information Authority of Japan website (https://terras.gsi.go.jp). The F5 data are readily available at https://terras.gsi.go.jp with a manual on how to access the data. Graphs were created using the GMT software package (*36*). The network inversion filter program used in this study is available at the Zenodo Open Access Repository (*37*). Because certain source codes contain routines from a proprietary library, only binary programs are available.

SUPPLEMENTARY MATERIALS

science.org/doi/10.1126/science.adu7076
Materials and Methods; Figs. S1 to S36; References (*38*–*50*)

Submitted 18 November 2024; accepted 1 May 2025

10.1126/science.adu7076

PALEONTOLOGY

Origin and radiation of squids revealed by digital fossil-mining

Shin Ikegami[1]†, Yusuke Takeda[2]†, Jörg Mutterlose[3], Yasuhiro Iba[1]*†

The evolution of soft-bodied squids, which provide a major part of the biomass in modern oceans globally, is poorly understood owing to their patchy fossil record. We provide a comprehensive evolutionary history of squids through "digital fossil-mining" techniques, revealing a new lagerstätte. The more than 250 fossil beaks of 40 species show that squids originated and rapidly radiated by 100 million years ago. Our data suggest that the radical shift from heavily shelled, slowly moving cephalopods to soft-bodied forms did not result from the end-Cretaceous mass extinction (66 million years ago). Early squids had already formed large populations, and their biomass exceeded that of ammonites and fishes. They pioneered the modern-type marine ecosystem as intelligent, fast swimmers.

Squids (orders Oegopsida and Myopsida) are the most diverse and globally distributed group of cephalopods in modern oceans (*1*–*3*). They are exceptional invertebrates with lens eyes, flexible arms, and a large brain (*4*–*6*), giving them a sophisticated cognition and mobility comparable to that of vertebrates (*6*–*8*). They are adept predators, competing with fishes while being essential prey for whales and sharks (*8*–*10*). These characteristics make squids a principal component of the marine ecosystem.

The origin of squids is marked by the reduction of the large, mineralized shell that was initially a key trait of cephalopods (*11*–*13*). The shell demineralization is the greatest innovation in the 500-million-year (Myr) history of cephalopods. It initially arose in the stem group of octopuses and later, probably independently, occurred in both the Oegopsida and Myopsida (*11*–*13*). Squids benefited from this evolution by becoming faster swimmers coupled with acquiring improved cognitive abilities (*11*, *13*). Modern squids are well studied (*2*), but little is known about their origin and evolution because soft-bodied organisms are rarely fossilized (*11*, *14*). Very few squid fossils have been reported, almost all of which are from the middle Eocene [~45 million years ago (Ma)] onward (*15*). Most of these fossils are statoliths, which are small calcareous particles supporting the sense of balance (*15*, *16*). Previous studies thus speculated that squids only radiated after the Cretaceous-Paleogene (K-Pg) mass extinction (~66 Ma), in which shelled cephalopods such as ammonites perished (*2*). In other approaches, molecular phylogenetics have yielded estimates of speciation ages from extant squids (*6*, *17*–*19*), but the lack of fossils prevented a precise understanding of their early evolution. Because of this shortcoming in the fossil record, these studies are subject to large errors in the estimation of absolute ages (~50 Myr of confidence intervals) and the variability in the topology of their phylogenetic trees (*17*, *18*).

Beaks: The key to squid evolution

Mesozoic fossils of squids are absent even in fossil lagerstätten, owing to the poor preservational potential of their soft-tissue bodies (*20*). Although fossil statoliths of non-squid cephalopods have been recorded from the Jurassic (~150 Ma), those of squids are not conserved in Mesozoic sediments for unknown reasons (*15*, *21*). To overcome the limitations of the record of fossil squids, we focused on their beaks. All cephalopods have an upper and lower beak, a distinctive hard tissue composed of chitin-protein complexes (fig. S1) (*22*). The morphology of cephalopod lower beaks is constrained by phylogenetic relationships rather than by their feeding habits (*23*–*25*). The lower-beak morphology of squids varies on the species level (*25*–*28*). Squid beaks also offer precise insights into body length on the basis of their size and growth stage through pigmentation patterns (*27*, *29*). These characteristics apply to fossil beaks, particularly in which their three-dimensional (3D) morphology is retained (*26*). Carbonate concretions are likely the best source for 3D preserved beaks (*30*). Fossil squid beaks are, however, difficult to discover and extract from hard rocks because of their fragility and morphological complexity. Therefore, only one fossil beak has been described for squids (*30*, *31*) (supplementary text). Conventional fossil extraction techniques, including physical preparation and chemical dissolution, have not solved this problem (Fig. 1).

In this study, we developed "digital fossil-mining," a new approach that replaces conventional techniques, allowing mass and flawless extraction of fossils (Fig. 1). Our method converts whole rocks into full-color digital volume data and allows us to discover all hidden fossils as 3D models. This breakthrough was enabled by a fully automated grinding tomography system with the highest resolution ever obtained and high-performance image processing that uses red, green, and blue (RGB) data (*32*). Digitally, we collected fossil squid beaks from carbonate concretions of Cretaceous shelf deposits in Japan (from an interval of 110 to 70 Ma; see table S1).

Discovery of numerous fossil squids

A total of 263 squid lower beaks, documenting micrometer-scale structures and pigmentation patterns, are described in this study (Fig. 2). We obtained 1000 cephalopod beaks, consisting of 671 coleoids (a cephalopod group without an external shell), 326 ammonites, and three nautiloids (table S2). The coleoid beaks include 322 upper and 349 lower beaks, indicating the absence of a fossilization bias among them. To avoid duplicate counts of paired beaks, subsequent examinations were conducted only for the lower beaks. These lower beaks were assigned to 263 squids, 48 vampyromorphs, 12 octopuses, and 26 taxonomically indeterminate non-squid coleoids. Beaks of cuttlefish, spirulids, and belemnites were not encountered (table S2).

The numerous fossil squids that we discovered represent 40 species, 23 genera, and 5 families (Fig. 3A; taxonomic descriptions, the taxonomic key, and the evaluation of morphological disparity are provided in the supplementary materials). All species were assigned to the Oegopsida or Myopsida. The lengths of fossil squid beaks discovered here range from 1.23 to 19.32 mm (table S3). The average is 3.87 mm, about 6% of the size of the only known fossil squid beak, which belongs to *Haboroteuthis poseidon* (*30*). The minimum thickness of these fossil beaks was always <10 μm. These results show that numerous squid beaks are hidden as millimeter-scaled microfossils and explain why they have been overlooked in previous studies. Our digital approach transfers the carbonate concretions into a "fossil lagerstätte of squids" (Fig. 1).

Squids originated 100 million years ago

Our findings document that squids originated near the Early-Late Cretaceous (100 Ma) boundary, followed by rapid diversification (Fig. 3B). Throughout the Late Cretaceous, squid diversity was maintained at a high level (Fig. 3B). The oldest squids reported here include both Oegopsida and Myopsida (Fig. 3A). The oldest record thus far of the Oegopsida is from the middle Late Cretaceous (~85 Ma) (*30*), and that of Myopsida is from the middle Eocene (~45 Ma) (*15*). This study thus extends the fossil record of both orders by ~15 Myr and ~55 Myr, respectively. Five out of the six oldest oegopsid species all have characters rarely seen in stratigraphically younger specimens, such as a

[1]Department of Earth and Planetary Sciences, Hokkaido University, Sapporo, Japan. [2]Spectroscopy and Imaging Division, Japan Synchrotron Radiation Research Institute, Sayo, Japan. [3]Institute of Geology, Mineralogy and Geophysics, Ruhr University Bochum, Bochum, Germany. ***Corresponding author. Email: iba@sci.hokudai.ac.jp** †These authors contributed equally to this work.

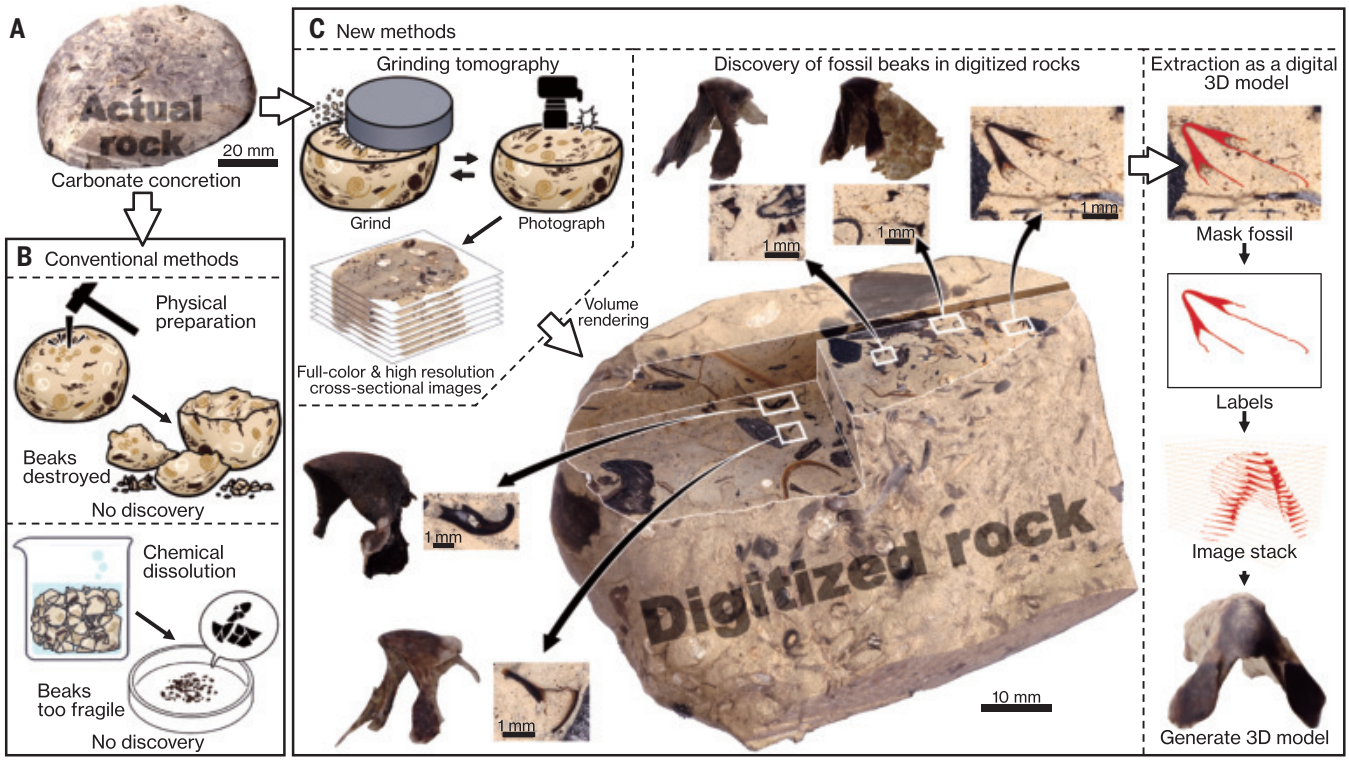

Fig. 1. Digital fossil-mining of squid beaks. (**A**) A studied carbonate concretion (sample no. 6). (**B**) Conventional fossil-extraction techniques, physical preparation, and chemical dissolution. Thin, tiny, and complex fossil beaks cannot be discovered or extracted. (**C**) Digital fossil-mining applied in this study. (Top left) Concretions are converted into full-color digital volume data by automated grinding tomography. (Middle) Beak fossils are discovered in the digitized concretions that can be freely sliced and magnified. (Right) Discovered fossils are completely separated from host rocks as label data and extracted as a 3D model.

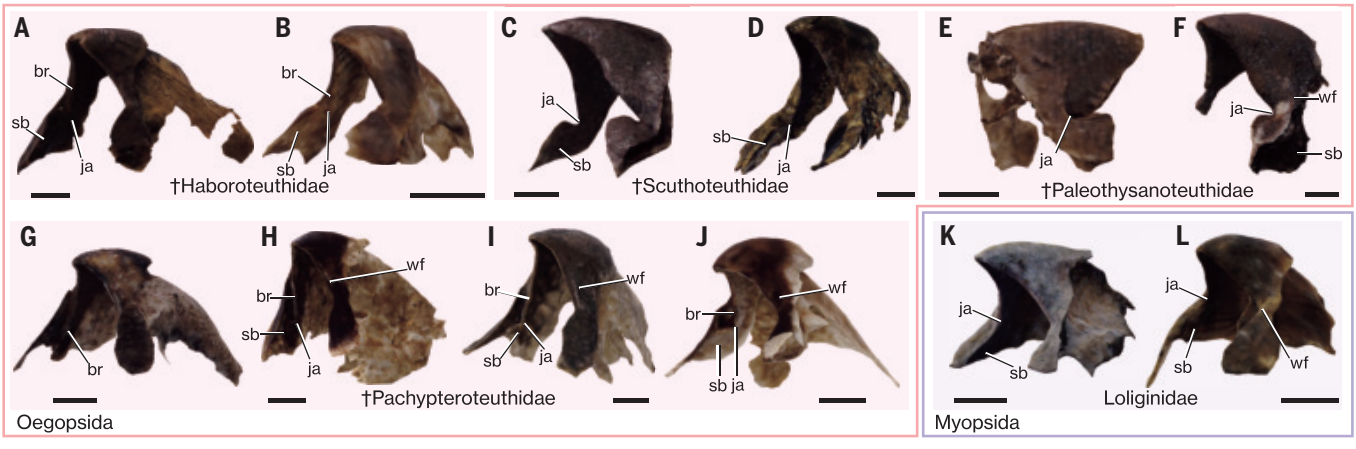

Fig. 2. Fossil lower beaks of squids from the Late Cretaceous (~100 to 70 Ma). (**A**) *Pachygephyra callisto.* (**B**) *Hoplitopteryx solida.* (**C**) *Scuthoteuthis kawataro.* (**D**) *Grossiscapula angusta.* (**E**) *Paleothysanoteuthis complicatus.* (**F**) *Aetorhynchus incisus.* (**G**) *Pachypteroteuthis adiacens*. (**H**) *Gerontoteuthis acutissimus*. (**I**) *Thalassasboides watatsumi*. (**J**) *Sepultipons castor*. (**K**) *Psiloteuthis naucrates*. (**L**) *Streptopteryx bidentata*. All taxonomic orders and families discussed in this study are shown here. Important diagnostic characters are indicated for each model: br, bridge; ja, jaw angle; sb, shoulder blade; wf, wing fold. All scale bars, 1 mm. See table S3 for fossil accession numbers.

small rostrum and indistinct shoulder blades (supplementary materials). Within 6 Myr after the origination of these six species, which include two families, all other fossil families appeared. These findings suggest a fast morphological evolution of the early Oegopsida. All myopsid species encountered here can be included in one extant family, showing the early origin of true modern forms. Our results reveal that Oegopsida and Myopsida emerged earlier than all other living orders of 10-armed cephalopods, such as Sepiida (cuttlefish) (*11*, *33*).

The rise of squids uncovered here is synchronous with a regional extinction of belemnites—a Mesozoic, internally shelled group of cephalopods occupying the same niche—across many oceanic regions (e.g., Tethys and North Pacific; Fig. 3) (*21*, *34*, *35*). These opposing trends indicate that the turnover in cephalopods from heavily shelled to soft-bodied forms is not the consequence of the K-Pg mass extinction (66 Ma). Squids outcompeted shelled forms at least in the North Pacific—the largest ocean in the Cretaceous—and survived this extinction.

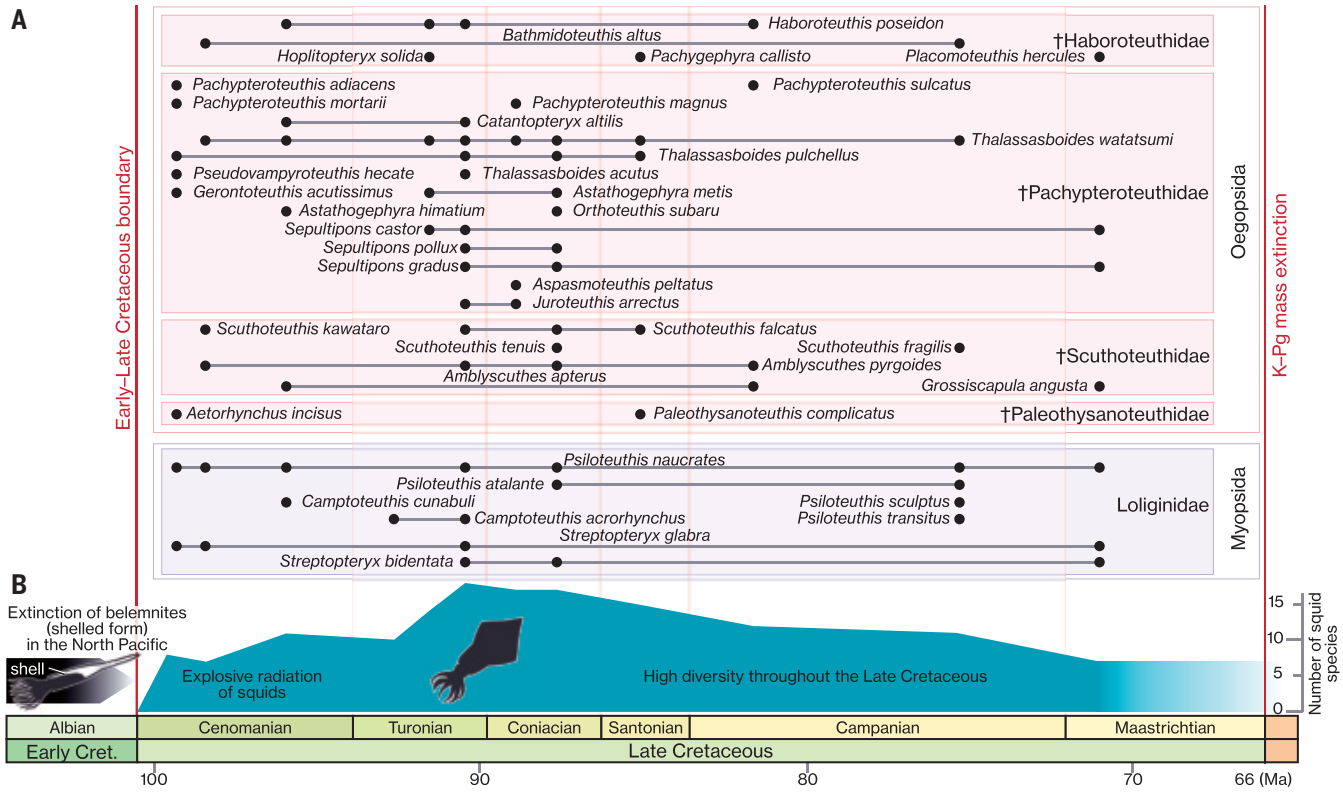

Fig. 3. Stratigraphic distribution and diversity pattern of early squids. (**A**) Stratigraphic distribution of the fossil squid species, based on our findings. Occurrences of fossils are indicated as dots. The stratigraphic ranges are shown with horizontal lines. (**B**) Species diversity curve is compiled from (A).

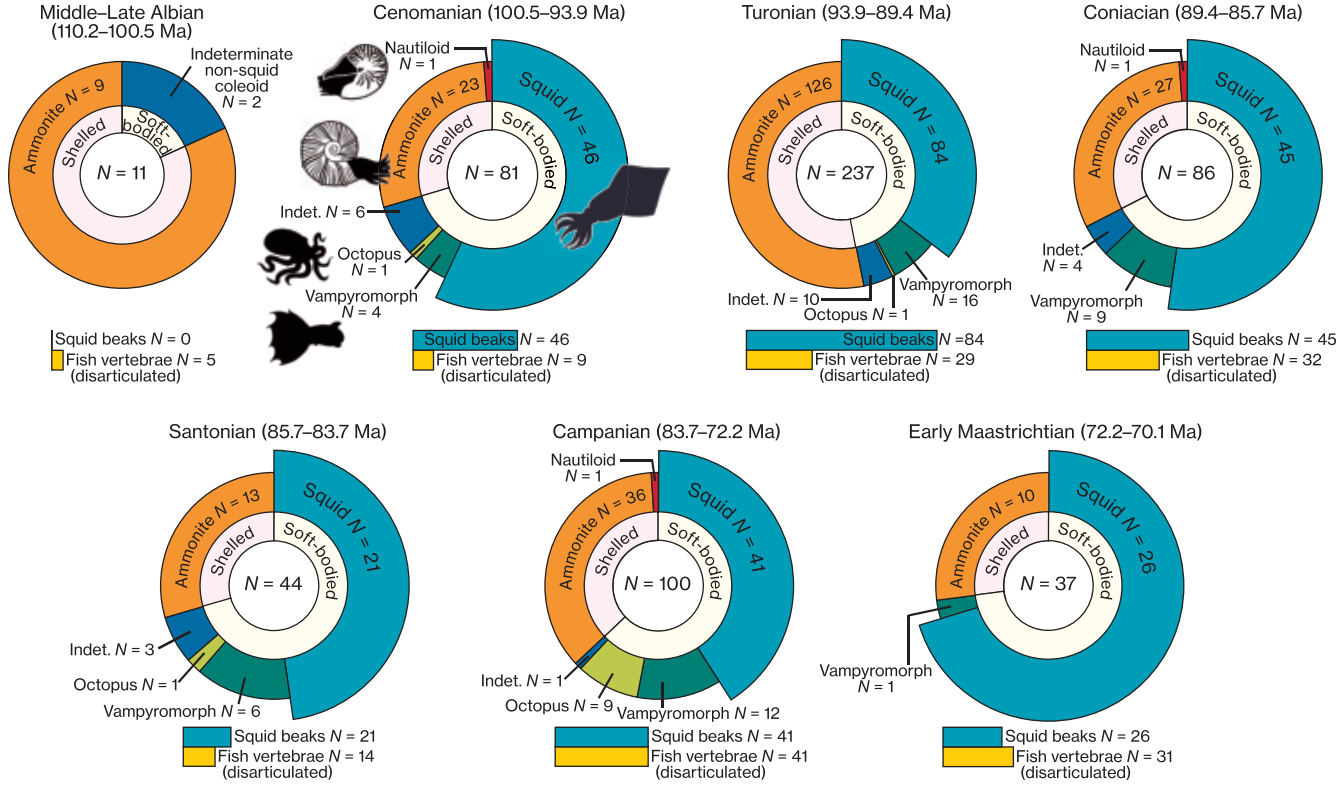

Fig. 4. Relative abundance of squids throughout the Albian-Maastrichtian. Pie charts show the abundance of squids, vampyromorphs, octopuses, indeterminate non-squid coleoids, ammonites, and nautiloids. In the center of the pie charts, *N* indicates the total number of lower beaks observed. The two horizontal bars beneath the charts show the numbers of squid beaks (blue) and bony fish vertebrae (yellow), respectively. These pie charts and bars include all specimens discovered in this study (table S2).

The Cretaceous squid ocean

Our data suggest that the abundance of Late Cretaceous squids exceeded that of cooccurring ammonites and bony fishes (Fig. 4 and table S2). Because the carbonate concretions formed in a few weeks (*36*), the faunal composition can be examined even on the basis of the fragile beaks that would have been decomposed quickly. The chemical composition of beaks makes a strong taphonomic bias unlikely and thus enables reliable population analyses of cephalopods with and without shells. Late Cretaceous sediments of Japan yield abundant ammonites (*37*), as seen in the studied concretions (*38*). Notably, the number of squids discovered here is 1.1 to 2.6 times higher than that of ammonites. It is only in the Turonian that squids came second to ammonites, but they still formed a major component of the cephalopod assemblage. We also obtained 161 disarticulated vertebrae of bony fishes from the same concretions (table S2). These data indicate that squids were much more common than bony fishes (Fig. 4), because individuals of the latter group are known to have more than 16 vertebrae each (*39*). Fish vertebrae are thicker and have a more robust structure than beaks, so they would be expected to fossilize at higher rates. Ammonites are known as extremely successful Mesozoic cephalopods, and bony fishes were most likely leading competitors of squids in the Cretaceous (*8*, *40*).

Further comparisons of the estimated body sizes, based on material from the same concretions, suggest that many of the squids were larger than ammonites, having the same size as some large bony fishes. Squids have long arms, a head, and a mantle; the beak is small with respect to the entire body (*8*, *27*). Extant squids that reach 100 mm in total body lengths have beaks that are only 2 to 4 mm long (*27*). The beak sizes observed in the fossil material suggest an average mantle size of 70.33 to 90.99 mm for the Oegopsida and of 50.29 to 157.92 mm for the Myopsida (tables S4 to S6) (*32*). These sizes are similar to those of typical modern squids (e.g., California market squid) (*41*).

Large-sized ammonites are known from the studied sections, but they are quantitatively a minor component. Only 18 out of more than 1000 ammonite shells encountered in the examined concretions were larger than 50 mm. This result implies that squids were larger than ammonites, because the mantle of the latter lies inside their shell (*22*). The average body length of cooccurring bony fishes, estimated from the size of vertebrae (*32*), ranges from 122.06 to 238.93 mm (tables S7 and S8). Considering that the estimates for the size of squids do not include the length of their head and the long arms, Cretaceous squids were probably as large as bony fishes. The estimated body sizes, along with relative abundance, indicate that Late Cretaceous squids provided a larger biomass than any other coexisting nektonic organism.

The origin of squids would have imposed crucial effects on the evolution of the marine ecosystem. The present marine food web is characterized by intelligent, fast swimmers and dominated by bony fishes, marine mammals, and squids (*42*, *43*). The radiation of bony fishes and marine mammals is well known to have occurred after the K-Pg mass extinction (*44*, *45*). Our study reveals that squids prospered more than 30 Myr earlier than these marine vertebrates, shaping the modern-type ecosystem as pioneers of intelligent, fast swimmers.

REFERENCES AND NOTES

1. D. P. Tittensor *et al.*, *Nature* **466**, 1098–1101 (2010).
2. P. Boyle, P. Rodhouse, Eds. *Cephalopods: Ecology and Fisheries* (Blackwell Science, 2005).
3. K. N. Nesis, *Berl. Paläobiol. Abh* **3**, 199–224 (2003).
4. J. Cai, J. P. Townsend, T. C. Dodson, P. A. Heiney, A. M. Sweeney, *Science* **357**, 564–569 (2017).
5. W. M. Kier, F. H. Schachat, *J. Exp. Biol.* **211**, 164–169 (2008).
6. C. B. Albertin *et al.*, *Nat. Commun.* **13**, 2427 (2022).
7. P. Amodio *et al.*, *Trends Ecol. Evol.* **34**, 45–56 (2019).
8. A. Packard, *Biol. Rev. Camb. Philos. Soc.* **47**, 241–307 (1972).
9. F. Visser *et al.*, *Sci. Adv.* **7**, eabf5908 (2021).
10. S. Dedman *et al.*, *Science* **385**, adl2362 (2024).
11. B. Kröger, J. Vinther, D. Fuchs, *BioEssays* **33**, 602–613 (2011).
12. D. Fuchs, Y. Iba, *Swiss J. Palaeontol.* **134**, 187–197 (2015).
13. D. Fuchs, Y. Iba, H. Tischlinger, H. Keupp, C. Klug, *Lethaia* **49**, 433–454 (2016).
14. D. M. Raup, J. J. Sepkoski Jr., *Science* **215**, 1501–1503 (1982).
15. P. Neige, H. Lapierre, D. Merle, *PLOS ONE* **11**, e0154062 (2016).
16. M. R. Clarke, J. E. Fitch, *Nature* **257**, 380–381 (1975).
17. A. R. Tanner *et al.*, *Proc. Biol. Sci.* **284**, 20162818 (2017).
18. J. E. Uribe, R. Zardoya, *J. Molluscan Stud.* **83**, 133–144 (2017).
19. D. A. López-Córdova *et al.*, *Mol. Phylogenet. Evol.* **166**, 107331 (2022).
20. T. Clements, C. Colleary, K. De Baets, J. Vinther, *Palaeontology* **60**, 1–14 (2017).
21. C. Klug, G. Schweigert, D. Fuchs, I. Kruta, H. Tischlinger, *Biol. Lett.* **12**, 20150877 (2016).
22. C. Klug, D. Korn, K. De Baets, I. Kruta, R. H. Mapes, Eds., *Ammonoid Paleobiology: From Anatomy to Ecology*, vol. 43 of *Topics in Geobiology* (Springer, 2015).
23. M. R. Clarke, L. Maddock, in *Paleontology and Neontology of Cephalopods*, M. R. Clarke, E. R. Trueman, Eds. (Academic Press, 1988), pp. 123–131.
24. J. C. Xavier *et al.*, *Front. Physiol.* **13**, 1038064 (2022).
25. A. Sánchez-Márquez *et al.*, *Rev. Fish Biol. Fisheries* **33**, 221–239 (2023).
26. M. R. Clarke, *Nature* **193**, 560–561 (1962).
27. M. R. Clarke, *A Handbook for the Identification of Cephalopod Beaks* (Clarendon Press, 1986).
28. H. Y. Tan *et al.*, *PeerJ* **9**, e11825 (2021).
29. V. Hernández-García, *Berl. Paläobiol. Abh.* **3**, 131–140 (2003).
30. K. Tanabe, A. Misaki, T. Ubukata, *Acta Palaeontol. Pol.* **60**, 27–38 (2015).
31. K. Tanabe, A. Misaki, *Cretac. Res.* **151**, 105624 (2023).
32. Materials and methods are available as supplementary materials.
33. D. Fuchs *et al.*, *Palaeontology* **56**, 1081–1106 (2013).
34. P. Doyle, *Palaeogeogr. Palaeoclimatol. Palaeoecol.* **92**, 207–216 (1992).
35. Y. Iba *et al.*, *Geology* **39**, 483–486 (2011).
36. H. Yoshida *et al.*, *Sci. Rep.* **5**, 14123 (2015).
37. R. Takashima *et al.*, *Cretac. Res.* **25**, 365–390 (2004).
38. Y. Iba, S. Ikegami, Y. Takeda, J. Mutterlose, Animations of cross-sectional images of Cretaceous carbonate concretions from the Yezo Group, Japan, version 1, Figshare+ (2025); https://doi.org/10.25452/figshare.plus.25735515.
39. J. S. Nelson, T. C. Grande, M. V. H. Wilson, *Fishes of the World* (Wiley, 2016).
40. K. Tanabe, *Science* **331**, 37–38 (2011).
41. A. I. Arkhipkin *et al.*, *Rev. Fish. Sci. Aquacult.* **23**, 92–252 (2015).
42. G. Roth, *Philos. Trans. R. Soc. London Ser. B* **370**, 20150049 (2015).
43. I. A. Hatton, R. F. Heneghan, Y. M. Bar-On, E. D. Galbraith, *Sci. Adv.* **7**, eabh3732 (2021).
44. F. G. Marx, M. D. Uhen, *Science* **327**, 993–996 (2010).
45. M. E. Alfaro *et al.*, *Nat. Ecol. Evol.* **2**, 688–696 (2018).
46. S. Ikegami, Y. Takeda, J. Mutterlose, Y. Iba, Fossil lower beaks of Cretaceous squids, version 1, Figshare+ (2025); https://doi.org/10.25452/figshare.plus.25736631.
47. S. Ikegami, Y. Takeda, J. Mutterlose, Y. Iba, Morphological disparity analyses of Cretaceous squid species, version 1, Figshare+ (2025); https://doi.org/10.25452/figshare.plus.28377848.

ACKNOWLEDGMENTS

We thank A. J. Hetherington, S. Sano, K. Kubo, R. Taniguchi, and Y. Kashiyama for comments on the manuscript; S. Sasaki, K. Sugiura, A. Kubota, H. Nishida, T. Ishii, T. Tajima, T. Kawase, A. Shikakura, T. Ohno, N. Tsuchiya, T. Ishimura, T. Kaneko, Y. Ito, and M. Takei for assistance in developing the digital fossil-mining system; M. Manabe, C. Sakata, E. Kosugi, H. Ito, A. Koshimizu, and R. Nozaki for assisting in archiving data; and A. Misaki and Y. Hikida for access to the previously described specimens. We dedicate this paper to K. Tanabe. **Funding:** This work was supported by Japan Society for the Promotion of Science grant 22J13936 (S.I.), Japan Society for the Promotion of Science grant 23K17274 (Y.T.), Japan Society for the Promotion of Science grant 19H02010 (Y.I.), Japan Society for the Promotion of Science grant 23H02544 (Y.I.), Japan Aerospace Exploration Agency grant JX-PSPC-540452 (Y.I.), and the Canon Foundation 2019 (Y.I.). **Author contributions:** Conceptualization: Y.I.; Data curation: S.I., Y.T., Y.I.; Funding acquisition: S.I., Y.T., Y.I.; Investigation: S.I., Y.I.; Methodology: S.I., Y.T., Y.I.; Project administration: S.I., Y.I.; Resources: S.I., Y.T., Y.I.; Supervision: Y.I.; Validation: Y.T., J.M., Y.I.; Visualization: S.I., Y.T.; Writing – original draft: S.I., Y.T., J.M., Y.I.; Writing – review & editing: S.I., Y.T., J.M., Y.I. **Competing interests:** The authors declare that they have no competing interests. **Data and materials availability:** The original tomographic images of carbonate concretions are archived in the National Museum of Nature and Science, Tokyo. The collection number of those images is listed in table S1. The animations of these tomographic images are available from Figshare+ (*38*). The 3D models, the label data, and the cropped cross-sectional images of the discovered squid beaks are available from Figshare+ (*46*). The character matrices and R codes used for morphological disparity analyses are available from Figshare+ (*47*). All other data supporting the findings of this study are available in this paper and in the supplementary materials. All nomenclatural acts in this study are registered in ZooBank, and the Life Science Identifier for this publication is urn:lsid:zoobank.org:pub:911EDBD4-283A-4258-92CA-3AD77EC38810.

SUPPLEMENTARY MATERIALS

science.org/doi/10.1126/science.adu6248
Materials and Methods; Supplementary Text; Figs. S1 to S12; Tables S1 to S8; References (*48*–*72*); MDAR Reproducibility Checklist

Submitted 15 November 2024; accepted 5 May 2025

10.1126/science.adu6248

DRUG DELIVERY

Bespoke plant glycoconjugates for gut microbiota–mediated drug targeting

Wei Jen Ma[1]†, Changqing Wang[2]†, Jagatheeswaran Kothandapani[2], Matthew Luzentales-Simpson[1], Susan C. Menzies[1], Danisa M. Bescucci[3], Máximo E. Lange[3], Alexander S. C. Fraser[2], Jenny F. Gusse[3]‡, Kathaleen E. House[3], Paul E. Moote[3], Xiaohui Xing[3], Julie M. Grondin[2], Benjamin Wei-Qiang Hui[2], Sandra T. Clarke[3], Tara G. Shelton[3], Natasha Haskey[4], Deanna L. Gibson[4], Eric C. Martens[5], D. Wade Abbott[3], G. Douglas Inglis[3]‡, Laura M. Sly[1]*, Harry Brumer[2]*

The gut microbiota of mammals possess distinctive metabolic pathways with untapped therapeutic potential. Using molecular insights into dietary fiber metabolism by the human gut microbiota, we designed a targeted drug delivery system, called GlycoCaging, that is based on bespoke glycoconjugates of a complex plant oligosaccharide. GlycoCaging of exemplar anti-inflammatory drugs enabled release of active molecules triggered by specific glycosidases of autochthonous gut bacteria. GlycoCaging ensured that drug efficacy was potentiated, and off-target effects were eliminated in murine models of inflammatory bowel disease. Biochemical and metagenomic analyses of gut microbiota of individual humans confirmed the broad applicability of this strategy.

Recent functional studies of the human gut microbiota have revealed specific, multiprotein systems that enable the breakdown and metabolism of individual complex glycans that make up dietary fiber (*1*, *2*). For example, xyloglucans (XyGs; Fig. 1) constitute a family of highly branched polysaccharides in the cell walls of fruits and vegetables that are abundant in the human diet (*3*). Several autochthonous colonic *Bacteroides* species produce suites of specific glycosidases and accessory proteins for XyG metabolism (Fig. 1A), which are encoded by multigene xyloglucan utilization loci (XyGULs; Fig. 1B) (*4*–*6*). Dietary selection pressure ensures that XyGULs are ubiquitous in human microbiomes (*4*). Human genomes do not encode XyG-degrading enzymes (or other dietary fiber–degrading enzymes), so humans are entirely dependent on our microbiota for this critical aspect of nutrition (*2*, *7*). In this work, we show that XyG metabolism offers potential for the treatment of gastrointestinal (GI) diseases.

Targeted delivery of orally administered pharmaceuticals to the distal GI tract remains a long-standing, unresolved challenge in human health (*8*–*10*). Building on our knowledge of microbiota enzyme specificity (*1*, *2*, *4*–*6*), we hypothesized that covalent conjugation of small-molecule drugs to a singular XyG heptasaccharide via a glycosidic linkage (Fig. 1C) could make a molecular platform for GI targeting, in a strategy we call GlycoCaging (fig. S1). The hydrophilic, branched oligosaccharide should prevent premature absorption in the upper GI tract yet enable targeted release in situ by specific xyloglucanases of the colonic microbiota, resulting in amelioration of disease. Here, we combined synthetic glycochemistry with efficacy studies in two preclinical models of inflammatory bowel disease (IBD) (*11*–*13*). The data show that GlycoCaging reduces both drug dose and its systemic uptake and has the potential to improve established and emerging GI drugs.

Facile chemical syntheses of glycoconjugate prodrugs

Aminosalicylates and corticosteroids (Fig. 1D) are commonly prescribed to treat GI inflammation but often have restrictive therapeutic indices [(*13*) and references therein]. Leveraging our experience in XyG chemistry (*14*, *15*), we developed efficient synthesis routes to produce 21-*O*-steroid (fig. S2) and 2-*O*-5-aminosalicylate (fig. S3) β-glycosides of the heptasaccharide XXXG [Xyl_3Glc_4; Fig. 1D; see (*3*) for a description of the standard XyG shorthand nomenclature].

A key enabling feature of the syntheses was the highly scalable access to the heptasaccharide building block by controlled hydrolysis of bulk tamarind seed XyG with an *endo*-xyloglucanase and a β-galactosidase (*16*). Subsequent per-O-acetylation, anomeric activation, glycosylation, and final deprotection gave XXXG-dexamethasone (XXXG-Dex, compound **5**), XXXG-budesonide (XXXG-Bude, compound **9**), and XXXG-prednisolone (XXXG-Pred, compound **7**) in good yields over six chemical steps (fig. S2). Initial attempts using classic Königs-Knorr glycosylation of steroids with per-O-acetylated XXXG-α-Br [compound **1**; (*14*, *15*)] resulted in poor yields (<10% in the case of dexamethasone), necessitating conversion into the trichloroacetimidate (*17*) donor (compound **3**). By contrast, good yield of the XXXG β-glycoside of 5-aminosalicylate (XXXG-5-ASA, compound **13**) was obtained in four chemical steps from the α-bromide (compound **1**; fig. S3).

Enzymatic release of GlycoCaged drugs in vitro

It was essential to demonstrate that the drug payloads could be released from the glycoconjugates upon contact with specific enzymes produced by gut microbiota. XyGULs of human gut *Bacteroides* spp. invariably encode an *endo*-xyloglucanase from glycoside hydrolase family 5, subfamily 4 (GH5_4), which initiates polysaccharide backbone hydrolysis at the cell surface (Fig. 1, B and C). *Bo*GH5_4, BuGH5_4A, and BuGH5_4B from *Bacteroides ovatus* and *Bacteroides uniformis* are the most widespread *endo*-xyloglucanases in human gut metagenomes (*4*–*6*). All three XXXG-steroids were substrates for recombinant forms of these enzymes in vitro, with comparable concentration-dependent hydrolysis kinetics (Fig. 1F and table S1). These results recall previous observations that *endo*-xyloglucanases are generally able to cleave XyGOs with noncarbohydrate leaving groups (aglycons), for example, aryl β-glycosides, as substrate analogs (*4*, *14*, *15*).

Among the corticosteroids, dexamethasone is potently anti-inflammatory, yet side effects hinder its use in GI treatment (*18*, *19*). Hence, we selected XXXG-Dex as a prototype to demonstrate the ability of GlycoCaging to improve targeting, as well as highlight its potential to enable drug repurposing. Initially, we extended our enzyme-release experiments to live *B.* cells in liquid medium in vitro, using XyG to induce *Bo*GH5_4 *endo*-xyloglucanase production at the bacterial cell surface (*2*, *4*) (fig. S4). We tested XyG concentrations in the range of 0.1 to 2 g/liter and showed that all concentrations were sufficient to enable XXXG-Dex hydrolysis. Using the highest concentration of 5-g/liter XyG (aqueous stock solutions become highly viscous at concentrations >10 g/liter), we observed a time-dependent release of dexamethasone over several hours. This result is particularly notable in showing that the natural substrate did not outcompete the drug glycoconjugate as a substrate for the *endo*-xyloglucanase at the bacterial cell surface. Thus, the observed hydrolysis of XXXG-Dex in this in vitro system, which mimics the presence of XyG in plant cell wall digesta in the GI tract, anticipated successful release in vivo.

[1]Department of Pediatrics and BC Children's Hospital, University of British Columbia, Vancouver, BC, Canada. [2]Michael Smith Laboratories and Department of Chemistry, University of British Columbia, Vancouver, BC, Canada. [3]Lethbridge Research and Development Centre, Agriculture and Agri-Food Canada, Lethbridge, AB, Canada. [4]Department of Biology, University of British Columbia–Okanagan Campus, Kelowna, BC, Canada. [5]Department of Microbiology and Immunology, University of Michigan, Ann Arbor, MI, USA. ***Corresponding author. Email: laura.sly@ubc.ca (L.M.S.); brumer@msl.ubc.ca (H.B.)** †These authors contributed equally to this work. ‡Deceased.

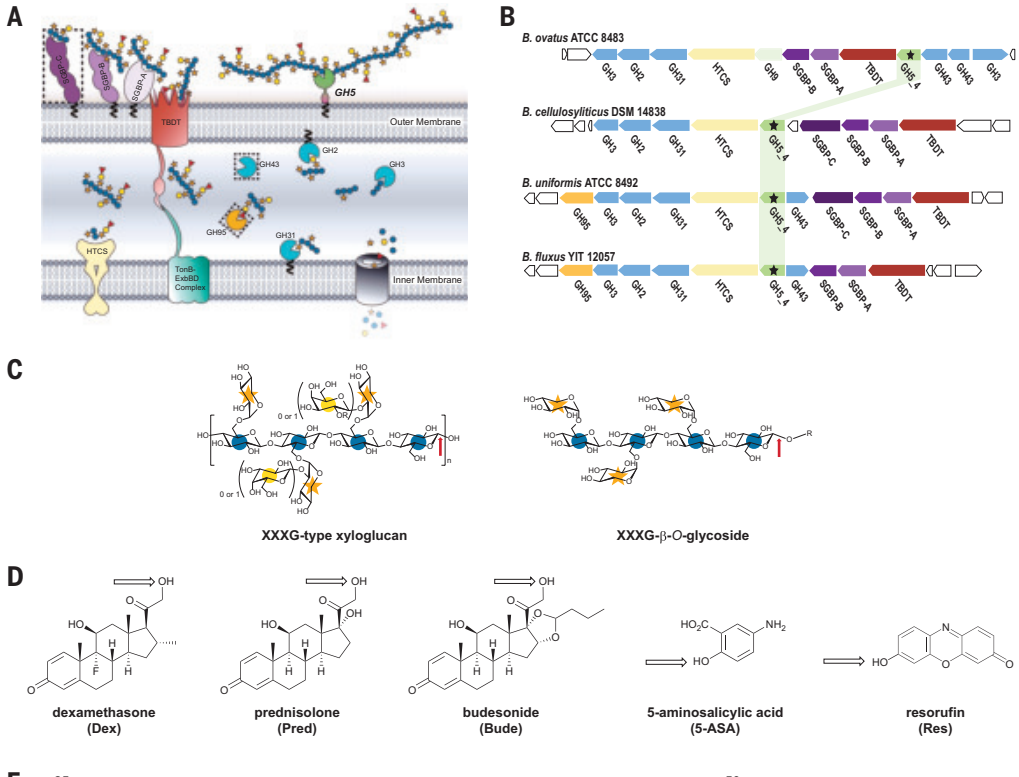

Fig. 1. Harnessing XyG utilization systems of human gut *Bacteroides* for targeted drug delivery. (**A**) XyG utilization systems in the cell envelope of autochthonous human gut *Bacteroidota* (syn. *Bacteroidetes*). Monosaccharides are indicated by the Consortium for Functional Glycomics symbol representation: blue circle, β(1,4)-D-glucopyranose; orange star, α(1-2)-D-xylopyranose; yellow circle, β(1,2)-D-galactopyranose; and red triangle α(1,2)-L-fucopyranose. Proteins are indicated as follows: GH, glycoside hydrolase, including CAZy family number; SGBP, cell-surface glycan-binding protein (SGBP-A is a SusD homolog) and TBDT (SusC homolog); and HTCS, hybrid two-component system sensor/regulator. Variable proteins are indicated in dotted boxes. (**B**) Representative, biochemically validated XyGULs (*4*–*6*). Black stars indicate conserved GH5_4 XyG-specific *endo*-glucanase (*endo*-xyloglucanase). For clarity, a second nonsyntenic *B. uniformis* XyGUL, herein "XyGUL2" is not shown; for structure, see (*6*). [Credit: (A) and (B) are adapted from (*5*)] (**C**) Chemical structure of XXXG-type XyG (general dicot XyG, R = fucose; and tamarind seed XyG, R = H) and the corresponding XyG heptasaccharide β-*O*-glycoside [XXXG denotes the Xyl_3Glc_4 heptasaccharide repeating unit in the standard shorthand nomenclature (*4*,*5*,*15*)]. Red arrows indicate bonds cleaved by canonical *endo*-xyloglucanases. (**D**) Common anti-inflammatory compounds amenable to GlycoCaging via O-glycosylation with XXXG. The resorufin β-*O*-glycoside of XXXG serves as a fluorogenic prodrug proxy for enzyme activity assays (*14*). (**E**) Initial-rate kinetics of the hydrolysis of XXXG-Dex, XXXG-Pred, and XXXG-Bude by recombinant *Bacteroides* GH5_4 *endo*-xyloglucanases. Error bars represent standard error of the mean ($n = 3$ technical replicates), and lines represent fitting of the Michaelis-Menten equation to the data; corresponding kinetic constants are provided in table S1. v_0, initial reaction velocity.

GlycoCaging improves dexamethasone targeting and efficacy in mice

Release of drug payloads from XXXG glycoconjugates in animal GI tracts depends on both the presence of XyGUL-containing bacteria and the induction of *endo*-xyloglucanase expression by dietary XyG. We showed that, like that of humans, the microbiota of mice in our facilities contained *endo*-xyloglucanase–producing *Bacteroides* species, including *B. ovatus* and *B. uniformis* (see supplementary text and figs. S5 to S7).

T cell transfer murine model of colitis

The T cell transfer model of colitis is generated by adoptive transfer of naïve $CD4^+$ T cells, in the absence of T regulatory cells, into lymphocyte-deficient hosts. It provides a reproducible model of intestinal inflammation that replicates features of IBD in humans, including immune cell infiltration and crypt abscess formation (*20*). The T cell transfer model has been used as a preclinical model to assess the efficacy of present IBD drugs and those in development (*21*, *22*). Importantly, dexamethasone [3 mg per kg body weight (mg/kg)] reduces colonic inflammation in this model (*23*, *24*).

After adoptive transfer of $CD4^+$ $CD45RB^{hi}$ T cells into *Rag1*-deficient mice (C57BL/6 background), mice were treated from 4 to 9 weeks (experimental endpoint) by oral gavage with dexamethasone or XXXG-Dex to compare dose-dependent efficacy. T cell transfer was confirmed in all mice in each treatment group (fig. S8A). As a control, the highest concentration of free dexamethasone used (7.6 mmol/kg; 3.0 mg/kg) did not cause pathosis or inflammation in $Rag1^{-/-}$ mice (fig. S8B). Female mice did worse than male mice in all gross pathology parameters assessed (fig. S8, C to G). T cell transfer caused weight loss in mice (fig S8, A and B). When comparing equivalent doses, XXXG-Dex significantly improved weight loss relative to free dexamethasone at 0.76 μmol/kg (Fig. 2A).

Free dexamethasone did not reduce colon weight:length ratios, a routine measure of inflammation (*25*, *26*), at any dose applied, whereas XXXG-Dex was effective at both 2.6 and 0.76 μmol/kg (Fig. 2B and see fig. S8C for gross pathology and fig. S8D for individual measures of colon length and weight). Histological damage (table S2) was assessed in the proximal colon, where it was most profound (Fig. 2, C and D), and the distal colon (fig. S8, E and F). The highest dose of free dexamethasone (7.6 μmol/kg) reduced the median histological damage, and this effect appeared to be titratable, although differences were not statistically significant. By contrast, XXXG-Dex reduced the median histological damage to values comparable to those of healthy mice, and observed damage was less than that in vehicle-treated control and dexamethasone-treated mice at 2.6 μmol/kg ($p = 0.016$) and 0.76 μmol/kg (not significant).

The highest dose of free dexamethasone (7.6 μmol/kg) reduced mean concentrations of the proinflammatory cytokines interferon-γ (IFN-γ; not significant) and interleukin-1β (IL-1β; $p = 0.016$) in full-thickness

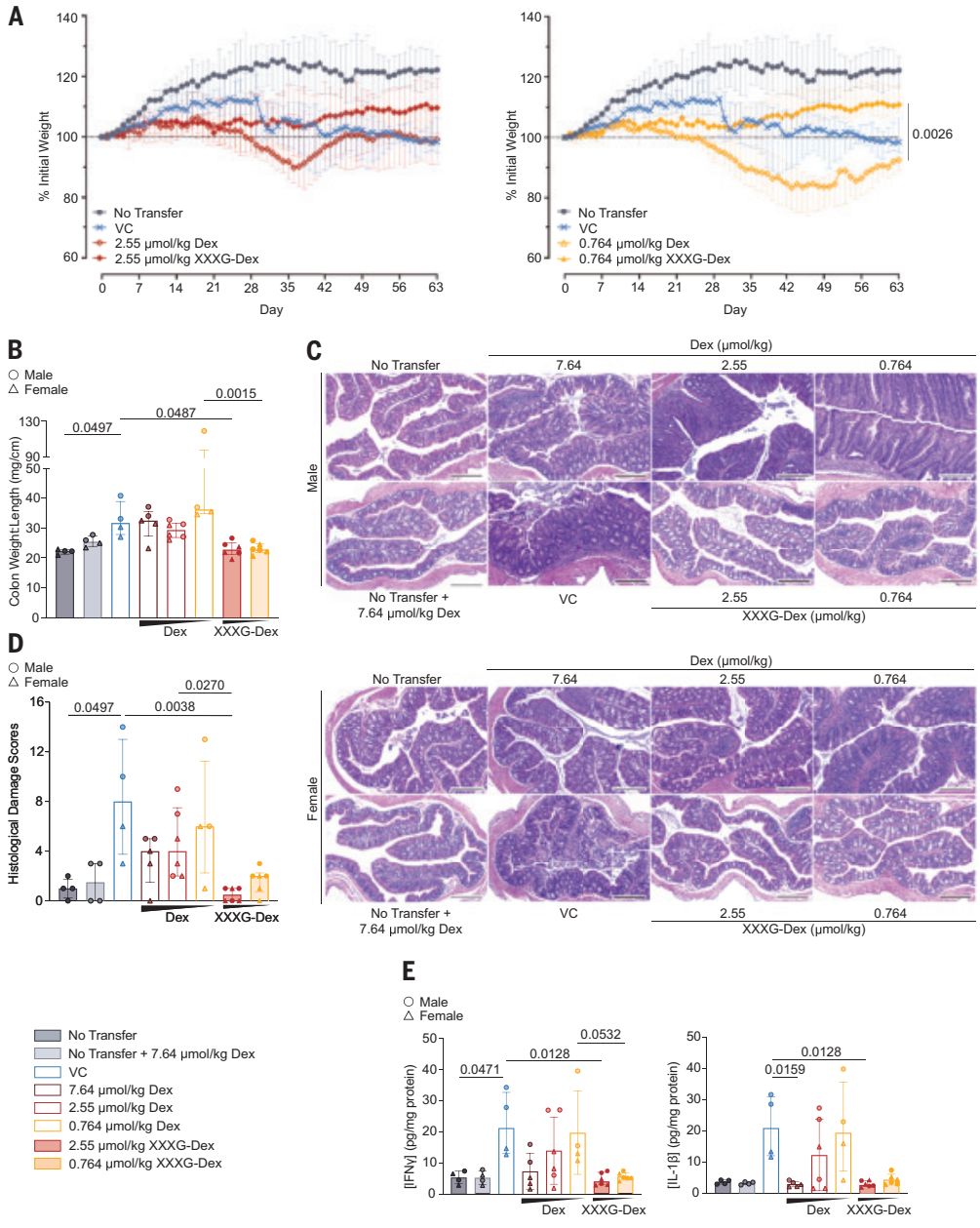

Fig. 2. Colon inflammation in T cell transfer model of colitis is treated by XXXG-Dex at a 3- to 10-fold-lower concentration than uncaged dexamethasone. Eight-week-old *Rag1*$^{-/-}$ mice were injected intraperitoneally with CD3^{+}CD4^{+}CD25^{-} CD45RB^{high} isolated from age- and sex-matched CD45.1 wild-type mice to induce colitis. Mice were treated with 0.764, 2.55, or 7.64 µmol/kg of dexamethasone (Dex) or vehicle control (VC; 0.5% β-cyclodextrin); or 0.764 or 2.55 µmol/kg of XXXG-Dex daily for 5 weeks starting at week 4 after T cell transfer. (**A**) Body weight changes for mice (percentage compared with baseline) throughout the 9-week experiment. (**B**) Colon weight:length ratio (mg/cm). (**C**) Representative hematoxylin and eosin (H&E)–stained cross sections of the proximal colon from each group (scale bars are 250 µm). (**D**) Histological damage scores for the proximal colons (table S2). (**E**) IFN-γ and IL-1β concentrations in full-thickness proximal colon tissue homogenates. In (A), (B), (D), and (E), data are presented as median ± interquartile range. In (D), median histological scores from two independent scorers blinded to experimental conditions are reported. The *p* values were calculated using mixed-effects analysis of variance (ANOVA) followed by Tukey post hoc test in (A) or Kruskal-Wallis with Dunn's post hoc test in (B), (D), and (E). T cell transfer model. Statistical differences, $p < 0.05$, are noted on the graphs; all other comparisons were not statistically different.

colon tissue homogenates, and the effect appeared to be titratable (Fig. 2E). XXXG-Dex was again more effective at reducing tissue cytokine concentrations of IFN-γ ($p = 0.013$) and IL-1β ($p = 0.013$) to levels observed in healthy control mice at 2.6 and 0.76 µmol/kg (not significant). Concentrations of proinflammatory tumor necrosis factor–α (TNFα) were likewise more attenuated by administration of XXXG-Dex than free dexamethasone, in a dose-dependent manner (fig. S8F). Together, these data show that XXXG-Dex was as effective, or more effective, at reducing pathosis and inflammation in the T cell transfer model of colitis at a 3- to 10-fold-lower equivalent dose of the drug than free dexamethasone.

We investigated the pharmacokinetics of XXXG-Dex to establish that improved efficacy was the result of improved targeting of the corticosteroid by GlycoCaging. C57BL/6 mice (the same genetic background for Rag$^{-/-}$ mice used in the T cell transfer experiments) were used for pharmacokinetics analyses because of the number of mice required. We observed greatly reduced systemic circulation and targeted delivery of dexamethasone in mice on oral administration of XXXG-Dex versus dexamethasone (fig. S9). Serum and tissue concentrations of dexamethasone spiked in mice orally gavaged with the free steroid (fig. S9, A and C), indicating rapid uptake and systemic distribution. In marked contrast, oral administration of XXXG-Dex resulted in no spike in circulating dexamethasone levels (fig. S9B), indicating that absorption in the upper GI tract had been prevented. Notably, the delayed appearance of dexamethasone in colonic tissue after XXXG-Dex administration was commensurate with typical GI transit times (>2 hours; fig. S9D). Serum concentrations, although low throughout, also followed this temporal pattern (fig. S9B), indicating that free dexamethasone was specifically entering the circulatory system through the lower GI tract after microbiota-mediated decaging of the drug.

SHIP$^{-/-}$ murine model of intestinal inflammation

To validate our findings in a second preclinical model of intestinal inflammation, we selected the SHIP$^{-/-}$ mouse model of Crohn's disease–like ileitis. Inflammation in SHIP$^{-/-}$ mice is driven by the innate immune system, in which macrophage-derived IL-1β promotes disease (*27*–*30*). Disease occurs in 100% of mice by 6 weeks of age and is restricted to the distal ileum, the most common site of inflammation in people with Crohn's disease (*27*, *28*, *30*). Hallmarks of disease include immune cell infiltration, edema, proinflammatory cytokine production, and fibrosis (*28*, *31*). SHIP abundance and activity are significantly reduced in people with Crohn's disease, in a manner inversely proportional to production of proinflammatory IL-1β (*30*).

SHIP$^{-/-}$ mice were treated orally from 6 to 8 weeks of age with decreasing amounts of dexamethasone or XXXG-Dex to determine the minimum effective dose of each. As a control, the highest applied dose of free dexamethasone, 7.6 μmol/kg, did not cause pathology in healthy, wild-type SHIP$^{+/+}$ mice (fig. S10). In SHIP$^{-/-}$ mice, gross pathology was eliminated, histopathologic changes were ameliorated, and histological damage scores (table S3) were significantly reduced by 2.6 and 7.6 μmol/kg, but not by 0.76 μmol/kg, of free dexamethasone (Fig. 3). XXXG-Dex ameliorated gross pathological changes and reduced histopathological damage scores at a lower equivalent dose, that is, 0.76 μmol/kg, than free dexamethasone (Fig. 3C). At a 0.26-μmol/kg dose of XXXG-Dex, the difference between the overall histopathological damage score versus the control (water vehicle) was less defined, although tissue sections showed a healthy epithelial architecture, similar to that seen in mice given the 0.76-μmol/kg dose of XXXG-Dex (Fig. 3C).

IL-1β concentrations were significantly reduced in SHIP$^{-/-}$ mice by oral administration of free dexamethasone at the two highest doses, that is, 7.6 and 2.6 μmol/kg, but not by 0.76 μmol/kg (Fig. 3D). Conversely, lower doses of XXXG-Dex, that is, 0.76 and 0.26 μmol/kg, respectively, reduced ileal IL-1β concentrations. Here again, XXXG-Dex was more effective than the free corticosteroid at the equivalent concentration of 2.6 μmol/kg (Fig. 3D). These data indicate that drug release by the microbiota is sufficient to ameliorate disease in the distal ileum of mice despite lower enzyme concentrations than in the cecum or colon (fig. S5C). Moreover, XXXG-Dex was effective at reducing Crohn's disease–like ileal inflammation at a 3- to 10-fold-lower dose than its uncaged counterpart.

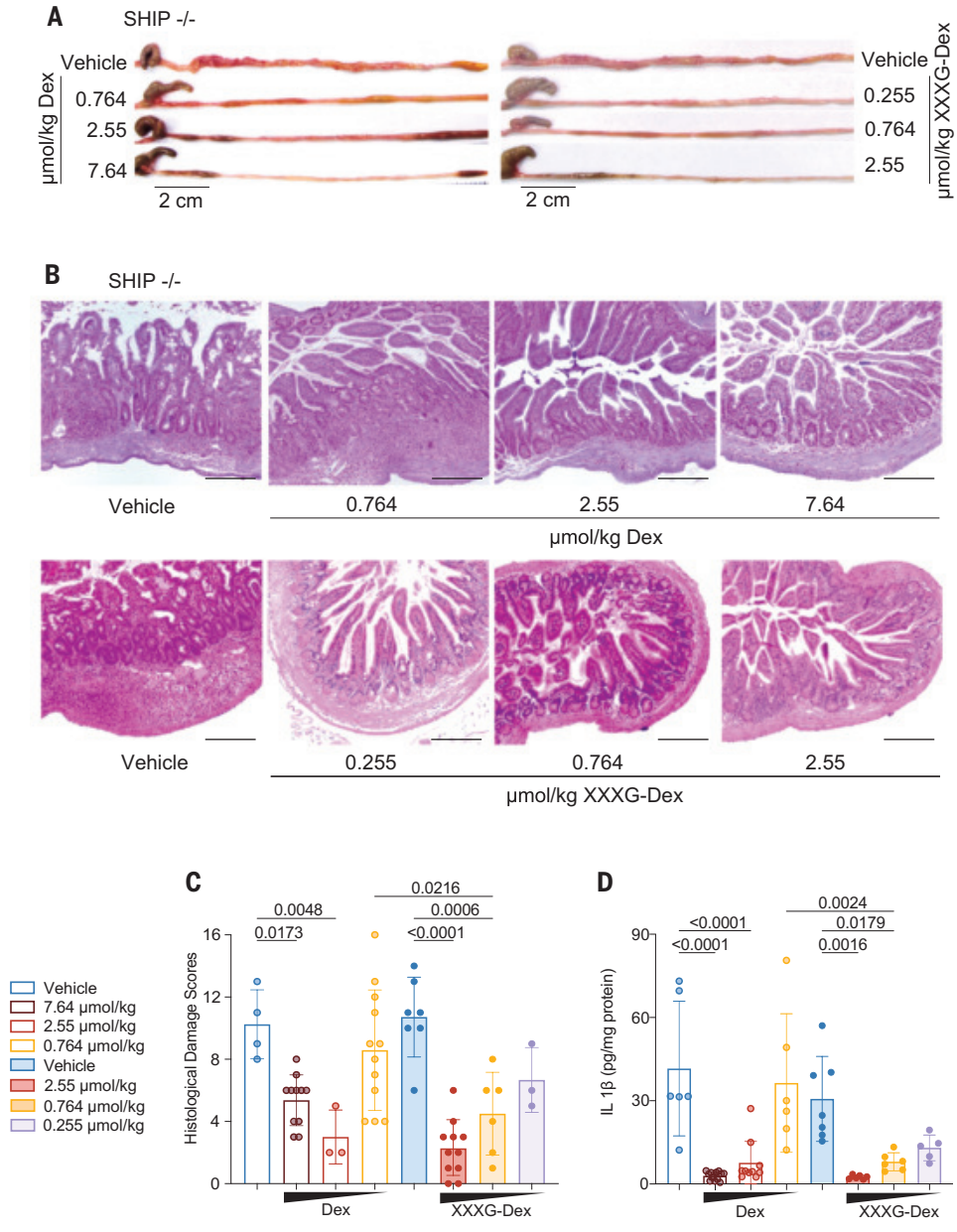

Fig. 3. Ileal inflammation in SHIP-deficient mice is effectively treated by XXXG-Dex at a 3- to 10-fold-lower concentration than uncaged dexamethasone. SHIP$^{-/-}$ mice (6 weeks old) were treated with 0.764, 2.55, or 7.64 μmol/kg of dexamethasone (Dex) or vehicle control (VC; 0.5% β-cyclodextrin); or 0.255, 0.764, or 2.55 μmol/kg of XXXG-Dex or VC (water) daily for 2 weeks. (**A**) Gross pathology of the distal ilea for one representative mouse from each group. (**B**) Representative H&E-stained cross sections of the distal ileum for one representative mouse from each group. Scale bars are 250 μm. (**C**) Histological damage scores (compare table S3). (**D**) IL-1β concentrations in full-thickness ileal tissue homogenates. In (C) and (D), $n = 6$ to 15 mice per group. In (C), means from two independent scorers blinded to experimental condition are reported. In (D), means ± SD are reported. The p values were calculated using one-way ANOVA, followed by Bonferroni correction for multiple comparisons. Statistical differences, $p < 0.05$, are noted on the graphs; all other comparisons were not statistically different.

In addition to ileitis, SHIP$^{-/-}$ mice also exhibit systemic inflammation, including lung pathology (*32*). Lungs from SHIP$^{-/-}$ mice were enlarged and exhibited white patches on their surfaces, characteristic of extensive leukocyte infiltration. Oral administration of dexamethasone (7.6 or 2.6 μmol/kg) resulted in lungs that were smaller and less firm, with reduced patchiness, whereas lungs from XXXG-Dex–treated mice appeared comparable to those from untreated SHIP$^{-/-}$ mice (Fig. 4A and compare table S4). Histology further revealed that lungs from mice treated with free dexamethasone appeared healthy, with resolved inflammation. By contrast, lungs from SHIP$^{-/-}$ mice administered XXXG-Dex at 0.76 and 2.6 μmol/kg appeared similar to those from untreated SHIP$^{-/-}$ mice (Fig. 4B). Thus, whereas the free corticosteroid was able to enter the circulatory system and exert systemic effects on the lungs, GlycoCaging greatly reduced systemic circulation to the point that off-target (non-GI) effects were eliminated. These results further support the potential of GlycoCaging to mitigate drug side effects in people with IBD.

Pharmacokinetics analyses of serum and tissue samples along the GI tract corroborated these pathological indicators of successful

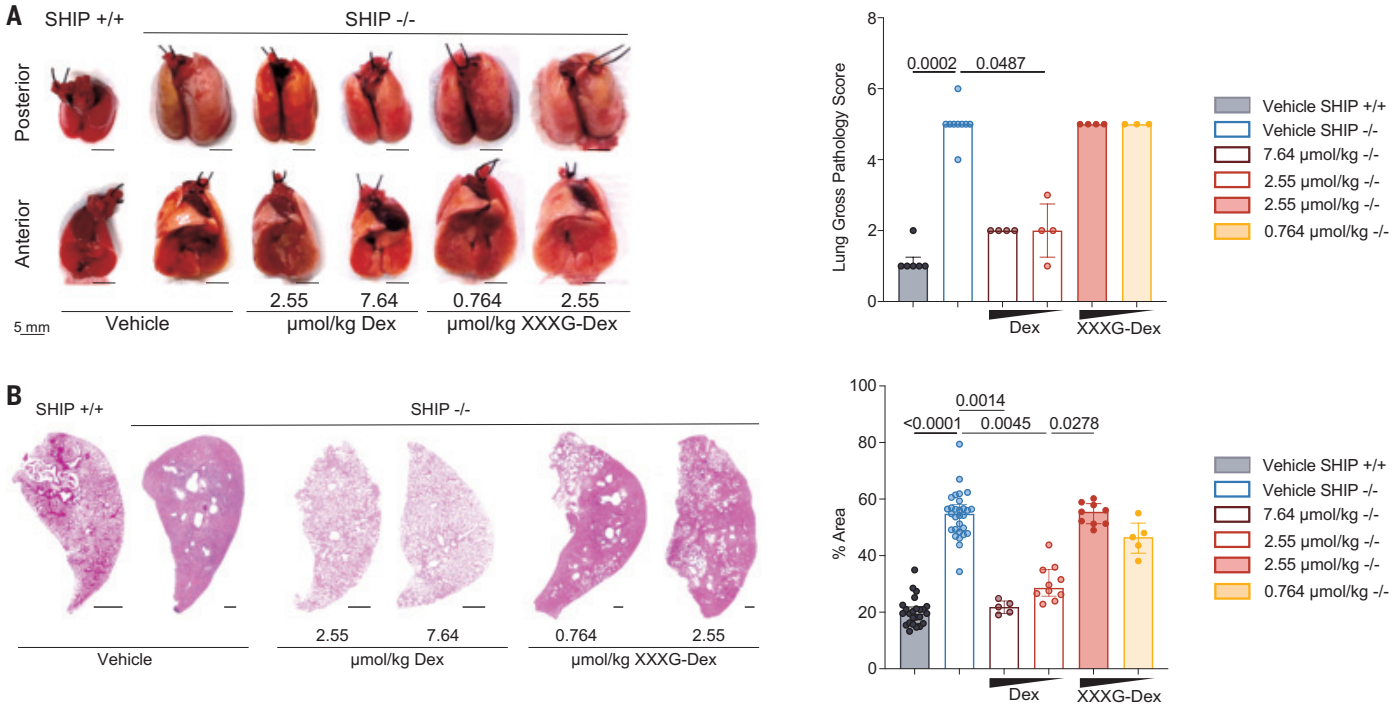

Fig. 4. XXXG-Dex does not reduce lung inflammation in SHIP-deficient mice. SHIP$^{-/-}$ mice (6 weeks old) were treated with 0.764, 2.55, or 7.64 μmol/kg of dexamethasone (Dex) or vehicle control (VC; 0.5% β-cyclodextrin); or 0.255, 0.764, or 2.55 μmol/kg of XXXG-Dex or VC (water) daily for 2 weeks. (**A**) Gross anatomy of the lungs (left) from representative healthy control SHIP$^{+/+}$ mice and dexamethasone– or XXXG-Dex–treated SHIP$^{-/-}$ mice (scale bars are 5 mm) and lung gross pathology score (right) reported as median ± interquartile range (compare table S4). (**B**) H&E-stained sections from one representative lung lobe from one mouse per group. Scale bars are 1 mm. Percentages of H&E-stained area in total lung sections across treatment groups are reported as mean ± SD. The *p* values were calculated using Kruskal-Wallis with Dunn's post hoc test in (A) and one-way ANOVA with Bonferroni correction for multiple comparisons in (B).

drug targeting. Dexamethasone was measured in serum and in tissues in several locations along the GI tract (proximal, middle, and distal small intestine; cecum; proximal and distal colon) in both SHIP$^{+/+}$ and SHIP$^{-/-}$ mice after oral gavage of free dexamethasone or XXXG-Dex (fig. S11). Administration of free dexamethasone caused a rise in serum dexamethasone concentrations within 30 min. GlycoCaging resulted in lower total systemic uptake of dexamethasone, which nonetheless peaked at 4 hours after oral gavage, consistent with GI transit. In tissues, administration of free dexamethasone likewise caused a spike in all locations within 30 min, again consistent with systemic distribution. By contrast, XXXG-Dex minimized uptake in proximal, middle, and distal small intestinal tissues yet enabled delivery of the corticosteroid into the cecum and colon (proximal and distal). The lack of appearance of dexamethasone in these tissues until 2 to 4 hours after gavage showed that the specificity of targeting is consistent with microbiota-mediated release (fig. S11). These data are concordant with our data on C57BL/6 mice (fig. S9), indicating that GlycoCage pharmacokinetics are essentially independent of mouse genetic background.

Translation to human gastrointestinal tract diseases

To reveal the potential of GlycoCaging to improve the clinical treatment of human IBD and other GI diseases, we directly assayed decaging activity (*33*) in human fecal samples using the fluorogenic prodrug proxy XXXG-resorufin (XXXG-Res) [Fig. 1E; (*14*)]. We first validated the assay using feces from 24 (12 female, 12 male) healthy humans (median age of 42 years) whose diets were not controlled (fig. S12). *endo*-Xyloglucanase activity was ubiquitous in these subjects, which showed that the production of decaging enzymes by the microbiota is sustained by normal dietary intake of XyG in fruit and vegetable cell walls [see (*4*, *5*) and references therein].

Turning our attention to people with IBD, fecal samples from a study cohort comprising five healthy control participants and 23 people with IBD were assayed. Decaging activity was present in all participants, with no statistically significant difference between healthy and IBD cohorts (Fig. 5A). However, there was a distinctly broad distribution of activity values in people with IBD, comprising three orders of magnitude, with most exhibiting higher decaging activity than the average for healthy participants. To gain further insight into this distribution, data for people with IBD were stratified according to fecal calprotectin as an indicator of inflammation and disease: 0 to 20 (uninflamed), 20 to 200 (potential IBD, retesting indicated), and >200 (active IBD) (Fig. 5B). However, there were no statistically significant differences in decaging activity between groups of people stratified for degree of IBD.

Consistent with these observations, a metagenomic survey of 124 individuals from the Integrative Human Microbiome Project (*34*), using genes (Fig. 1C) of biochemically validated *Bacteroides* GH5_4 *endo*-xyloglucanases (*4*–*6*) as molecular markers, revealed that decaging potential was similarly widespread among people with IBD and healthy participants (Fig. 5, C and D, and figs. S13 and S14). Notably, a longitudinal analysis indicated that the presence of *endo*-xyloglucanase genes was typically stable in individuals over a 1-year monitoring period and that individuals lacking XyGUL GH5_4 members generally had confounding variables (e.g., antibiotic use, lower sequencing depth, etc.; figs. S13 and S14).

Together, these direct-assay and metagenomic survey data indicate that people with IBD, in general, intrinsically possess the microorganisms

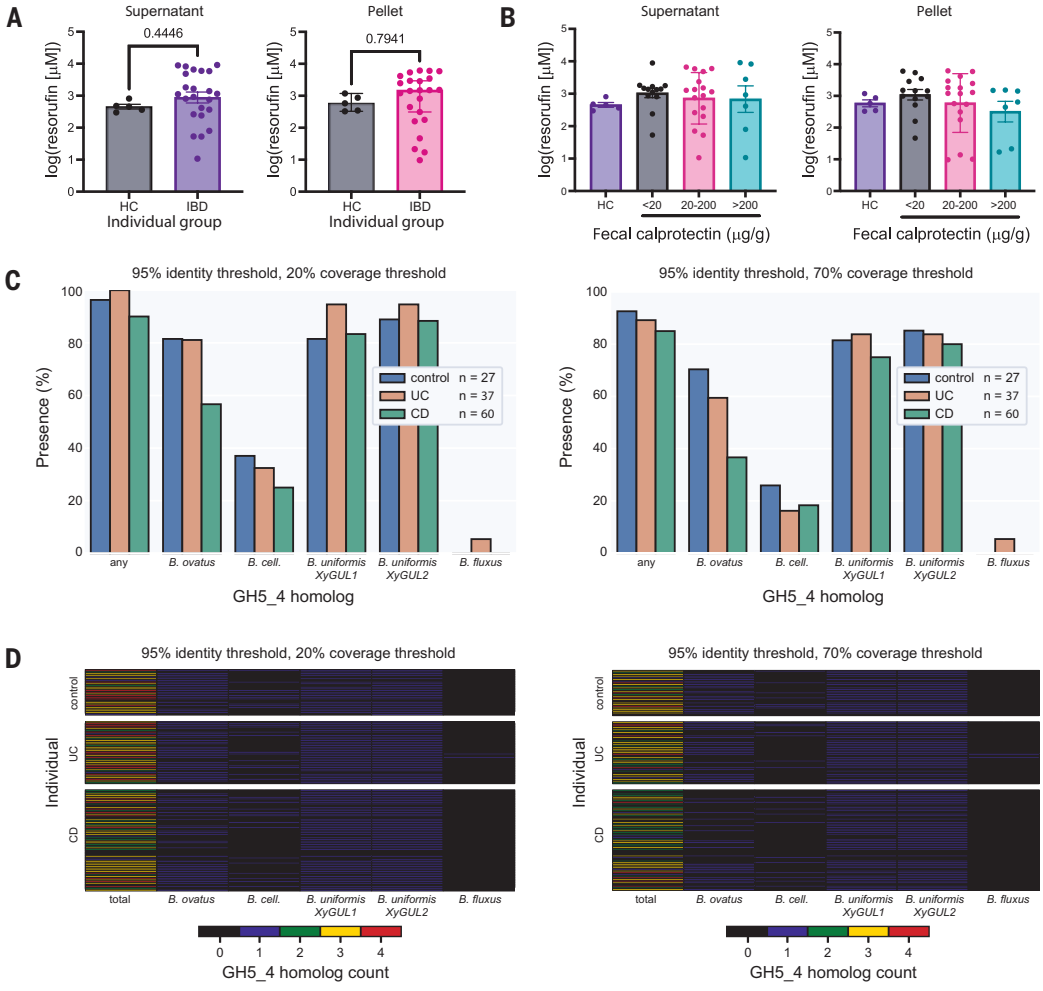

Fig. 5. Decaging activity is ubiquitous in people with IBD. (**A**) Fecal material from healthy control participants (HC; $n = 5$) and people with IBD ($n = 28$) was assayed for decaging activity using XXXG-Res [Fig. 1B; (*14*)]. There were no significant differences between groups, as determined using a Mann-Whitney *U* test for raw data or an unpaired *t* test for log-transformed data. (**B**) Activity in people with IBD stratified according to fecal calprotectin, a marker of inflammation. There were no significant differences between groups using a Kruskal-Wallis test for raw data or a one-way ANOVA for log-transformed data (from left to right; $p = 0.960$, 0.739, 0.305, and 0.405). Vertical lines associated with histogram bars are standard errors of the mean. (**C**) Presence of decaging *endo*-xyloglucanase–encoding genes from GH5_4 in metagenomes of control, ulcerative colitis (UC), and Crohn's disease (CD) individuals in the Human Microbiome Project 2 study (*34*), determined by Magic-BLAST at 95% sequence identity and permissive (20%, left) and strict (70%, right) nucleotide coverage thresholds. Individuals were considered to possess a decaging *endo*-xyloglucanase if the corresponding gene (or genes) was observed in at least one longitudinal sample; in general, gene presence was stable over 1 year (figs. S13 and S14). (**D**) Stratification of GH5_4 *endo*-xyloglucanase genes in individual metagenomes. Each row represents one individual, grouped according to cohort (control, UC, CD). As in (C), individuals were considered *endo*-xyloglucanase–positive (blue line) if the corresponding gene was observed in at least one longitudinal sample; see fig. S14 for the full longitudinal analysis. *B. uniformis* and *B. ovatus* represent the most prevalent sources of XyGUL GH5_4 *endo*-xyloglucanases, with redundancy in many individuals (left-most column, totals).

and associated enzymes required for GlycoCaged prodrug cleavage. In a personalized medicine approach, individuals who lack suitable decaging bacteria can be identified by microbiome sequencing, with the possibility to address any deficiencies by probiotic supplementation. Moreover, prebiotic strategies, that is, dietary vegetable or purified XyG supplementation, may be useful to ensure that individuals have sustained decaging activity as a result of XyGUL up-regulation (*2*, *4*). Although likely not necessary in most individuals, routine molecular diagnostics, that is, sequencing- and assay-based techniques, can be readily envisioned to maximize the potential for effective treatment.

Conclusions

GI diseases, such as IBD and colorectal cancer, will continue to exert major personal and economic burdens in the foreseeable future, owing to their complex etiology and lack of curative therapeutics. It is notable that oral administration of free dexamethasone and other corticosteroids in humans is limited by a spike in serum concentrations (*35*), on a timescale similar to that seen in mice (Fig. 3), because of the rapid uptake of these drugs in the proximal GI tract. The use of a glycoconjugate comprising a complex plant oligosaccharide, as a natural component of dietary fiber cleavable only by gut microbiota (*8*, *36*, *37*), offers the prospect of treatment strategies to improve the therapeutic indices of GI drugs. As shown here, GlycoCaging hydroxy compounds by direct O-glycosylation was straightforward, and could be applicable to amine-, thiol-, and carboxylate-containing drugs through self-immolating linker strategies (*38*) (e.g., fig. S15). We foresee that this approach, based on a preassembled, branched glycan donor, will enable convergent synthesis of a wide range of prodrugs for the treatment of

diverse GI associated diseases. GlycoCaging may offer a route to rescue promising drug candidates that presently show unacceptable systemic toxicity.

REFERENCES AND NOTES

1. J. A. Briggs, J. M. Grondin, H. Brumer, *Environ. Microbiol.* **23**, 15–35 (2021).
2. E. C. Martens, A. G. Kelly, A. S. Tauzin, H. Brumer, *J. Mol. Biol.* **426**, 3851–3865 (2014).
3. H. V. Scheller, P. Ulvskov, *Annu. Rev. Plant. Biol.* **61**, 263–289 (2010).
4. J. Larsbrink *et al.*, *Nature* **506**, 498–502 (2014).
5. G. Déjean, A. S. Tauzin, S. W. Bennett, A. L. Creagh, H. Brumer, *Appl. Environ. Microbiol.* **85**, e01491-19 (2019).
6. J. M. Grondin, G. Déjean, F. Van Petegem, H. Brumer, *Appl. Environ. Microbiol.* **88**, e0156621 (2022).
7. A. El Kaoutari, F. Armougom, J. I. Gordon, D. Raoult, B. Henrissat, *Nat. Rev. Microbiol.* **11**, 497–504 (2013).
8. D. R. Friend, *Adv. Drug Deliv. Rev.* **57**, 247–265 (2005).
9. R. Sabra, N. Billa, *Front. Bioeng. Biotechnol.* **9**, 645923 (2021).
10. A. Awad *et al.*, *Adv. Drug Deliv. Rev.* **181**, 114076 (2022).
11. G. G. Kaplan, *Nat. Rev. Gastroenterol. Hepatol.* **12**, 720–727 (2015).
12. S. Alatab *et al.*, *Lancet Gastroenterol. Hepatol.* **5**, 17–30 (2020).
13. Crohn's and Colitis Canada, "2018: Impact of inflammatory bowel disease in Canada" (2018); http://crohnsandcolitis.ca/Crohns_and_Colitis/documents/reports/2018-Impact-Report-LR.pdf.
14. F. M. Ibatullin *et al.*, *Plant Physiol.* **151**, 1741–1750 (2009).
15. F. M. Ibatullin, M. J. Baumann, L. Greffe, H. Brumer, *Biochemistry* **47**, 7762–7769 (2008).
16. A. M. Rodd, W. M. Mawhinney, H. Brumer, *Biotechnol. Biofuels Bioprod.* **17**, 116 (2024).
17. X. Zhu, R. R. Schmidt, *Angew. Chem. Int. Ed.* **48**, 1900–1934 (2009).
18. C. Lautenschläger, C. Schmidt, D. Fischer, A. Stallmach, *Adv. Drug Deliv. Rev.* **71**, 58–76 (2014).
19. H. Schäcke, W. D. Döcke, K. Asadullah, *Pharmacol. Ther.* **96**, 23–43 (2002).
20. C. F. Pearson, K. J. Maloy, *Curr. Protoc.* **4**, e1092 (2024).
21. F. Powrie *et al.*, *Immunity* **1**, 553–562 (1994).
22. T. Lindebo Holm, S. S. Poulsen, H. Markholst, S. Reedtz-Runge, *Int. J. Inflamm.* **2012**, 412178 (2012).
23. D. Hirano, S. Kudo, *J. Pharmacol. Sci.* **110**, 169–181 (2009).
24. Y. L. Chen *et al.*, *Sci. Rep.* **6**, 35635 (2016).
25. J. N. Chai *et al.*, *Sci. Immunol.* **2**, eaal5068 (2017).
26. A. K. Czopik *et al.*, *Nat. Commun.* **15**, 8042 (2024).
27. S. Fernandes *et al.*, *Front. Immunol.* **9**, 1100 (2018).
28. K. W. McLarren *et al.*, *Am. J. Pathol.* **179**, 180–188 (2011).
29. E. N. Ngoh *et al.*, *Genes Immun.* **16**, 452–461 (2015).
30. E. N. Ngoh *et al.*, *Gastroenterology* **150**, 465–476 (2016).
31. Y. Lo, J. P. Sauve, S. C. Menzies, T. S. Steiner, L. M. Sly, *Mucosal Immunol.* **12**, 1187–1200 (2019).
32. C. D. Helgason *et al.*, *Genes Dev.* **12**, 1610–1620 (1998).
33. I. Miko, *Nature Educ.* **1**, 137 (2008).
34. J. Lloyd-Price *et al.*, *Nature* **569**, 655–662 (2019).
35. S. M. C. Spoorenberg *et al.*, *Br. J. Clin. Pharmacol.* **78**, 78–83 (2014).
36. B. Haeberlin, W. Rubas, H. W. Nolen III, D. R. Friend, *Pharm. Res.* **10**, 1553–1562 (1993).
37. H. Elferink, J. P. J. Bruekers, G. H. Veeneman, T. J. Boltje, *Cell. Mol. Life Sci.* **77**, 4799–4826 (2020).
38. R. Madec-Lougerstay, J. C. Florent, C. Monneret, *J. Chem. Soc., Perkin Trans. 1* **1999**, 1369–1376 (1999).
39. W. J. Ma *et al.*, Bespoke plant glycoconjugates for gut microbiota-mediated drug targeting. Dryad (2025); https://doi.org/10.5061/dryad.np5hqc04q.
40. A. Fraser, Bespoke plant glycoconjugates for gut microbiota-mediated drug targeting – metagenomics code. Zenodo (2025); https://doi.org/10.5281/zenodo.14828870.

ACKNOWLEDGMENTS

We thank J. Cartmell, J. Zheng, B. Reiz, and R. Whittal (Department of Chemistry, University of Alberta) for liquid chromatography–mass spectrometry (LC-MS) analysis service. We thank A. Rodd (Brumer Laboratory) for recombinant enzyme production. L.M.S. is the recipient of a Canadian Association of Gastroenterology/Crohn's and Colitis Canada/CIHR New Investigator Salary Award and is a Biomedical Scholar of the Michael Smith Foundation for Health Research. We thank T. Lowary (Academica Sinica), B. Henrissat (Danish Technical University), and K. Sharkey (University of Calgary) for providing valuable comments on this manuscript before submission. We dedicate this study to the memory of Doug Inglis and Jenny Gusse, who died in September 2023 during a backpacking trip in the Canadian wilderness. https://stories.ulethbridge.ca/dr-doug-inglis-jenny-gusse-memorial-fund/ https://canadianglycomics.ca/remembering-dr-doug-inglis-a-tribute-to-a-life-well-lived/ **Funding:** This work was funded by Natural Sciences and Engineering Research Council of Canada through the Canadian Glycomics Network (GlycoNet, A Network of Centres of Excellence), projects CD-13 (H.B.), CD-30 (H.B., G.D.I., D.W.A.), CD-50 (H.B., G.D.I., D.W.A., L.M.S.), and CD-84 (H.B., L.M.S.); Michael Smith Health Research BC, I2C project 18713 (H.B., G.D.I.), Matching Funds Program MF-2024-04397 (H.B., L.M.S.); Alberta Innovates project CD-60 (G.D.I.); Agriculture and Agri-Food Canada project J-002249 (G.D.I.); Crohn's and Colitis Canada, Innovations in IBD Research (H.B.), Grant-in-Aid of Research (L.M.S.), Grant-in-Aid of Research (D.L.G.); Canadian Institutes of Health Research projects MOP-133607 (L.M.S.) and PJT-518617 (L.M.S., H.B.); and the Innovation, Science and Economic Development Canada Strategic Science Fund through the Canadian Glycomics Network, project CT-9 (H.B., L.M.S.). **Author contributions:** H.B., L.M.S., G.D.I., and D.W.A. obtained funding and directed research. C.W., B.W.-Q.H., and J.K. developed synthetic methodology and performed prodrug syntheses. W.J.M. and S.C.M. performed analyses in the T cell transfer model. M.L.-S., W.J.M., and S.C.M. performed analyses in the SHIP$^{-/-}$ model. D.M.B. and M.E.L. performed pharmacokinetics and additional studies in mice. J.F.G. and W.J.M. assayed *endo*-xyloglucanase activity in murine and/or human fecal samples, and J.F.G. quantified bacterial densities by quantitative PCR (qPCR). X.X. and J.K. established and applied analytical methodology for pharmacokinetics. J.K. and J.M.G. measured prodrug hydrolysis in vitro. S.T.C. and T.G.S. performed in vivo studies for the development of the XyG-enriched mouse diet. X.X., J.F.G., D.M.B., M.L-S., and W.J.M. developed and optimized the XXXG-Res–based assay to quantify xyloglucanase activity in biological samples. P.E.M., K.E.H., and J.F.G. established and applied the methodology to screen and identify xyloglucanase-positive bacteria. N.H. and D.L.G. provided human fecal samples and assisted with data interpretation. E.C.M. assisted with metagenomic study design, which was performed by A.S.C.F. H.B., L.M.S., G.D.I., and D.W.A. produced the manuscript, with input of data, figures, and text from all co-authors. **Competing interests:** H.B., B.W.-Q.H., C.W., G.D.I., S.T.C., and D.W.A. are inventors on a patent application (WO2020198878) filed by The University of British Columbia, Her Majesty The Queen In Right Of Canada as Represented By The Minister Of Agriculture And Agri-Food, and the Governors of the University Of Alberta that covers XyG-containing prodrugs related to this work. D.L.G. is cofounder and chief scientific officer at Melius MicroBiomics. **Data and materials availability:** In addition to the data presented in the main text and the supplementary materials, data files are available at Dryad (*39*). Software scripts used for metagenome data analysis are available on Zenodo and Github (*40*). Samples of noncommercial materials may be made available upon reasonable request to the corresponding authors.

SUPPLEMENTARY MATERIALS

science.org/doi/10.1126/science.adk7633
Materials and Methods; Supplementary Text; Figs. S1 to S27; Tables S1 to S10; References (*41*–*67*); MDAR Reproducibility Checklist; Data S1

Submitted 18 September 2023; resubmitted 10 December 2024; accepted 5 March 2025; published online 1 May 2025

10.1126/science.adk7633

ZEOLITES

Accelerated discovery of stable, extra-large-pore nano zeolites with micro-electron diffraction

Chao Ma[1]†, Zhenghan Zhang[1]†, Mengdi Zhang[1]†, Xudong Tian[1], Cong Lin[2]*, Lei Han[3], Guangchao Li[2], Benedict Tsz Woon Lo[2], Ka-Fu Yung[2], Haitao Song[3], Wei Lin[3]*, Miguel A. Camblor[4], Le Xu[5,6], Jian Li[1,6,7]*

Stable zeolites with extra-large pores and nano dimensions that are capable of processing large molecules are in high demand but have been difficult to produce. Their complex structures and nanoscale crystal sizes present challenges for analysis using conventional x-ray diffraction techniques, leading to inefficiencies in material development. We report NJU120-1 and NJU120-2, two robust and fully connected aluminosilicate nano zeolites featuring interconnected channel systems with extra-large 22-ring pores. NJU120-1 is a nanosheet with only about 8-nanometer thickness, corresponding to 1.5 unit cells, and NJU120-2 is a nanorod with 50 by 250 nanometer dimensions. Their synthesis optimization was greatly accelerated through rapid structure determination with MicroED, revealing their multidimensional pore structures. Their very large largest-free-sphere diameters of approximately 1.2 nanometers coupled with nano morphologies enabled catalytic cracking of large molecules.

Zeolites are crystalline microporous materials that are decorated with controllable acid centers for size- and shape-selective catalysis (*1*, *2*). Access of molecules through diffusion into and out of their inner confined space, where adsorption and reactions occur, is crucial to their functionalities and is determined by their pore apertures and lengths for mass transfer. However, current industrial zeolites are commonly larger crystal bulk and have micropores with aperture diameters <1 nm (*3*). These properties hinder the molecular diffusion of reactants and products and often lead to rapid coking and unwanted side reactions.

To overcome these challenges, the synthesis of nanosized or extra-large-pore (ELP) zeolites provides promising approaches (*4*, *5*). Nano zeolites, especially nanosheet ones, have much shorter diffusion pathways and an increased fraction of accessible external surface with exposed active sites compared with their bulk counterparts, which enhances mass transfer (*6*, *7*). They are commonly made by strategies such as exfoliating layered zeolites, using templated crystallization, introducing mesopores, and using additive-assisted synthesis. Unfortunately, these methods necessitate expensive surfactants, specially designed organic structure–directing agents (OSDAs) with long chain alkyl groups, as well as intricate processes such as swelling, pillaring, and delamination, which make them too costly for industrial use. Moreover, they are typically applicable only to a limited range of zeolites, including the MFI (*6*), FAU (*8*), MOR (*9*), MWW (*10*, *11*), and FER (*12*) types, none of which qualifies as an ELP zeolite that can process molecules larger than those currently manageable.

ELP zeolites, which are characterized by larger pore apertures delimited by rings encircled with >12 TO_4 tetrahedra (where T represents framework atoms coordinating with O, like Si and Al) and larger largest free sphere (LFS) that can pass through the framework by at least one lattice translation, provide another effective strategy to overcome the mass transfer limitations through broadened diffusion pathways (*13*, *14*). Specifically, molecules are blocked if their sizes surpass the pore aperture or LFS diameter of a given zeolite. For example, the LFS diameter of industrial ultrastable Y (USY) zeolite (FAU topology) with a 12-membered ring (12MR) channel system is only 0.74 nm, which seriously restricts its catalytic application in processing heavier hydrocarbons (*15*). This limitation has spurred demands for ELP zeolites with pore apertures exceeding 12MR and LFS diameters >1 nm.

Over the past 30 years, 40 ELP zeolites have been identified (table S1); however, 30 of them have interrupted frameworks with terminal –OH groups or contain elements such as Ge, Ga, P, or Be (*16*). These features diminish their thermal and hydrothermal stability and limit practical applications. Furthermore, the few stable pure silicate or borosilicate ELP zeolites have failed to fully meet catalytic requirements because of the challenges in incorporating sufficient active aluminum into their frameworks. High-silicon ELP zeolites with stable catalytic sites remain exceedingly rare. Notable exceptions include ZEO-1 (*17*) and ZMQ-1 (*18*), which is characterized by large crystal dimensions.

The combination of nano dimensions with ELPs, or nano ELP zeolites, could have both shortened and broadened diffusion pathways, which would greatly boost mass transfer and enable higher catalytic performance compared with conventional zeolites. Despite their great potential, such nano ELP zeolites remain underexplored, and their development has many challenges. Specifically, during synthesis, various factors such as reagents (especially OSDAs) and their ratios, as well as synthetic temperature and duration, require careful selection and optimization (*19*). High-throughput screening can identify many variables in a timely manner but requires equally effective phase identification and structure determination. For nano ELP zeolites, this requirement poses difficulties because such zeolites often have rather complex framework structures and crystallize as nanocrystal powders mixed with other phases, which complicates their analysis by routine techniques such as x-ray diffraction (XRD).

We present a strategy to accelerate nano ELP zeolite development by combining state-of-the-art MicroED (microcrystal electron diffraction) with combinatorial chemistry. First, a wide range of compositions was tested and the resulting compounds were characterized in parallel with a combinatorial approach. Subsequently, their phase elucidation and structure determination were rapidly completed within multiphase polycrystalline samples by high-throughput MicroED, which can isolate crystallites with different phases and compositions. Based on these findings, synthetic conditions were then pertinently optimized and pure products were finally obtained.

Using the above strategy, two stable and fully connected nano ELP aluminosilicate zeolites, NJU120-1 and NJU120-2 (Nanjing University zeolites 1 and 2 discovered on the occasion of the 120th anniversary of Nanjing University), which have high Si/Al ratios, were developed within similar systems. NJU120-1 has an impressive nanosheet morphology characterized by multilamellar stacks of only 1.5 unit-cell thickness, whereas NJU120-2 exhibits a nanorod morphology with dimensions of 50 by 250 nm. These zeolites feature in their structures multidimensional and interconnected channels with 22 × 10 × 10 MR and 22 × 12 × 10 MR pores, respectively. Moreover, their 22MR pore apertures surpass all of our previously reported stable ELP zeolites, including ZEO-1 (aluminosilicate with 16MR pores, JZO topology) (*17*),

[1]State Key Laboratory of Coordination Chemistry, School of Chemistry and Chemical Engineering, Nanjing University, Nanjing, China. [2]Department of Applied Biology and Chemical Technology, The Hong Kong Polytechnic University, Kowloon, Hong Kong S.A.R., China. [3]State Key Laboratory of Petroleum Molecular & Process Engineering, Research Institute of Petroleum Processing (RIPP), SINOPEC, Beijing, China. [4]Instituto de Ciencia de Materiales de Madrid, Consejo Superior de Investigaciones Científicas (ICMM-CSIC), Madrid, Spain. [5]State Key Laboratory of Materials-Oriented Chemical Engineering College of Chemical Engineering, Nanjing Tech University, Nanjing, China. [6]Suzhou Laboratory, Suzhou, China. [7]Beijing National Laboratory for Molecular Sciences, Beijing, China.
***Corresponding author. Email: cong.lin@polyu.edu.hk (C.L.); linwei.ripp@sinopec.com (W.L.); jian.li@nju.edu.cn (J.L.)** †These authors contributed equally to this work.

ZEO-3 (pure silicate with 16MR pores, JZT topology) (*20*), and ZEO-5 (pure silicate with 20MR pores, HZF topology) (*21*).

Both NJU120-1 and NJU120-2 demonstrate impressive LFS diameters of ~1.2 nm, exceeding most known zeolites and only slightly smaller than ZMQ-1. Coupled with intrinsic aluminum catalytic active centers embedded in their ELP structures and nano morphologies, NJU120-1 and NJU120-2 enabled efficient heavy-oil conversion and selectivity to fuels during the fluid catalytic cracking (FCC) process and outperformed ZEO-1 and the highly optimized USY zeolite. This work not only showcases the effectiveness of our powerful strategy by applying MicroED to accelerate the discovery of new nano ELP zeolites such as NJU120-1 and NJU120-2, but also paves the way for future innovations in zeolite synthesis and characterizations.

Preparation and structure determination of NJU120-1 and NJU120-2

Di(1-adamantyl)-*n*-butyl-methylphosphonium was used as the OSDA (fig. S1) for synthesizing NJU120-1 and NJU120-2 in the absence of hydrofluoric acid. In the initial synthesis batch for the combinatorial approach, 16 gel compositions (table S2) were prepared and subjected to crystallization under two hydrothermal conditions: 463 K for 24 days and 448 K for 42 days. Powder XRD (PXRD) analysis revealed that 12 of the combinations crystallized into products with unknown phases under the first condition, and eight of them yielded distinct crystalline products under the second condition (figs. S2 and S3).

Because of the PXRD complexity of the obtained mixtures, high-throughput MicroED was used for rapid phase identification and structure analysis. Before this, these products were calcined at 873 K for 6 hours to recognize those potentially containing new stable zeolites, and entries E01a and E11b were selected for further analysis because of the persistence of their PXRD peaks after calcination (fig. S3). Within just two MicroED sessions (~8 hours), two new nano ELP zeolites, NJU120-1 and NJU120-2, were identified with 10 and three datasets, respectively (Fig. 1, A and C, and tables S3 and S4). After the initial synthesis of impure NJU120-1 and NJU120-2, gel compositions and synthetic conditions were accordingly optimized, and pure products were quickly obtained in just the second synthesis, as confirmed by the synchrotron PXRD (SPXRD) measurements (Fig. 1, B and D).

NJU120-1 and NJU120-2 are both nanocrystals, with nanosheet and nanorod morphologies, respectively (figs. S4 and S5). Such small sizes made it rather challenging to achieve their accurate structures, especially with routine XRD methods. We thus used the advanced continuous rotation electron diffraction (cRED) technique to implement MicroED, which effectively overcame the difficulties associated with nanocrystals and electron beam damage during structure determination (*22*–*27*). Typical reconstructed reciprocal lattices from the cRED datasets are shown in Fig. 1, A and C, and figs. S6 and S7. The complex structures of NJU120-1 and NJU120-2 were then determined with exceptional details using high-quality MicroED data, achieving 82.7 and 94.2% completeness and 0.8 and 1.0 Å resolution after merging 10 and three datasets, respectively.

NJU120-1 crystallized in an orthorhombic unit cell, with the systematic extinctions indicative of the *Imma* space group and dimensions of a = 19.040(4) Å, b = 20.560(4) Å, and c = 40.910(8) Å, whereas NJU120-2 crystallized in a monoclinic unit cell with the space group $P2_1/n$ and dimensions of a = 12.860(3) Å, b = 26.457(5) Å, c = 28.927(6) Å, and β = 98.28(3)° (table S5). All of their T and O atoms were located directly ab initio with *SHELXLT* (*28*), and the resulting framework structures were refined using *SHELXL*, yielding an unweighted residual factor (*R1*) of 0.1622 for NJU120-1 and 0.1433 for NJU120-2. These structures further underwent Rietveld refinement against SPXRD for both as-made and calcined NJU120-1 and NJU120-2, achieving more

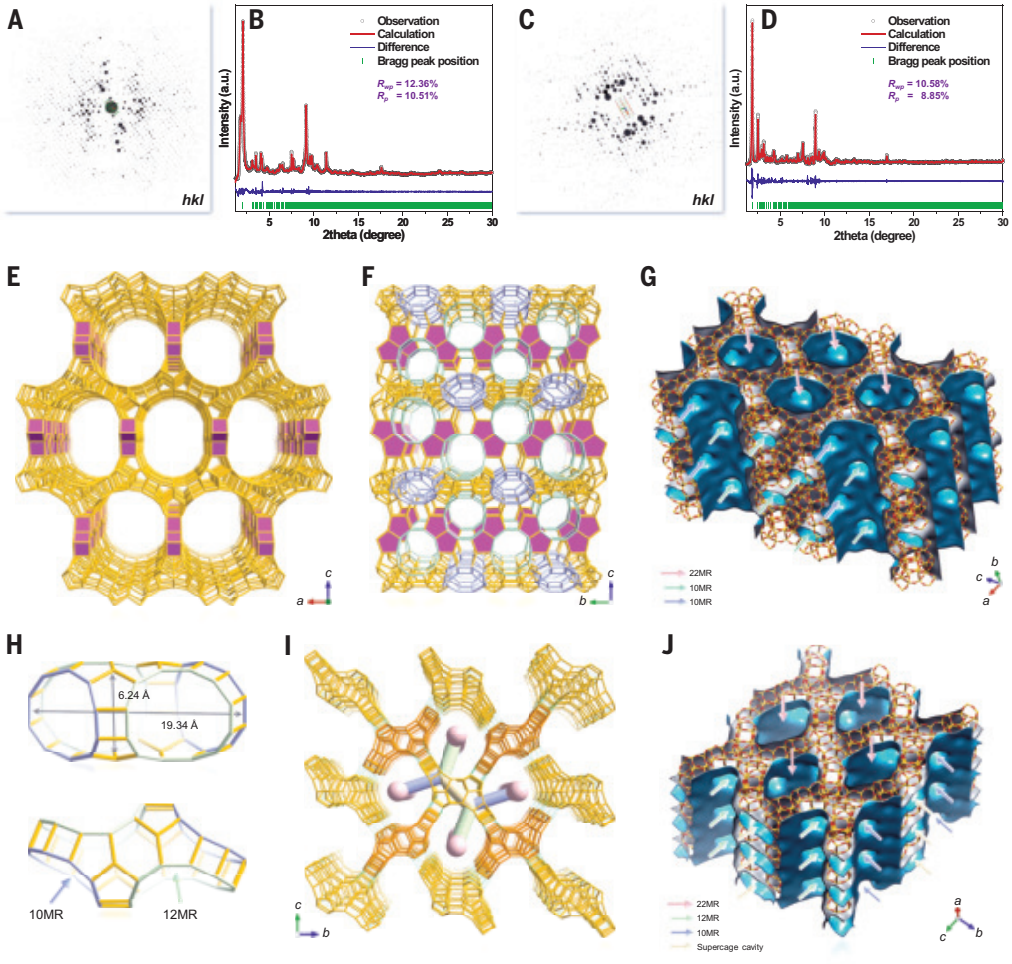

Fig. 1. Identification and structures of NJU120-1 and NJU120-2. (**A** to **D**) Typical reciprocal lattices reconstructed from MicroED and Rietveld refinement plots of SPXRD for as-made NJU120-1 [(A) and (B)] and NJU120-2 [(C) and (D)]. (**E** and **F**) Framework structure of NJU120-1 viewed along the [010] (E) and [100] (F) directions, highlighting the 10MR in the pore wall (light jade), 10MR in the porous layer (light sky blue), and the pillar (or pore wall, orchid). (**G**) Three dimensional (3D) channel system of NJU120-1 with the structure superimposed. (**H** and **I**) NJU120-2 supercage (H) and framework structure formed by two supercage columns (gold and orange) with additional T pairs (translucent green) and viewed along the [100] direction (I), highlighting the 12MR and 10MR pores and apertures (light jade and light sky blue, respectively), supercage cavity (light gold), 22MR pores (light red), and connection among supercages and additional T pairs (translucent green). (**J**) 3D channel system of NJU120-2 with the structure superimposed.

accurate structures with chemically reasonable bond lengths and angles while also confirming sample purity (Fig. 1, B and D; figs. S8 and S9; and tables S6 to S17).

OSDAs within NJU120-1 and NJU120-2 frameworks were determined through a combined MicroED and SPXRD refinement on as-made samples. Specifically, difference electronic potential density maps revealed two crystallographically independent OSDA molecules occupying 22MR pores for both zeolites (figs. S10 and S11). Their number from Rietveld refinement was 14.51 and 8.0 per unit cell for NJU120-1 and NJU120-2, respectively, consistent with the compositions from various chemical analyses: $\backslash C_{25}H_{42}P\backslash_{14.13}\cdot[Si_{179.04}Al_{12.96}O_{384}]$ for NJU120-1 and $\backslash C_{25}H_{42}P\backslash_{8.12}\cdot[Si_{102.23}Al_{9.77}O_{224}]$ for NJU120-2 (fig. S12 and table S18). In NJU120-1, OSDAs extended their long butyl chains into the 10MR pores, whereas in NJU120-2, one crystallographically distinct OSDA stretched an adamantyl group and the butyl chain into the supercage through 12MR pore aperture, along with the latter oriented toward 10MR aperture. These findings suggest that the large adamantyl head and long butyl tail of the OSDA are crucial in directing 22MR, 12MR, and 10MR pores in NJU120-1 and NJU120-2.

Structures of NJU120-1 and NJU120-2

NJU120-1 contained 14 T and 31 O atoms in its crystallographic asymmetry unit (tables S7, S10, and S19), whereas NJU120-2 featured 28 T and 56 O atoms (tables S13, S16, and S20), indicating their complex structures. The large number of unique atoms in NJU120-2 makes it one of the most intricate fully connected zeolites resolved to date, even surpassing the recently reported ZMQ-1 with 18 T and 40 O atoms despite having larger pores. Only zeolites PST-20 (no assigned code so far) and the disordered SSZ-57 (*SFV topology), with respective 29 and 99 T atoms, are more complex (*29*, *30*).

NJU120-1 can be formally viewed as a layer-pillared framework structure and featured a multidimensional 22 × 10 × 10 MR channel system (Fig. 1, E to G; figs. S13 and S14; and table S21). The straight elliptical 22MR ELP runs along the [010] direction (Fig. 1E), whereas the straight 10MR pore in the pore wall and the sinusoidal 10MR pore in the porous layer both extend along the [100] direction (Fig. 1F), and all are interconnected (Fig. 2G and fig. S15). Further topological analysis of the layer-pillared structure, combined with nanosheet morphology and preferred orientation of NJU120-1 (see below) and informed by the principles of reticular chemistry in porous materials (*29*, *31*), enabled us to propose a new and fully connected ELP zeolite family named NJU120-1-G*n* (*n*th generation of NJU120-1). This family uses the porous layer and pore pillar as its structural elements and can be systematically tailored by modulating the layer gliding and the number of interlayer pillars (fig. S16). NJU120-1 represents the third generation, whereas the recent ZMQ-1 also belongs to this family as the fourth generation (*18*). Their successful synthesis strongly demonstrates the feasibility of this predicted ELP zeolite family.

The most distinctive structural feature of NJU120-2 is the presence of a large supercage, with a cavity dimension that approaches 2 nm (Fig. 2H) and surpasses that of the cage in the USY zeolite (1.12 nm). The supercage in NJU120-2 opens through two 12MR and two 10MR pore apertures that are connected through the inner cavity (fig. S17). These supercages are stacked on top of each other along the [100] direction to form two columns, colored gold and orange in Fig. 1I and fig. S18, which are related by the operation ($-x + 1/2$, $y + 1/2$, $-z + 1/2$) and connected by additional T pairs. With this configuration, the NJU120-2 framework structure was achieved, characterized by a multidimensional interconnected 22 × 12 × 10 MR channel system (Fig. 1J, figs. S19 and S20, and table S22). The straight 22MR ELP extends along the [100] direction, whereas the sinusoidal 12MR and 10MR pores run along the [010] and [001] directions, respectively. These pores were all mutually connected through the supercage cavity and 22MR pores, providing a confined yet extended space to facilitate guest diffusion.

The pores in NJU120-1 and NJU120-2 interconnect through 22MR apertures as well as other 10MR or 12MR apertures, forming multidimensional channel systems (Fig. 2, A to H, and figs. S15 and S20). The crystallographic dimension of the 22MR pore aperture in NJU120-1 measured ~15.49 × 12.34 Å (Fig. 2B and table S23), accommodating an LFS with a diameter of 12.05 Å. This LFS surpasses in size those found in other stable and fully connected zeolites, including USY (7.29 Å) and our previously reported ZEO-1 (9.45 Å), ZEO-3 (8.44 Å), and ZEO-5 (11.07 Å) (Fig. 2I and fig. S21). It is also near the LFS of ZMQ-1 (12.15 Å), with larger 28MR pores, which can be attributed to the nearly fixed spacing between adjacent pore walls in the NJU120-1-G*n* family (fig. S16).

These findings indicated that in addition to the number of pore membered rings, LFS diameter may be crucial for evaluating zeolite pore dimensions, because the former cannot guarantee a pore shape adequate for applicable diffusion. In addition, the two 10MR pores in NJU120-1 are also larger than those in industrial ZSM-5 and TS-1 zeolites (both MFI topology) (Fig. 2, C and D). The 22MR pore in NJU120-2 is also impressive, with a larger crystallographic aperture of ~16.64 ×

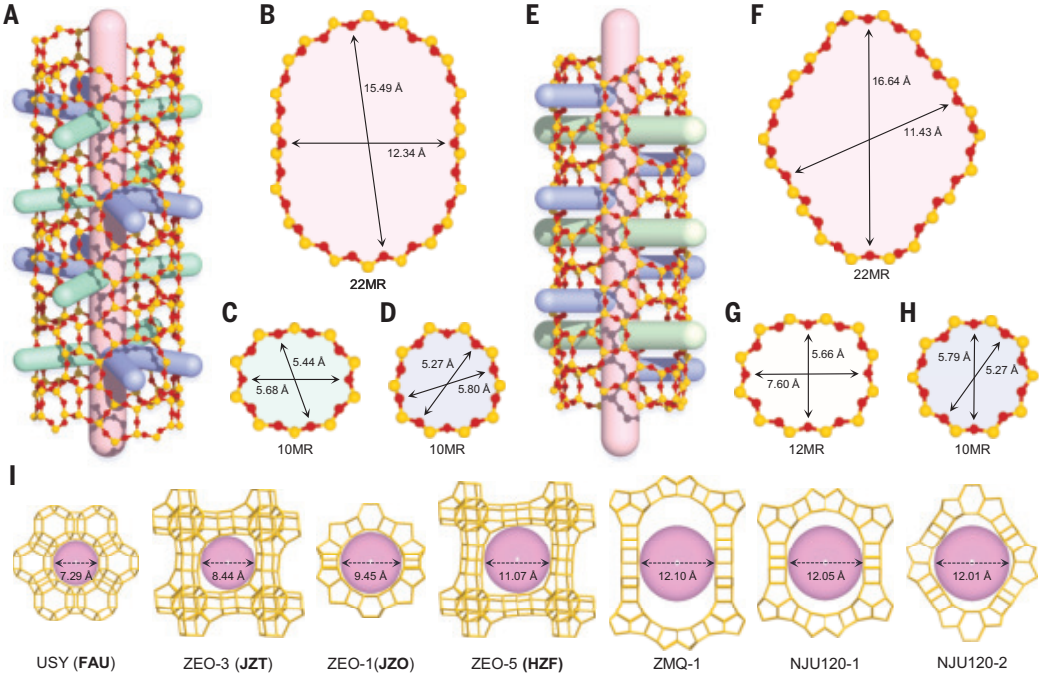

Fig. 2. Pores of NJU120-1 and NJU120-2. (**A**) 3D interconnected channel system of NJU120-1. (**B** to **D**) Crystallographic pore apertures of NJU120-1. (**E**) 3D interconnected channel system of NJU120-2. (**F** to **H**) Crystallographic pore apertures of NJU120-2. (**I**) Comparison of the LFS diameters of zeolites USY, ZEO-3, ZEO-1, ZEO-5, and ZMQ-1 with those of NJU120-1 and NJU120-2.

11.43 Å (Fig. 2F) and an LFS of diameter of 12.01 Å. In addition, the 12MR and 10MR pore apertures in NJU120-2 were comparable to those in industrial USY and MFI zeolites, respectively. Such exceptional pore characteristics endowed NJU120-1 and NJU120-2 with a low calculated density of 1.296 and 1.272 g/cm^3 (in SiO_2 form) and a low framework density of 12.99 and 12.75 T/1000 Å^3, respectively. Although the framework densities of NJU120-1 and NJU120-2 are higher than that of ITQ-70 (10 T/1000 Å^3), a recent pure silica zeolite with smaller 18MR pores and highly concentrated ordered defects (*32*), only ZMQ-1 and ZEO-5 had a lower framework density among the fully connected zeolites (table S23). These pore properties place NJU120-1 and NJU120-2 among the few zeolites with the largest pores and most open framework structures.

Physicochemical properties and catalysis

The structures of NJU120-1 and NJU120-2 were further validated by spherical aberration (Cs)–corrected scanning transmission electron microscopy (STEM). Examination of the cross section of NJU120-1 revealed that the overall thickness of the multilamellar stacked nanosheets was ~8 nm, which corresponded to the *c*-axis dimension of just 1.5 unit cells (Fig. 3, A to D, and figs. S22, A and B, and S23). The nanosheets were so thin, they were even flexible. These ultrathin NJU120-1 nanosheets were directly synthesized without precursor exfoliation or the use of expensive surfactants with associated treatments. Such a low thickness is also exceptionally rare among all known zeolites, and to our knowledge, NJU120-1 is the first reported ELP zeolite with an ultrathin nanosheet morphology of unit-cell thickness.

The NJU120-1 nanosheets extend in the *ab* plane, with the 22MR and 10MR pores aligned parallel to the nanosheet plane (fig. S22, C and D). This preferential growth might result from the inherent layer-pillared structure of NJU120-1, likely driven by the higher crystallization energy along the *c*-axis (perpendicular to the porous layers).

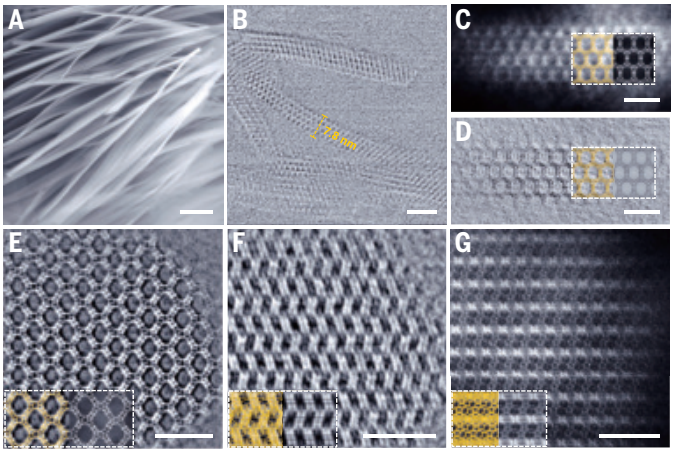

Fig. 3. Electron microscopy structures of NJU120-1 and NJU120-2. (**A**) Scanning electron micrograph (SEM) image of NJU120-1 nanosheets. (**B**) Unit-cell-thick NJU120-1 nanosheets with clear 22MR ELPs treated with a Wiener filter to reduce low-frequency signals for enhanced contrast (*33*). (**C** and **D**) Images of integrated differential phase contrast STEM (C) and annular bright-field STEM (D) of a single NJU120-1 nanosheet with straight and elliptical 22MR pores viewed along the [010] zone axis. (**E** to **G**) Integrated differential phase contrast STEM [(E) and (F)] and high-angle annular dark-field STEM (G) images of NJU120-2, with the straight and rhombic 22MR ELPs viewed along the [100] zone axis (E), sinusoidal 10MR pores viewed along the [001] zone axis (F), and overlapped sinusoidal 12MR and 10MR pores viewed along the [011] zone axis (G). Superimposed insets highlighted by white dotted boxes in (C) to (G) are corresponding framework structures (left) and simulated STEM images (right). Scale bars, 200 nm for (A), 10 nm for (B), and 5 nm for (C) to (G).

In terms of NJU120-2, which features a nanorod morphology with an average diameter of ~50 nm and a length of ~250 nm, STEM investigation on its cross section uncovered that its 22MR pores run along the long axis of the nanorod, indicating its preferential crystallization along the [100] direction (Fig. 3, E to G, and fig. S22, E to H). These findings supported the NJU120-1 and NJU120-2 structures obtained from MicroED.

During synthesis, the OSDA remained intact within the NJU120-1 and NJU120-2 pores, as confirmed by the ^{31}P and ^{13}C nuclear magnetic resonance (NMR) measurements (figs. S24 and S25). Upon calcination at 873 K in air, these OSDA molecules decomposed, leaving behind phosphate-like species, whereas the framework structures were well preserved, as seen from the ^{29}Si and ^{27}Al NMR spectra, although some Al species became hexacoordinated and slightly pentacoordinated during this process (figs. S26 and S27). After treatment with an NH_4Cl solution, the phosphate-like species was removed and the hexacoordinated and minor pentacoordinated Al atoms disappeared by both removal and reversion to tetrahedral sites (figs. S24 and S27), resulting in phosphorus-free (P-free) zeolites with clean and accessible pores and an increased Si/Al ratio (table S18).

Both NJU120-1 and NJU120-2 exhibited Ia-type N_2 adsorption behavior (figs. S28 and S29), and their specific surface areas and micropore volumes were calculated to be as high as 957 and 1007 m^2/g and 0.32 and 0.35 cm^3/g, respectively. In addition, the pore size distributions, determined from the Ar adsorption measurements using nonlocal density functional theory methods, peaked at ~10.16 and 16.86 Å for NJU120-1 and at ~10.9 and 16.88 Å for NJU120-2, which matched the 22MR pore apertures and aligned well with their crystallographic values (figs. S30 and S31). Furthermore, NJU120-1 and NJU120-2 both displayed an H4 hysteresis loop in their adsorption and desorption profiles, indicative of the presence of a number of mesopores corresponding to the accumulated voids formed between nanocrystals. The P-free NJU120-1 and NJU120-2 frameworks demonstrated high thermal stability at temperatures up to 1273 K and relatively high hydrothermal stability upon steaming at 1073 K under 50% relative humidity (figs. S32 and S33).

The aluminum species within the NJU120-1 and NJU120-2 frameworks can serve as the solid-state acid centers for catalysis, which largely remain preserved after steam treatment, as shown by NH_3 temperature programmed desorption (NH_3-TPD; figs. S37 and S39 and table S25). To assess their intrinsic catalytic capabilities without the influence of occluded phosphorus, we conducted benchmark FCC tests using commercial vacuum gas oil (VGO; table S26) on P-free NJU120-1 and NJU120-2, with P-free ZEO-1 and commercial zeolites USY and Beta as the controls. NJU120-1 exhibited superior cracking efficiency for VGO, with less coke formation and higher conversion of heavy oil (Fig. 4 and table S27). In addition, it favored a larger fraction of high-value fuels, particularly gasoline and diesel, which together accounted for nearly 60% of the total products.

By contrast, although NJU120-2 initially exhibits lower heavy oil conversion with higher coke formation, its FCC performance notably improves after regeneration: The fraction of high-value fuels approaches 51% in the fifth run, alongside reduced coke formation and enhanced heavy oil conversion (fig. S40 and table S28). In addition, among the liquefied petroleum gas products, both NJU120-1 and NJU120-2 demonstrated a higher selectivity for propylene, an essential petrochemical feedstock, over propane, a performance not observed with any of the control catalysts. Even after consecutive catalytic runs, the product distribution of NJU120-1 remained nearly unchanged, whereas it became favorable for NJU120-2, indicating activity retention and catalytic activation, respectively (fig. S40 and table S28). This was further corroborated by their retained framework structures after FCC cycles despite a slight decrease in specific surface area and micropore volume (figs. S32 to S35 and table S24). These preliminary catalytic tests underscore the potential of NJU120-1 and NJU120-2

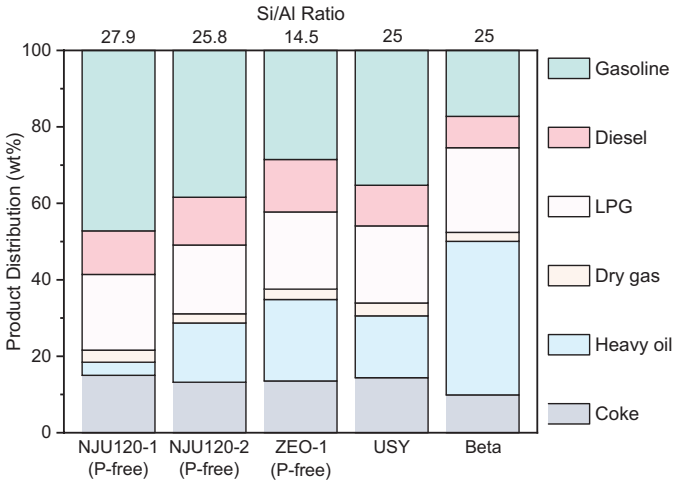

Fig. 4. FCC performance of VGO over zeolite catalysts. The performance of NJU120-2 shown is from the fifth run. Reaction conditions: 0.18- to 0.45-mm fraction, catalyst/oil ratio of 1, pressure of 1 atm, temperature of 773 K, and weight hourly space velocity of 51.4 hours^{-1}.

as efficient acid-based heterogeneous catalysts. Their exceptional performance can be attributed to the larger 22MR pores and nano morphologies for facilitated mass transfer, highlighting the importance of developing nano ELP zeolites with enhanced catalytic activity.

Outlook

Stable and fully connected zeolites with ELPs and nano dimensions are highly sought after because of their ability to boost diffusion pathways for enhanced applications, and this is well exemplified by NJU120-1 and NJU120-2 reported herein. Although the designed synthesis of such nano ELP zeolites faces considerable challenges, our study offers a compelling example for the future development of this field. A key factor in achieving these targeted structure features and properties lies in the OSDAs applied. The MicroED technique for the rapid polycrystalline multiphase structure analysis, combined with combinatorial chemistry synthesis, could help in the development of new nano ELP zeolites, including the missing members of the NJU120-1-G*n* family, and may also enhance our understanding of the relationships among synthetic conditions, OSDAs, and the resulting zeolite structures.

REFERENCES AND NOTES

1. H. Dai *et al.*, *Nat. Mater.* **19**, 1074–1080 (2020).
2. E. M. Gallego *et al.*, *Science* **355**, 1051–1054 (2017).
3. B. Yilmaz, U. Müller, *Top. Catal.* **52**, 888–895 (2009).
4. E.-P. Ng, D. Chateigner, T. Bein, V. Valtchev, S. Mintova, *Science* **335**, 70–73 (2012).
5. J. Jiang, J. Yu, A. Corma, *Angew. Chem. Int. Ed.* **49**, 3120–3145 (2010).
6. M. Choi *et al.*, *Nature* **461**, 246–249 (2009).
7. X. Wang, Y. Ma, Q. Wu, Y. Wen, F.-S. Xiao, *Chem. Soc. Rev.* **51**, 2431–2443 (2022).
8. A. Inayat, I. Knoke, E. Spiecker, W. Schwieger, *Angew. Chem. Int. Ed.* **51**, 1962–1965 (2012).
9. K. Lu *et al.*, *Angew. Chem. Int. Ed.* **59**, 6258–6262 (2020).
10. H. Y. Luo, V. K. Michaelis, S. Hodges, R. G. Griffin, Y. Román-Leshkov, *Chem. Sci.* **6**, 6320–6324 (2015).
11. V. J. Margarit, M. E. Martínez-Armero, M. T. Navarro, C. Martínez, A. Corma, *Angew. Chem. Int. Ed.* **54**, 13724–13728 (2015).
12. Y. Wang *et al.*, *J. Mater. Chem. A* **7**, 7573–7580 (2019).
13. H. Yu, L. A. Villaescusa, Z. R. Gao, M. A. Camblor, *Angew. Chem. Int. Ed.* **63**, e202412170 (2024).
14. Y. Li, J. Yu, *Chem. Rev.* **114**, 7268–7316 (2014).
15. M. D. Foster, I. Rivin, M. M. J. Treacy, O. Delgado Friedrichs, *Microporous Mesoporous Mater.* **90**, 32–38 (2006).
16. https://www.iza-structure.org/databases/
17. Q.-F. Lin *et al.*, *Science* **374**, 1605–1608 (2021).
18. P. Lu *et al.*, *Nature* **636**, 368–373 (2024).
19. A. J. Mallette, K. Shilpa, J. D. Rimer, *Chem. Rev.* **124**, 3416–3493 (2024).
20. J. Li *et al.*, *Science* **379**, 283–287 (2023).
21. Z. R. Gao *et al.*, *Nature* **628**, 99–103 (2024).
22. T. Yang, T. Willhammar, H. Xu, X. Zou, Z. Huang, *Nat. Protoc.* **17**, 2389–2413 (2022).
23. Z. Huang, E. S. Grape, J. Li, A. K. Inge, X. Zou, *Coord. Chem. Rev.* **427**, 213583 (2021).
24. Z. Huang, T. Willhammar, X. Zou, *Chem. Sci.* **12**, 1206–1219 (2020).
25. W. Wan, J. Sun, J. Su, S. Hovmöller, X. Zou, *J. Appl. Crystallogr.* **46**, 1863–1873 (2013).
26. Z. Zhang, Z. Liang, C. Ma, C. Lin, J. Li, *Sci. China Chem.* **67**, 4158–4166 (2024).
27. Z. Zhang, C. Lin, J. Li, *Small Methods* **9**, e2401461 (2024).
28. G. M. Sheldrick, *Acta Crystallogr. A Found. Adv.* **71**, 3–8 (2015).
29. P. Guo *et al.*, *Nature* **524**, 74–78 (2015).
30. C. Baerlocher, T. Weber, L. B. McCusker, L. Palatinus, S. I. Zones, *Science* **333**, 1134–1137 (2011).
31. O. M. Yaghi, M. J. Kalmutzki, C. S. Diercks, *Introduction To Reticular Chemistry: Metal-Organic Frameworks and Covalent Organic Frameworks* (Wiley, 2019).
32. J. I. Tirado *et al.*, *Angew. Chem. Int. Ed.* **64**, e202416515 (2025).
33. R. Kilaas, *J. Microsc.* **191**, 45–51 (1998).
34. C. Ma *et al.*, Data for: Accelerated discovery of stable, extra-large-pore nano zeolites with micro-electron diffraction, Zenodo (2025); https://doi.org/10.5281/zenodo.15245451.

ACKNOWLEDGMENTS

We thank J. Shi (Chongqing University) and S. Guo (NJU) for valuable discussions on OSDA design; Y. Deng (NJU) for assistance with TEM characterizations; K. Yan (PolyU) and C. F. Chan (PolyU) for assistance with NMR measurements; the State Key Laboratory of Coordination Chemistry (NJU), J. Zuo (NJU), and C. Duan (NJU) for support in the startup of our research group; beamlines BL14B1 and BL17B of the National Facility for Protein Science (NFPS) at the Shanghai Synchrotron Radiation Facility (SSRF) and 19A of the Taiwan Photo Source (TPS) in SPXRD for data collection; the Sub-Atomic Resolution Electron Microscopy Laboratory at the College of Engineering and Applied Sciences of Nanjing University (NJU) for MicroED data collection; and the University Research Facility in Chemical and Environmental Analysis (UCEA) of The Hong Kong Polytechnic University (PolyU) for NMR measurements. **Funding:** This work was supported by the National Key Research and Development Program of China (grant 2024YFA1510301), the Fundamental Research Funds for Central Universities of China (grant 0205-14380334), the National Natural Science Foundation of China (grants 22371121 and 22403080), the Natural Science Foundation of Jiangsu Province (grant BK20230772), the Beijing National Laboratory for Molecular Sciences (grant BNLMS202402), and Start-up Fund for RAPs under the Strategic Hiring Scheme of the Hong Kong Polytechnic University (grant P0047841). **Author contributions:** J.L. conceived the project and supervised the study. C.M. and M.Z. performed the synthesis. Z.H.Z. conducted structure analysis and the (S)TEM characterizations. C.L., G.C.L., B.T.W.L. and K.F.Y. performed the structure and topology analysis, SPXRD, and NMR measurements. L.H., H.T.S., and W. L. performed the catalytic tests. X.T. and L.X. performed the NH_3-TPD experiments. J.L., C.L., and M.A.C. prepared the initial draft of the manuscript. All authors discussed the results and contributed to revising the final manuscript. **Competing interests:** J.L. and C.M. have filed a patent on NJU120-1 and NJU120-2 (Chinese patent application no. 202410861721.5), for which Nanjing University holds the rights. The remaining authors declare no competing interests. **Data and materials availability:** All datasets generated and/or analyzed in the present study are available in the main text or the supplementary materials. The adsorption information files (AIFs) for NJU120-1 and NJU120-2 used in the adsorption studies have been deposited at Zenodo (*34*). The crystallographic information files (CIFs) for the structures of NJU120-1 and NJU120-2, refined using cRED data and Rietveld refinement against SPXRD data, have been deposited at the Cambridge Crystallographic Data Centre (www.ccdc.cam.ac.uk/) under reference numbers 2427489 (NJU120-1_as-made_cRED), 2427488 (NJU120-2_as-made_cRED), 2427920 (NJU120-1_as-made_SPXRD), 2427486 (NJU120-2_as-made_SPXRD), 2427485 (NJU120-1_cal_SPXRD), and 2427487 (NJU120-2_cal_SPXRD).

SUPPLEMENTARY MATERIALS

science.org/doi/10.1126/science.adv5073
Materials and Methods; Supplementary Text; Figs. S1 to S40; Tables S1 to S28; References (*35*–*85*)

Submitted 22 December 2024; accepted 30 April 2025

10.1126/science.adv5073

ADAPTATION

Rapid polygenic adaptation in a wild population of ash trees under a novel fungal epidemic

Carey L. Metheringham[1,2]†, William J. Plumb[1,2,3]‡, William R. M. Flynn[4,5], Jonathan J. Stocks[1,2]§, Laura J. Kelly[1,2], Miguel Nemesio Gorriz[3]¶, Stuart W. D. Grieve[4,6], Justin Moat[2], Emily R. Lines[7], Richard J. A. Buggs[1,2]*, Richard A. Nichols[1]*

Rapid evolution through small shifts in allele frequencies at thousands of loci is a long-standing neo-Darwinian prediction but is hard to characterize in the wild. European ash tree (*Fraxinus excelsior*) populations have recently come under strong selection by the invasive fungal pathogen *Hymenoscyphus fraxineus*. Using genomic prediction models based on field trial phenotypes and 7985 loci, we show a shift in genomically estimated breeding values in an ancient woodland, between adult trees established before the epidemic started and juvenile trees established since. Using simulations, we estimate that natural selection has eliminated 31% of the juvenile population. Thus, we document a highly polygenic heritable microevolutionary adaptive change over a single generation in the wild.

Whether complex traits typically adapt to new environments through large allele frequency changes in a few loci or through small allele frequency changes in many loci is an open question in evolutionary biology (*1*–*5*). While theory suggests that a highly polygenic response should be rapid and effective (*3*–*6*), it is far easier in nature for population geneticists to demonstrate cases of natural selection involving low numbers of loci with a large effect size (*7*–*10*). Although the methods of quantitative genetics can show, by statistical comparison of related individuals, that additive genetic variance exists for complex traits under selection, it has often not been possible to show by these methods that response to selection is occurring (*11*–*14*). This situation has led to a disconnect between population genetics and quantitative genetics. Genomic prediction approaches, developed for agricultural breeding, that use genome-wide single-nucleotide polymorphism (SNP) data to predict individuals' genetic merit for a quantitative trait of interest, can enable us to bridge this gap (*5*, *15*, *16*). If we can show genome-wide allele frequency differences before and after the arrival of a new selective pressure (*17*) or in different age classes at a single time point (*12*, *18*–*22*), affecting genetic merit, a polygenic response to selection could be demonstrated.

The possibility of a rapid adaptive response is of particular interest in the case of the ash dieback epidemic that has swept across Europe in the past three decades, caused by the fungus *Hymenoscyphus fraxineus*, an invasive from East Asia (*23*). Numerous studies based on planted trials suggest that heritable variation in susceptibility to the fungus exists within European ash (*Fraxinus excelsior*) populations (*24*–*27*). The intensity of selection on viability may be stronger in smaller, younger ash trees, as they are observed to die more rapidly from ash dieback infection than larger, older trees (*28*, *29*). Rapid juvenile mortality may occur because the fungus can more quickly encircle the main stem and because smaller trees are closer to the leaf litter where *H. fraxineus* apothecia are produced. Recruitment of the next generation may also be affected by reduced reproduction by adult trees damaged but not yet killed by the fungus (*30*, *31*).

It has been hypothesized that mortality of susceptible juvenile trees and reduced reproduction by susceptible adult trees will drive changes in allele frequencies leading to an increase in disease resistance in the next generation of ash (*24*, *27*). In a previous study, based on 38,784 ~7-year-old ash trees from British, Irish, and German provenances growing in field trials, we sequenced the 623 healthiest trees [a score of 7 on the scale of Pliūra *et al.* (*32*)] and 627 trees whose woody tissues were highly damaged by ash dieback (mainly scores 4 or 5). We used a genome-wide association study (GWAS) to rank loci associated with these phenotypes by *P* value (*26*) and used sets from 100 to 50,000 of the top loci to train genomic prediction models, which were tested on 148 trees. We found that 10,000 loci gave genomic estimated breeding values (GEBVs) with the highest frequency of correct allocations of test trees (0.67) (*26*). We here calculate that these GEBVs explained 24.0% [confidence interval (CI): 11.5 to 37.0%] of the phenotypic variation in the test population's damage due to the fungus (see materials and methods in the supplementary materials).

If natural selection is acting on natural ash populations under high disease pressure, we would expect to see GEBVs increase in the younger generation of trees that have been exposed to infection since germination, with shifts in allele frequencies that correlate with their effect sizes. In this study, we tested this hypothesis in a woodland located within the geographic sample range of Stocks *et al.* (*26*).

Phenotypic and genomic characterization of an ash population

Our study site, Marden Park wood, is an ancient seminatural woodland dominated by *F. excelsior*, where the pathogen *H. fraxineus* is thought to have been present since 2012 (fig. S1). It is located in UK Native Seed Zone number 405, a provenance included in the previous trials (*26*). Phenotypic assessments of this woodland in 2019, when we collected ash tissue samples for sequencing, found *H. fraxineus* symptoms on the majority of trees (Fig. 1) and no evidence for felling or removal of dead trees. Damage from the fungus had further increased by 2021, especially in juvenile trees (Fig. 1). This fits with widespread documentation of the ongoing progress of the ash dieback epidemic throughout Europe (*29*, *33*).

We generated short-read sequence data for 580 individuals (128 adults, which had established pre-epidemic, and 452 post-epidemic juveniles; fig. S2) and 30 technical replicates at ~11× whole-genome coverage and estimated allele frequencies at ~9 million SNP loci. Of the 10,000 SNPs used for genomic prediction in the trials (see above), 7985 were variable in the Marden Park dataset and passed allele frequency and quality thresholds. This smaller number of polymorphic SNPs reflects the lower genetic diversity present in Marden Park wood than in the planted trials, which included many seed zones. Of the 2015 SNPs that were not variable in the Marden Park population, 1055 were fixed for the allele associated with low ash dieback damage in the planted trials and 960 for the allele associated with high damage.

We calculated GEBVs for the Marden Park trees from the 7985 polymorphic SNPs using the parameters of the genomic prediction model trained on the field trials (*26*). Our visual assessments of ash dieback damage, scored on a five-point scale for juveniles (a similar method to that used in the trials) and as percentage canopy cover in adults, showed no significant relationship with individual's GEBV scores (figs. S3 and S4). A weak relationship between individual GEBVs and phenotypes assessed in the field is expected because of the large environmental component of damage phenotypes in the wild, owing to local microenvironments, age differences within cohorts, and presence of other microorganisms. In addition, the phenotypic scoring method we

[1]School of Biological and Behavioural Sciences, Queen Mary University of London, London, UK. [2]Science Directorate, Royal Botanic Gardens, Kew, Richmond upon Thames, UK. [3]Forestry Development Department, Teagasc, Dublin, Republic of Ireland. [4]School of Geography, Queen Mary University of London, London, UK. [5]Department of Plant Sciences, University of Cambridge, Cambridge, UK. [6]Digital Environment Research Institute, Queen Mary University of London, London, UK. [7]Department of Geography, University of Cambridge, Cambridge, UK. ***Corresponding author. Email: r.buggs@kew.org (R.J.A.B.); r.a.nichols@qmul.ac.uk (R.A.N.)** †Present address: School of Life Sciences, University of Dundee, Nethergate, Dundee, Scotland, UK. ‡Present address: Jealott's Hill International Research Centre, Syngenta, Bracknell, Berkshire, UK. §Present address: Forestry England, Lyndhurst, Hants, UK. ¶Present address: Mejora y Conservación de Recursos Genéticos Forestales, Grupo Tragsa–SEPI, Paterna, Valencia, Spain.

used on adult trees is, by necessity, different to the method used to evaluate juveniles in the field trials. Hence, we might not expect the canopy cover of a mature tree in a woodland to be an accurate predictor of its breeding value for susceptibility to fungal damage in juvenile trees.

When environmental effects are large, breeding values of adult trees are better estimated from the phenotypes of their progeny than from their own phenotype (*34*). For 36 adult trees, we were able to apply this approach by identifying offspring ($n = 121$) among the juveniles, using the sequoia R package (*35*) on 1000 SNPs. For these, we found significant correlation between the GEBV of the parent trees and the mean health score of their offspring [Pearson correlation coefficient (r) = 0.368, $P = 0.029$, $n = 36$; Fig. 2A], suggesting that our GEBVs are predicting breeding values relevant to the vulnerable juvenile stage (this will be an underestimate if selection has already eliminated the more susceptible individuals; see below). In contrast, our visual assessment of the parent trees' health was a poor predictor of the mean phenotypic health score of the offspring ($r = 0.112$, $P = 0.54$, $n = 36$; Fig. 2B).

A more systematic assessment of adult tree health was obtained from the rate of spring green-up from April to June in the 53 largest trees. These rates were estimated from three-dimensional red-green-blue point cloud data using structure-from-motion analysis of sensor imagery from a consumer-grade uncrewed aerial vehicle. The progress of each tree's greening was measured by the normalized green chromatic coordinate. Green-up occurred at a higher rate, s, in trees with higher GEBVs [estimated s:GEBV interaction = 0.23, 95% CI = 0.01 to 0.53; table S4 and fig. S5]. This trend is consistent with the positive association between the degree of leaf bud burst in early May and resistance to ash dieback in a Lithuanian study (*36*).

Evidence for allele shifts due to natural selection

We found a shift in mean disease susceptibility GEBV between adult trees and juvenile trees in our population. The mean GEBV of juvenile trees ($\mu = 0.22$, $n = 452$) was higher than the mean GEBV of adult trees ($\mu = 0.15$, $n = 128$; Fig. 3A), with a shift of 0.07 (95% CI: −0.016 to 0.142). This shift is 18% of the standard deviation of adult GEBVs (0.39), which, given a heritability (h^2) of 0.24, is equivalent to an improvement in damage score by 9% (0.18h) of its SD. The statistical significance of the 0.07 increase in mean GEBV cannot be evaluated by treating each juvenile tree as an independent observation, as some adults have left multiple offspring. Instead, we compared the GEBV score of each juvenile individual with that predicted from its ancestry. If the surviving juveniles have atypically high GEBV scores, then, on average, their scores should be higher than predicted from their ancestry. To capture this ancestry, we characterized relatedness between juveniles and adults by selecting 5793 loci, which do not contribute to our estimate of breeding value, that were not in close linkage with the 7985 GEBV sites or with one another, had no missing data, and had minor allele frequencies of >0.3. The additive relatedness matrix among adults and juveniles calculated from these 5793 loci was used to predict the juvenile GEBVs from the actual GEBVs of related adults. These predictions were significantly lower ($P = 0.001$, t test of the intercept in regression) than the actual juvenile GEBVs (regression in Fig. 3B), giving a shift of 0.054. The higher-than-predicted GEBV in the living juveniles would be expected if part of their cohort with lower GEBV had not survived. This difference is smaller in magnitude than the 0.07 difference between adult and juvenile means. We would expect the 0.054 value to be an underestimate, as it deliberately excludes the variation in mating success of adults because those effects could include random differences in fertility and fecundity that are components of genetic drift (not selection).

Three additional lines of evidence show that the changes in allele frequencies between parents and offspring are due to selection. First, the variance in allele frequency between parents and juveniles is much greater at GEBV loci than at unlinked putatively neutral loci, unless we remove the effects of selection in the former. The intergenerational change for the 5793 neutral loci was $F = 0.00033$ (SE: 0.00005), indicating minimal genetic change between adult and juvenile cohorts, corresponding to an effective population size, $1/(2F)$, of 1515. In contrast, the 7985 GEBV loci had more than double the variance, $F = 0.00079$ (SE: 0.0007), which is significantly greater ($P = 0.0006$, permutation test). To estimate the effect of drift on the GEBV loci, we modeled and removed the selective component of change, modeled as a function of effect sizes and frequency of alleles at each locus, yielding a drift estimate of $F = 0.00028$, a value that is very close to, and not significantly different ($P = 0.65$) from, the value for the neutral loci. Thus, the contribution of genetic drift to changes at the GEBV loci is indistinguishable from the neutral loci, and the larger allele shift in the GEBV loci is attributable to selection.

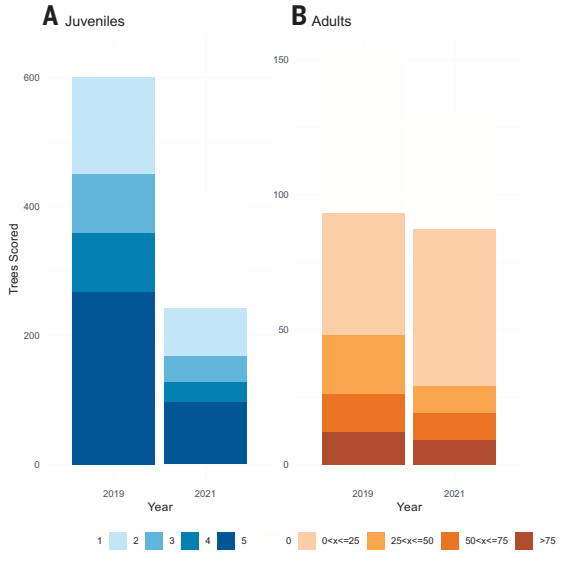

Fig. 1. Phenotypic health assessments of trees that were labeled and genome sequenced in 2019. (**A**) Juvenile tree health scores (where a score of 5 is the most healthy) in 2019 and 2021. (**B**) Adult tree percentage canopy coverage estimates in 2019 and 2021. A number of labels were missing by 2021, especially among juveniles, and only labeled trees were reassessed.

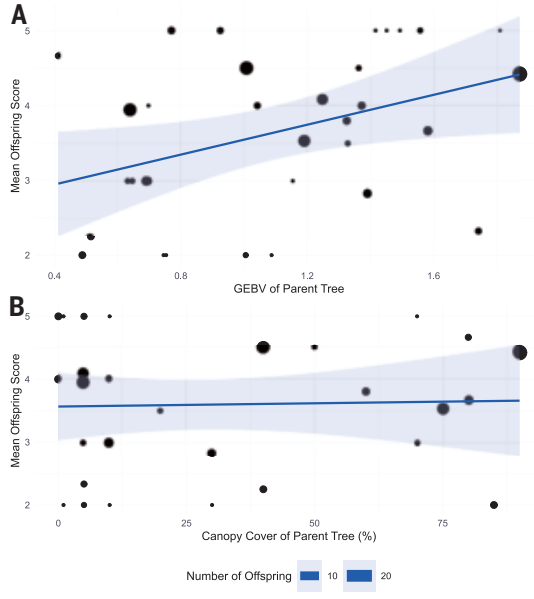

Fig. 2. Correlation of GEBVs and phenotypes of parent trees with phenotypes of offspring. (**A**) GEBV of 36 adult parent trees and (**B**) canopy cover of the same trees correlated with the mean phenotypic health score of 121 juvenile offspring (as assigned in sequoia), weighted by the number of offspring trees assigned to each parent.

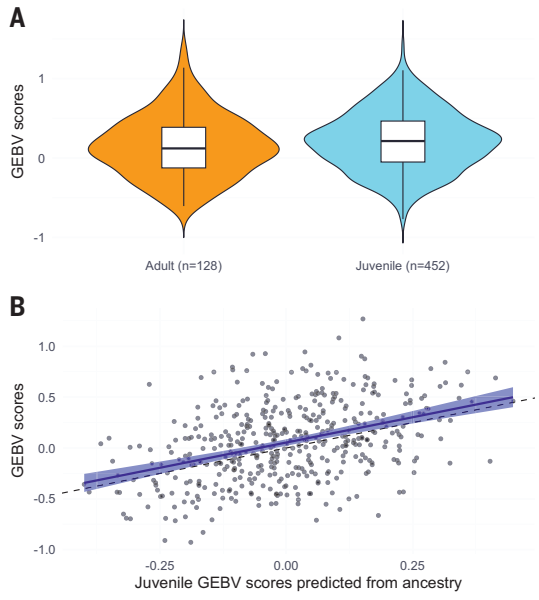

Fig. 3. Shift in GEBV between adult and juvenile trees. (**A**) Genomic estimates of breeding values for 128 adult trees and 452 juvenile trees calculated from 7985 SNP loci using the model trained on large planted trials. (**B**) Each juvenile tree's GEBV based on the 7985 loci, plotted against an alternative prediction based on ancestry alone via an rrBLUP model trained on the adult trees' GEBVs. The fitted regression line (blue) is significantly greater than the 1:1 line (dashed black), demonstrating higher-than-expected GEBVs in the juvenile cohort. Standard error of the fitted regression is shown by the blue shaded area.

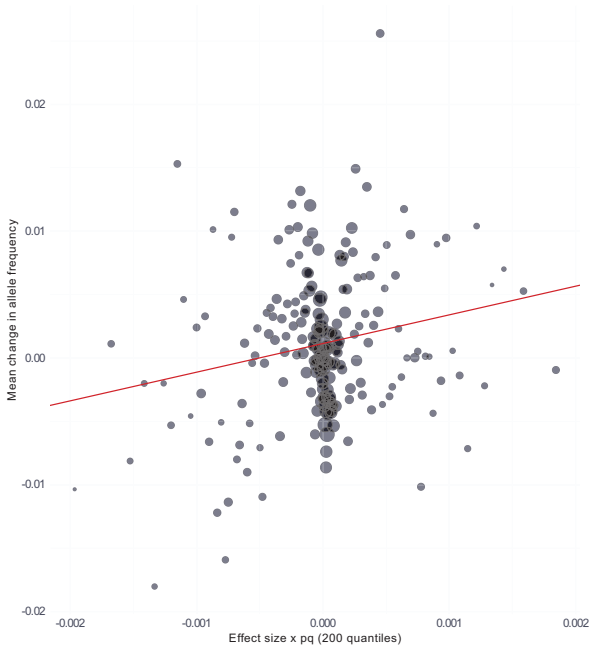

Fig. 4. Mean change in allele frequency between adults and juveniles. Mean change in allele frequency plotted against the product of effect size and the allele frequencies of the major and minor alleles (p and q, respectively) minor allele frequency. The values for 7985 sites have been combined into 200 points. Each point represents the average of 39 or 40 sites (adjacent values of effect size x pq, binned), with area representing the precision of the mean change [1/var(Δp)]. The red line is the fitted linear regression.

Second, we also detect a pattern whereby the direction and size of changes are proportional to the estimated effect sizes and frequency of alleles at each locus, so that larger changes are at alleles at intermediate frequencies with large effect sizes (Fig. 4). The regression was highly significant ($r = 0.0015$, $P = 0.00038$, $F = 12.64$ on 1 and 7983 degrees of freedom). This pattern also supports the case that the changes at GEBV loci are caused by selection rather than chance. To test whether the regression was affected by the precision of the estimates of E_i for each locus (as measured by its standard error SE_i) the regression was repeated with each locus inversely weighed by SE_i^2. The result was essentially unaffected, with the regression coefficients differing by only 0.03%.

Third, an individual-focused prediction of the change in GEBV allele frequencies can be directly tested in the case of the 121 juveniles for which we were able to assign at least one parent with confidence (see above). In these cases, we could predict the allele frequencies expected by random transmission. The observed frequencies were significantly different from these random expectations ($P < 0.05$, Wilcoxon rank sum test with Bonferroni correction). The advantageous alleles, associated with low susceptibility to ash dieback, were overrepresented, the excess frequency being correlated with effect size ($r = 0.0595$, $P < 10^{-6}$). This pattern again suggests that the offspring carrying these alleles had a selective advantage, making them more likely to survive to become part of our sample (compared with siblings that did not).

To further explore the polygenic nature of the shift in GEBVs between adults and juveniles, we calculated the proportion of total variance in GEBVs contributed by the loci on each 1-kbp (kilo–base pair) segment of our contig assembly. To explain 90% of the variance required 2123 of these segments, which carried 3752 GEBV SNPs (out of 7985), which are on 1342 different contigs (out of 2783 carrying GEBV SNPs). To exclude the possibility that the shift in GEBV between parents and offspring was explained by a few segments of large effect, we reran the analysis, excluding the segments of the genome accounting for the top 25% of variance. The remaining loci still showed a substantial and highly significant shift of 0.046 ($P = 0.0012$) between juveniles' GEBVs and that predicted for them by their relatedness to adults. This consistent pattern across the genome underlines the highly polygenic nature of the selection occurring in the woodland.

Simulation

To evaluate the effectiveness of our study design in estimating small effects at a large number of loci and to quantify selection over a single generation, we conducted a simulation of our entire study. First, we simulated the pooled-GWAS and genomic prediction experimental design (*26*). Genotypes at 7985 loci were generated as random binomial draws using the empirical estimates of the allele frequencies. Susceptibility phenotypes were calculated for these genotypes using the empirical estimates of the corresponding effect sizes and a random environmental effect that conferred a heritability of 0.4. High and low susceptibility pools were generated corresponding to the proportion of trees selected for the pools in the real experiment. These pools were used to estimate a relative effect size for each locus using rrBLUP. The relative effect sizes (E) were estimated convincingly (fig. S6), albeit with some error [coefficient of determination (R^2) = 0.30]. When the effects at multiple loci are summed, they allow for accurate genomic prediction ($R^2 = 0.39$; fig. S7).

Next, we simulated a population with the observed adult GEBV scores and the observed additive relationship matrix at the neutral loci. We implemented selective deaths caused by a range of truncation selection intensities on the underlying latent variable (the score describing susceptibility to the fungus). The implementation allowed for the reduced response to selection due to expected error on our estimate of effect sizes influencing the realized heritability ($h = 0.24$). By regressing the shift in GEBV score on the quantile of the truncation selection, we were able to estimate that the observed shift of 0.054 would have been produced by the selective elimination of the lower 31% of the latent variable scores.

The magnitude and direction of the change in allele frequencies between generations (Δp) in the simulation were comparable to those found in our field study. There was a highly significant regression of Δp on $p(1 - p)E$, with a relatively low correlation (multiple $R^2 = 0.0011$, $P = 0.0025$, $F = 9.102$ on 1 and 7983 degrees of freedom; fig. S8). The small

R^2 value is explained by the relatively large error in estimates of E at each locus combined with stochastic variation in the allele frequency change, whereas the combined evidence over many loci is highly significant.

Conclusions

We have thus documented a heritable microevolutionary adaptive change occurring over a single generation as a result of small allelic shifts in thousands of loci. To have demonstrated a shift in additive genetic variation without genome sequencing would have involved producing large numbers of clones or offspring from many adult and juvenile trees in the woodland and growing these in uniform conditions for several years under ash dieback inoculum pressure. Even then, such an approach would not have given us information about the number of loci involved in the adaptive shift. We were only able to characterize this highly polygenic shift in allele frequencies because we could use estimates of effect sizes at genome-wide loci obtained from large field trials. Our approach also relied on the existence of multiple generations coexisting in nature, the older of which are known to die more slowly, and thus retains the ancestral allele frequencies. It also required population genome sequencing of a large number of individuals, which was facilitated by the relatively small size of the ash genome (~880 mega–base pairs).

Few other studies have thus far sought evidence for microevolutionary change through shifts in GEBVs (*15*), although several studies in animals have examined shifts in predicted breeding values on the basis of pedigrees (*37*). A recent study showed an increase in GEBVs calculated using genomic prediction algorithms for adult weight in a 35-year dataset for Soay sheep that aligned with changes in predicted breeding values (from pedigree-based studies), although phenotypic body weight decreased over this time span (*16*). In the present study, by contrast, we used the difference between predicted GEBV (based on relatedness) and observed GEBV (based on loci associated with the trait of interest) to infer that changes in allele frequency could be attributed to selection. These strategies could be extended to other organisms in the search for highly polygenic allelic shifts associated with a trait under selection, to produce neo-Darwinian evolution. It is likely that such shifts are common (*5*).

The action of natural selection in the wild for increased health of European ash under ash dieback is good news. Selection for low ash dieback susceptibility may occur partly by reduced seed or pollen production from adult trees damaged by ash dieback (*30*, *31*, *38*) and partly through rapid death of young trees infected by ash dieback, constituting a missing fraction that did not survive. The significant shift that we detected in the GEBVs of juveniles compared with their GEBVs based only on relatedness to the adults demonstrates the latter selective mechanism. Whether the rate of change we observed will be sufficient for evolutionary rescue to occur (*39*), and whether sufficient standing genetic variation is available for cumulative selection of a fully resistant tree, is as yet unknown. The speed of polygenic evolution may be inhibited by linkage among loci (*40*, *41*), and heritability may be low across natural landscapes. As the epidemic progresses, decreases in the populations of the host and pathogen may reduce gene flow of beneficial alleles in the host and selective pressure from the pathogen. This will diminish the speed of evolution. Management interventions could enhance the rate of evolutionary change, for example, protecting natural regeneration and introducing genetic diversity from other seed sources or from trees selected, or bred, for high resistance. Several breeding programs for ash dieback resistance are currently underway in Europe, with parental trees selected on the basis of their ash dieback damage phenotypes. A breeding program for increased disease resistance based on GEBVs would allow more-accurate selection of parents with high breeding values and would also allow parental pairs with complementary sets of alleles associated with resistance to be selected for crossing.

REFERENCES AND NOTES

1. R. A. Fisher, *The Genetical Theory of Natural Selection* (Clarendon Press, 1930).
2. D. S. Falconer, *Introduction to Quantitative Genetics* (Oliver and Boyd, 1962).
3. P. W. Messer, D. A. Petrov, *Trends Ecol. Evol.* **28**, 659–669 (2013).
4. I. Höllinger, P. S. Pennings, J. Hermisson, *PLOS Genet.* **15**, e1008035 (2019).
5. N. H. Barton, *Proc. Natl. Acad. Sci. U.S.A.* **119**, e2122147119 (2022).
6. L. K. Hayward, G. Sella, *eLife* **11**, e66697 (2022).
7. C. R. Linnen, E. P. Kingsley, J. D. Jensen, H. E. Hoekstra, *Science* **325**, 1095–1098 (2009).
8. A. E. Van't Hof *et al.*, *Nature* **534**, 102–105 (2016).
9. Y.-T. Lai *et al.*, *Proc. Natl. Acad. Sci. U.S.A.* **116**, 2152–2157 (2019).
10. S.-B. Zong, Y.-L. Li, J.-X. Liu, *Mol. Biol. Evol.* **38**, 1317–1329 (2021).
11. B. Pujol *et al.*, *Trends Ecol. Evol.* **33**, 337–346 (2018).
12. J. A. Endler, *Natural Selection in the Wild* (Princeton Univ. Press, 1986).
13. J. Merilä, B. C. Sheldon, L. E. Kruuk, *Genetica* **112**, 199–222 (2001).
14. A. Charmantier, D. Garant, L. E. B. Kruuk, Eds., *Quantitative Genetics in the Wild* (Oxford Univ. Press, 2014).
15. S. E. McGaugh, A. J. Lorenz, L. E. Flagel, *Proc. Biol. Sci.* **288**, 20210693 (2021).
16. D. C. Hunter *et al.*, *Proc. Biol. Sci.* **289**, 20220330 (2022).
17. P. W. Messer, S. P. Ellner, N. G. Hairston Jr., *Trends Genet.* **32**, 408–418 (2016).
18. R. J. Berry, J. H. Crothers, *J. Zool.* **155**, 5–17 (2009).
19. R. W. Hiorns, G. A. Harrison, *Hum. Biol.* **42**, 53–64 (1970).
20. W. F. R. Weldon, *Biometrika* **1**, 109–124 (1901).
21. R. J. Berry, W. N. Bonner, J. Peters, *J. Zool.* **189**, 385–398 (2009).
22. W. H. Dowdeswell, *Heredity* **16**, 39–52 (1961).
23. M. McMullan *et al.*, *Nat. Ecol. Evol.* **2**, 1000–1008 (2018).
24. W. J. Plumb *et al.*, *Plants People Planet* **2**, 29–40 (2019).
25. A. Lobo, L. V. McKinney, J. K. Hansen, E. D. Kjær, L. R. Nielsen, *For. Pathol.* **45**, 379–387 (2015).
26. J. J. Stocks *et al.*, *Nat. Ecol. Evol.* **3**, 1686–1696 (2019).
27. L. V. McKinney *et al.*, *Plant Pathol.* **63**, 485–499 (2014).
28. A. Erfmeier *et al.*, *Front. Plant Sci.* **10**, 658 (2019).
29. T. L. R. Coker *et al.*, *Plants People Planet* **1**, 48–58 (2019).
30. D. Semizer-Cuming, R. Finkeldey, L. R. Nielsen, E. D. Kjær, *Ann. For. Sci.* **76**, 16 (2019).
31. D. Semizer-Cuming, I. J. Chybicki, R. Finkeldey, E. D. Kjær, *Ann. For. Sci.* **78**, 14 (2021).
32. A. Pliūra, V. Lygis, V. Suchockas, E. Bartkevičius, *Balt. For.* **17**, 17–34 (2011).
33. J.-P. George, T. G. M. Sanders, V. Timmermann, N. Potočić, M. Lang, *Sci. Rep.* **12**, 4764 (2022).
34. J. L. Lush, *J. Dairy Sci.* **18**, 1–19 (1935).
35. J. Huisman, *Mol. Ecol. Resour.* **17**, 1009–1024 (2017).
36. A. Pliura, V. Lygis, D. Marčiulyniene, V. Suchockas, R. Bakys, *IForest* **9**, 12–22 (2016).
37. E. Postma, *J. Evol. Biol.* **19**, 309–320 (2006).
38. A.-K. Eisen, L. Buchner, B. Fussi, S. Jochner-Oette, *J. For. Res.* **35**, 16 (2023).
39. S. M. Carlson, C. J. Cunningham, P. A. H. Westley, *Trends Ecol. Evol.* **29**, 521–530 (2014).
40. W. G. Hill, A. Robertson, *Genet. Res.* **8**, 269–294 (1966).
41. J. M. Comeron, A. Williford, R. M. Kliman, *Heredity* **100**, 19–31 (2008).
42. T. King, S. Butcher, L. Zalewski, Apocrita - High Performance Computing Cluster for Queen Mary University of London, Zenodo (2017); http://doi.org/10.5281/zenodo.438045.
43. C. L. Metheringham *et al.*, Dataset for Rapid polygenic adaptation in a wild population of ash trees under a novel fungal epidemic [Data set], Zenodo (2024); https://doi.org/10.5281/zenodo.10808942.

ACKNOWLEDGMENTS

We thank the Woodland Trust for access to Marden Park wood and T. Hodges and K. Harvey for their support and assistance. This research made use of the Queen Mary University of London (QMUL) Apocrita High Performance Computing facility (*42*), which is supported by QMUL Research-IT. **Funding:** UK Government Department for Environment Food and Rural Affairs (Defra) grants under the Future Proofing Plant Health Programme and the Centre for Forest Protection to R.J.A.B.; Department of Agriculture, Food and the Marine, Ireland, Teagasc Walsh Fellowship to W.J.P.; Natural Environment Research Council London DTP PhD studentship to W.R.M.F.; and UK Research and Innovation (UKRI) Future Leaders Fellowship (MR/T019832/1) to E.R.L. **Author contributions:** Conceptualization: C.L.M., R.J.A.B., R.A.N.; Methodology: R.A.N., C.L.M., W.R.M.F., R.J.A.B., J.M.; Fieldwork: C.L.M., W.J.P., W.R.M.F., J.J.S., L.J.K., M.N.G., R.A.N., R.J.A.B., S.W.D.G., E.R.L.; Investigation: C.L.M., R.J.A.B., R.A.N., W.R.M.F.; Visualization: C.L.M., J.M., R.A.N.; Funding acquisition: E.R.L., R.J.A.B.; Project administration: R.J.A.B.; Supervision: R.A.N., R.J.A.B., E.R.L., S.W.D.G.; Writing – original draft: C.L.M., R.J.A.B., R.A.N.; Writing – review & editing: C.L.M., W.R.M.F., L.J.K., E.R.L., R.J.A.B., R.A.N. **Competing interests:** The authors declare that they have no competing interests. **Data and materials availability:** Raw reads for all sequenced samples are available in the European Nucleotide Archive (ENA) under accession PRJEB44697 (ERP128769). Analysis scripts and associated data are available in Zenodo (*43*) and Github (https://github.com/CareyMetheringham/MardenPark).

SUPPLEMENTARY MATERIALS

science.org/doi/10.1126/science.adp2990
Materials and Methods; Figs. S1 to S8; Tables S1 to S4; References (*44*–*58*); MDAR Reproducibility Checklist

Submitted 18 March 2024; accepted 25 April 2025

10.1126/science.adp2990

PHYSICAL CHEMISTRY

Spontaneous formation of urea from carbon dioxide and ammonia in aqueous droplets

Mercede Azizbaig Mohajer[1]†, Pallab Basuri[1]†, Andrei Evdokimov[2], Grégory David[1], Daniel Zindel[1], Evangelos Miliordos[2], Ruth Signorell[1]*

Urea is a key molecule in the search for the origin of life and a basic chemical produced in large quantities by industry. Its formation from ammonia and carbon dioxide requires either high pressures and temperatures or, under milder conditions, catalysts or additional reagents. In this study, we observed the spontaneous formation of urea under ambient conditions from ammonia and carbon dioxide in the surface layer of aqueous droplets. Single, optically trapped droplets were probed by using Raman bands as markers. We found the surface layer to act like a microscopic flow reactor, with chemical gradients providing access to unconventional reaction pathways. This observation revealed a general mechanistic scheme for distinctive droplet chemistry. Interfacial chemistry is a possible nonenergetic route for urea formation under prebiotic conditions.

Urea plays a key role in the amino acid metabolisms of mammals and amphibians through the urea cycle, by which toxic ammonia is removed from the body (*1*, *2*). It is one of the most important industrial chemicals, used primarily in the fertilizer industry but also in many other applications, from the production of resins and explosives to medical purposes and road deicing (*3*). Urea is also relevant to astrobiology and is considered a fundamental building block for the formation of biological molecules in connection with the question of the origin of life [(*4*–*10*) and references therein]. With its N–C single bond, it may have played a role as a reactant in the prebiotic synthesis of cytosine and uracil as well as in phosphorylation reactions. How urea was formed in the carbon dioxide–rich atmosphere of early Earth, which also contained small amounts of ammonia, has not yet been conclusively clarified.

In 1829, Friedrich Wöhler showed that urea—a byproduct of life—could be synthesized from exclusively inorganic materials (*11*), thereby refuting the theory of vitalism. Today, the industrial process synthesizes urea (NH_2CONH_2) from ammonia (NH_3) and carbon dioxide (CO_2) in an overall exothermic reaction. The first step is the strongly exothermic formation of ammonium carbamate (NH_2COONH_4), which decomposes into urea and water (H_2O) in the endothermic second step. Le Chatelier's principle thus imposes contradictory requirements for shifting the equilibria toward urea, the first step being favored by low temperature and high pressure and the second by high temperature and low pressure. The industrial process finds a compromise at high pressure (12.5 to 25.0 MPa) and high temperature (170° to 220°C) (*3*). The high energy consumption and the harsh conditions of this process have prompted the search for alternative catalytic pathways for urea formation [(*12*–*19*) and references therein].

[1]Department of Chemistry and Applied Biosciences, ETH Zurich, Zurich, Switzerland. [2]Department of Chemistry and Biochemistry, Auburn University, Auburn, AL, USA. ***Corresponding author. Email: rsignorell@ethz.ch** †These authors contributed equally to this work.

Here, we report an intriguing pathway for urea formation that has not been previously reported: the spontaneous formation of urea in aqueous ammonia [NH_3(aq)] droplets in the presence of CO_2 gas [CO_2(g)] under ambient conditions and without catalyst or additional reactants. In bulk reactions, urea formation from NH_3 and CO_2 under ambient conditions is hindered by the endothermicity of the decomposition of ammonium carbamate into urea and water. This led us to propose a droplet mechanism where distinct chemical gradients across the surface layer of the droplet provided access to an unconventional proton-catalyzed reaction pathway in which neutral carbamic acid (NH_2COOH) replaced carbamate (NH_2COO^-) as the key intermediate. Gradients across the droplet surface region enabled the reaction of neutral carbamic acid—which requires acidic conditions—with NH_3, which is favored by basic conditions. The distinctiveness of droplets as chemical reactors and their relevance to atmospheric processes and the formation of biomolecules in the prebiotic area have attracted considerable attention in recent years [(*6*, *18*, *20*–*40*) and references therein]. For example, conversion reactions of CO_2 into small organic molecules have been reported in microdroplets. Corresponding bulk reactions, by contrast, are either much slower or not observed at all (*18*, *28*, *29*, *31*). Notably, the formation of protonated and deprotonated carbamic acids in CO_2-amine microdroplet reactions was proposed to originate from the superacid and superbase properties of the aqueous droplet surface (*31*). The key role of the droplet pH has often been highlighted in the context of distinctive droplet chemistry, raising the question about stable internal pH gradients and intrinsic differences compared with pHs of bulk systems—a topic that is hotly debated because of contradictory experimental results [(*32*, *33*) and references therein]. Owing to the complexity of aerosolized droplet ensembles, it is generally challenging to provide reliable explanations for the origins and mechanisms of unusual and accelerated chemistry in these systems.

To reduce uncertainties associated with droplet ensemble studies, we probed urea formation directly in single, optically trapped aerosol droplets using in situ single-droplet Raman spectroscopy (Fig. 1A and supplementary text S1 and S11) (*41*, *42*). With radii of only a few micrometers and femtoliter volumes, the droplets that we investigated had a thousandfold-higher surface-to-volume ratio than microdroplets of a few tens of micrometers and thus a considerably increased sensitivity to surface phenomena and product formation. The immobilization of a single droplet in a gaseous environment enables rapid Raman detection over longer periods of time (many hours), precise determination of the droplet size, and control of the surrounding gas phase. In this way, the droplet size could be kept constant throughout the measurements. Isolation of a single droplet in the gas phase combined with in situ detection reduced potential issues with contamination and side reactions, e.g., catalytic processes at container walls. A caveat is the limited number of applicable in situ characterization methods; standard analytical methods are not sensitive enough. We thus supplemented the single-droplet studies with droplet ensemble experiments (supplementary text S2) using ex situ characterization with gas chromatography–mass spectrometry (GC-MS) and carbon-13 nuclear magnetic resonance (^{13}C NMR) after sample collection. On the basis of the evidence for spontaneous urea formation gained from the experimental results, we proposed a mechanism highlighting the distinctive role of the droplet surface region.

Urea formation in single droplets

Representative Raman spectra for different droplet and gas phase compositions are summarized in Fig. 1, B to E (additional data are provided in supplementary text S6 and S7). Figure 1B shows Raman spectra in the region of the strong C–N stretching band of urea of a single, aqueous ammonia solution [(NH_3(aq)] droplet before (t < 0 min, light gray) and after (t > 0 min, medium and dark gray)

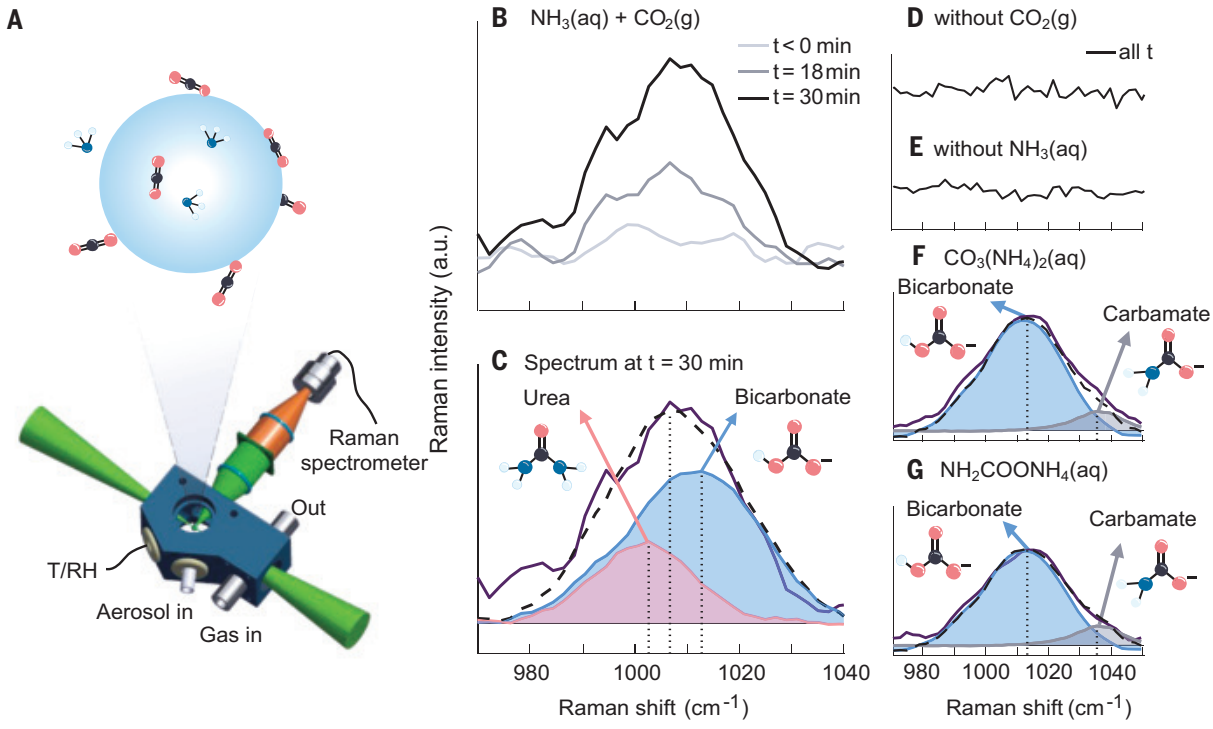

Fig. 1. Single-droplet experiments. (**A**) (Top) Schematic representation of a single droplet with ammonia and carbon dioxide molecules. (Bottom) Trapping cell (blue) for immobilization of a single droplet by counter-propagating optical tweezers (green cones). (**B**) Single-droplet Raman spectra recorded before ($t < 0$ min) and after ($t > 0$ min) exposure of an aqueous ammonia [NH_3(aq)] droplet (radius 2 μm) to CO_2 gas [CO_2(g)]. (**C**) The decomposition of the Raman spectrum at $t = 30$ min (full black line) shows that urea (red, 33 mM) was formed in addition to bicarbonate (blue, 83 mM). The dashed black line is the sum spectrum of urea and bicarbonate. The vertical dotted lines indicate the positions of the band maxima of urea (1003 cm^{-1}), the sum spectrum (1008 cm^{-1}), and the bicarbonate (1013 cm^{-1}). (**D**) Single-droplet spectrum of an NH_3(aq) droplet in nitrogen gas (N_2), i.e., without the addition of CO_2(g). (**E**) Single-droplet spectrum of a water droplet (i.e., without NH_3) in CO_2(g). No Raman bands, and thus no urea formation, was seen for (D) and (E). (**F**) Single-droplet spectrum of a 1 M ammonium carbonate droplet in CO_2(g). (**G**) Single-droplet spectrum of a 1 M ammonium carbamate droplet in CO_2(g). Spectra in (F) and (G) do not show detectable amounts of urea. The decomposition of the Raman spectra (full black lines) shows that bicarbonate (blue, maxima 1013 cm^{-1}) and carbamate (gray, 1037 cm^{-1}) were formed. The dashed black lines indicate the sum spectra. The vertical dotted lines indicate the positions of the band maxima of bicarbonate (1013 cm^{-1}), the sum spectrum (1013 cm^{-1}), and carbamate (1037 cm^{-1}). The droplet size was kept constant over the course of the measurement for all single-droplet experiments by adding NaCl and matching the relative humidity (~80%; supplementary text S1, S6, and S7). a.u., arbitrary units.

exposure to humidified CO_2(g) (0.5 to 1 bar). No signal was detected before CO_2 exposure. After CO_2 exposure, a Raman band around 1008 cm^{-1} appeared, increasing in intensity within the first ~30 min ($t = 30$ min). Equivalent results were obtained by exposing an aqueous droplet (without ammonia) to a gaseous environment containing a few millibar NH_3 before the exposure to CO_2 (table S2 and supplementary text S6 and S11). The observed band could be decomposed into two components (Fig. 1C), one arising from urea [red area, band maximum ~1003 cm^{-1} (*43*)] and the other from bicarbonate HCO_3^- (blue area, band maximum ~1013 cm^{-1}). HCO_3^-, together with carbamate, carbonate (CO_3^{2-}), and ammonium (NH_4^+), is part of the pH-dependent chemical equilibrium that establishes in an aqueous CO_2/NH_3 system (R_1 to R_5 in supplementary text S11). For the spectral decomposition in Fig. 1C, we recorded reference Raman spectra of aqueous urea and bicarbonate droplets, respectively (fig. S5, lower panel). Clearly, urea spontaneously formed under the distinctive conditions in droplets (Fig. 1, B and C). Different single-droplet experiments showed an average urea concentration of 42 ± 10 mM after about 30 min (supplementary text S4 and S6). Inferred bicarbonate concentrations together with the absence of significant amounts of carbamate (band maximum ~1037 cm^{-1}) and CO_3^{2-} (band maximum ~1065 cm^{-1}) placed the average droplet pH at ~6.7 for reaction times > ~ 18 min (assuming equilibrium; details in supplementary text S5 and S11). By varying the intensity of the trapping laser, we verified that urea formation was neither photoinduced nor thermally induced.

The essential components for the formation of urea in droplets are NH_3 and CO_2. If CO_2 was replaced by nitrogen (N_2) gas under otherwise identical conditions, no urea was formed (Fig. 1D). The same held in the absence of dissolved ammonia in the droplet (Fig. 1 E). In that case, the equilibrium concentration of bicarbonate lay below the detection limit of the droplet Raman spectra (~10 mM) because of the low pH of ~4 (supplementary text S5). To clarify whether the formation of urea was controlled by presence of NH_4^+(aq) or unprotonated NH_3(aq), we conducted experiments with droplets containing different ammonium salts (table S2). Figure 1, F and G, illustrates the case of aqueous ammonium carbonate and ammonium carbamate droplets in CO_2(g), respectively. The two spectra show similar contributions from bicarbonate (blue area) and carbamate (gray area), which is consistent with a droplet pH of ~7.6 (supplementary text S5), but no detectable amounts of urea. The NH_4^+ concentration calculated for chemical equilibrium is almost 10 times larger than that shown in Fig. 1C (supplementary text S5). If urea was formed from NH_4^+, the salt spectra in Fig. 1, F and G, should have shown an even stronger urea signal than was shown in Fig. 1C. The fact that no urea was detected in the salt spectra

provided evidence that unprotonated NH_3(aq) rather than NH_4^+(aq) is essential for the formation of urea in droplets.

Reaction in droplet ensembles and in bulk liquid

In complementary droplet ensemble experiments (Fig. 2A and supplementary text S2 and S8), an aqueous ammonia solution was sprayed into a round-bottom flask filled with humidified CO_2(g) (1 bar) and a small amount of liquid water at the bottom. After deposition of the droplets, the liquid at the bottom was analyzed with GC-MS, ^{13}C NMR, and Raman spectroscopy. The maximum reaction time in the droplet phase was limited by the short residence time of the droplets in the gas phase (<3 min), yielding only very minor amounts of urea per droplet compared with the single-droplet experiment (Fig. 1C). GC-MS indeed confirmed the formation of urea (Fig. 2C). Very weak signals of urea could also be identified by ^{13}C NMR at chemical shifts of ~162.8 ppm (Fig. 2B). The Raman spectrum showed the presence of bicarbonate (blue) and carbamate (gray) (Fig. 2D) but lacked the sensitivity to detect urea in such small concentrations. The formation of urea in a droplet spray has very recently also been observed in an independent study (*44*). Although the GC-MS and ^{13}C NMR did confirm urea formation, droplet ensemble measurements alone would have been insufficient to confirm formation in the droplet phase as opposed to, e.g., reactions on container surfaces. However, together with the single-droplet measurements, these additional datasets provided convincing evidence for urea formation from NH_3 and CO_2 in the distinctive environment of small droplets.

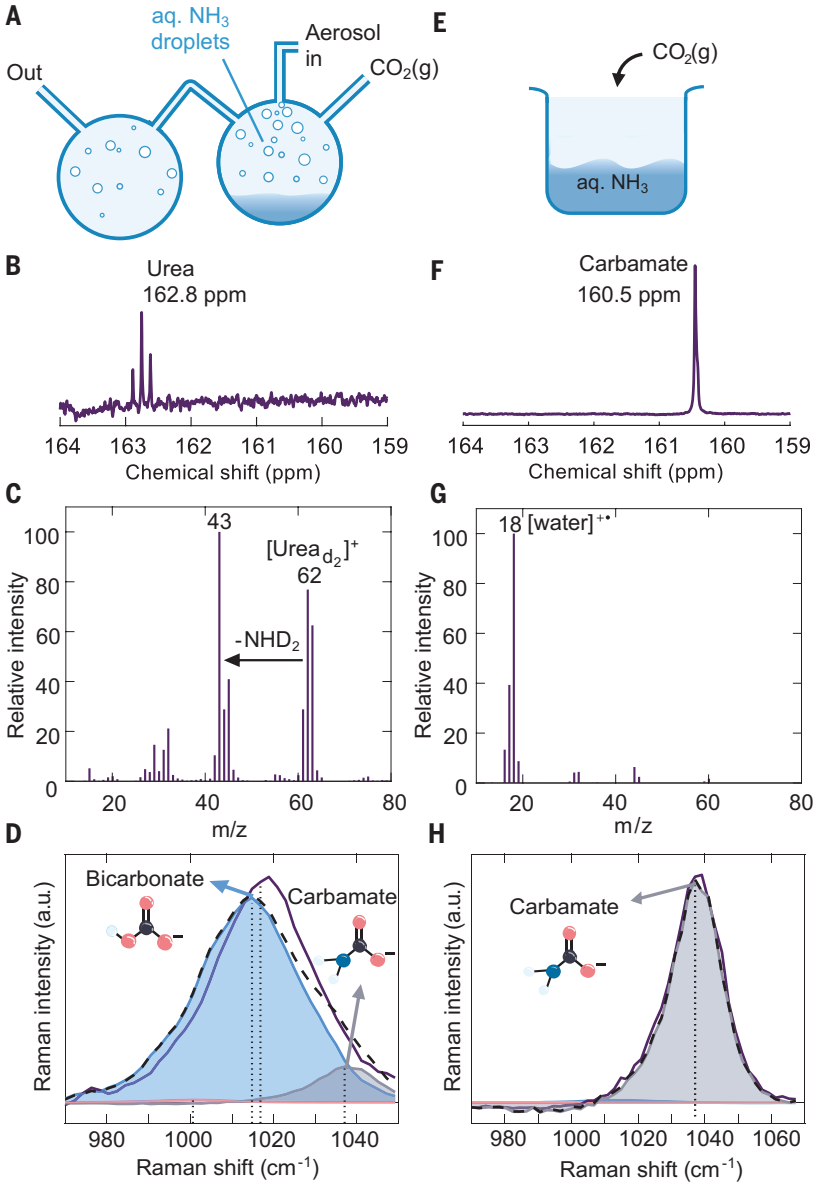

Fig. 2. Droplet ensemble and bulk experiments. (**A**) Schematic representation of the droplet ensemble setup. (**B**) The ^{13}C NMR spectrum of the droplet ensemble sample shows a weak urea signal at 162.8 ppm. (**C**) The mass spectrum from GC-MS of a partially deuterated droplet ensemble sample shows the characteristic patterns of partially deuterated urea ($urea_{d2}$, $^-NHD_2$) (supplementary text S8). (**D**) The Raman spectrum of the droplet ensemble sample does not show a detectable urea band, but as in Fig. 1, F and G, shows contributions from bicarbonate (blue) and carbamate (gray). (**E**) Schematic representation of the setup for bulk studies. (**F**) The ^{13}C NMR spectrum of the bulk sample shows a carbamate signal at 160.5 ppm but no urea. (**G**) The mass spectrum from GC-MS of a partially deuterated bulk sample contains mostly water but no urea. (**H**) The Raman spectrum of the bulk sample shows only the carbamate band (gray) but no urea.

As is well known and as confirmed by bulk control experiments (Fig. 2, E to H, and supplementary text S3), this reaction does not take place in conventional liquid bulk reaction systems at ambient temperatures and pressures. In the range of interest, ^{13}C NMR and Raman spectra showed only signals from carbamate (at 160.5 ppm and maximum at 1037 cm^{-1}, respectively) but not from urea. The GC-MS also confirmed the absence of urea in these bulk experiments.

Proposed mechanism

The confined space of droplets must have opened a new reaction pathway. What could be the mechanism? The fact that urea formation from CO_2 and NH_3 occurred exclusively in droplets (Fig. 1, B and C, and Fig. 2, B to D), but not in the bulk (Fig. 2, F to H), implies that the reaction took place near the surface, presumably in the interfacial region governed by pronounced concentration gradients. In the industrial synthesis of urea at high temperature and pressure, carbamate is the key intermediate (*3*). This is clearly not the case for the formation of urea under the ambient conditions of our experiments, in which ammonium carbamate did not react any further, neither in the bulk (Fig. 2, F to H) nor in the droplets (Fig. 1, F and G)—at least not to a measurable extent. A conceivable reaction intermediate was carbamic acid itself. Although unstable with respect to decomposition into NH_3 and CO_2, it could still play the role of the reactive intermediate in a reaction in the droplet surface region under sufficiently acidic conditions.

To form urea from carbamic acid requires the addition of a second NH_3 molecule, which must be provided in unprotonated form (see above). If this occurred in the droplet interior, one would have expected a much more pronounced urea contribution to the ammonium salt spectra than is observed in Fig. 1, F and G, where the NH_3(aq) concentration was one to two orders of magnitude larger than in the case of Fig. 1C (supplementary text S5). Instead, we hypothesized that the addition of the second NH_3 to form urea involved the reaction with partially solvated NH_3(aq) molecules in

a more acidic subsurface region. In the case of Fig. 1, B and C, the spraying of the initial aqueous ammonia solution into the trapping cell (Fig. 1A) loaded the inner surfaces of the cell with macroscopic amounts of NH_3(aq), establishing a continuous supply of gaseous ammonia [NH_3(g)] in the droplet's environment at an initial NH_3 partial pressure in the millibar range (supplementary text S11). Upon addition of CO_2(g), the pH-dependent system of equilibria (R1 to R5, supplementary text S11) reduced the NH_3(g) partial pressure to an estimated value around 0.4 Pa within about 30 min (supplementary text S5 and S11).

To corroborate our mechanistic hypothesis on a molecular level, we combined quantum chemical calculations (supplementary text S10) with a detailed reaction diffusion model (supplementary text S11). The quantum chemical calculations were for a cluster model embedded in a polarizable water continuum to represent local conditions in an interfacial layer at the surface (*45*, *46*) (supplementary text S10). CO_2 was present in an acidic subsurface layer extending about 1 nm below the surface, where it reacted with partially solvated NH_3(aq). To avoid artifacts in the energetics, we kept the number of hydrogen bonds constant throughout each reaction step (supplementary text S10). The calculations confirmed the thermodynamically and kinetically favorable formation of neutral carbamic acid in an acidic aqueous environment (Fig. 3, steps A→→D). The critical steps for the formation of urea were the addition of the second ammonia (step D→E) and the subsequent elimination of H_2O [step E→F (*19*)]. In contrast to carbamic acid, its conjugate base, carbamate, did not even add NH_3 in the cluster model (supplementary text S10 and table S4, models S11 and S12), which is consistent with the observation that urea did not form from carbamate in aqueous bulk solutions under ambient conditions (Fig. 2, F to H). Additional cluster calculations also indicated that the formation of urea from carbamic acid was specifically catalyzed by H_3O^+ (e.g., not by NH_4^+; supplementary text S10 and table S4, models S9 and S10), implying the requirement of an at least locally low pH. This would be consistent with the idea of a substantially reduced subsurface pH (referring H_3O^+ activity to the locally decreased reference chemical potential; supplementary text S11) compared with the average droplet pH of ~ 6.7. A reduction by about two pH units corresponds to a stabilization of H_3O^+ in the perturbed water structure in the subsurface layer by the equivalent of a hydrogen bond energy. It is further plausible that partially solvated NH_3(aq) also experiences a small stabilization in the subsurface, increasing its availability in that region (supplementary text S11). On the basis of these assumptions and the quantum chemically predicted reaction path, we formulated a reaction diffusion model (supplementary text S11, eq. S3 and S4) that led to an effective rate law for urea formation, $v_c = 10^{10-pH}\ dm^6 mol^{-2} s^{-1}\ [NH_3]^2\ [CO_2]$ (supplementary text S11, eq. S1 and S2). The model predicted urea concentrations on the order of some 10 mM in the droplets, which is consistent with the experimentally determined values (see above). The proposed mechanism thus offered a plausible explanation for the spontaneous urea formation in droplets. Overall, the mechanism consists of the proton-catalyzed formation of neutral carbamic acid, which continues to react with unprotonated NH_3, again in a proton-catalyzed reaction, to form urea. The mass spectroscopic observation of protonated carbamic acid formed by the reaction of CO_2 with amines in electrosprayed acetonitryl droplets in the presence of water (*31*) lent further support to our proposed mechanism. The addition of a second amine to form substituted urea derivatives was not observed in that study. Whether this was due to the much shorter timescale (milliseconds) than was used in our experiments (minutes to hours) or to intrinsic kinetic or thermodynamic hindrance remains unclear. Our general scheme of enhanced surface chemistry as a result of increased interfacial activity of reactants—and in our case H_3O^+ as catalyst—is also consistent with recent studies of condensation reactions such as the dimerization of pyruvic acid in droplets [(*47*, *48*) and references therein].

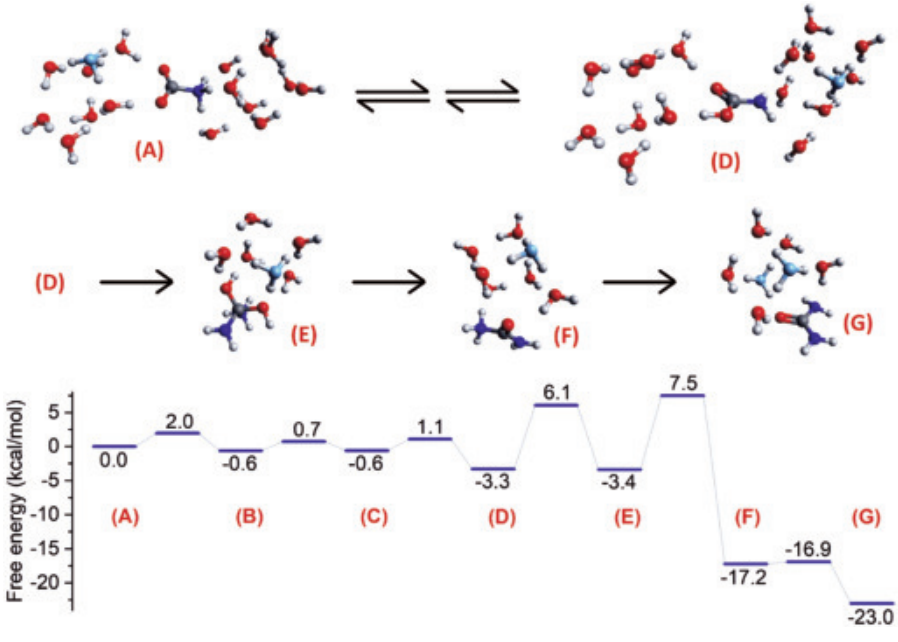

Fig. 3. Structures and free energy diagram for the formation of urea from NH_3 and CO_2. Red, blue, gray, and white balls represent O, N, C, and H atoms, respectively. Light blue indicates the O atom of hydroniums. (Top row) Formation of carbamic acid as reactive intermediate through a number of fast reversible steps [(A) to (D)] establishing a quasi-equilibrium. (Middle row) Rate-determining addition of the second NH_3 to carbamic acid. (supplementary text S10 and fig. S17). (Bottom row) Free energy diagram.

The spontaneous formation of urea is a prime example of droplet chemistry that is different from bulk reactions, highlighting a general mechanistic scheme distinctive to droplets. The high surface-to-volume ratio of a droplet gives prominence to reactions in the interfacial layer near the surface, where pronounced concentration gradients can establish the microscopic equivalent of a flow reactor connected by molecular transport to the reservoirs of the droplet interior on one side and the gas phase on the other (to supply the reactants) (Fig. 4). In this way, interfacial reaction systems could solve the dilemma of bulk reactions hindered by mutually exclusive conditions for the coexistence of key reactants. In our study, these conditions were, first of all, the requirement for an acidic environment to provide neutral carbamic acid and enable proton catalysis, and contrastingly, the need for unprotonated NH_3. The pH gradient across the interfacial layer created the required acidic environment, and a continuous supply of NH_3 was provided in the form of partially solvated molecules. The product—urea—was continuously removed from the reaction area by diffusion into the droplet interior.

We anticipate that the general mechanistic scheme proposed here is of relevance to a number of unusual droplet reactions. Chemical potential gradients across the surface layer enable reactions between reactants that do

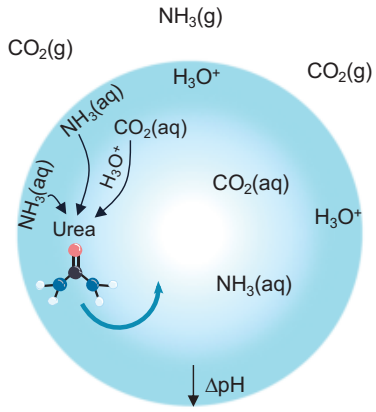

Fig. 4. Graphical representation of the proposed mechanism for urea formation in a droplet. Urea is formed in a multistep, proton-catalyzed reaction between partially solvated ammonia [NH_3(aq)] and carbon dioxide [CO_2(aq)] in a subsurface layer, where a pH gradient (referring H_3O^+ activity to the locally decreased reference chemical potential; supplementary text S11) creates the necessary acidic conditions.

not coexist in sufficient amounts under equilibrium conditions in the bulk, thereby opening up alternative, unconventional reaction pathways. As we have shown, urea forms at aqueous surfaces in a CO_2-rich atmosphere containing small amounts of NH_3. Such conditions likely existed on prebiotic Earth, where the surfaces of aerosol droplets, lakes, and oceans thus offered a reaction site for the abiotic synthesis of precursor molecules, such as urea, and the subsequent formation of simple biomolecules necessary for the evolution of life (*4*–*6*).

REFERENCES AND NOTES

1. H. A. Krebs, K. Henseleit, *Hoppe Seylers Z. Physiol. Chem.* **210**, 33–66 (1932).
2. D. L. Nelson, M. M. Cox, A. L. Lehninger, *Lehninger Principles of Biochemistry* (W. H. Freeman and Company, ed. 6, 2013).
3. J. H. Meessen, in *Ullmann's Encyclopedia of Industrial Chemistry* (Wiley-VCH, 2010), pp. 657–695.
4. G. Horneck, C. Baumstark-Khan, *Astrobiology: The Quest for the Conditions of Life* (Springer, ed. 1, 2012).
5. V. M. Kolb, Ed. *Astrobiology: An Evolutionary Approach* (Taylor & Francis Group, ed. 1, 2015).
6. R. J. Rapf, V. Vaida, *Phys. Chem. Chem. Phys.* **18**, 20067–20084 (2016).
7. F. S. Brigiano, Y. Jeanvoine, A. Largo, R. Spezia, *Astron. Astrophys.* **610**, A26 (2018).
8. A. Potapov, P. Theulé, C. Jäger, T. Henning, *Astrophys. J. Lett.* **878**, L20 (2019).
9. M. Förstel *et al.*, *Chem. Commun.* **52**, 741–744 (2016).
10. S. L. Miller, H. C. Urey, *Science* **130**, 245–251 (1959).
11. F. Wöhler, *Ann. Phys.* **88**, 253–256 (1828).
12. F. Barzagli, F. Mani, M. Peruzzini, *Green Chem.* **13**, 1267–1274 (2011).
13. Y. Manaka, Y. Nagatsuka, K. Motokura, *Sci. Rep.* **10**, 2834 (2020).
14. B. Srinivas *et al.*, *Photochem. Photobiol.* **88**, 233–241 (2012).
15. X. Zhu, X. Zhou, Y. Jing, Y. Li, *Nat. Commun.* **12**, 4080 (2021).
16. Y. Liu *et al.*, *Angew. Chem. Int. Ed.* **62**, e202300387 (2023).
17. C. Chen *et al.*, *Nat. Chem.* **12**, 717–724 (2020).
18. X. Song *et al.*, *J. Am. Chem. Soc.* **145**, 25910–25916 (2023).
19. J. Ding *et al.*, *Nat. Commun.* **14**, 4586 (2023).
20. R. Kusaka, S. Nihonyanagi, T. Tahara, *Nat. Chem.* **13**, 306–311 (2021).
21. S. Rossignol *et al.*, *Science* **353**, 699–702 (2016).
22. P. Corral Arroyo *et al.*, *Science* **376**, 293–296 (2022).
23. T. Liu, J. P. D. Abbatt, *Nat. Chem.* **13**, 1173–1177 (2021).
24. G. Rovelli *et al.*, *Chem. Sci.* **11**, 13026–13043 (2020).
25. C. J. Chen, E. R. Williams, *Chem. Sci.* **14**, 4704–4713 (2023).
26. D. T. Holden, N. M. Morato, R. G. Cooks, *Proc. Natl. Acad. Sci. U.S.A.* **119**, e2212642119 (2022).
27. S. Murke, W. Chen, S. Pezzotti, M. Havenith, *J. Am. Chem. Soc.* **146**, 12423–12430 (2024).
28. M. A. Mehrgardi *et al.*, *Adv. Sci.* **11**, e2406785 (2024).
29. P. Basuri *et al.*, *Angew. Chem. Int. Ed.* **63**, e202403229 (2024).
30. J. E. Klijn, J. B. F. N. Engberts, *Nature* **435**, 746–747 (2005).
31. K.-H. Huang, Z. Wei, R. G. Cooks, *Chem. Sci.* **12**, 2242–2250 (2020).
32. R. L. Craig *et al.*, *Anal. Chem.* **90**, 11232–11239 (2018).
33. M. Li *et al.*, *Chem* **9**, 1036–1046 (2023).
34. S. Narayan *et al.*, *Angew. Chem. Int. Ed.* **44**, 3275–3279 (2005).
35. Z. Wei, Y. Li, R. G. Cooks, X. Yan, *Annu. Rev. Phys. Chem.* **71**, 31–51 (2020).
36. S. Banerjee, E. Gnanamani, X. Yan, R. N. Zare, *Analyst* **142**, 1399–1402 (2017).
37. K. R. Wilson, A. M. Prophet, *Annu. Rev. Phys. Chem.* **75**, 185–208 (2024).
38. X. Yan, R. M. Bain, R. G. Cooks, *Angew. Chem. Int. Ed.* **55**, 12960–12972 (2016).
39. X. Yan, *Int. J. Mass Spectrom.* **468**, 116639 (2021).
40. X. Song, R. N. Zare, *Chem. Sci.* **15**, 3670–3672 (2024).
41. K. Esat, G. David, T. Poulkas, M. Shein, R. Signorell, *Phys. Chem. Chem. Phys.* **20**, 11598–11607 (2018).
42. J. P. Reid, *J. Quant. Spectrosc. Radiat. Transf.* **110**, 1293–1306 (2009).
43. R. Keuleers, H. O. Desseyn, B. Rousseau, C. Van Alsenoy, *J. Phys. Chem. A* **103**, 4621–4630 (1999).
44. Y. Meng, Y. Xia, J. Xu, R. N. Zare, *Sci. Adv.* **11**, eadt8979 (2025).
45. I. R. Ariyarathna, F. Pawłowski, J. V. Ortiz, E. Miliordos, *J. Phys. Chem. A* **124**, 505–512 (2020).
46. T. Yanai, D. P. Tew, N. C. Handy, *Chem. Phys. Lett.* **393**, 51–57 (2004).
47. P. Kim *et al.*, *J. Phys. Chem. Lett.* **15**, 11131–11138 (2024).
48. M. Li, C. Boothby, R. E. Continetti, V. H. Grassian, *J. Am. Chem. Soc.* **145**, 22317–22321 (2023).
49. M. Azizbaig Mohajer *et al.*, Spontaneous formation of urea from carbon dioxide and ammonia in aqueous droplets, Data Collection, ETH Zürich Research Collection (2025); https://doi.org/10.3929/ethz-b-000731364.

ACKNOWLEDGMENTS

We are grateful to P. Albrecht, M. Steger, B. Yoder, J. Schürmann, and the NMR and the Molecular and Biomolecular Analysis Services at ETHZ for technical support. We thank O. Reich and M. Gleichweit for discussions regarding the trapping setup. **Funding:** This project has received funding from the Swiss National Science Foundation (project 200020_200306) and the US NSF (grant no. CHE-1940456). This work was completed using computational resources provided by the Auburn University Hopper and Easley Clusters. R.S. acknowledges support by the Centre for Origin and Prevalence of Life (COPL) at ETHZ. **Author contributions:** Conceptualization: P.B., R.S.; Funding acquisition: E.M., R.S.; Investigation: M.A.M., P.B., A.E., G.D., D.Z., E.M., R.S.; Methodology: M.A.M., P.B., G.D., E.M., R.S.; Project administration: R.S.; Supervision: E.M., R.S.; Visualization: M.A.M., P.B., A.E., E.M., R.S.; Writing – original draft: M.A.M., P.B., E.M., R.S.; Writing – review & editing: M.A.M., P.B., A.E., G.D., D.Z., E.M., R.S. **Competing interests:** The authors declare that they have no competing interests. **Data and materials availability:** All data that reproduce the analyses are available in a data repository (*49*). All (other) data needed to evaluate the conclusions in the paper are present in the paper or the supplementary materials.

SUPPLEMENTARY MATERIALS

science.org/doi/10.1126/science.adv2362
Supplementary Text; Figs. S1 to S20; Tables S1 to S4; References (*50*–*87*)

Submitted 10 December 2024; resubmitted 17 March 2025; accepted 18 April 2025
10.1126/science.adv2362

EARLY EARTH

Evidence for Hadean mafic intrusions in the Nuvvuagittuq Greenstone Belt, Canada

C. Sole[1], J. O'Neil[1]*, H. Rizo[2], J.-L. Paquette[3], D. Benn[1], J. Plakholm[2]

Many questions remain regarding Earth's earliest crust owing to the rarity of Hadean (>4.03 billion-year-old) rocks and minerals. The Nuvvuagittuq Greenstone Belt (NGB) in Canada may be the only known remnant of Hadean crust, although its age is debated, ranging from ≥3.75 to 4.3 billion years old. Mafic intrusions within this belt were specifically sampled and analyzed to investigate the timing of their magmatic differentiation. Correlations between samarium/neodymium (Sm/Nd) and $^{143}Nd/^{144}Nd$ and $^{142}Nd/^{144}Nd$ ratios correspond to ages of 4157 ± 174 and 4196^{+53}_{-81} million years for the long-lived ^{147}Sm-^{143}Nd and the short-lived ^{146}Sm-^{142}Nd systems, respectively. The age agreement between both extant and extinct radiogenic systems, in rocks related through igneous fractionation, is compelling evidence for preservation of Hadean rocks in the NGB, opening a rare window into Earth's earliest times.

Our ability to study how and when the first crust formed on Earth is heavily impaired by the sparseness of early geological records. The oldest felsic rocks from the Acasta Gneiss Complex in northwestern Canada mark the Archean-Hadean boundary at 4.03 billion years ago (Ga) defined by the International Commission on Stratigraphy, and rare detrital and xenocrystic zircons are the only undisputed direct terrestrial samples from the Hadean eon (>4.03 Ga) (*1*–*6*). The host rocks of these ancient zircons, however, have been eroded away, so their resistant trace minerals are all that remain to provide valuable, yet limited, constraints on Earth's primitive crust. Therefore, many questions remain regarding the nature and origin of Earth's primordial crust. Zircon-bearing felsic rocks, which constitute most of the preserved Archean crust, can provide robust geochronological constraints but are primarily formed through melting of an older mafic or felsic crustal precursor, rather than directly derived from melting of the mantle, and likely do not represent the first stage of crust formation. Mantle-derived mafic and ultramafic rocks can, however, be challenging to date, as they usually lack zircon and have experienced metamorphic histories that commonly lead to less precise and sometimes inaccurate determinations of their original igneous age. Nevertheless, as mafic rocks may have constituted an important portion of Earth's earliest crust (*7*), efforts to better constrain the age of the oldest mafic and ultramafic rocks can provide important insight into the origin of Earth's primitive crust.

For more than a decade, the Nuvvuagittuq Greenstone Belt (NGB), located in northeastern Canada (Fig. 1), has been the object of scientific debate with regard to its exact age [see (*8*) for review], as it could represent the only known remnant of Hadean crust. The NGB is dominated by cummingtonite-rich metabasalts called the Ujaraaluk unit (*9*), interpreted to represent a vestige of ancient oceanic crust (*8*). Rare thin zircon-bearing trondhjemitic bands intruding the Ujaraaluk unit set a minimum age of ~3.77 Ga for the NGB (*10*, *11*), but ^{142}Nd isotopic evidence suggests that the Ujaraaluk unit is as old as ~4.3 Ga (*12*, *13*). This Hadean age has been challenged (*14*–*18*), but if correct, the NGB would include the oldest rocks preserved on Earth. Therefore, strong geochronological constraints on the NGB rocks are crucial, as they could provide an unparalleled window into the early Earth with broad implications for the formation of our planet's earliest crust (*9*), the early tectonic regimes operating on Earth (*19*, *20*), the composition of ancient seawater (*21*), and environments where life could have begun (*22*).

The interpretation that the NGB Ujaraaluk unit represents a vestige of Hadean crust is largely based on variations in $^{142}Nd/^{144}Nd$ ratios. Neodymium-142 is the decay product of samarium-146, and given its short half-life of 103 to 92 million years (*23*, *24*), variation in $^{142}Nd/^{144}Nd$ can only be produced by chemical fractionation of Sm and Nd that occurred before ~4.0 Ga, while ^{146}Sm was extant. The $^{142}Nd/^{144}Nd$ ratios measured in the chemically differentiated Ujaraaluk subunits correlate with their Sm/Nd ratios, which, if interpreted as an isochron, would be consistent with an age of ~4.3 Ga (*12*, *13*). However, the variation in $^{142}Nd/^{144}Nd$ of the NGB rocks has conversely been interpreted to reflect interaction with an enriched Hadean component (mantle or crust), in which case the correlation between $^{142}Nd/^{144}Nd$ and Sm/Nd reflect a mixing line with no geochronological meaning (*15*). Efforts to obtain further direct age constraints on the NGB Ujaraaluk rocks have been unsuccessful; uranium-lead (U-Pb) ages on zircon in the Ujaraaluk unit have yielded Neoarchean (2.5 to 2.8 Ga) ages consistent with regional metamorphism (*25*), and long-lived isotopic systems such as ^{147}Sm-^{143}Nd and ^{176}Lu-^{176}Hf (lutetium-hafnium) have shown evidence of postmagmatic disturbance in the Ujaraaluk unit (*10*, *13*), precluding a clear and robust crystallization age determination.

Differentiated metagabbros intruding the Ujaraaluk unit

In this study, we focused on a distinct mafic lithology within the NGB consisting of large differentiated metagabbroic intrusions. These metagabbros intruded the Ujaraaluk unit, providing a minimum age on the dominant metabasaltic rocks and offering an opportunity to better define the NGB geochronology. Here, we present new U-Pb and coupled long- and short-lived $^{146\text{-}147}Sm$-$^{142\text{-}143}Nd$ data in samples with mineralogy and textures reflective of magmatic fractionation of the mafic intrusions, specifically targeted at constraining the timing of igneous differentiation. Although the zircons found in the metagabbroic intrusions appear to have reequilibrated or crystallized during Neoarchean regional metamorphism, Sm-Nd isochrons from both the long- and short-lived isotopic systems yield identical Hadean ages, imposing a minimum age of ~4160 million years (Ma) on the intruded Ujaraaluk rocks.

The NGB includes two generations of metamorphosed plagioclase-hornblende mafic intrusive rocks, referred to here as metagabbros. The younger metagabbros display a distinctive coarse-grained, homogeneous texture (fig. S2, O and P) and locally intrude the NGB chemical metasediments, confirming their younger age. Zircons from two samples of these younger coarse-grained metagabbros have yielded identical U-Pb ages of 2693 ± 12 and 2693 ± 3 Ma (*25*, *26*). Additionally, a mineral internal Sm-Nd isochron age of 2719 ± 100 Ma (*13*) and whole-rock ^{147}Sm-^{143}Nd and ^{176}Lu-^{176}Hf isochron ages between approximately 2861 and 2746 Ma (fig. S10 and table S5) have been obtained on the same lithology. This is consistent with a Neoarchean age for the coarse-grained metagabbros and emplacement during the peak thermal event recorded by garnet growth and metamorphic zircon in the Ujaraaluk unit (*13*, *25*). In contrast, the older generation of metagabbros, locally intruded by the coarse-grained Neoarchean metagabbros (fig. S2, Q and R) and consisting mostly of differentiated mafic sills up to 100 m wide (Fig. 1 and fig. S2A), display a characteristic fine-grained gneissic texture (fig. S2, B to I) and can be continuously traced over more than 1 km within the NGB Ujaraaluk unit (Fig. 1). Well-defined correlations between the highly incompatible element Zr and other incompatible elements

[1]Department of Earth and Environmental Sciences, Ottawa-Carleton Geoscience Centre, University of Ottawa, Ottawa, ON, Canada. [2]Department of Earth Sciences, Ottawa-Carleton Geoscience Centre, Carleton University, Ottawa, ON, Canada. [3]Laboratoire Magmas et Volcans, Université Clermont Auvergne, CNRS, IRD, OPGC, Clermont-Ferrand, France.
*Corresponding author. Email: jonathan.oneil@uottawa.ca

such as Nb (niobium), Nd (neodymium), and chondrite-normalized La/Yb (lanthanum/ytterbium) ratios (fig. S5, D to F) in the gneissic metagabbro samples suggest that magmatic differentiation largely controls the variation in whole-rock geochemical compositions for the most immobile elements. A series of samples from these gneissic metagabbros have previously been analyzed for Sm-Nd isotopes and yielded a ^{147}Sm-^{143}Nd isochron suggesting an age of ~4115 ± 100 Ma with limited scatter [mean square weighted deviation (MSWD) = 4.8] (*13*), supportive of a Hadean age. Whole-rock Lu-Hf systematics exhibit a more scattered ^{176}Lu-^{176}Hf isochron age of ~3400 ± 350 Ma (MSWD = 186) (*10*). Yet removing samples with anomalously low Lu/Hf ratios decreases the scatter and gives older (perhaps Hadean) ^{176}Lu-^{176}Hf isochron ages between approximately 3.90 and 4.14 Ga, albeit with uncertainties (see supplementary text in the supplementary materials; fig. S8).

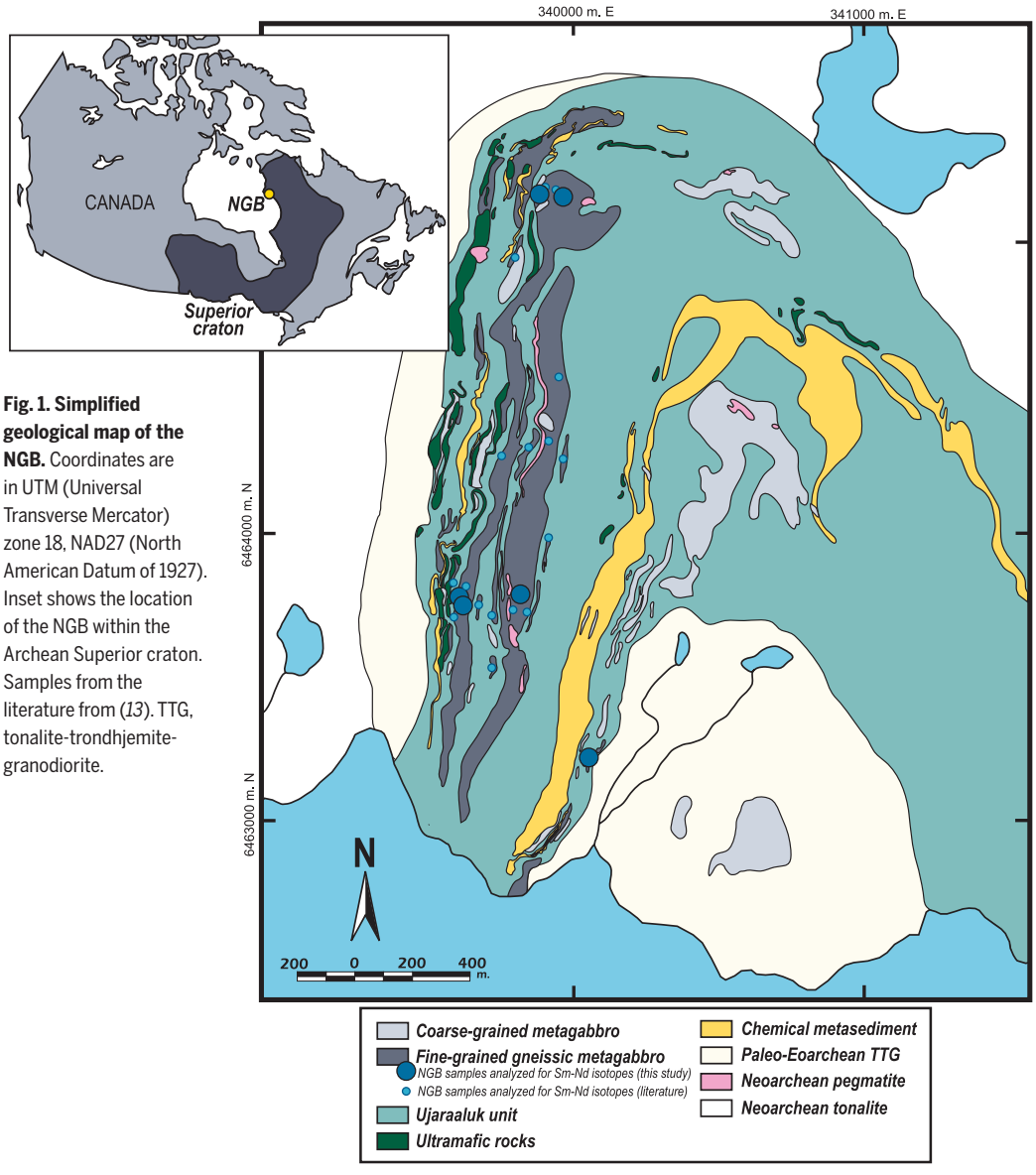

Fig. 1. Simplified geological map of the NGB. Coordinates are in UTM (Universal Transverse Mercator) zone 18, NAD27 (North American Datum of 1927). Inset shows the location of the NGB within the Archean Superior craton. Samples from the literature from (*13*). TTG, tonalite-trondhjemite-granodiorite.

Given the important implications of a potential Hadean magmatic age, additional gneissic metagabbro sill samples were collected, following a comprehensive sampling approach aimed at better constraining their igneous crystallization age. Only samples for which a cogenetic origin could reasonably be inferred from the field were collected. The continuous exposure of the large gabbroic intrusions allowed targeting samples within the same sills that exhibit variable mineralogical proportions, consistent with their original formation through magmatic differentiation. Samples from the gneissic metagabbros also range from hornblende-rich amphibolites to plagioclase-rich rocks forming the most evolved portions of the intrusions (Fig. 2, A to C). These plagioclase-rich layers display gradational contacts with the more homogeneous plagioclase-hornblende gabbroic parts of the sills (fig. S2, K and L), indicating that the mineralogical variation likely resulted from magmatic differentiation. Major element whole-rock composition of the hornblende-rich amphibolites and plagioclase-rich layers further supports the interpretation that their igneous protoliths were pyroxene and plagioclase cumulates, with other sill samples being a mixture of both minerals (Fig. 2D).

Zircons from two compositionally evolved samples from the gneissic metagabbro sills yielded U-Pb Concordia ages between 2644 and 2668 Ma (fig. S7), interpreted to record regional metamorphism. The metamorphic origin of these zircons is supported by their rounded shapes and dark homogeneous cathodoluminescence emissions (fig. S6), as well as low Th/U (thorium/uranium) ratios (table S7). A plagioclase-rich layer yielded zircons defining an older U-Pb Concordia age of 2762.3 ± 9.5 Ma (fig. S7), but their texture and Th/U ratios (fig. S6 and table S7) reflect recrystallization of zircon subsequent to the breakdown of an older Zr-bearing phase, such as baddeleyite, which is often readily converted to polycrystalline zircon during the initial stages of metamorphism (*27*, *28*). U-Pb dating of such polycrystalline zircons has been shown to record the timing of the breakdown of baddeleyite, which can predate peak metamorphism (*29*). This would explain the slightly older age of the zircons from the plagioclase-rich sample compared with the other metamorphic zircons. Therefore, zircons from the most evolved parts of the differentiated sills are highly unlikely to reflect their igneous crystallization age. Given the high affinity of Hf for zircon, the Neoarchean crystallization of metamorphic zircon and/or prior recrystallization events may explain the greater extent of isotopic disturbance for the Lu-Hf system in the gneissic metagabbros (*10*) compared with the Sm-Nd system (*13*), as the latter would be less affected by parent-daughter fractionation from zircon crystallization (supplementary text).

New Hadean age constraints on the Nuvvuagittuq gneissic metagabbros

Despite the absence of primary igneous zircon or baddeleyite to constrain the crystallization age of the gneissic metagabbros, the Sm-Nd isotopic system, which appears relatively undisturbed in comparison to the Lu-Hf system (*10*, *13*), could be used in the newly collected series

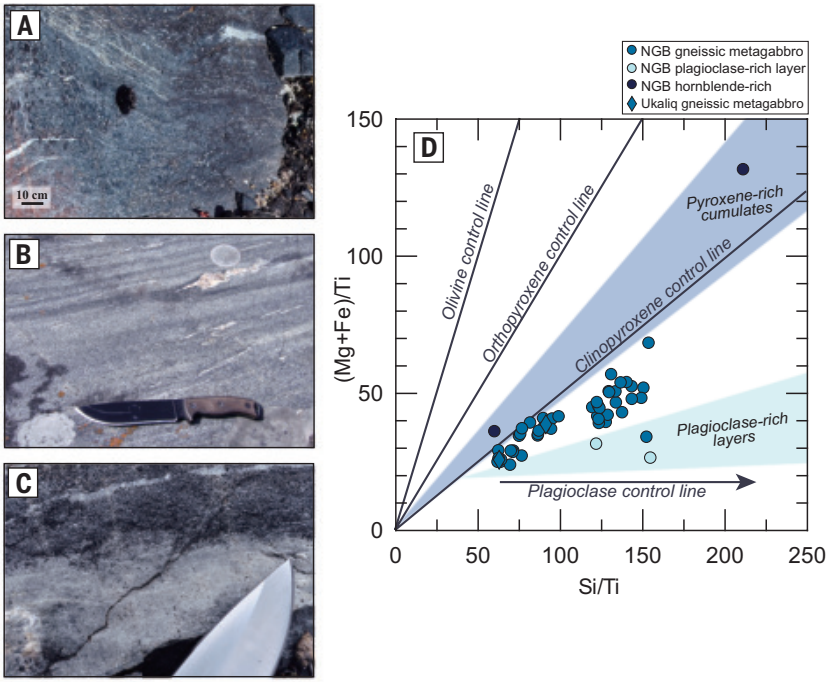

Fig. 2. Outcrop photos of the NGB metagabbros. (**A**) Meter-scale hornblende-rich cumulate layers. (**B**) Gneissic metagabbros with comparable proportions of plagioclase and hornblende, showing the fine-scale gneissic texture. (**C**) Plagioclase-rich layer within the gneissic metagabbro exhibiting a gradational contact with the more hornblende-rich metagabbroic parts of the sill. (**D**) Pearce element–type diagrams for the gneissic metagabbros with expected variation (control lines) for fractionation of the main rock-forming minerals for mafic rocks.

of magmatically fractionated samples to determine the timing of igneous differentiation. Moreover, given the potential Hadean age for the differentiated metagabbros (*13*), along with the compositional variation of the studied samples, slight variations in $^{142}Nd/^{144}Nd$ could be expected, providing additional chronological constraints on their magmatic differentiation.

A suite of six metagabbro sill samples collected within the NGB, along with two metagabbro samples from the nearby Ukaliq area (fig. S3), interpreted as a smaller enclave of supracrustal rocks likely equivalent to the NGB (*15*, *30*–*32*), were analyzed for both the long-lived ^{147}Sm-^{143}Nd and short-lived ^{146}Sm-^{142}Nd systems (tables S2 and S3). The samples from the NGB include a plagioclase-rich evolved layer and a hornblende-rich cumulate as well as other samples with variable mineralogical (plagioclase-hornblende) proportions, exhibiting different degrees of magmatic differentiation. The Ukaliq samples display comparable mineralogy and geochemical compositions to the NGB differentiated metagabbros as well as the same characteristic fine-grained gneissic texture (figs. S2H and S4). All metagabbro samples analyzed in this study display well-defined correlations between Sm/Nd ratios and $^{143}Nd/^{144}Nd$ and $^{142}Nd/^{144}Nd$ (10.3 parts per million variation) (Fig. 3). The best-fit slopes of these correlations correspond to undistinguishable ages of 4157 ± 174 Ma (MSWD = 7.0) and 4196^{+53}_{-81} Ma (MSWD = 0.99) for the ^{147}Sm-^{143}Nd system and ^{146}Sm-^{142}Nd system [using a half-life of 103 Ma for ^{146}Sm (*23*)], respectively. If the two Ukaliq samples are not considered, similar ages are obtained at 4144 ± 300 Ma (MSWD = 9.3) and 4152^{+83}_{-208} Ma (MSWD = 0.83). When all NGB gneissic metagabbro samples previously analyzed (*13*) are considered with the newly analyzed NGB samples, the ages become 4119 ± 158 Ma (MSWD = 16; $n = 21$) and 4176^{+54}_{-87} Ma (MSWD = 1.0; $n = 13$) for the long-lived and short-lived Sm-Nd systems, respectively.

One of the arguments used to challenge the Hadean age of the Ujaraaluk unit suggested by the correlation between $^{142}Nd/^{144}Nd$ and Sm/Nd it displays is the younger isochron ages obtained from the long-lived ^{147}Sm-^{143}Nd and ^{176}Lu-^{176}Hf isotopic systems in these NGB rocks (*17*, *18*). Although this discrepancy between the isochron ages from the long- and short-lived systems was argued to be the result of post–4 Ga geochemical disturbance only affecting the long-lived systems with limited effects on the ^{146}Sm-^{142}Nd isochron (*13*), the apparent age disagreement between the long- and short-lived systems still casts doubt on a Hadean age for the NGB Ujaraaluk rocks. However, the NGB gneissic metagabbro sill samples yield isochron ages that are highly consistent, at ~4160 Ma for both the long-lived and short-lived Sm-Nd isotopic systems, providing strong evidence that the metagabbro sills formed and magmatically differentiated in the Hadean.

Mafic Hadean crust derived from a near chondritic mantle

The intrusive nature of the gneissic metagabbros imposes a minimum age of ~4160 Ma on the intruded Ujaraaluk metavolcanic rocks. It has been suggested that the oldest zircon in what was interpreted as a fuchsitic quartz-rich detrital sedimentary unit within the metavolcanic rocks placed a 3780 Ma upper limit on the age of the Ujaraaluk unit (*16*), but both the interpretation of the nature of that silica-rich host rock and whether it offers any stratigraphic constraint on the age of the Ujaraaluk rocks have been debated (*8*, *25*). For example, an alternative interpretation suggests that the fuchsitic quartzites were instead deposited along a transposed unconformity after 3.4 Ga, and likely as late as 3.04 Ga, across the older NGB metavolcanic rocks (*33*), consistent with other metasedimentary units in the NGB (*25*). Nevertheless, if the NGB mafic rocks are not Hadean, their most likely age would be ~3770 Ma (*15*–*18*), corresponding to the zircon age of associated felsic lithologies. In this scenario, the $^{142}Nd/^{144}Nd$ versus $^{147}Sm/^{144}Nd$ correlation observed in the Ujaraaluk rocks would be the result of mixing with an enriched Hadean reservoir characterized by negative $\mu^{142}Nd$ values, during their emplacement at 3770 Ma. Such a model involving the metasomatic alteration of the mantle through subduction of a low-$\mu^{142}Nd$ Hadean crust was proposed for the Ukaliq mafic and ultramafic rocks (*15*, *30*). It could be argued that the variation in $^{142}Nd/^{144}Nd$ and $^{143}Nd/^{144}Nd$ displayed here by the NGB gneissic metagabbros is the result of the same metasomatic mixing process. When the $^{143}Nd/^{144}Nd$ ratios for the gneissic metagabbro samples analyzed here are calculated at 3770 Ma, a positive correlation with $^{147}Sm/^{144}Nd$ is observed (Fig. 4A), which can be the result of (i) ingrowth of ^{143}Nd between 4160 Ma and 3770 Ma if the rocks are Hadean or (ii) mixing at 3770 Ma with an enriched, low $^{143}Nd/^{144}Nd$ and low-$\mu^{142}Nd$ reservoir, if the rocks were emplaced in the Eoarchean (4.0 to 3.6 Ga). The latter scenario would be comparable to the mixing models previously proposed to explain the correlation between $^{142}Nd/^{144}Nd$ and $^{147}Sm/^{144}Nd$ observed in the Ujaraaluk unit (*15*, *18*). However, a putative 4.3 Ga enriched reservoir, as inferred by these models, with an $^{142}Nd/^{144}Nd$ and $^{147}Sm/^{144}Nd$ low enough to account for the Ujaraaluk $^{142}Nd/^{144}Nd$ versus Sm/Nd correlation would evolve to $^{143}Nd/^{144}Nd$ ratios at 3.77 Ga too low to produce the variation in $^{143}Nd/^{144}Nd_{(3.77\ Ga)}$ observed in the metagabbroic rocks (Fig. 4A). If derived from a parent reservoir with chondritic Sm/Nd ratio, a low-$\mu^{142}Nd$ enriched reservoir with $^{147}Sm/^{144}Nd$ between 0.13 and 0.10 would need to have formed at ~4285 Ma to evolve to the appropriate $\mu^{142}Nd$ (between −15 and −21; Fig. 4B) to fit the Ujaraaluk correlation. These Hadean enriched reservoirs, however, would have evolved to $^{143}Nd/^{144}Nd$ ratios by 3770 Ma yielding mixing lines with apparent ages between 4360 Ma and 4400 Ma, assuming mixing with a reservoir

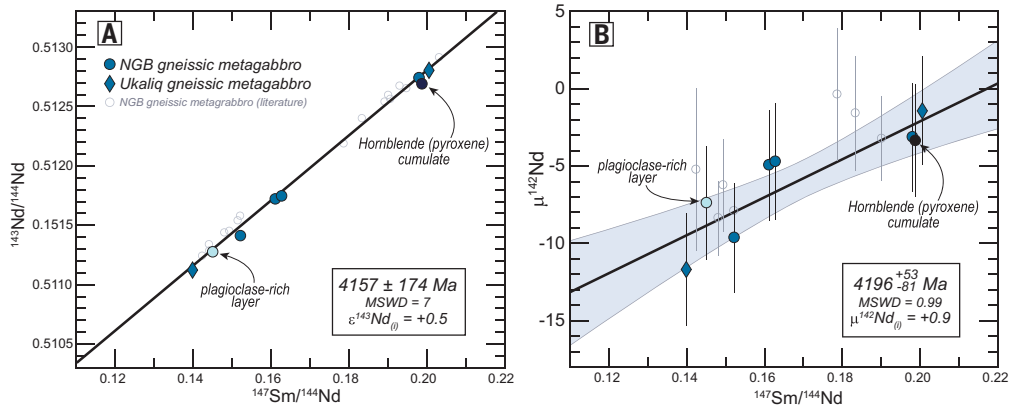

Fig. 3. Sm-Nd isochron diagrams for the gneissic metagabbros. (**A**) Isochron diagram for the long-lived ^{147}Sm-^{143}Nd system. $n = 8$ samples for this study and $n = 15$ samples for literature data. Age and initial $^{143}Nd/^{144}Nd$ were calculated using IsoplotR (*39*). Errors for $^{143}Nd/^{144}Nd$ and $^{147}Sm/^{144}Nd$ are smaller than the symbols. (**B**) Isochron diagram for the short-lived ^{146}Sm-^{142}Nd system. $\mu^{142}Nd$ represents the variation in $^{142}Nd/^{144}Nd$ compared with the measured ratio for the JNdi-1 standard, in parts per million. The initial $\mu^{142}Nd$ [$\mu^{142}Nd_{(i)}$] was calculated using the $^{142}Nd/^{144}Nd$ from the isochron intercept and normalized to a reservoir that evolved with a chondritic Sm/Nd ratio to the present-day $^{142}Nd/^{144}Nd$ ratio of the modern upper mantle (*34*) at the age of the isochron. Regression was obtained using IsoplotR (*39*), and the age was calculated using a half-life of 103 Ma for ^{146}Sm and initial $^{146}Sm/^{144}Sm = 0.00828$ (*23*). $n = 8$ samples for this study and $n = 7$ samples for literature data. Errors for $\mu^{142}Nd$ are 2 SE and are smaller than the symbols for $^{147}Sm/^{144}Nd$. Literature data from (*13*).

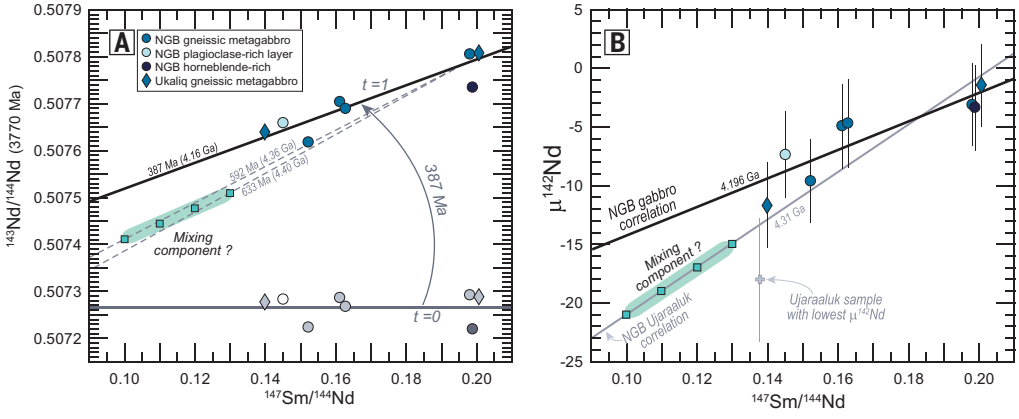

Fig. 4. Modeling for isotopic mixing with a Hadean enriched reservoir. (**A**) $^{143}Nd/^{144}Nd$ calculated at 3770 Ma versus $^{147}Sm/^{144}Nd$ for the gneissic metagabbros. The correlation could either suggest mixing occurring at 3770 Ma or variation in $^{143}Nd/^{144}Nd$ caused by radiogenic ingrowth between 4160 Ma and 3770 Ma. Gray symbols are the same samples but showing $^{143}Nd/^{144}Nd$ calculated at 4160 Ma [time (t) = 0]. The regression through the $^{143}Nd/^{144}Nd$ data calculated at 3770 Ma yields a slope corresponding to 387 Ma ($t = 1$). Ages for slopes are at 3770 Ma, and ages in parentheses are the corresponding ages today. Errors for $^{143}Nd/^{144}Nd$ and $^{147}Sm/^{144}Nd$ are smaller than the symbols. (**B**) $\mu^{142}Nd$ versus $^{147}Sm/^{144}Nd$ for the gneissic metagabbros. Errors for $\mu^{142}Nd$ are 2 SE and are smaller than the symbols for $^{147}Sm/^{144}Nd$. The NGB Ujaraaluk sample showing the lowest measured $\mu^{142}Nd$ of −18 is shown with the gray cross. Data for this sample are from (*13*) and Ujaraaluk correlation from (*8*). The $\mu^{142}Nd$ values for the putative mixing components in (B) are set to lie on the Ujaraaluk correlation between $^{147}Sm/^{144}Nd$ of 0.10 and 0.13 (square symbols). Resulting $^{143}Nd/^{144}Nd$ at 3770 Ma for these enriched reservoirs are shown in (A) as square symbols, producing mixing lines (assuming mixing with a reservoir with chondritic Sm/Nd) with ages between 4.36 and 4.40 Ga.

with a chondritic Sm/Nd ratio (Fig. 4A). We examined the possibility that alternative enriched low-$\mu^{142}Nd$ reservoirs could represent a suitable mixing end-member to explain identical apparent ages for the long-lived and short-lived Sm-Nd systematics in the NGB metagabbros, but none could account for the age agreement between the ^{147}Sm-^{143}Nd and ^{146}Sm-^{142}Nd metagabbro correlations (see supplementary text). Moreover, if the Sm-Nd systematics of both the Ujaraaluk unit and metagabbros are the result of binary mixing, at least two unpreserved Hadean-enriched reservoirs would be required, one having affected only the Ujaraaluk rocks (Fig. 4B) and one having affected only the metagabbros. This scenario involving multiple Hadean-enriched reservoirs independently and concurrently interacting with the Ujaraaluk metavolcanic rocks and the differentiated metagabbro sills, closely associated in the field with the latter intruding the former, is highly unlikely.

Finally, regarding the metagabbros, it is unlikely that mixing between unrelated isotopically distinct reservoirs would produce apparent isochrons with identical ages for both the long-lived ^{147}Sm-^{143}Nd and short-lived ^{146}Sm-^{142}Nd systems, especially given the fact that mixing would have occurred after the extinction of one radiogenic system (i.e., $^{142}Nd/^{144}Nd$ no longer evolving after the mixing event), while the other is still extant (i.e., $^{143}Nd/^{144}Nd$ evolving during more than 3.7 billion years after the mixing event). The age agreement between both Sm-Nd isotopic systems, in rocks petrologically and texturally related through

magmatic differentiation, is therefore compelling evidence that the age of the NGB metagabbro sills is ~4160 Ma.

The NGB gneissic metagabbro sills exhibit textural, petrological, geochemical and $^{147\text{-}146}$Sm-$^{143\text{-}142}$Nd isotopic characteristics expected for magmatically differentiated Hadean mafic rocks. Their initial ε^{143}Nd and μ^{142}Nd of +0.5 and +0.9, respectively, at ~4160 Ma, where $\varepsilon^{143}Nd_{(i)}$ is compared with the chondritic uniform reservoir while $\mu^{142}Nd_{(i)}$ is normalized to a reservoir evolving with a chondritic Sm/Nd ratio to the present-day $^{142}Nd/^{144}Nd$ ratio of the modern upper mantle (*34*) (Fig. 3), suggest derivation from an expectedly near chondritic mantle in the Hadean rather than requiring the involvement of an exotic enriched Hadean mantle reservoir. Several recent studies using a wide array of geochemical and isotopic tracers proposed models requiring the existence of extensive Hadean mafic crust (*35*–*38*). The data presented here suggest that at least a small remnant of this Hadean mafic crust is preserved in the NGB, providing invaluable insights into the Hadean Earth.

REFERENCES AND NOTES

1. J.-L. Paquette *et al.*, *Precambrian Res.* **271**, 49–55 (2015).
2. S. A. Wilde, J. W. Valley, W. H. Peck, C. M. Graham, *Nature* **409**, 175–178 (2001).
3. B. L. Byerly *et al.*, *Geology* **46**, 967–970 (2018).
4. G.-F. Xing *et al.*, *Sci. Rep.* **4**, 5143 (2014).
5. T. Chaudhuri, Y. Wan, R. Mazumder, M. Ma, D. Liu, *Sci. Rep.* **8**, 7069 (2018).
6. P.-L. Cui *et al.*, *Int. Geol. Rev.* **55**, 1902–1908 (2013).
7. R. W. Carlson, M. Garçon, J. O'Neil, J. Reimink, H. Rizo, *Chem. Geol.* **530**, 119321 (2019).
8. J. O'Neil, R. Carlson, D. Papineau, Y. Levine, D. Francis, in *Earth's Oldest Rocks*, M. Van Kranendonk, V. Bennett, E. Hoffmann, Eds. (Elsevier, ed. 2, 2019), pp. 349–374.
9. J. O'Neil, D. Francis, R. W. Carlson, *J. Petrol.* **52**, 985–1009 (2011).
10. J. O'Neil, M. Boyet, R. W. Carlson, J.-L. Paquette, *Earth Planet. Sci. Lett.* **379**, 13–25 (2013).
11. N. Cates, S. Mojzsis, *Earth Planet. Sci. Lett.* **255**, 9–21 (2007).
12. J. O'Neil, R. W. Carlson, D. Francis, R. K. Stevenson, *Science* **321**, 1828–1831 (2008).
13. J. O'Neil, R. W. Carlson, J.-L. Paquette, D. Francis, *Precambrian Res.* **220**, 23–44 (2012).
14. L. E. Augland, J. David, *Earth Planet. Sci. Lett.* **428**, 162–171 (2015).
15. G. Caro, P. Morino, S. Mojzsis, N. Cates, W. Bleeker, *Earth Planet. Sci. Lett.* **457**, 23–37 (2017).
16. N. L. Cates, K. Ziegler, A. K. Schmitt, S. J. Mojzsis, *Earth Planet. Sci. Lett.* **362**, 283–293 (2013).
17. M. Guitreau, J. Blichert-Toft, S. J. Mojzsis, A. S. Roth, B. Bourdon, *Earth Planet. Sci. Lett.* **362**, 171–181 (2013).
18. A. S. Roth *et al.*, *Earth Planet. Sci. Lett.* **361**, 50–57 (2013).
19. J. O'Neil, H. Rizo, M. Boyet, R. Carlson, M. Rosing, *Earth Planet. Sci. Lett.* **442**, 194–205 (2016).
20. S. Turner, T. Rushmer, M. Reagan, J.-F. Moyen, *Geology* **42**, 139–142 (2014).
21. I. Bindeman, J. O'Neil, *Earth Planet. Sci. Lett.* **586**, 117539 (2022).
22. M. S. Dodd *et al.*, *Nature* **543**, 60–64 (2017).
23. N. Marks, L. Borg, I. Hutcheon, B. Jacobsen, R. Clayton, *Earth Planet. Sci. Lett.* **405**, 15–24 (2014).
24. N. M. Chiera *et al.*, *Sci. Rep.* **14**, 17436 (2024).
25. J. Darling *et al.*, *Am. J. Sci.* **313**, 844–876 (2013).
26. J. David, L. Godin, R. Stevenson, J. O'Neil, D. Francis, *Geol. Soc. Am. Bull.* **121**, 150–163 (2009).
27. L. Heaman, A. LeCheminant, *Chem. Geol.* **110**, 95–126 (1993).
28. A. Davidson, O. Van Breemen, *Contrib. Mineral. Petrol.* **100**, 291–299 (1988).
29. U. Söderlund, F. Hellström, S. Kamo, *J. Metamorph. Geol.* **26**, 539–560 (2008).
30. T. Grocolas, P. Bouilhol, G. Caro, S. J. Mojzsis, *Contrib. Mineral. Petrol.* **177**, 39 (2022).
31. W. Chowdhury *et al.*, *Lithos* **372**, 105673 (2020).
32. J. Greer *et al.*, *Lithos* **364**, 105520 (2020).
33. W. Bleeker, N. Rayner, "Not so old: The Nuvvuagittuq greenstone remnant of the northern Superior craton," Geological Association of Canada–Mineralogical Association of Canada, Volume of Abstracts, vol. 45, pp. 57–58 (Geological Association of Canada, 2022).
34. D. Peters, H. Rizo, J. O'Neil, C. Hamelin, S. Shirey, *Geochem. Perspect. Lett.* **29**, 51–56 (2024).
35. N. Drabon *et al.*, *Proc. Natl. Acad. Sci. U.S.A.* **118**, e2004370118 (2021).
36. J. O'Neil, R. W. Carlson, *Science* **355**, 1199–1202 (2017).
37. J. Tusch *et al.*, *Proc. Natl. Acad. Sci. U.S.A.* **119**, e2120241119 (2022).
38. D. Wang, X.-F. Qiu, R. W. Carlson, *Earth Planet. Sci. Lett.* **605**, 118037 (2023).
39. P. Vermeesch, R. Isoplot, *Geoscience Frontiers* **9**, 1479–1493 (2018).

ACKNOWLEDGMENTS

Nakurmiimmarialuk (ᓇᓄᖏᑦᓱᓕᓪᓚᐅᒃ) to the Pituvik Landholding Corporation of Inukjuak and the local Inuit community for their hospitality and permission to conduct research on their land as well as for facilitating fieldwork. We also thank R. W. Carlson for insightful scientific discussions as well as three anonymous reviewers whose valuable comments and criticism greatly helped improve this contribution. **Funding:** Natural Sciences and Engineering Research Council of Canada Discovery grants and Northern Supplement grants RGPIN 435589-2013 (J.O.) and RGPIN-477144-2015 (H.R.); Ontario Early Researcher Award ER14-10-141 (J.O.). **Author contributions:** Conceptualization: J.O.; Methodology: C.S., J.O., D.B., J.P., H.R., J.-L.P.; Investigation: C.S., J.O., D.B., J.P., H.R.; Funding acquisition: J.O., H.R.; Supervision: J.O., H.R.; Writing – original draft: C.S., J.O.; Writing – review & editing: C.S., J.O., H.R. **Competing interests:** The authors declare that they have no competing interests. **Data and materials availability:** The metagabbro and other samples were obtained from the sources listed in table S1 and are described in the supplementary materials. All data are available in the supplementary materials, where table S1 includes the whole-rock geochemical compositions, tables S2 to S5 and S7 include all isotopic analyses, and table S6 details the operating conditions and instrument settings for U-Pb isotopic analyses.

SUPPLEMENTARY MATERIALS

science.org/doi/10.1126/science.ads8461
Materials and Methods; Supplementary Text; Figs. S1 to S12; Tables S1 to S7; References (*40*–*56*); Data S1

Submitted 2 September 2024; accepted 2 May 2025

10.1126/science.ads8461

ORGANIC CHEMISTRY

Carbonyl-to-sulfur swap enabled by sequential double carbon-carbon bond activation

Zining Zhang and Guangbin Dong*

In drug development, replacement of a skeletal carbon with a sulfur atom can result in analogs of bioactive compounds with improved properties. Currently, the sulfur analogs are almost exclusively prepared by de novo synthesis; the existing approach to swap carbon with sulfur is inefficient and involves stoichiometric mercury reagents. In this study, we report a two-step carbonyl-to-sulfur (CO-to-S) atom swap approach, enabled by a rationally designed *N*′-alkyl-hydrazonamide (NAHA) reagent that promotes forming pre-aromatic intermediates twice sequentially by different mechanisms, thereby achieving homolytic cleavage of both α-C–C bonds of the ketone substrates. A Ts–S–Ts (Ts, *p*-toluenesulfonyl) reagent mediates this process through successive intermolecular and intramolecular alkyl radical trapping by the central sulfur. This method shows a broad substrate scope and excellent chemoselectivity, providing a streamlined route to sulfur-containing scaffolds from readily available ketones.

Late-stage functionalization has become an increasingly important strategy for rapid access to diverse analogs of biologically active compounds by avoiding labor-intensive de novo syntheses (*1*–*3*). Among various late-stage functionalization tactics, "atom swap" reactions, where one atom is directly replaced with another within a molecular backbone, are particularly attractive, as they can offer skeletally altered analogs that would otherwise be difficult to prepare by conventional approaches (*4*, *5*). To date, substantial advances have been made in atom swap reactions involving aromatic substrates, enabling a range of impactful transformations (*6*–*12*). By contrast, exchanging atoms in saturated systems has been rare (*13*), likely owing to the inherent challenges of activating σ bonds. Given the growing demand to "escape from flatland" in small-molecule drug design, developing an atom swap platform for three dimensional, sp^3-rich systems could be highly valuable (*14*).

Among various atoms that a skeletal carbon atom could be exchanged with, sulfur stands out as an intriguing but underexplored target. As one of the most prevalent heteroatoms in small-molecule drugs and agrichemicals after oxygen and nitrogen, sulfur is present in backbones of nonaromatic systems in the form of, e.g., thioethers, sulfoxides, sulfonamides, and sulfones (*15*). A number of structure-activity relationship (SAR) studies have shown that replacing a skeletal carbon atom with sulfur can greatly impact biological activities. For example, substitution of a methylene group in the pyrimidinone-derived bicyclic compound with a sulfur atom (XAV939) led to 31-fold-greater potency for inhibiting tankyrase 2 (TNKS2) (*16*, *17*) (Fig. 1A). Additionally, compared with the carbonyl (CO)–derived oxazolidinone compound, the corresponding thioether analog (sutezolid) showed a sevenfold increase in antibacterial activity against *Staphylococcus aureus* (*18*, *19*). Similarly, the benefits of replacing carbonyl groups with sulfur can be seen in the cases of developing inhibitors for bromodomain-containing protein 4 (*20*) and 5-lipoxygenase (*21*).

Department of Chemistry, University of Chicago, Chicago, IL, USA. *Corresponding author. Email: gbdong@uchicago.edu

Currently, the sulfur-containing analogs were almost all prepared through de novo synthesis, as effective strategies for carbon-to-sulfur atom swap have yet to be established. Although the synthesis of thiasteroids from natural steroids has long been of interest (*22*), existing approaches for carbon-to-sulfur substitution involve lengthy synthetic sequences, multiple redox reactions, and the use of stoichiometric mercury reagents (Fig. 1B). For example, converting a cholesterol derivative into its thioether analog requires six steps (*23*), whereas a cholic acid derivative undergoes a nine-step transformation to achieve the "CO-to-S" conversion (*24*). To address this challenge, we describe the development of a straightforward CO-to-S swap through sequential double C–C bond activation, enabled by a rationally designed *N*′-alkyl-hydrazonamide (NAHA) reagent (Fig. 1C).

Reaction development

Since 2021, our group has been developing a class of carbonyl activation reagents, namely *N*′-alkyl-hydrazonamides (NAHAs) (*25*), which can break C–C bonds of alkyl ketones using aromatization as a driving force (Fig. 2A). The first-generation NAHA reagents contain a *N*-methyl group and can efficiently condense with ketones to form a pre-aromatic intermediate (PAI), which then undergoes aromatization-driven C–C bond cleavage to generate an alkyl radical triggered by either a hydrogen-atom transfer (HAT) or single-electron transfer (SET) process (*26*–*31*). The resulting radical can be trapped by various reagents (black circle, Fig. 2A) to form C–H, C–D (*32*), C–C (*26*, *33*), or C–heteroatom bonds (*34*, *35*), or it can be oxidized to an alkene (*25*), leading to various deacylative transformations for linear ketones. However, when a cyclic ketone is used, although C–C cleavage can still take place, the resulting aromatic by-product, the 1,2,4-triazole fragment, would be covalently attached to the ring-opened product, resulting in a "dead end" (*26*). Hence, the key challenge for realizing the desired CO-to-S transformation is how to activate the second C–C bond, i.e., the one linking the alkyl group and the 1,2,4-triazole, for further functionalization.

Inspired by the recent development of radical-mediated aryl transfer reactions (*36*), we hypothesized that the alkyl-triazole bond could be cleaved with a new type of NAHA reagents that contain an aryl halide moiety. We posited that, after a halogen-atom transfer (XAT) process, i.e., abstracting the halogen atom by an Si or Sn radical species, the resulting highly reactive aryl radical would attack the triazole intramolecularly to regenerate a PAI radical (*37*), which should promote cleavage of the alkyl-triazole bond to form a more stable alkyl radical that undergoes further transformations and releases a triazole-based tricyclic by-product. This alkyl radical can then be trapped intramolecularly by the functional group installed during the first activation to furnish the atom swap, with the excised carbonyl carbon residing in the triazole-based tricyclic by-product. To test this hypothesis, 1,2,4-triazole compounds (**1-ai**) tethered with an aryl bromide moiety were used as the model to study the second C–C bond activation process (Fig. 2B). The alkyl-triazole bond can indeed be cleaved by using azobisisobutyronitrile (AIBN) as the radical initiator with $(TMS)_3SiH$ as the XAT reagent and hydrogen atom source. Given that HAT between an aryl radical and $(TMS)_3SiH$ is extremely fast with a rate constant of 10^8 M^{-1} s^{-1} (*38*), a pronounced Thorpe-Ingold effect was observed in this reaction. Although the simple *gem*-dimethyl linker was not adequate to suppress the competing HAT pathway, the analog containing a "trimethyl lock" linkage (*39*) was found to be highly efficient to promote the desired intramolecular cyclization in a highly selective manner.

With the key knowledge obtained for the second C–C bond activation and the design principle of the NAHA reagent, we next focused on the development of the CO-to-S reaction (Fig. 3). Cholesterol-derived ketone **1q** was chosen as the model substrate, and the NAHA reagent with a dangling aryl iodide moiety in a trimethyl lock setting was found to be optimal. The condensation of **1q** with NAHA proceeded

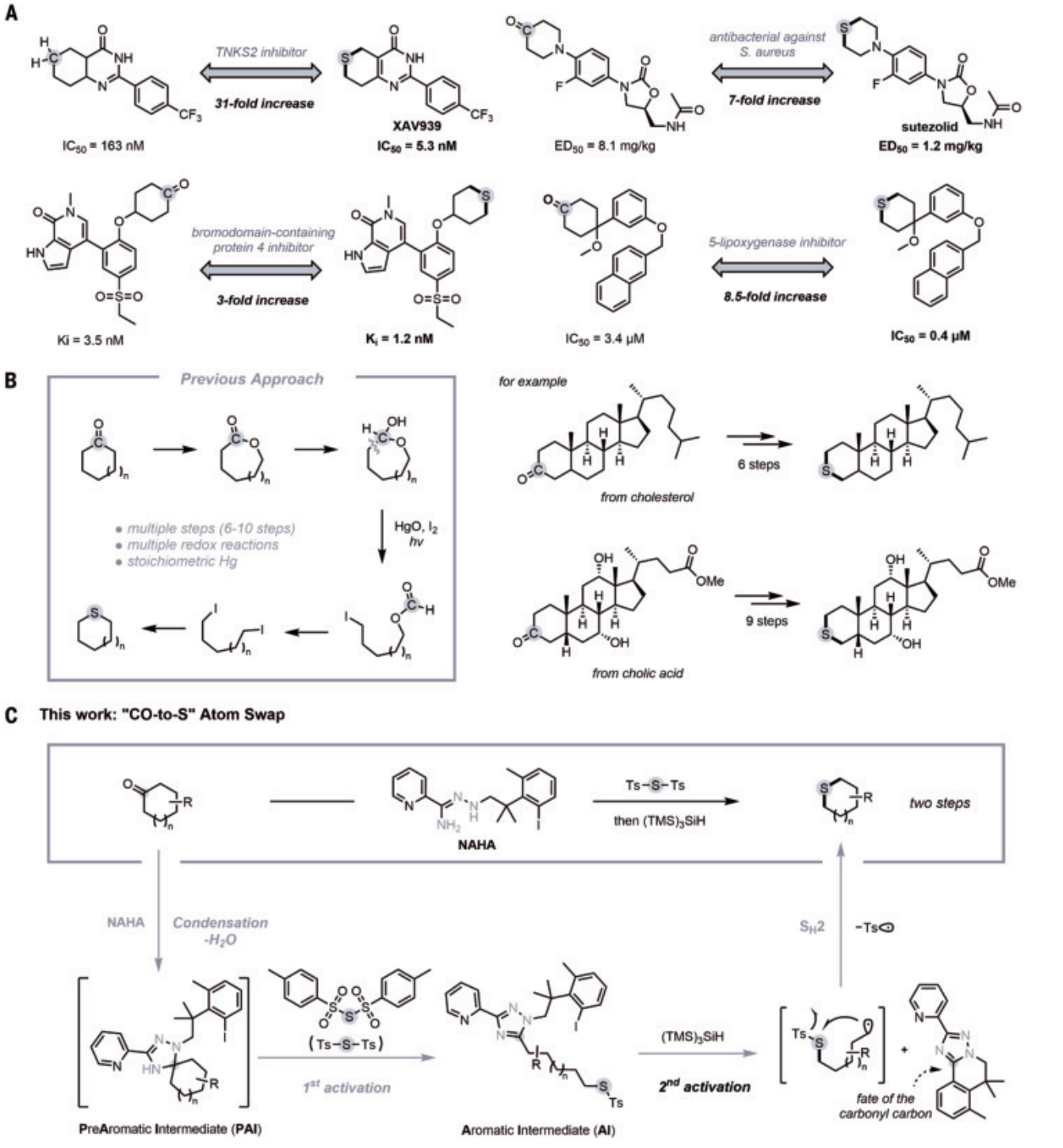

Fig. 1. Replacement of carbon with sulfur in molecular skeletons. (**A**) Importance of sulfur-based skeletons on bioactive molecules. (**B**) The previous approach to access thioethers from the corresponding cyclic ketones and syntheses of thiasteroids from natural steroids. (**C**) The proposed CO-to-S atom swap through a sequential double C–C activation strategy. IC_{50}, median inhibitory concentration; ED_{50}, median effective dose; K_i, inhibitory constants; *hv*, light.

with a nearly quantitative conversion in the presence of activated 4-Å molecular sieves with a mixed solvent of $PhCF_3$ and acetic acid (CH_3COOH) (AcOH) (1:1, total volume 0.08 mL) at 40°C. The key for the next step was to identify an efficient sulfur atom transfer (SAT) reagent. We expected that this reagent should contain two radical leaving groups on sulfur, and the central sulfur can react twice, in the intermolecular quenching of the alkyl radical after the first C–C bond cleavage and then in intramolecular ring closure after the second C–C bond cleavage to close the loop through another SAT (Fig. 1C). To the end, Ts–S–Ts was posited to be an appropriate SAT reagent. This was because Ts radical is not only an excellent leaving group in bimolecular homolytic substitution (S_H2) reactions but also an established initiator to trigger PAI fragmentation (*34*, *35*). Indeed, treatment of crude **1q-PAI** with 3.0 equiv of Ts–S–Ts, 1.0 equiv of bis(trimethylsilyl)acetamide (BSA)

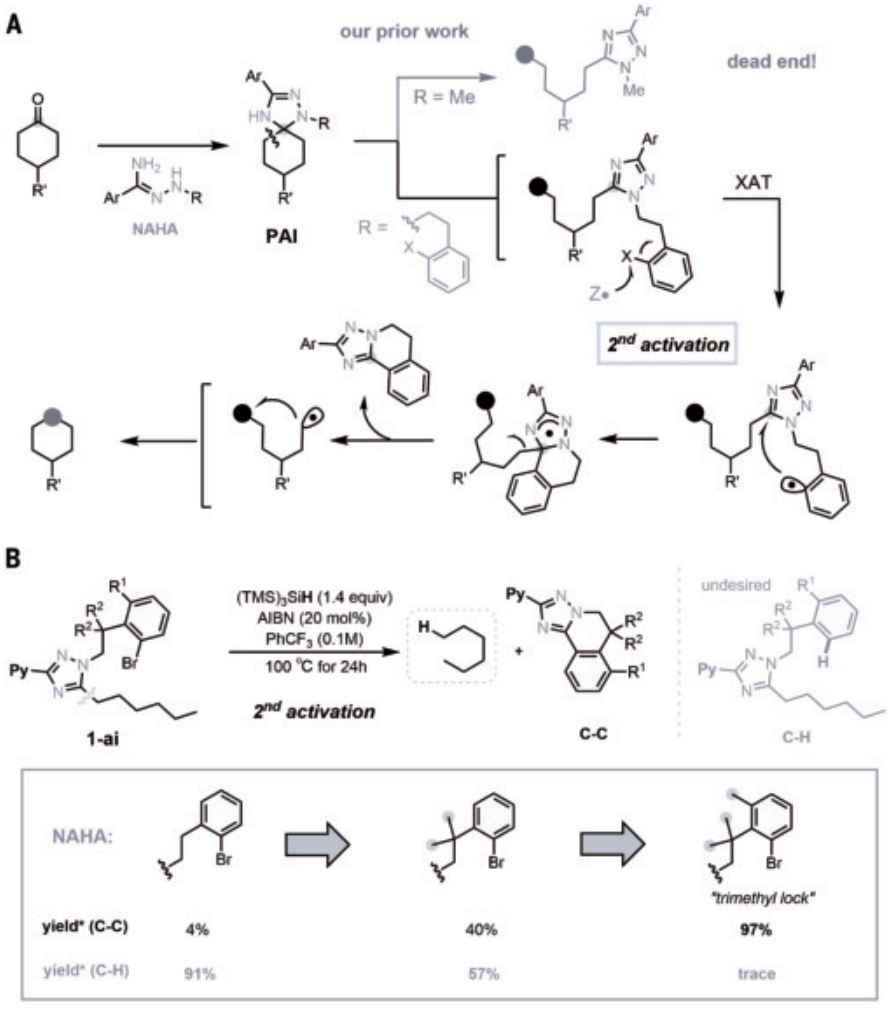

Fig. 2. Design principle for the NAHA reagent. (**A**) Enabling the second C–C bond cleavage through intramolecular aryl radical addition. (**B**) A model study on the second activation shows a strong Thorpe-Ingold effect on the linker design. *All yields are nuclear magnetic resonance (NMR) yields. Z, a halogen atom–abstracting group; TMS, trimethylsilyl; AIBN, azobisisobutyronitrile; Py, 2-pyridyl.

as a water scavenger, and 2.0 equiv of Cs_2CO_3 in 1 mL of $PhCF_3$ at 50°C for 12 hours afforded the ring-opened sulfonyl thiolate product **2q** in 65% yield with a 1:1 ratio of two isomers (entry 1). Control experiments revealed that reducing the loading of NAHA slightly decreased the yield, whereas the absence of AcOH drastically reduced the efficiency of the condensation (entries 2 and 3). The thiolation with Ts–S–Ts proved sensitive to the reaction temperature, as higher temperatures led to serious decomposition of **2q** (entry 4). Using only 1 equiv of Ts–S–Ts decreased the yield (entry 5), likely because the intermolecular S_H2 reaction with the primary alkyl radical benefits from a high concentration of the SAT reagent. In addition, the SAT reaction prefers nonpolar solvents, and replacement of $PhCF_3$ with tetrahydrofuran substantially reduced the yield (entry 6). Furthermore, whereas the absence of BSA did not greatly influence the yield (entry 7), Cs_2CO_3 was critical for suppressing side-product formation (entry 8; see supplementary materials for details).

The stage was now set to explore the ring closure step to construct the cyclic thioether. After careful optimizations, thiane ***3q*** was obtained in 93% yield when simply treating **2q** with 1.2 equiv of $(TMS)_3SiH$, 10 mol % AIBN, and 1.0 equiv of 4-Å molecular sieves in $PhCF_3$ at 100°C (entry 9, Fig. 3). The role of $(TMS)_3SiH$ is proposed to be twofold: (i) the silyl radical generated from this reagent can abstract the iodine from **2q** to form the corresponding aryl radical, and (ii) it can quench the Ts radical to form TsH and regenerate the silyl radical to allow radical chain propagation. Further control experiments showed that neither $(TMS)_3SiH$ nor AIBN was strictly essential (entries 10 and 11), possibly owing to the inherent high lability of the aryl iodide bond in the trimethyl lock setting (see the supplementary materials for the computed bond dissociation energy). Replacement of $(TMS)_3SiH$

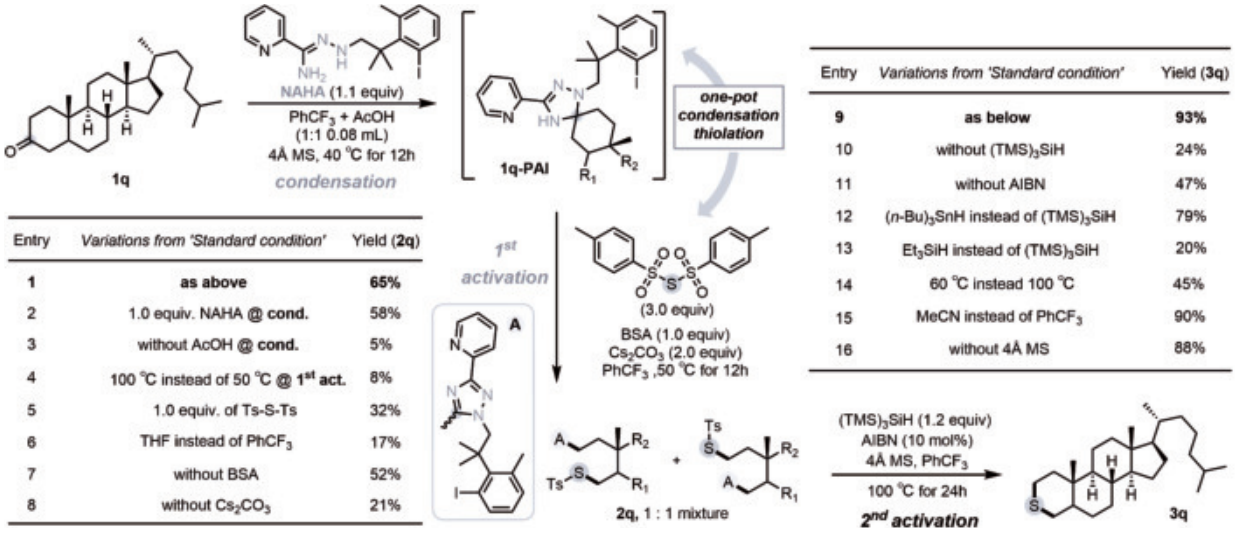

Entry	Variations from 'Standard condition'	Yield (2q)
1	as above	65%
2	1.0 equiv. NAHA @ cond.	58%
3	without AcOH @ cond.	5%
4	100 °C instead of 50 °C @ 1st act.	8%
5	1.0 equiv. of Ts-S-Ts	32%
6	THF instead of $PhCF_3$	17%
7	without BSA	52%
8	without Cs_2CO_3	21%

Entry	Variations from 'Standard condition'	Yield (3q)
9	as below	93%
10	without $(TMS)_3SiH$	24%
11	without AIBN	47%
12	$(n\text{-}Bu)_3SnH$ instead of $(TMS)_3SiH$	79%
13	Et_3SiH instead of $(TMS)_3SiH$	20%
14	60 °C instead 100 °C	45%
15	MeCN instead of $PhCF_3$	90%
16	without 4Å MS	88%

Fig. 3. Reaction development for the CO-to-S swap. Unless mentioned otherwise, all reactions were run with **1q** (0.1 mmol). The yield was determined by ^1H NMR with 1,1,2,2-tetrachloroethane as the internal standard. THF, tetrahydrofuran.

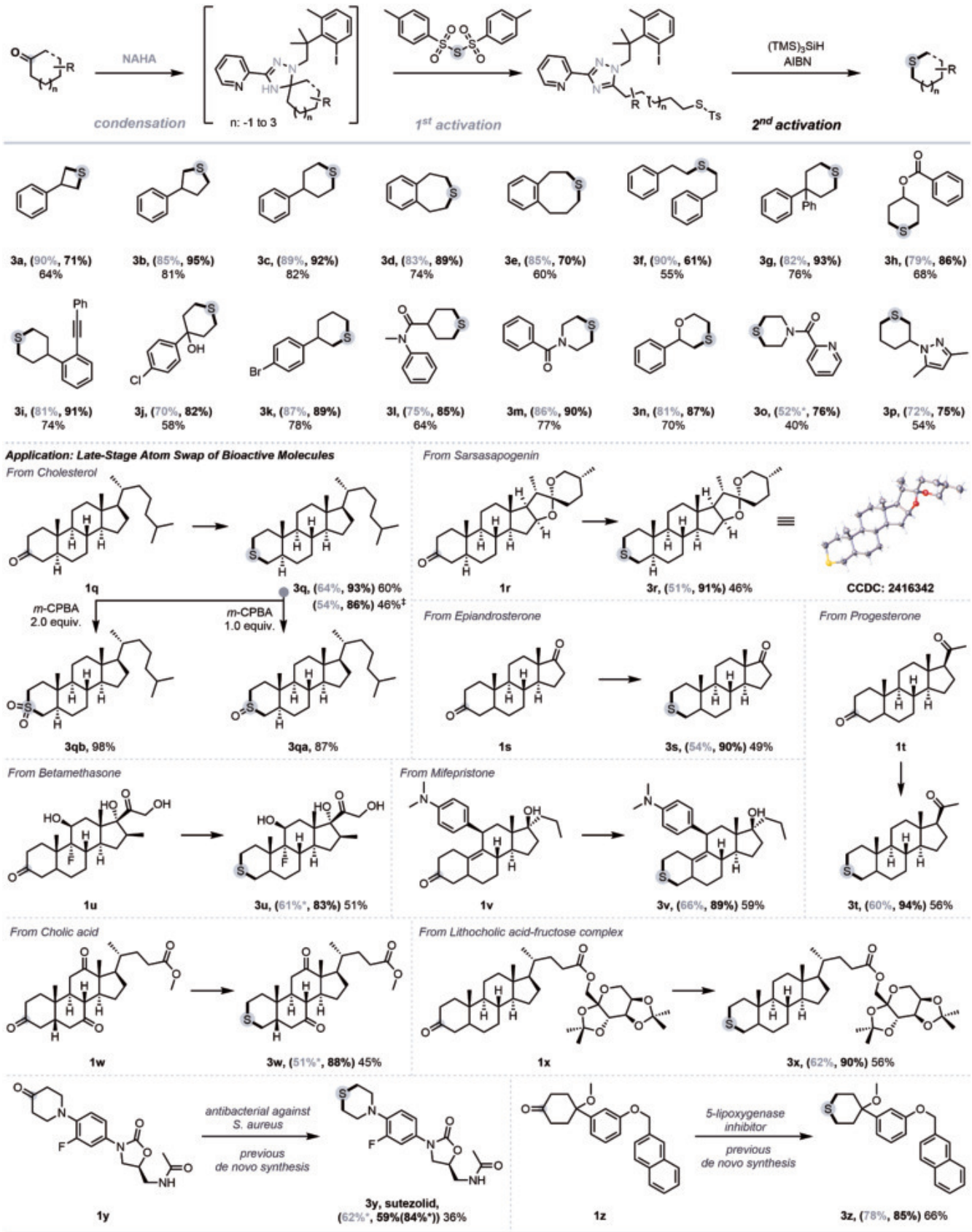

Fig. 4. Substrate scope and applications to the late-stage functionalization of complex bioactive compounds for analog synthesis. Unless noted otherwise, reported yields are for isolated product. *The yield was determined by ^{1}H NMR integration with 1,1,2,2-tetrachloroethane as the internal standard. ‡The reaction was run on a 1-mmol scale.

with (n-Bu)$_3$SnH gave slightly lower yield, whereas Et_3SiH was not effective (entries 12 and 13). Running the second activation step at low temperatures was not as efficient (entry 14). The annulation also worked well in other solvents, such as acetonitrile (entry 15). Lastly, the use of 4-Å molecular sieves only slightly improved the yield (entry 16).

Substrate scope

With the optimized reaction conditions established, the scope of the two-step CO-to-S swap reaction was explored (Fig. 4). The transformation was not limited to forming six-membered thianes; good to excellent yields were obtained for four- to eight-membered cyclic thioethers (**3a** to **3e**) and even linear (**3f**) structures. In addition, 4,4-disubstitution (**3g**), which could potentially resist ring opening, did not affect the reactivity. Moreover, a variety of functional groups, including ester (**3h**), alkyne (**3i**), free tertiary alcohol and aryl chloride (**3j**), aryl bromide (**3k**), amide (**3l** and **3m**), ether (**3n**), pyridine (**3o**), and pyrazole (**3p**), were compatible. Encouraged by the high chemoselectivity, we next explored the CO-to-S swap strategy in the context of late-stage functionalization of complex bioactive molecules. Aside from the model cholesterol substrate (**3q**), derivatives of natural products, such as sarsasapogenin (**3r**), epiandrosterone (**3s**), progesterone (**3t**), betamethasone (**3u**), mifepristone (**3v**), cholic acid (**3w**), and lithocholic acid (**3x**), all underwent smooth CO-to-S swap transformations. Slightly lower yield was obtained on a larger scale (1 mmol, **3q**). This method showed not only great compatibility with the complex skeletons of steroids but also the tolerance of additional sensitive functional groups, such as ketal (**3r**); unprotected primary, secondary, and tertiary alcohols (**3u**); amine (**3v**); and olefin (**3v**). Given that the condensation with the NAHA reagent is sensitive to the steric environment of the ketone substrate, the CO-to-S swap reaction exhibited excellent site selectivity favoring the less sterically hindered ketone, when multiple ketones exist in the substrates (**1s**, **1t**, **1u**, and **1w**). To allow sterically hindered ketones to react, efforts on investigating silylated NAHA reagents are ongoing. Furthermore, it is established that thioethers can be easily converted to the corresponding sulfoxides (**3qa**) or sulfones (**3qb**) through controlled oxidation (*23*, *40*); thus, this method also offers late-stage access to sulfoxide and sulfone analogs, which are valuable for medicinal chemistry studies. Lastly, the use of this atom swap strategy for rapid access to sutezolid (**3y**) (*18*) and a more potent 5-lipoxygenase inhibitor (**3z**) (*21*) from the corresponding less active carbonyl analogs proved to be successful and avoided de novo syntheses. Notably, amide N–H bonds can be tolerated in the case of sutezolid (**3y**).

We have developed a two-step CO-to-S atom swap strategy that enables streamlined conversion of ketones into the corresponding thioethers. The rationally designed bifunctional NAHA reagents allow for two-stage C–C bond activations, permitting sequential functionalization of both carbon termini. The broad substrate scope and mild redox-neutral reaction conditions along with the high efficiency and chemoselectivity of these radical-mediated processes make this strategy suitable for late-stage modification of structurally complex bioactive compounds. It is anticipated that the specific activation mode enabled by this class of NAHA reagents should serve as a versatile platform for diverse skeletal modification of sp^3-rich organic molecules in the future.

REFERENCES AND NOTES

1. D. C. Blakemore *et al.*, *Nat. Chem.* **10**, 383–394 (2018).
2. Y.-F. Liang *et al.*, *Chem. Rev.* **123**, 12313–12370 (2023).
3. N. J. Castellino, A. P. Montgomery, J. J. Danon, M. Kassiou, *Chem. Rev.* **123**, 8127–8153 (2023).
4. D. L. Boger, *J. Org. Chem.* **82**, 11961–11980 (2017).
5. J. Jurczyk *et al.*, *Nat. Synth.* **1**, 352–364 (2022).
6. T. J. Pearson *et al.*, *Science* **381**, 1474–1479 (2023).
7. D. Kim *et al.*, *Science* **386**, 99–105 (2024).
8. J. Woo, C. Stein, A. H. Christian, M. D. Levin, *Nature* **623**, 77–82 (2023).
9. Q. H. Luu, J. Li, *Chem. Sci.* **13**, 1095–1100 (2022).
10. S. C. Patel, N. Z. Burns, *J. Am. Chem. Soc.* **144**, 17797–17802 (2022).
11. Q. Cheng *et al.*, *Nat. Chem.* **16**, 741–748 (2024).
12. H. Zhong *et al.*, *Nat. Commun.* **14**, 5273 (2023).
13. H. Lyu, I. Kevlishvili, X. Yu, P. Liu, G. Dong, *Science* **372**, 175–182 (2021).
14. F. Lovering, J. Bikker, C. Humblet, *J. Med. Chem.* **52**, 6752–6756 (2009).
15. K. A. Scott, J. T. Njardarson, *Top. Curr. Chem. (Cham)* **376**, 5 (2018).
16. S.-M. A. Huang *et al.*, *Nature* **461**, 614–620 (2009).
17. M. D. Shultz *et al.*, *J. Med. Chem.* **56**, 6495–6511 (2013).
18. H. Yamada, K. Munesada, M. Taniguchi, Preparation of (piperidinophenyl)oxazolidinone derivatives as antimicrobial agents, Patent WO9525106 A1 (1995).
19. M. R. Barbachyn, S. J. Brickner, D. K. Hutchinson, Substituted oxazine and thiazine oxazolidinone antimicrobials, European Patent WO1995007271 A1 (1996).
20. L. P. Wang *et al.*, Pyrrolopyridinone derivatives as bromodomain inhibitors and their preparation, Patent WO2013097601 A1 (2013).
21. G. C. Crawley *et al.*, *J. Med. Chem.* **35**, 2600–2609 (1992).
22. M. Ibrahim-Ouali, M. Santelli, *Steroids* **71**, 1025–1044 (2006).
23. H. Suginome, S. Yamada, J. B. Wang, *J. Org. Chem.* **55**, 2170–2176 (1990).
24. M. Ibrahim-Ouali, L. Rocheblave, *Steroids* **75**, 701–709 (2010).
25. X. Zhou, Y. Xu, G. Dong, *J. Am. Chem. Soc.* **143**, 20042–20048 (2021).
26. Y. Xu *et al.*, *Nature* **567**, 373–378 (2019).
27. S.-C. Chen *et al.*, *J. Am. Chem. Soc.* **143**, 14046–14052 (2021).
28. L. Wen *et al.*, *Science* **382**, 458–464 (2023).
29. A. J. Smaligo *et al.*, *Science* **364**, 681–685 (2019).
30. H. G. Yayla, H. Wang, K. T. Tarantino, H. S. Orbe, R. R. Knowles, *J. Am. Chem. Soc.* **138**, 10794–10797 (2016).
31. M. Šimek, S. Mahato, B. W. Dehnert, O. Kwon, *J. Am. Chem. Soc.* **147**, 2664–2674 (2025).
32. X. Zhou, T. Yu, G. Dong, *J. Am. Chem. Soc.* **144**, 9570–9575 (2022).
33. X. Zhou, Y. Xu, G. Dong, *Nat. Catal.* **4**, 703–710 (2021).
34. X. Zhou, D. Pyle, Z. Zhang, G. Dong, *Angew. Chem. Int. Ed.* **62**, e202213691 (2023).
35. Z. Zhang, Q. Zhu, D. Pyle, X. Zhou, G. Dong, *J. Am. Chem. Soc.* **145**, 21096–21103 (2023).
36. X. Wu, Z. Ma, T. Feng, C. Zhu, *Chem. Soc. Rev.* **50**, 11577–11613 (2021).
37. I. B. Seiple *et al.*, *J. Am. Chem. Soc.* **132**, 13194–13196 (2010).
38. C. Chatgilialoglu, C. Ferreri, Y. Landais, V. I. Timokhin, *Chem. Rev.* **118**, 6516–6572 (2018).
39. M. N. Levine, R. T. Raines, *Chem. Sci.* **3**, 2412–2420 (2012).
40. R. Nagarajan, B. H. Chollar, R. M. Dodson, *Chem. Commun.* **1967,** 550–552 (1967).

ACKNOWLEDGMENTS

We thank A. Barb (University of Chicago) for some compound characterizations and B. Wu (University of Chicago) for helpful discussions. **Funding:** The research was supported by NIGMS (R01GM109054) and the university of Chicago. Z.Z. thanks a BMS graduate fellowship. **Author contributions:** Z.Z. and G.D. conceived and designed the experiments. Z.Z. performed experiments. Z.Z. and G.D. wrote the manuscript. G.D. directed the research. **Competing interests:** A provisional patent has been filed on the NAHA reagents and their utilities (Zining Zhang, Guangbin Dong, University of Chicago). **Data and materials availability:** Metrical parameters for the structure of **3r** and PAI-Cyclohexanone are available free of charge from the Cambridge Crystallographic Data Centre (https://www.ccdc.cam.ac.uk/) under reference numbers CCDC 2416342 and CCDC 2423701. All other data are available in the manuscript or the supplementary materials.

SUPPLEMENTARY MATERIALS

science.org/doi/10.1126/science.adx2723
Materials and Methods; Supplementary Text; Figs. S1 to S5; Tables S1 to S7; References (*41*–*80*)

Submitted 6 March 2025; accepted 30 April 2025; published online 12 June 2025
10.1126/science.adx2723

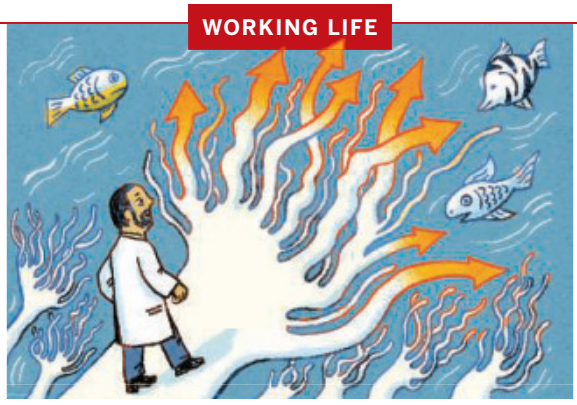

The power of reinvention

Iván M. Moya

I stared at my home aquarium, weary and uncertain about my professional future. Some years after returning home to Ecuador to lead a research group, I was battling the challenges of doing science in a resource-limited environment. The mesmerizing coral structures offered some comfort, until something unpleasant caught my attention: a single *Aiptasia*, the tiny, persistent anemone that aquarists regard as a pest. No matter how often you scrape them off, they grow back stronger. Then, I smiled. These humble-looking anemones, often dismissed, stood for something deeper: regeneration, resilience, and adaptation, all themes of my own professional journey.

My first scientific love was embryonic development—itself a form of reinvention. During my undergraduate studies I encountered *Gastrotheca riobambae*, a frog endemic to the Ecuadorian Andes that carries its eggs in a pouch on its back. How these bunches of cells self-organize to form a complex organism was a real marvel, and I thought I would study frogs for the rest of my life.

But Ecuador had no doctoral programs. To continue my training, I needed to look abroad. I was excited to get a spot in a program in Belgium—though none of the labs offered the opportunity to continue my frog work. So, I made my first pivot and joined a zebrafish lab, studying how fish embryos develop.

It didn't go as I hoped. Disoriented by the new culture, language, and research environment, I wrestled with whether I should try to stick it out and push through, or pivot yet again. After much reflection and several discussions with the program director, I came to understand that the lab environment simply wasn't a good fit for me—and that changing course wasn't failure, it was adaptability.

I still wanted to study embryonic development, but the opportunities were limited; the closest fit was in a mouse lab studying blood vessel development. I wasn't immediately inspired by the topic. But the more I learned, the more invested I became. It was a reassuring reminder that reinvention was also evolution. For my postdoc, I took another turn and returned to studying how tissues rebuild themselves, this time in the mouse liver. The science was exciting, and I felt professionally anchored. But once again, life pulled me in another direction.

My partner and I separated, and she returned to Ecuador with our children. I followed, though leaving my thriving postdoc behind and returning to a country where high-impact research felt almost impossible seemed like walking away from the future I had worked so hard for. I spent 2 years traveling back and forth between my native country and my postdoc lab, until a university in Ecuador trusted in the potential of my work and offered me a position as a lab head, allowing me to be home full time.

I was thrilled to be able to spend more time with my children. Professionally, though, it was a tough transition. Funding was scarce, infrastructure was limited, and I had to build everything from scratch. Lacking the specialized facilities and readily available reagents I once took for granted, I had to rely on resourcefulness and improvisation. Mouse models had to be adapted from a local zoo and validated for research. Mouse food had to be prepared by hand mixing supermarket ingredients. I had to convince government authorities that the antibodies and other basic reagents I wanted to work with were not public health threats. Meanwhile, the pressure to publish kept mounting. Could I truly make a difference here?

That's when I found myself staring at the *Aiptasia*—a cheap and accessible model organism that I suddenly saw as a fresh way to ask impactful questions about regeneration, resilience, and stress. That was 9 months ago. Since then, I've reinvented my research again, using *Aiptasia* to study how environmental stress and pollutants affect reef organisms.

My future is still uncertain; that's the nature of doing science in Ecuador. I'm counting on reinvention to re-emerge in moments of need. For many of us building research careers in the Global South, it is how we survive, grow, and keep moving forward. I no longer see reinvention as a deviation from a plan. It has become the most transformative force shaping my path. □

Iván M. Moya is an investigator at Ecuador's University of the Americas.
Send your career story to SciCareerEditor@aaas.org.

ILLUSTRATION: ROBERT NEUBECKER

myIDP ScienceCareers
INDIVIDUAL DEVELOPMENT PLAN

Features in myIDP include:

- Exercises to help you examine your skills, interests, and values.
- 20 career paths with a prediction of which ones best fit your skills and interests.
- A tool for setting strategic goals with optional reminders to keep you on track.
- Articles and resources to guide you through the process.
- Options to save materials online and print them for further review and discussion.
- A certificate of completion for users that finish myIDP.

Start planning your future today!
myIDP.sciencecareers.org

In partnership with:

FASEB Federation of American Societies for Experimental Biology
UMASS University of Massachusetts Medical School
UCSF University of California San Francisco
UIC
BURROUGHS WELLCOME FUND